

UNIVERSITY OF SOUTHAMPTON

Mesosopic Simulation of Polymers and Colloids

by

Danial Irfachsyad

Thesis submitted in partial fulfillment of the requirements for the
degree of Doctor of Philosophy

Department of Chemistry

Faculty of Science

May, 2002

UNIVERSITY OF SOUTHAMPTON

ABSTRACT

FACULTY OF SCIENCE

CHEMISTRY

Doctor of Philosophy

Mesoscopic Simulation of Polymers and Colloids

by

Danial Irfachsyad

This thesis reports the application of mesoscale modelling technique to study of the behaviour of complex fluids. We demonstrated their usefulness in the areas where conventional molecular simulation is not applicable due to the size, complexity and long relaxation time of such systems. We gave a brief introduction of two techniques of mesoscopic modelling, the Brownian dynamics method and the dissipative particle dynamics method. Both techniques use the Langevin equation to describe the motion of the particles. The Brownian dynamics method represents the case where the solvent particles can be described implicitly. We simulated colloidal particles immersed in an ionic solution using this technique. The dynamics of the colloidal particles were studied at different ionic strength and suspension density. The simulation showed the formation of aggregates and percolating structures depending on the position of the system in the phase diagram. We studied the local structure evolution after the quench and its relation to the mechanical stability.

In the dissipative particle dynamics, we included the solvent explicitly along with other components in the simulation. The method was used to simulate two layers of grafted polymer chains brought into close contact and sheared with respect to each other. We studied the system under different shear rates and observed the shear thinning property of the system. The viscosity was shown to vary at any point relative to the grafting surfaces due to the effect of polymer chains resisting the movement of the solvent particles. We studied the system under varying compression and shown that the off-diagonal and the normal pressure tensor were increasing exponentially with the pore width. The friction coefficient was found to be insensitive to the compression but in the absence of solvent, the friction coefficient decreased with decreasing pore width. We also studied the system at different solvent qualities and observed a narrow collapse transition of the layers as the solvent quality was varied from a good to a poor solvent.

Declaration

I hereby declare that the work presented within this thesis is my own and was undertaken wholly whilst registered as a full-time postgraduate at the University of Southampton.

Danial Irfachsyad

May 2002

TABLE OF CONTENTS

1. Introduction	1
1.1 Mesoscopic simulation	1
1.2. Brownian Dynamics	3
1.2.1. The Brownian dynamics algorithm	6
1.3. Dissipative particle dynamics	14
1.3.1. The DPD algorithm	17
1.4. Summary	22
2. Colloidal systems	26
2.1. Colloidal Interaction	27
2.2. DLVO interaction	31
2.3. Structure and dynamics	35
2.4. Rheological behaviour	39
3. Phase diagram construction	41
3.1. Theory	41
3.2. The Effective diameter	44
3.2.1. The hard sphere reference system	46
4. The model and the simulations	56
5. Particle gels formation with the inverse Debye length	62
5.1. Local structure and short range order	70
5.2. Long-range order	81
5.3. Mechanical stability	87
5.4. Summary	97
6. Particle gels formation with the volume fraction	99
6.1. Local structure and short range order	107
6.2. Long-range order	112
6.3. Mechanical stability	119
6.5. Summary	123
7. Polymer brushes	126
8. The model and the simulations	132
9. Theta solvent determination	138

10. Polymer brushes under varying shear rates	145
10.1 Brushes structure	145
10.2 Rheological behaviour.....	153
10.3 Summary.....	163
11. Polymer brushes under varying compression.....	166
11.1 Wet brushes	166
11.2 Dry brushes.....	173
11.3 Summary.....	178
12. Changes of polymer brushes with solvent quality	180
12.1 Brushes structure	180
12.2 Rheological behaviour.....	184
12.3 Summary.....	190
13. Conclusions	192
13.1 Part I: Brownian dynamics simulation of colloidal particles in ionic solution	192
13.2 Part II: Dissipative particle dynamics simulation of polymer brushes.....	196
13.3 Future research	198
References.....	199

LIST OF FIGURES

1.1	An illustration showing how the solvent particles are treated as a continuum in the Brownian dynamics technique.	3
1.2	Schematic description shows how DPD particles represent groups of particles in molecular scale.	14
1.3	Different form of interaction potentials: (a) The hard sphere potential, (b) The soft-sphere potential, (c) The Lennard Jones potential and (d) the DPD potential and force.	18
2.1	Sketch of the formation of aggregates after a quench due to the presence of (a) non-adsorbent polymers and (b) charged ions in a colloid system.	27
2.2	The typical plot for the depletion potential. The hard sphere potential has range σ .	29
2.3	Schematic illustration of the colloidal particles surrounded by the depletion regions of thickness R_g , which are the shaded areas. These are the regions that are not accessible to the polymers. The increase of the overlap zone, which is coloured black, will give an extra free volume for the polymers.	29
2.4	The sketch of the interaction potential for the DLVO. The hard sphere potential has a range of σ .	31
2.5	The effect of increasing (a) the surface potential and (b) the salts concentration towards the net interaction potential of colloids in ionic concentration.	34
3.1	The schematic profile of the DLVO, reference and the attractive perturbation potentials as a function interparticle distance. The corresponding locations for the primary maximum and the secondary minimum are included.	44
3.2	The effective hard sphere diameter as a function of the inverse Debye length at different surface potentials calculated using the Barker-Henderson equation.	45
3.3	Comparison between the $g(r)$ obtained analytically and from the Monte Carlo simulations for (a) fluid and (b) solid phases (fcc) at several values of volume fraction.	50

3.4	The schematic phase diagram and the plot of free energy per unit volume for one value of inverse Debye length, κ , to illustrate how the phase diagram is constructed.	52
3.5	The phase diagram for the DLVO potential at different surface potentials, showing the solid-fluid binodal and the spinodal lines.	53
3.6	The height of the primary maximum as a function of the inverse Debye length for three different values of surface potential.	54
4.1	The illustration showing the step-strain is imposed by moving the image of the simulation box at the top and bottom in the opposite direction at the first step of the simulation runs.	59
4.2	(a) The step-strain is applied at $t = 0$ and (b) the stress responses of the solid and fluid to the step-strain.	60
5.1	The average configurational energy as a function of time at different κ	63
5.2	The pictures of the resulting structures taken at times $471.24\tau_R$ and $\phi = 0.3$ for $\kappa =$ (a) $200\sigma^{-1}$, (b) $220\sigma^{-1}$, (c) $230\sigma^{-1}$ and (d) $250\sigma^{-1}$.	65
5.3	The mean square displacement as a function of time at different inverse Debye length.	66
5.4	The distribution profiles of the displacement at different stages for $\kappa =$ (a) $220\sigma^{-1}$ and (b) $250\sigma^{-1}$.	67
5.5	The snapshots of the structural evolution in the system containing 1372 particles at $\kappa = 220\sigma^{-1}$ and $\phi = 0.3$. The snapshots are taken at times (a) $94.25\tau_R$, (b) $164.93\tau_R$, and (c) $282.74\tau_R$ and (c) $400.55\tau_R$. The snapshots illustrate how the gel network develops.	69
5.6	The distribution profiles of the coordination numbers shown as a function of time for $\kappa\sigma$ equals to (a) $120\sigma^{-1}$, (b) $200\sigma^{-1}$ and (c) $210\sigma^{-1}$.	71
5.7	The distribution profiles of the coordination numbers shown as a function of time for κ equals to (a) $220\sigma^{-1}$, (b) $230\sigma^{-1}$ and (c) $250\sigma^{-1}$.	73
5.8	(a) The average coordination numbers as a function of time at different κ values and (b) the fraction of particles which are parts of the crystal domain.	74

5.9	The radial distribution function for system at equilibrium for systems (a) above and (b) below the spinodal line. The plots in 9(a) and 9(b) are shifted by 1 and 2 decades respectively for clarity.	77
5.10	The radial distribution function for $\kappa =$ (a) $220\sigma^{-1}$, (b) $230\sigma^{-1}$ and (c) $250\sigma^{-1}$ as a function of time. Each point is averaged over 1 τ_R .	80
5.11	The structure factors calculated from the structure factor as a function of time for $\kappa =$ (a) $120\sigma^{-1}$, (b) $200\sigma^{-1}$, (c) $210\sigma^{-1}$, (d) $220\sigma^{-1}$, (e) $230\sigma^{-1}$ and (f) $250\sigma^{-1}$.	82
5.12	The changes in (a) the position and (b) the height of the structure factor peaks as a function of time.	84
5.13	The plots of (a) $n(r)$ of the gel system at $\kappa = 220\sigma^{-1}$ at different gel ages. The dashed line is the guideline with the slope of 3. (b) The resulting fractal dimension calculated from the plots of $n(r)$ at various κ as a function of time.	86
5.14	(a) The storage modulus at infinite frequency as a function of the step strain, taken at different times during the run for $\kappa = 250\sigma^{-1}$ and $\phi = 0.3$ and (b) The comparison of the G_∞ obtained using 3 different methods for systems with 2 different κ values.	88
5.15	The storage modulus at infinite frequency as a function of time for various κ values at 30 % volume fraction.	90
5.16	The decays of the normalized shear modulus after the gel is subjected to a 0.5 % step-strain as a function of time, taken at $t = 282.7\tau_R$ for two different κ values at $\phi = 0.3$.	91
5.17	The stress decay after the step-strain is for system of various κ and 30 % volume fraction, taken at $t = 483\tau_R$. The plot for $\kappa = 200\sigma^{-1}$ is fitted to a power-law function and the plot for $\kappa = 220\sigma^{-1}$ is fitted to the stretch-exponential function.	91
5.18	The stress decay after the step-strain for systems of (a) $\kappa = 220\sigma^{-1}$ and (b) $\kappa = 250\sigma^{-1}$ taken at different gel ages. The plot are fitted to the stretch – exponential and the power –law function	93

5.19	(a) The equilibrium modulus as a function of the step strain, taken at different times during the run for $\kappa\sigma = 250$ and $\phi = 0.3$ and (b) the temporal evolution of the equilibrium modulus for several different step-strain.	95
5.20	The equilibrium modulus for various κ at different gel ages.	96
6.1	The pictures of the resulting structures taken at times $471.24\tau_R$ and $\kappa = 250\sigma^{-1}$ for $\phi =$ (a) 0.05, (b) 0.10, (c) 0.20 and (d) 0.40.	101
6.2	The mean square displacement, $W(t)$, as a function of time at different ϕ .	102
6.3	The distribution profiles of the displacement at different stages for $\phi =$ (a) 0.05 and (b) 0.40	103
6.4	The average interaction potential as a function of time at different κ .	105
6.5	(a) The negative of the interaction energy as a function of time plotted in the double-log axis. The dashed lines are the fitted power law approximation and (b) the power-law exponent for early time as a function of volume fraction.	106
6.6	The distribution profiles of the coordination numbers shown as a function of time for ϕ equals to (a) 0.05, (b) 0.20 and (c) 0.40.	108
6.7	(a) The fraction of particles with the maximum coordination number and (b) the average coordination numbers as a function of time for different volume fractions.	110
6.8	The radial distribution function for ϕ equals to (a) 0.05, (b) 0.20 and (c) 0.40. Each point is an average over $1 \tau_R$.	111
6.9	The structure factors calculated from the structure factor as a function of time for ϕ equals to (a) 0.05, (b) 0.10, (c) 0.20 and (d) 0.40	112
6.10	The temporal changes in (a) the location of the peak at long wavelength, k_{\max} , and (b) the size of the corresponding peaks of the structure factors, $S(k_{\max})$, at different volume fraction.	113
6.11	The phase separation process at early times after the quench for colloidal suspension of $\phi = 0.1$.	115
6.12	The phase separation process at early times after the quench for colloidal suspension of $\phi = 0.2$.	116

6.13	The plots of (a) the fractal dimensionality calculated from the plots of $n(r)$ at several volume fractions as a function of time and (b) the changes of the $n(r)$ as of r at $\phi = 0.05$ at various times.	117
6.14	(a) The storage modulus at high frequency as a function of time for various ϕ at $\kappa = 250\sigma^{-1}$ and (b) G_∞ plotted as a function of volume fraction at several gel ages.	120
6.15	The stress decay after the step-strain for systems $\kappa = 250\sigma^{-1}$ taken at different volume fraction. The plots are taken at $t = 282.74\tau_R$.	121
6.16	The equilibrium modulus for various κ at different gel ages.	122
7.1	The schematic illustrations of polymer chains grafted onto flat surface at different spacing, D . (a) $D > R_F$, (b) $D \leq R_F$ and (c) two grafted polymer surfaces are compressed against each other. L_Z is the separation distance between the grafted layers.	127
8.1	Schematic representation of the simulation box, showing the solvent and polymer	133
8.2	Temperature profile at different σ_R ($\Delta t = 0.02$, $\dot{\gamma} = 0.2$).	135
8.3	Graph of reduced temperature versus timestep ($\sigma_R = 50.0$, $\delta t = 0.02$).	136
9.1.	The figure illustrates different repulsive forces experienced by particles when they interact with like or unlike species.	139
9.2	The structure factors for polymers of different chain lengths in an athermal solution. The straight line shows the range of k where the scaling function is valid.	141
9.3	The structure factors of a polymer in a solution of different quality. The polymer chain consists of 50 beads.	142
9.4	The scaling exponent calculated from the structure factor as a function of solvent quality.	143
9.5	The mean square of the radius of the gyration for polymers immersed in dilute athermal, theta and poor solvents.	144
10.1	Density profiles for solvent particles and monomers at different shear rates	146

10.2	Density profiles for free-end of polymer chains at different shear rates.	147
10.3	Schematic illustration of the density profile between interpenetrating	148
10.4	The amount of interpenetration, $I(L_Z)$ as a function of shear rates at constant L_Z .	149
10.5	The mean end-to-end distance of polymer chains and its components	150
10.6	(a) The azimuthal distribution $n(\theta)$ and (b) The distribution of tilt angles, $n(\cos \theta)$ for different shear rates.	151
10.7	Velocity profile in the x-direction at different applied shear rates. The fitted hyperbolic tangential functions are plotted as black lines.	153
10.8	The shear rate profile at different applied shear rates.	154
10.9	(a) The off-diagonal and (b) the normal component of the stress tensor profiles with varying shear rates.	156
10.10	The plots of (a) the off-diagonal and the normal components of stress tensor and (b) the friction coefficient against shear rate.	158
10.11	(a) The shear viscosity profile and (b) the viscosity measured at the middle of the pore at different applied shear rates.	159
10.12	The Illustration of the hydrodynamics screening length within the brush.	160
10.13	The screening length profiles along z-axis ($\dot{\gamma} = 0.05$).	162
10.14	The screening length as a function of density. ($\dot{\gamma} = 0.05$).	163
10.15	Snapshots of the polymer brushes system at different shear rates, $\dot{\gamma}$.	165
11.1	Velocity profiles along z-axis at different value of pore width. The coordinates are normalised by the pore width.	166
11.2	The plots of the screening length at the surface, $\xi_l(0)$, at different pore widths, L_Z .	167
11.3	Density profiles of the lower brush at varying pore width as a function of $(z/L_Z)^2$. The profiles for L_Z equals to 17.035, 13.035 and 8.035 are shifted vertically by 0.2, 0.4 and 0.6 respectively for clearer view.	168

11.4	(a) The density profiles of the free-ends from both brushes and (b) from the lower brush only at varying pore width as a function of (z/L_Z) . All the plots are shifted vertically by 0.02 from each other for a clearer view.	169
11.5	Amount of interpenetration at varying pore width for wet brushes system.	170
11.6	(a) The mean off-diagonal and the normal stress tensor and (b) friction coefficient as a function of pore width, L_Z .	171
11.7	End-to-end distance with its components, parallel and perpendicular lengths, as a function of pore width for wet brushes.	172
11.8	The density profiles of the lower brush at varying pore width. For $L_Z = 13.035$ and 8.035 , the profiles are shifted by 0.5 and 1.0 respectively.	174
11.9	The contribution of each brush to the overall monomer density in the opposite region. For $L_Z = 13.035$ and 8.035 , the profiles are shifted vertically by 0.05 and 0.1 respectively.	174
11.10	Amount of interpenetration, as calculated using Eqn. 11.1 for dry brushes and also wet brushes for comparison.	175
11.11	Off-diagonal and normal stress tensors as a function of pore width and (b) the comparison of friction coefficient for dry and wet brushes with varying pore width.	176
11.12	The end-to-end length with its components, parallel and perpendicular lengths, as a function of pore width for both dry brushes.	177
11.13	Snapshots of the polymer brushes system at different pore widths.	179
12.1	The density profiles for polymer brushes surrounded by solvent particles with varying solvent quality. Negative values denote good solvent, the more positive the number, the poorer the solvent.	181
12.2	The density profiles of free ends polymer brushes with varying solvent quality.	182
12.3	End-to-end distance as a function of solvent quality.	183
12.4	The velocity profiles for polymer brushes surrounded by solvent particles with varying quality.	184
12.5	(a) The off-diagonal and (b) normal stress tensor profiles for polymer brushes system with varying solvent quality.	185

12.6	The averages of normal and off-diagonal stress tensor of polymer brushes as a function of solvent quality.	187
12.7	The friction coefficient and the amount of interpenetration as a function of solvent quality	188
12.8	Profiles of integral of difference between lateral and vertical components of stress tensor at different solvent quality, measured in ξ . The profile for $\xi = -10$ and -20 are shifted by 2 and 4 respectively.	189
12.11	Snapshots of the polymer brushes system at different solvent quality	191

LIST OF TABLES

4.1	The values for the parameters used in the simulation.	58
8.1	The values for the parameters used in the DPD simulation.	137

ACKNOWLEDGMENTS

First and foremost, I would like to thank my supervisor, Professor Dominic Tildelsey. He has provided me with guidance and encouragement needed to complete the work presented in this dissertation. I am very grateful to him for teaching me how to conduct research, how to clearly and effectively present my work, and how to organize and write technical papers. Special thanks to Dr. Neil Spenley and Dr. Maarten Hagen for many useful discussions and everyone in Statistics and Modelling unit, Unilever Research Port Sunlight, for their support during my time at the laboratories and making it very enjoyable and stimulating. I am thankful to know such quality people. Many thanks to Dr. John Melrose and Dr. Geoff Soga for their discussions in Brownian dynamics and colloids and for providing valuable references. Many thanks to Dr. Patrice Malfreyt for his discussions on the polymer brushes. I am also grateful for financial support through the studentship from The University of Southampton and Unilever Research Port Sunlight. I wish to acknowledge Dr. Jonathan Essex for his assistance and along with Dr George Attard for serving on my MPhil to PhD transfer examination. I would like to thank Hendro for all the help in Southampton. Finally, I would like to thank Hira and my family for who have always been tremendously supportive. They always encourage me to excel and to pursue my dreams.

Chapter 1

Introduction

1.1 Mesoscopic simulation

A complex fluid is a multicomponent heterogeneous system such as an emulsion, a liquid crystal, a colloidal suspension or a polymer mixture. There has been a considerable challenge to adequately model complex fluid systems in order to study their equilibrium and dynamical behaviour.

In principle, it is possible to simulate a multicomponent or complex fluid system using the conventional molecular dynamics (MD) method. That is to solve the Newtonian equation of the constituent atoms using a numerical method. The characteristic time and length scale of a complex system is often much larger than that can be routinely simulated using current computer technology. As an illustration, consider a typical time-step used in molecular dynamics simulation which is of the order of 1 femtosecond. If we set the simulation to run for 10^6 steps, the total time span will be about 1 nanosecond. The time needed for the long-time dynamical behaviour in a complex system, such as the timescale for the relaxation of an aggregated dispersion which can be estimated from the rate of the breakup for a doublet, shows that the simulation needs to be run for at least 6 orders of magnitude longer than this. Thus MD of atoms is inappropriate for studying systems containing colloidal particles and polymers over their natural timescales.

The large number of atoms also creates the need to simulate a larger system than normal. One example is a colloidal suspension system where the size and the number of colloidal particles are different in scale compared to the solvent particles. For example, the size range of the colloids is between 1 nm and 1 μm , which is up to 5 orders of magnitude greater than the size of the water molecules. Therefore if one is interested in studying the dynamic of the colloidal particles immersed in water, simulating the system in detail becomes expensive because of the large number of solvent particles that need to be included. Another difficulty arising from the large size ratio between the colloid and the

Introduction

solvent particles is the difference between the relaxation time of the solvent and the solute. As a comparison, the viscous relaxation time ($\rho\sigma^2/\eta$) for a buoyant colloidal particles whose diameter, σ , is 1 μm and immersed in water ($\rho = 1000 \text{ kg/m}^3$, $\eta = 10^{-3} \text{ Ns/m}^2$) is about 1 μs while the corresponding relaxation time for the water is in the order of 0.1 ps. This huge difference in the relaxation times clearly poses a problem if one wants to simulate the colloidal suspension system with atomistic detail.

Mesoscopic modelling attempts to overcome this problem. The method simulates a particle-based model of the system where the basic particle represents a colloidal particle or a significant fraction of a polymer chain. The solvent particles are averaged into the meso-particle-meso-particle interaction and do not appear explicitly in the model.

Two principal mesoscales modelling methods are the non-lattice and the lattice [5]. The lattice methods, such as the lattice gas[8] or lattice Boltzmann[7] methods, are faster than the non-lattice models. This is because the movement of the particles is restricted to a few sites defined by the lattice and their velocities are also restricted to values that ensure the movements only occur as a multiple integer of the lattice spacing. On the other hand, the non-lattice methods such as the Brownian dynamics and the dissipative particle dynamics methods, which we will employ in this thesis, allow the off-lattice motions and are therefore more realistic and more versatile. These methods are quite analogous to the molecular dynamics technique. The simplification for the description of the complex system in the simulation is achieved by inserting a stochastic term in the equations of motion. This term will represent the effect of the solvent components not described in detail in the model [2].

By ignoring some of the atomistic details, which are irrelevant for the fluid dynamics, a complex fluid system can be described and simulated within the capability of current computers. Here, we outline two non-lattice techniques to simulate such complex systems, namely the Brownian dynamics and the dissipative particle dynamics.

1.2. Brownian Dynamics

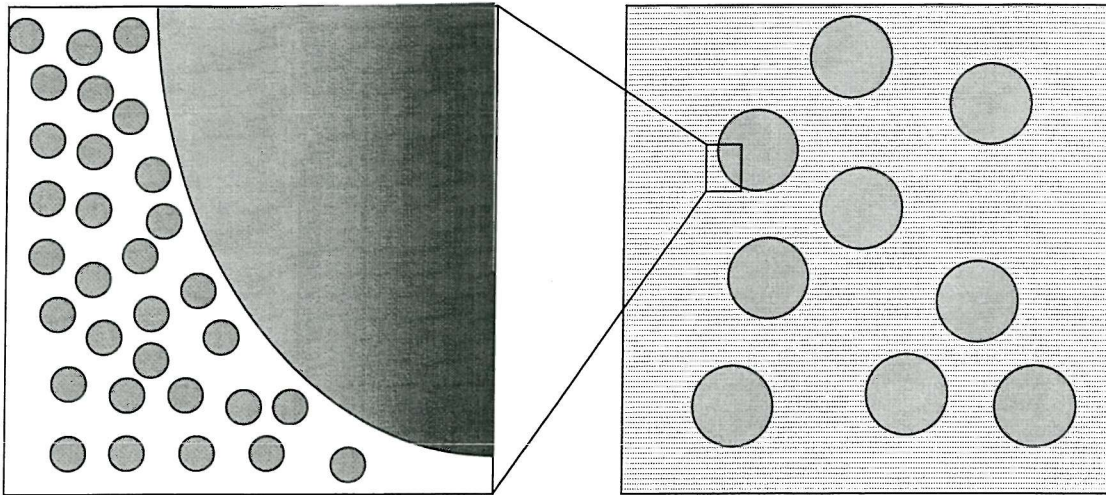


Figure 1.1. An illustration showing how the solvent particles are treated as a continuum in the Brownian dynamics technique.

The Brownian dynamics technique was first devised by Ermak and co-workers[8-11] and is now well established for simulation studies of complex system such as colloidal suspensions and polymer melts. The technique is based on the phenomenological equation from Langevin which describe the motion of macroscopic particles immersed in a background fluid. In this system, the particles are suspended in the fluid and they follow erratic trajectories due to constant bombardment of the solvent molecules. These solvent molecules are much smaller than the suspended particles. Typically the size of the solvent molecules is in the order of a few angstroms while the particles can be up to few microns.

The Brownian dynamics technique has been used to study systems such as polymers[11-14,42,165-168], proteins[169-172] and colloidal suspensions[15-16,173-176]. Ermak first utilised Brownian dynamics technique to study the motion of charged ions in a solution at infinite dilution[8]. The results were found to agree with the theoretical results calculated from Debye-Huckel theory and the Monte Carlo simulation.

Gaylor *et al.* [17] studied the many-body Brownian dynamics of strongly interacting particles in a dilute solution. They calculated the diffusion coefficient and found that under

Introduction

this condition, the effect of the hydrodynamic interactions on the dynamics of such systems was insignificant. Van Meegen and Snook[18] investigated the effect of neglecting the hydrodynamic interaction in the model of concentrated hard sphere dispersions. They calculated the time correlation function and compared the results from the Brownian dynamic simulation with and without a rigorous hydrodynamic treatment. They showed that employing a simple approximation for hydrodynamic interaction did not alter the features in the correlation function qualitatively, although they observed a faster rate of decay. They concluded that even though the Brownian dynamics technique was based on the equation of motion for a particle at infinite dilution, it could also be applied successfully to model systems at a moderate volume fraction of about 10 – 30 %.

The Brownian dynamics technique has been also extensively used to study the rheological behaviour of colloidal systems. Heyes and Mitchell [19] carried out the simulations of spherical colloidal particles with an r^{-n} inverse power repulsive interaction. The diffusion coefficient results with $n > 36$ are indistinguishable with the hard sphere results, suggesting that this value of n will give a reasonable representation of the hard sphere fluid. They have compared their simulation results with experimental measurements of the diffusion coefficient and find good agreement except in the case of high shear rates where the hydrodynamic interaction dominates over the Brownian force.

Bijsterbosch *et al.* [20] investigated the formation of particle gels by colloidal particles interacting with a short-range attractive potential. The model exhibited the formation of a flexible percolating network with a regular spacing and fractal structure commonly found in food particle gels. They found the volume fraction threshold of about 7 % above which a colloidal system will form a percolating structure. Bos and van Opheusden[21] reported a strong dependence of the fractal dimensionality of the gel networks on the well depth of the interaction potential. The gel is transient and it becomes more compact with age leading to a decrease in the fractal dimension.

An extensive study of colloidal particles interacting with a Lennard-Jones-type potential has been carried out by Lodge and Heyes[22-28]. They observed that the formation of the transient gels where the bonds within gel network are reversible. They found that the

morphology of the gel such as the thickness of the network linkage and the local order is sensitive to the range of the attractive part of the potential and also is the range of stability in the phase diagram. An amorphous or glassy structure was observed for longer range of interactions and the structure became more ordered with shorter range interactions. They characterised the rheological behaviour of the transient gel by calculating the linear stress relaxation function using the Green-Kubo equation. They observed a slower decay of the stress relaxation function when a longer-range interaction was applied. They also noted the rapid formation of compact clusters immediately after the quench which precedes the gel formation.

Soga *et al.* [29] reported an extensive study of the Brownian dynamics simulation of colloidal phase separation due to the presence of the soluble polymers in the suspension, known as the depletion flocculation. They studied the effect of the volume fraction and the range of interaction and observed a rich behaviour as the colloidal system was quenched into the fluid-crystal coexistence regime. They observed the formation of a percolating gel with either an ordered or glassy local structure which depended on the depth of the quench. They investigated the boundary where this percolation starts to occur[30] and noted a clear boundary between the fluid and the two-phase regions. For a system quenched into the two-phase region, the resulting structure exhibited a gel-like behaviour and showed the fractal characteristics of diffusion-limited aggregation. Although the timescale in their simulation is much shorter than the experiment, they found the evidence of aging in the gel which is identified by the restructuring of the local order.

A study of the kinetics of cluster formation in colloidal suspensions using Brownian dynamics was carried out by Puertas *et al.* [31]. The simulation modelled polymer latex particles interacting through the DLVO potential. The aggregation was studied by measuring the encounter probability of two colloidal particles. A good agreement was observed between the results of the simulation and from scattering experiments. They also observed a shift toward diffusion limited aggregation as the inverse Debye length of the interaction was increased.

Recently Hütter[32,178] studied coagulation in colloidal systems where the bonds forming the aggregates are irreversible. He analysed the effect of the coagulation rate on the local structure of the gel network at relatively high volume fraction. In the simulation, the colloidal particles interact through the DLVO potential. The rate of coagulation is varied by altering the shape of the primary maximum in the potential, which acts as a barrier for the irreversible aggregation. The results showed that in the case of the fast coagulation where there is no primary maximum barrier, the system formed a glassy disordered structure with no fractal regime. As the coagulation rate was reduced, the resulting structure becomes more porous.

1.2.1. The Brownian dynamics algorithm

In this section, we describe the background ideas behind the Brownian dynamics simulation and discuss the assumptions used to simplify the mesoscopic description. The technique as the name suggested, is based upon the idea of the erratic motion first discovered by John Brown when he observed pollen dispersed in water. Einstein[33] later developed the correct picture for the origin of this behaviour. The approximation is to assume the effect of the background solvent can be modelled as a sum of two terms in the equation of motion for the suspended particles. These are the friction force and the random Brownian force.

The friction force always acts in the opposite direction to the particle's motion and it is a function of the particle's velocity relative to the background fluid. The Brownian force describes the fluctuation experienced due to the constant collisions between the solvent and the suspended particles. In order to model the behaviour of the suspended particles, the time step must be much larger than the average collision time. The random force is then calculated from on the probability of a particle displacement as a result of many collisions with the surrounding solvent particles. Effectively, we treat the background solvent as a heat bath in which the energy is gained through the random force and dissipated through the friction force in order for the system to remain in thermal equilibrium. In the case where the mass and the size of the solute is much larger than the solvent particles, the Langevin equation can be used to describe the force experienced by a solute due to its interaction with the solvent particles. In the general form, the Langevin

equation is written as[34-35],

$$\mathbf{F}_i = m_i \frac{d \mathbf{v}_i(t)}{dt} = - \int_0^t K(t-t') \mathbf{v}_i(t') dt' + \mathbf{F}_i^B(t). \quad (1.1)$$

\mathbf{F}_i is the force acting on particle i , m_i is the particle's mass, \mathbf{v}_i is its velocity relative to the background fluid and \mathbf{F}_i^B is the random Brownian force. $K(t-t')$ is known as the memory function which reflects the contribution of the previous history of the particle motion towards the friction force. When the mass density of the solute is higher than the mass density of the solvent, the friction term can be further simplified and we obtain the strict Langevin equation, which will be used to compute trajectories in the Brownian dynamics,

$$\mathbf{F}_i = m_i \frac{d \mathbf{v}_i(t)}{dt} = - \xi \mathbf{v}_i(t) + \mathbf{F}_i^B(t). \quad (1.2)$$

ξ is the friction coefficient, which for the case of a dilute solution can be obtained using the Stoke's equation, $\xi = 3\pi\eta\sigma$, where η is the solvent viscosity and σ , the particle diameter.

Eqn (1.2) was first proposed by Langevin to describe the motion of Brownian particles while Eqn (1.1) is the result of a derivation from microscopic first principles. The derivation of Zwanzig[36] and Mori[37] is an attempt to create a formal basis for the phenomenological Langevin equation. They showed that the motion of the large particles can be described by using the generalized Langevin equation when the size of the large particles is many times larger than the solvent particles. In the special case where the mass density of the large particle is also much larger than the mass density of the solvent particles, the decay of the memory function is vary rapid. The system is essentially Markovian and hence the movement of the particles does not depend on their history. The equation then reduces further to the simpler form of the Langevin equation.

To solve the Langevin equation, we need to specify the characteristics of the random Brownian force. Firstly, we assume that the Brownian force has a zero mean over an

Introduction

ensemble of particles in thermal equilibrium,

$$\langle \mathbf{F}_i^B(t) \rangle = 0 \quad (1.3)$$

where $\langle \dots \rangle$ implies a time average. Secondly, the Brownian force is rapidly uncorrelated over a very short time,

$$\langle \mathbf{F}_i^B(t) \cdot \mathbf{F}_i^B(t + \tau) \rangle = 3C \delta(\tau), \quad (1.4)$$

where C is a constant and $\delta(\tau)$ is the Dirac delta function where

$$\delta(\tau) = 0 \text{ for } \tau \neq 0 \text{ and}$$

$$\int_{-\infty}^{\infty} \delta(\tau) d\tau = 1.$$

We can solve Eqn(1.2) by integrating it as a function of time to obtain

$$\mathbf{v}_i(t) = \exp\left(-\frac{\xi}{m} t\right) \left[\mathbf{v}_i(0) + \frac{1}{m} \int_0^t \exp\left(\frac{\xi}{m} t'\right) \mathbf{F}_i^B(t') dt' \right] \quad (1.5)$$

We calculate the ensemble average of the velocity and since $\langle \mathbf{F}_i^B(t) \rangle = 0$,

$$\langle |\mathbf{v}_i(t)| \rangle = |\mathbf{v}_i(0)| \exp\left(-\frac{\xi}{m} t\right). \quad (1.6)$$

Using Eqn (1.6), we can estimate the minimum time-step that is reasonable for our assumption that velocity decays at time considerably less than the time interval. Suppose that we define the time taken for the velocity to decay to just 1% of its initial value as the lower limit of for choosing the time step for the simulation. Recalling that $\xi = 3\pi\eta\sigma$ and $m = \rho\pi\sigma^3/6$ where ρ is the particle mass density, Eqn (1.6) then becomes,

$$\langle |\mathbf{v}_i(t)| \rangle = |\mathbf{v}_i(0)| \exp\left(-\frac{18\eta}{\rho\sigma^2} t\right). \quad (1.7)$$

We rearrange Eqn (1.7) to calculate the average decay time,

$$\langle t \rangle = \frac{\rho d^2}{18\eta} \ln \left(\frac{|\mathbf{v}_i(0)|}{\langle |\mathbf{v}_i(t)| \rangle} \right). \quad (1.8)$$

For a system of a chalk particle ($\rho = 2500 \text{ kg/m}^3$, $d = 1 \text{ }\mu\text{m}$) in water ($\eta = 0.001 \text{ Ns/m}^2$), the average time taken for the particle's velocity to decay to less than 1 % of its initial value is about $2.78 \times 10^{-7} \text{ s}$. This is long when compared with the average collision time which is in the order of 0.1 ps. Hence we would expect the Brownian force to vary much more rapidly than the velocity since the particles would have undergone many collisions during the time taken for the velocity to relax. The assumption also implies that the velocity and the Brownian force are independent of each other

$$\langle \mathbf{v}_i(0) \cdot \mathbf{F}_i^B(t) \rangle = 0. \quad (1.9)$$

Therefore the choice for the size of the timestep, Δt , is limited by the relaxation time for the velocity in the upper limit and the relaxation time for the Brownian force in the lower limit. The timestep is chosen so that the velocity has not changed significantly during one timestep but the force from the collisions with the solvent is expected to have fluctuated many times and uncorrelated with its initial value.

The ensemble average of the square of velocity is

$$\langle |\mathbf{v}_i(t)|^2 \rangle = |\mathbf{v}_i(0)|^2 e^{-\frac{2\xi t}{m}} + \frac{e^{-\frac{2\xi t}{m}}}{m^2} \int_0^t \int_0^t e^{\frac{\xi}{m}(t'+t'')} \langle \mathbf{F}_i^B(t') \cdot \mathbf{F}_i^B(t'') \rangle dt' dt''. \quad (1.10)$$

$\langle \mathbf{F}^B(t') \cdot \mathbf{F}^B(t'') \rangle$ is the correlation of the Brownian force at time t' with the Brownian force at time t'' . Substituting Eqn (1.4) gives

$$\langle |\mathbf{v}_i(t)|^2 \rangle = |\mathbf{v}_i(0)|^2 e^{-\frac{2\xi t}{m}} + \frac{e^{-\frac{2\xi t}{m}}}{m^2} \int_0^t \int_0^t e^{\frac{\xi}{m}(t'+t'')} C \delta(t' - t'') dt' dt''. \quad (1.11)$$

Introduction

$C\delta(t' - t'')$ has a peak at $t' = t''$ and it is a rapidly decreasing function away from these points. We let $t' - t'' = s_1$ and $t' + t'' = s_2$, the integral is then modified and written as

$$\langle |\mathbf{v}_i(t)|^2 \rangle = |\mathbf{v}_i(0)|^2 e^{-\frac{2\xi t}{m}} + \frac{3}{2} \frac{e^{-\frac{2\xi t}{m}}}{m^2} \int_0^{2t} e^{\frac{\xi}{m}(s_2)} ds_2 \int_{-\infty}^{\infty} C\delta(s_1) ds_1. \quad (1.12)$$

Eqn (1.12) is integrated to give,

$$\langle |\mathbf{v}_i(t)|^2 \rangle = |\mathbf{v}_i(0)|^2 e^{-\frac{2\xi t}{m}} + \frac{3C}{2m\xi} \left(1 - e^{-\frac{2\xi t}{m}} \right). \quad (1.13)$$

In the limit as t approaches infinity, the system will reach its equilibrium. We can relate C to the average energy, E , of a Brownian particle, which is given by the equipartition law of the classical statistical mechanics,

$$\langle E \rangle = \frac{1}{2} m \langle v^2 \rangle = \frac{1}{2} \frac{3C}{2\xi} = \frac{3}{2} k_B T. \quad (1.14)$$

Therefore we can rearrange Eqn (1.14) to give

$$C = 2\xi k_B T. \quad (1.15)$$

Substituting C in Eqn (1.4), the equation becomes

$$\langle \mathbf{F}_i^B(t) \cdot \mathbf{F}_i^B(t + \tau) \rangle = 6\xi k_B T \delta(\tau), \quad (1.16)$$

This is the expression for the fluctuation-dissipation theorem which links the friction and the Brownian forces. The equation ensures that the thermal equilibrium is maintained by specifying that the energy loss due to the dissipation by the friction force is channelled back into the system through the Brownian force.

Introduction

We obtain the particle's displacement by integrating the Langevin equation once more and the result is

$$\mathbf{r}_i(t + \Delta t) - \mathbf{r}_i(t) = \frac{\mathbf{v}_i(t) - \mathbf{v}_i(t + \Delta t)}{\xi} + \frac{1}{m\xi} \int_t^{t+\Delta t} \mathbf{F}_i^B(t') dt'. \quad (1.17)$$

In the non-inertial regime, the first term in the right-hand side is negligible and hence can be ignored. In an N -body simulation there is also an additional force between particles. This comes from the interaction between particles such as the repulsive hard sphere or Lennard-Jones potential, which is calculated as

$$\mathbf{F}_i^C = - \sum_{j \neq i}^N \frac{dU(r_{ij})}{dr} \frac{\mathbf{r}_{ij}}{r_{ij}}, \quad (1.18)$$

where \mathbf{F}_i^C is the conservative force acting on particle i and U is the corresponding interaction potential. It is therefore necessary to modify the equation of motion to take into account the effect of the interacting force. The equation then becomes,

$$\mathbf{r}_i(t + \Delta t) - \mathbf{r}_i(t) = \frac{1}{m\xi} \int_t^{t+\Delta t} [\mathbf{F}_i^C(t') + \mathbf{F}_i^B(t')] dt'. \quad (1.19)$$

With this additional term in the equation of motion, one would expect that the fluctuation-dissipation theorem should be modified to take into account the conservative force[38-39]. This is true in principal and Akesson and Johnson[40] have derived the fluctuation-dissipation theorem for the Brownian dynamics with interacting potential. They showed that the additional term in the fluctuation-dissipation theorem could be neglected in general cases where the force is varying slowly with the displacement.

If the time step that we choose is small enough so that the conservative force is largely unchanged over one time step, we can assume that the force is constant. We can then write the equation as

$$\mathbf{r}_i(t + \Delta t) = \mathbf{r}_i(t) + \frac{\Delta t}{m\xi} \mathbf{F}_i^C(t) + \Delta \mathbf{r}_i^B \quad (1.20)$$

where $\Delta \mathbf{r}_i^B$ is the displacement resulting from the Brownian force and is also taken to have a mean of zero. The mean square displacement contributed by the random force is assumed to be the same as the mean square displacement of a particle at infinite dilution,

$$\langle |\Delta \mathbf{r}_i^B| \rangle = 0 \quad (1.21)$$

and

$$\langle |\Delta \mathbf{r}_i^B|^2 \rangle = 2D_0 \Delta t \delta_{ij} . \quad (1.22)$$

We also need to obtain the correct distribution for the random force in order to model the simulation correctly. One requirement is that the Langevin equation should also obey the diffusion equation in the phase space described by the Smoluchowski equation[41],

$$\frac{\partial P}{\partial t} = \frac{\partial}{\partial x} \frac{1}{\xi} \left(k_B T \frac{\partial P}{\partial x} + P \frac{\partial U}{\partial x} \right), \quad (1.23)$$

where P is the probability distribution for the displacement Δr of particle i after a time interval Δt and U is again the potential due to particle's interaction with the surrounding particles. This is accomplished by specifying that the random displacement has the Gaussian distribution whose mean is zero and has the mean square average of $6D_0\Delta t$. The probability distribution of the random displacement at a given value of conservative force is written as,

$$P(\Delta r, \mathbf{F}^C(t)) = (4\pi D_0 \Delta t)^{-3/2} \exp \left[-\frac{(\Delta \mathbf{r} - D_0 \mathbf{F}^C(t) \Delta t / kT)^2}{4D_0 \Delta t} \right]. \quad (1.24)$$

D_0 is the diffusion coefficient and for a spherical particle at infinite dilution is equal to

$$D_0 = \frac{k_B T}{\xi} = \frac{k_B T}{3\pi\eta \sigma} . \quad (1.25)$$

Introduction

The probability distribution is Gaussian and the mean and the mean square displacement are written as,

$$\langle |\Delta \mathbf{r}| \rangle = \frac{D_0 \mathbf{F}(t) \Delta t}{k_B T}, \quad (1.26)$$

$$\langle |\Delta \mathbf{r}|^2 \rangle = 6D_0 \Delta t + \langle |\Delta \mathbf{r}| \rangle^2.$$

We neglect the many body hydrodynamic interactions in this study. We consider this as a valid assumption as the Brownian force is expected to dominate over the hydrodynamics force in the condition that we specify in the simulation.

We also assumed that during any one step, the momentum is hardly changed. This can be seen in the choice of units for our simulation. For the Brownian simulation in the overdamped limit which incorporates a relatively viscous solvent in the model, it is more appropriate to the viscosity as a unit. Hence the dimensionless unit of mass is $\eta^2 \sigma^4 / \epsilon$. If we take the following base units, the viscosity is that of water, $10^{-3} \text{Ns} / \text{m}^2$, the unit of energy as $k_B T$ and the unit of length is the particle diameter, taken to be $1 \mu\text{m}$. One unit of mass will correspond to $2.43 \times 10^{-10} \text{kg}$. If the colloidal particle is buoyant so that its density is roughly equal to the density of the water solvent ($\sim 1000 \text{kg} / \text{m}^3$), its mass is then equal to $5.24 \times 10^{-16} \text{kg}$ or 2.15×10^{-7} in reduced unit. This is small and hence we can assume that the inertial effects are insignificant. In other words, the simulations explore a system whose the Reynolds number is very small. The Reynolds number is the ratio between the inertial force and the viscous force, $\text{Re} = \rho v d / \eta$.

There are more rigorous treatments of hydrodynamic force proposed by various people[9,43-47,194]. The use of hydrodynamic tensors has been proven to be expensive and so far the simulation studies have been only limited to few particles. Because one of the our objective is to follow the dynamics of the system for reasonably long time to study the affect of aging, we decided to use the simplest approximation to compute the hydrodynamic force. Since the motion of the particles in the Brownian dynamics simulation is overdamped, there is no need to incorporate a thermostat which usually employed in molecular dynamics to stabilise the simulation.

1.3. Dissipative particle dynamics

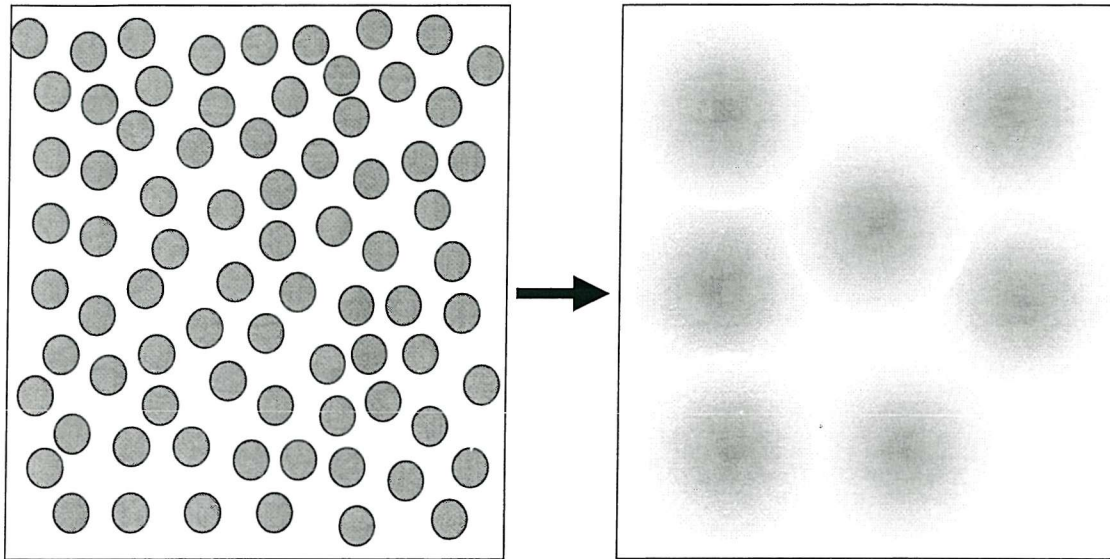


Figure 1.2. Schematic description shows how DPD particles represent groups of particles in molecular scale.

Another technique that can be used to carry out the computer simulation on the hydrodynamic scale is dissipative particle dynamics (DPD) method. This was first proposed by Hoogerbrugge and Koelman[48-49] and as in the Brownian dynamics, the method is also based on a Langevin-like equation.

The DPD simulation attempts to combine the fluid particle description of a lattice gas simulation with a particle-based method. In DPD, the fluid is modelled by a set of interacting particles, each of which represents a mesoscopic region of fluid, moving in continuous space and discrete time under mutual forces. By allowing each particle to describe not just a single atom, but a fluid element, a much larger system can then be described. As in a Brownian dynamics simulation, the particles interact via the conservative force, the random Brownian force and the friction or dissipative force. The conservative force originates from the particle overlap while the random and the dissipative forces act as a thermostat which keep the temperature of the system constant. Espanol and Warren[50] have specified the condition at which the simulation would

model the canonical ensemble at equilibrium conditions. This condition is satisfied when the dissipative and the random forces obey the fluctuation-dissipation theorem. All the forces are pairwise additive and satisfy Newton's third law and the total momentum in the system is therefore conserved although the energy is not conserved. Consequently, the system exhibits the correct hydrodynamic behaviour in the limit of long time and length scale. Coveney and Espanol[51] have shown that the detailed balance is also satisfied in the multicomponent system.

The DPD technique has recently gained acceptance as a method to simulate complex systems and has been used to model systems such as polymer solutions, colloidal suspensions and surfactants systems. DPD was first used to simulate a hard sphere colloidal suspension by Hoogerbrugge[49]. The colloids are modelled by linking several DPD particles. Boek *et al.* [52-53] extended the work to study the rheology of colloidal suspension using a non equilibrium method. They showed that the low and high shear viscosity from the model of spherical colloids gave good agreement with the experimental results by van der Werff and de Kruif[54].

Espanol[55] developed the coarse grained description of polymer chains. In the limit of a very long chain, the chain can be described by clusters connected by harmonic chains that interact elastically and dissipatively. The description of the interactions between the clusters is identical to the description of the fluid particles in DPD. Schlijper *et al.*[57] explored the use of DPD to model a non-Newtonian system. They simulated a rigid dumbbells system which was modelled by linking DPD particles with Fraenkel springs with high spring constant to restrict the spring extension. The model was shown to produce the shear thinning behaviour as predicted by theory. The solvent quality in the model was also varied to represent the solution of polymers in good and theta solvents. The simulation gave a reasonable fit to the predicted scaling relationship from the Rouse/Zimm model for polymer solutions.

Spensley[56] recently studied the scaling laws for a model polymer in dilute solution and in the melt to investigate whether DPD is appropriate to simulate such system. The results showed that for a polymer system in a good solvent, there is a satisfactory agreement with

the Rouse model, which predicts scaling law of polymers in a free draining solution.

DPD has been used also to study phase behaviour of a simple surfactant in solution by varying the concentration of the surfactant. Jury *et al.* [57] reported a simulation of a dense amphiphilic solution using a model of rigid dimers in a solvent. Several phases were observed including micellar, lamellar and hexagonal. The model mimics the real phase behaviour of the non-ionic surfactant, C₁₂EO₆. Another study with a longer block copolymer [58,193] has also been performed to study the formation of the mesophases. A comparative study between the DPD and the Brownian dynamics techniques has been undertaken for this system and it revealed significant differences in the dynamic formation of the hexagonal phase in a copolymer system. This suggests that the hydrodynamic interaction plays an important role in the mesoscale domain growth [59].

Gibson *et al.* [60-61] modelled the adsorption of a colloidal particle onto a surface using DPD. The simulation shows that the presence of polymers at low concentration promotes the adsorption process of the colloidal particle onto the surface. In the case where the polymers are adsorbed onto the surface, they studied the effect of the surface coverage and the length of the polymer chains on the deposition of the colloidal particles. Their results suggest the chain length of the adsorbed polymers is more important in controlling the particle deposition than the density of polymer chains.

Malfreyt and Tildesley [62] investigated the applicability of DPD to model the interaction between grafted polymer brushes. They showed that the simulation gave the correct density profile for the brushes as predicted by the self-consistent field theory. They varied the surface coverage and the length of the polymers while the systems are simulated at constant number density by varying the number of solvent particles. They demonstrated the sensitivity of the brushes profile to the surface coverage and the chain length.

Jones *et al.* [63] and Clark *et al.* [64] simulated a pendant drop under the influence of gravitational and shear fields. They compared the mechanism of the break up in the simulation with the experimental observation of the break up of a silicon droplet in a shear field. Both studies show good agreements with experiments. The model reproduced the

detachment process where the drop was seen to elongate and formed a neck support before it detached completely with increasing shear flow.

1.3.1. The DPD algorithm

As in molecular dynamics, the meso-particles move under the action of forces. In contrast with the Brownian dynamics method, all the forces are the results of the interactions with other particles and are pairwise additive. Each particle is described by its vector position and momentum, \mathbf{r}_i and \mathbf{p}_i respectively, and they move according to Newton's second law of motion,

$$\dot{\mathbf{p}}_i = \frac{d\mathbf{p}_i}{dt} = \sum_{i \neq j}^N \mathbf{F}_{ij} \quad (1.27)$$

where \mathbf{F}_{ij} is the total forces acting on particle i due to its neighbour j . The dot represents a time derivative. The velocity, \mathbf{v}_i , is defined as

$$\mathbf{v}_i = \dot{\mathbf{r}}_i = \frac{\mathbf{p}_i}{m_i} \quad (1.28)$$

For simplicity, we set the masses of all particles, m , to 1, so that the force acting on particles will be equal to the acceleration. This is in contrast with the Brownian dynamics where the viscosity is taken as unity.

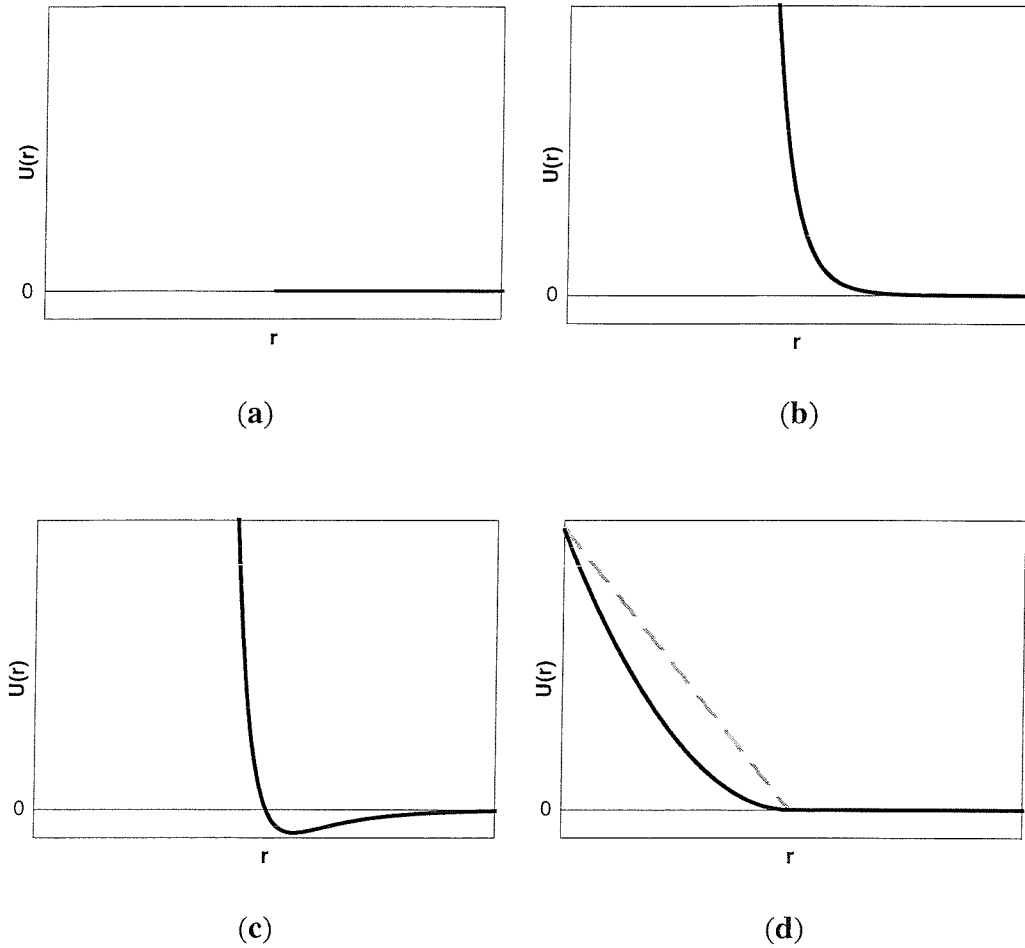


Figure 1.3. Different form of interaction potentials: (a) The hard sphere potential, (b) The soft-sphere potential, (c) The Lennard Jones potential and (d) the DPD potential and force (dashed line).

In the DPD method, each particle is subjected to three distinct forces: the conservative force, the dissipative force and the random force. These forces are pairwise additive and act along the line of centres and conserve linear momentum,

$$\mathbf{F}_{ij} = \sum_{j \neq i} (\mathbf{F}_{ij}^C + \mathbf{F}_{ij}^D + \mathbf{F}_{ij}^R). \quad (1.29)$$

The conservative force, \mathbf{F}_{ij}^C , is derived from the interparticle potentials. As the DPD particle is not actually representing a single atom or molecules, but a fluid element, it is not sensible to use a realistic intermolecular force. We expect that the interaction force on the mesoscopic scale is repulsive in nature. Since the particles in the simulation represent

Introduction

a fluid element, a soft potential would be appropriate to describe the interaction between the momentum carriers. The advantage of this force, which is linear with separation, is that the time-step in the simulation can be large. For a potential such as the Lennard-Jones potential, the force diverges as the particle separation becomes small. This would cause catastrophic problems when the time step is large since particles would overlap in one time step and the equation of motion would be too stiff to solve numerically. Fig 1.3 illustrates different form of interaction potential commonly used in molecular simulation compared with the potential utilised in DPD method.

In addition to soft repulsive interaction, we can add other types of conservative forces such as the electrostatic interactions and polymer spring forces. Indeed we will employ polymer spring forces in our simulation to simulate the polymer chains. It is important to remember that the spring forces must themselves be soft within the spirit of the method.

The conservative force is

$$\mathbf{F}_{ij}^c = \begin{cases} a_{ij} (1 - r_{ij}) \hat{\mathbf{r}}_{ij} & \text{for } r_{ij} < 1 \\ 0 & r_{ij} \geq 1 \end{cases} \quad (1.30)$$

where a_{ij} is the maximum repulsion between particle i and j , r_c is the cutoff radius, $r_{ij} = |r_i - r_j|$ and $\hat{\mathbf{r}}_{ij}$ is the unit vector from particle j to particle i . In our simulation, r_c , the cutoff radius, is set to 1.0.

The model also contains a dissipative force, F_{ij}^D , and a random force, F_{ij}^R . The forces are determined by the requirement that the dissipative force is a linear function of the momentum while the random force is independent of the momentum. One form of the forces proposed which can satisfy the requirements are

$$\mathbf{F}_{ij}^D = -\gamma w^D(r_{ij}) (\hat{\mathbf{r}}_{ij} \cdot \mathbf{v}_{ij}) \hat{\mathbf{r}}_{ij} \quad \text{and} \quad (1.31)$$
$$\mathbf{F}_{ij}^R = \sigma_{\text{ran}} w^R(r_{ij})_{ij} (\delta t)^{-1/2} \hat{\mathbf{r}}_{ij}$$

Introduction

where $\mathbf{v}_{ij} = \mathbf{v}_i - \mathbf{v}_j$. w^D and w^R are dimensionless weighting functions, σ_{ran} and γ are constants. ξ_{ij} is a randomly fluctuating variable whose mean is 0 and whose variance is $\langle \xi_{ij}(t) \xi_{kl}(t') \rangle = (\delta_{ij}\delta_{kl} + \delta_{il}\delta_{jk})\delta(t - t')$. The term $\delta t^{-1/2}$ is introduced because of the requirement for the variance to be independent of the size of the time step[65].

The dissipative force acts to slow the relative velocity of two particles and removes the kinetic energy. The random force, on the other hand, will convert the energy dissipated from the system into a Brownian force, producing random motion of the particles. Espanol and Warren[50] showed that in order to satisfy the fluctuation-dissipation theorem, dissipative and random forces should be related as follows

$$\begin{aligned} w^D(r_{ij}) &= [w^R(r_{ij})]^2 \text{ and} \\ \sigma_{\text{ran}}^2 &= 2 \gamma k_B T \end{aligned} \quad (1.33)$$

where k_B is Boltzmann's constant and T is the temperature of the system. Note that these results are exact in the limit $\delta t \rightarrow 0$ [37].

The weighting function of w^R is typically chosen to be

$$w^R(r_{ij}) = \begin{cases} 1 - r_{ij} & \text{for } r_{ij} < r_c \\ 0 & r_{ij} \geq r_c \end{cases} \quad (1.34)$$

The DPD algorithm is implemented by calculating the movement and interaction of the particles using the equation of forces above with a discrete time step.

In order to simulate polymer chains, we added another term to the conservative force to describe the additional forces between adjacent particles in the chain. We use

$$\mathbf{F}_{ij}^B = k (r_{ij} - r_{eq}) \hat{\mathbf{r}}_{ij} \quad (1.35)$$

where k is the spring constant which control the stiffness of the chains and r_{eq} is the

equilibrium spring length.

A modified velocity-Verlet algorithm is used to solve the equations of motion in the simulation, as suggested by Groot and Warren[65].

$$\begin{aligned} r_i(t + \delta t) &= r_i(t) + \delta t v_i(t) + \frac{1}{2} (\delta t)^2 F_i(t) \\ \tilde{v}_i(t + \delta t) &= v_i(t) + \lambda \delta t F_i(t) \\ F_i(t + \delta t) &= F_i(r_i(t + \delta t), \tilde{v}_i(t + \delta t)) \\ v_i(t + \delta t) &= \tilde{v}_i(t + \delta t) + \frac{1}{2} (\delta t) (F_i(t + \delta t)) \end{aligned} \tag{1.36}$$

In this algorithm, a more accurate computation is obtained by predicting an intermediate velocity first to calculate the force and then correcting this velocity in the final step. Since the force is still calculated once per iteration, there is virtually no increase in computational cost. The value of λ is chosen to be $\frac{1}{2}$. This is the value in which the actual velocity-Verlet algorithm would be recovered when the force is independent of the velocity.

1.4. Summary

In this chapter we have given a brief introduction to the two techniques of mesoscopic modelling, Brownian dynamics and the dissipative particle dynamics. Both techniques use the Langevin equation to describe the motion of the particles. In the Brownian dynamics technique, the motion of the particles is assumed to compose of the hydrodynamic friction force, the random Brownian force and the conservative force due to direct interaction with the neighbours. Its link with the microscopic system has been established by several author using the projection operator method proposed by Mori. These studies have highlighted the range of validity for the Langevin equation. The generalized Langevin equation is valid in the case where the ratio of the mass and the ratio of number density between the solute and the solvent are much larger than 1. In the case where the mass density of the solute is larger than the mass density of the solvent, the generalized Langevin equation can be reduced further to the original Langevin equation.

In the regime where the hydrodynamics have no significant effect such as in the dilute solution, the hydrodynamic force can be approximated using the Stoke's equation. This results in a very simple equation algorithm to solve the equations of motion. In the regime where the hydrodynamic interaction dominates, the description of the particle motion is more complicated because of the need to compute the hydrodynamics tensor. The Brownian dynamics technique, which incorporates this hydrodynamics tensor, is commonly known as Stokesian dynamics[43]. This technique enables the simulation to explore the regime where the hydrodynamics may be more important than the Brownian force. One drawback of this method is that the use of hydrodynamics tensor is very expensive computationally and hence the technique is limited to a few particles. So far the Stokesian dynamics has only been used in the small system simulation of up to 100 particles and mainly employed to study the break up of aggregates under shear and rheological studies of hard sphere system[190-192].

In DPD, all the forces are taken to be pairwise and the technique is momentum conserving. Hence DPD obeys the Navier-Stokes relationship so that we can expect the

Introduction

long-range hydrodynamics to appear naturally. The coarse-graining method is employed and the particles in the simulation are considered to represent a group of molecules. The coarse-graining method has been well established for simulating polymer system where the polymers are described as a chain of blobs and springs, which can be related to the real polymers through the persistence length. Since the solvent is also represented as particles in the model, the technique allows us to simulate the solvent in more details than with the Brownian dynamics method. The method is also Galilean invariant since the velocity is not measured relative to some background fluid. Hence DPD offers a promising technique to study complex system.

There has been also a study to investigate the effect of hydrodynamic interaction by comparing the simulation results from DPD and Brownian dynamics. Groot *et al.*[59] investigated the role of hydrodynamic interaction by simulating a melt of diblock copolymers using DPD and Brownian dynamics with simple hydrodynamic interactions. They observed a marked difference between the results from those models in the kinetics of the asymmetric block copolymers. The absence of hydrodynamic interaction was found to prevent the block copolymers reaching the hexagonal phase as observed in the experiment. In the case of symmetric block copolymer the difference is not noticeable in the evolution of the system and lamellar phases are formed spontaneously by spinodal decomposition.

In this work, we utilise the mesoscopic modelling technique to model two complex systems. In the first part we report the simulation study of a system containing colloidal particles immersed in an electrolyte solution. We vary the salt concentration that determines the effective interaction between colloidal particles. This results in a rich phase diagram. When the system is in the metastable state, we expect the formation of colloidal structure that can span the whole simulation box, commonly known as gels. We intend to study the gel formation and also the effect of the salt concentration on properties of the structure. We will probe the mechanical properties of the gels using the step-strain method.

In the second part, we present the study of two grafted polymer layers brought into close

Introduction

contact and moved under shear in the direction parallel to each other. We study the system with varying shear rates, pore separation and solvent quality. We also carry out a set of simulations of dry brushes with varying pore separation. We will employ the DPD method for the simulation. It has been reported that DPD is a simulation method suitable for polymer systems[55-56, 66-70,195-198]. One advantage for DPD is that we are able to represent solvent particles explicitly and this enables us to study the interaction between solvent particle and polymers in more detail.

PART I
BROWNIAN DYNAMICS
SIMULATION OF COLLOIDAL
PARTICLES IN IONIC SOLUTION

Chapter 2

Colloidal systems

A colloidal particle is commonly defined as a particle whose size is significantly larger than typical molecule and has a small enough mass so that it is largely buoyant when immersed in a solution. The size of a colloidal particle usually ranges from few nanometres up to about one micrometre. Many biological and complex materials are within the colloidal range, for example viruses, micelles, proteins and latex spheres[77-79,152,199-202].

There are numerous industrial processes which make use of colloids and they can be found in many everyday items ranging from yoghurt, paints and cosmetics to toothpaste. Hence the knowledge of the stability and the kinetic behaviour of colloidal system is relevant to Industry. A remarkable analogy exists between the statistical behaviour of the colloidal dispersion and the behaviour of a simple fluid in equilibrium. We can ignore the solvent in the colloidal system by renormalising the intercolloidal interaction and treating the colloidal particles as a set of atoms. The colloidal suspension is suitable as an ideal model to study the characteristics and dynamics of atomic systems in detail because it is easy to shape the interaction potential in the colloids system. This interaction potential is varied by adjusting the salt or free polymer concentration in the suspension.

2.1. Colloidal Interaction

In a suspension with particles interacting through complicated interactions, the phase behaviour becomes more interesting. In this situation, the phase behaviour, which is analogous to that of a molecular system, can be observed directly. Depending on the interaction between the particles, a colloidal solution in equilibrium may stay dispersed with a structure similar to a homogeneous fluid. It can also phase separate to form an aggregate structure similar to a crystal or an amorphous solid. The difference is that in the colloidal system, the existence of two-fluid phase (vapour-liquid) in equilibrium is not common since the range of interaction is short compared to the particle size. This phenomena has been observed in several simulation studies[71-73] in which the results showed that the two-fluid phase region vanished when the attractive interaction is insignificant beyond 1.4σ . In our simulation, the value of the DLVO potential falls to 1% of the minimum within the distance of 1.38σ . This is in comparison with, say, the Lennard Jones potential in which the corresponding distance is 2.71σ .

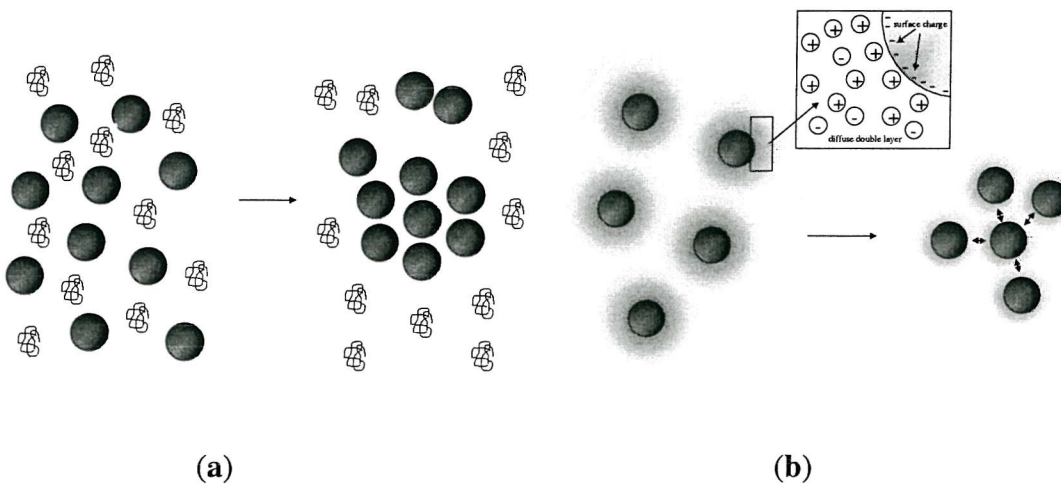


Figure 2.1. Sketch of the formation of aggregates after a quench due to the presence of (a) non-adsorbent polymers and (b) charged ions in a colloid system.

There are two types of contributions which will produce the net interaction between colloidal particles. One is the direct interaction between the colloids such as the excluded volume interaction due to their size. Another is the London-van der Waals interaction that comes from the fluctuation of instantaneous dipoles of the constituent atoms. The second interaction is mediated by the solvent. This may be mediated by the presence of polymers or charged ions in the solution. Fig 2.1 illustrates the formation of aggregates due to the presence of the polymers and charged ions in colloidal solution. These phenomena are observed experimentally.

The solution properties determine the effective interaction between the colloidal particles. This makes it possible to study the effect of the range and the shape of interaction on the behaviour of the system, since it is relatively easy to vary parameters, such as the polymer or salt concentration experimentally [15,74]. Fig 2.2 shows the depletion interactions due to the presence of non-adsorbing polymers or charged ions.

In a solution of colloids containing non-adsorbing polymers, the presence of the polymers can induce a net attractive force that will cause the colloids to aggregate. This force arising from the imbalance of the osmotic pressure due to some regions surrounding the colloidal particles that are not available to the polymers. The imbalance in osmotic pressure pushes the colloidal particles closer to increase the free space available for the polymers. The resulting attractive interaction between the colloidal particles is known as the depletion force. A model describing this interaction has been proposed by Asakura and Oosawa[149-150]. It has been found that this model work very well in describing colloidal solution with polymers of size up to ca. 70 % of the size of colloidal particle [71]. In their model, the polymers in the solution are described as spheres with the radius of gyration r_g . These polymers are able to interpenetrate each other but behave as hard spheres when interacting with the colloidal particles of diameter σ . This creates a layer of thickness r_g around the surface of the colloids that is not available for the polymers. The resulting depletion potential is given as

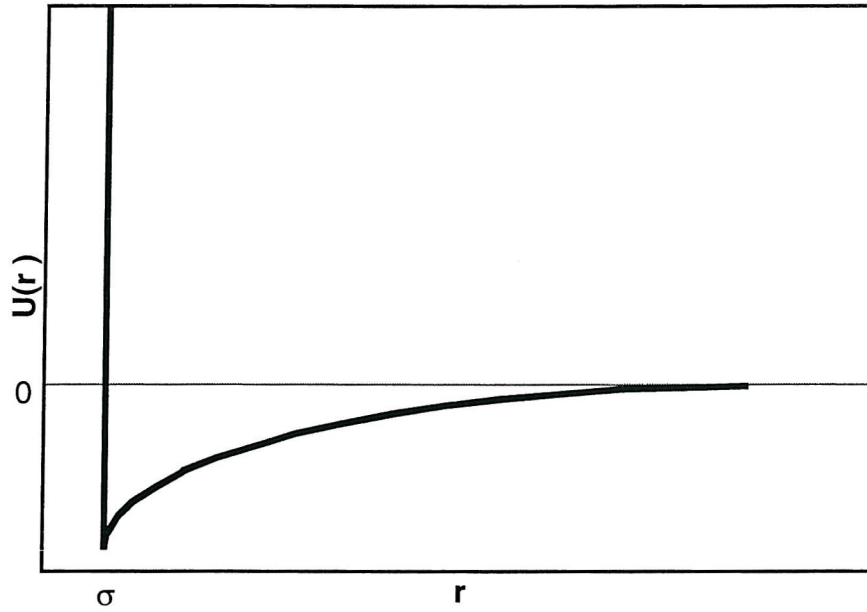


Figure 2.2. The typical plot for the depletion potential. The hard sphere potential has range σ .

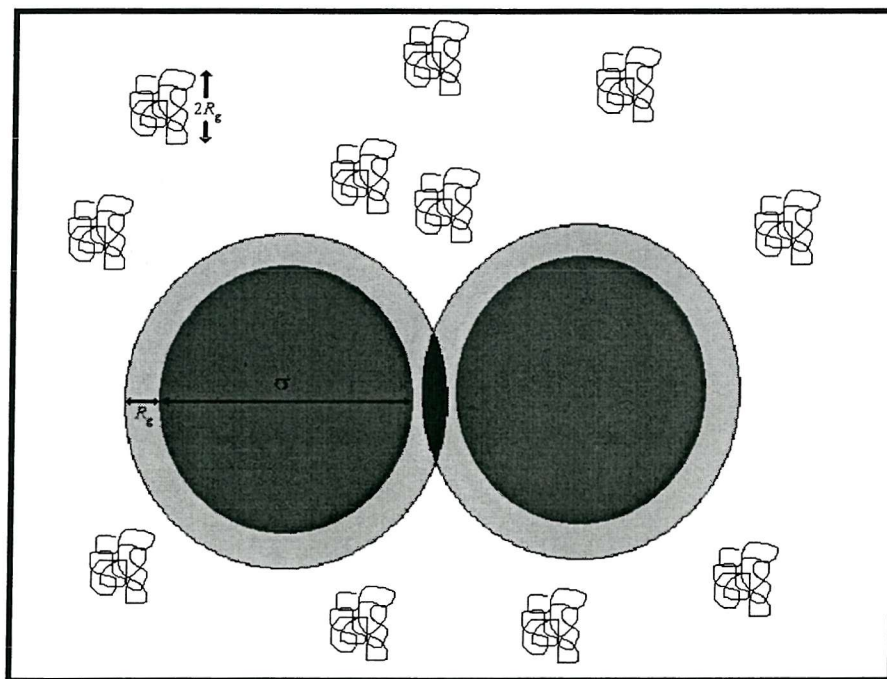


Figure 2.3. Schematic illustration of the colloidal particles surrounded by the depletion regions of thickness R_g , which are the shaded areas. These are the regions that are not accessible to the polymers. The increase of the overlap zone, which is coloured black, will give an extra free volume for the polymers.

$$U_{AO}(r_{ij}) = \begin{cases} -P_{os} V_{ov} & \text{for } \sigma \leq r_{ij} \leq \sigma + r_g \\ 0 & \text{for } r_{ij} > \sigma + r_g \end{cases} . \quad (2.1a)$$

$P_{os} = N_p k_B T / V_{free}$ is the osmotic pressure of the polymers where N_p is the number of the polymers and V_{free} is the free volume available for the polymers. The volume of the depletion zone, V_{ov} , due to two colloidal particles i and j of diameter σ which are overlapping at a distance of r_{ij} , is

$$V_{ov}(r_{ij}) = \left[1 - \frac{3r_{ij}}{\sigma(1+\xi)} + \frac{1}{2} \left(\frac{r_{ij}}{\sigma(1+\xi)} \right)^3 \right] \frac{\pi}{6} \sigma^3 (1+\xi)^3. \quad (2.1b)$$

ξ is the ratio between the radius of gyration of the polymers and the radius of the colloidal particles. This is the relative measure of the range of the attractive interaction compared to the size of the colloidal particles. The strength of the interaction is determined by the osmotic pressure, which in turn depends on the polymer concentration.

2.2. DLVO interaction

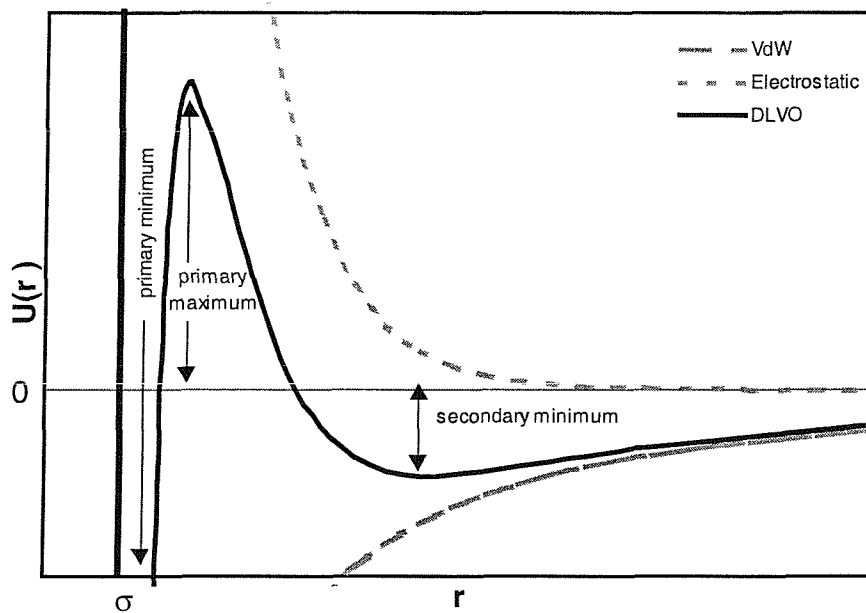


Figure 2.4. The sketch of the interaction potential for the DLVO. The hard sphere potential has a range of σ .

For colloidal particles immersed in an ionic solution, the interactions may be described by the theory developed by Derjaguin, Landau, Verwey and Overbeek[3, 75-78,163] (DLVO). According to DLVO theory, the net interaction between the charged particles, U_{DLVO} , is the sum of the electrostatic interaction, U_{el} , and the attractive van der Waals interaction, U_{vdw} ,

$$U_{DLVO}(r_{ij}) = U_{el}(r_{ij}) + U_{vdw}(r_{ij}). \quad (2.2)$$

The van der Waals attraction between two colloidal particles comes from the interaction of the induced dipole-dipole interaction between atoms which constitute the colloidal particles. This interaction is always present, as it does not need the existence of the permanent polarity. For two spherical particles of the same size, Hamaker derived the following expression for the van der Waals attractive interaction,

$$U_{\text{vdw}}(r_{ij}) = -\frac{A_H}{12} \left[\frac{\sigma^2}{r_{ij}^2 - \sigma^2} + \frac{\sigma^2}{r_{ij}^2} + 2 \ln \left(\frac{r_{ij}^2 - \sigma^2}{\sigma^2} \right) \right] \text{ for } r_{ij} \geq \sigma. \quad (2.3)$$

A_H is a constant known as the Hamaker constant whose value depends on the materials of the particles and the suspension medium. From the equation above, we see that the interaction potential goes to a very deep minimum at very close distance. The interaction then reaches infinity when two particles touch, although in reality this does not happen. This is because there will be a strong repulsion which prevent the overlap of the electron clouds. There is also the presence of the solvation force, associated with the finite size of the solvent molecules, which is not taken into account in the above equation. Nevertheless the potential minimum is still very deep and this is known as the primary minimum, Any particle that comes very close will eventually aggregate irreversibly or coagulate. We can prevent the coagulation by grafting the colloidal particles with the polymers, which will give sufficient repulsion to prevent colloidal particles coming too close.

The repulsive electrostatic interaction, which is due to the presence of the double layers, exists when the colloidal particles acquire surface charges. Most colloidal particles will have a surface electric charge when immersed in an ionic solution. These are either due to the ionisation of the surface groups or the preferential adsorption of one of the charged ions onto the surfaces of the colloids. The double layers consist of the Stern layers made of the tightly bound counterions adsorbed onto the surface and the Guoy layers, which are the diffuse regions that extend further away from the particles. When two particles approach one another, their double layers start to overlap and this results in the repulsive interaction. At sufficiently large repulsion, the presence of the double layers may mask the primary minimum and hence prevent coagulation.

By assuming that the charged ions in the double layers are many times smaller than the colloidal particles and they move more rapidly, they can be taken to be in equilibrium on the timescale of interest. The average spatial distribution of the charged ions is also taken to follow the Boltzmann distribution,

$$\rho = \rho_0 e^{[-ze\psi/k_B T]}. \quad (2.4)$$

ρ is the number density of the ions and ρ_0 is the corresponding density in the bulk solution. z is the valency, ψ is the electrostatic potential and e is the electronic charge. The electrostatic interaction potential then can be calculated by applying the Poisson's equation. In the case of low surface potential, about 25 mV for solution in room temperature, we may use the linearized Poisson-Boltzmann equation. In our simulation, we used the expression derived by Healy *et al.*[77] for the electrostatic potential,

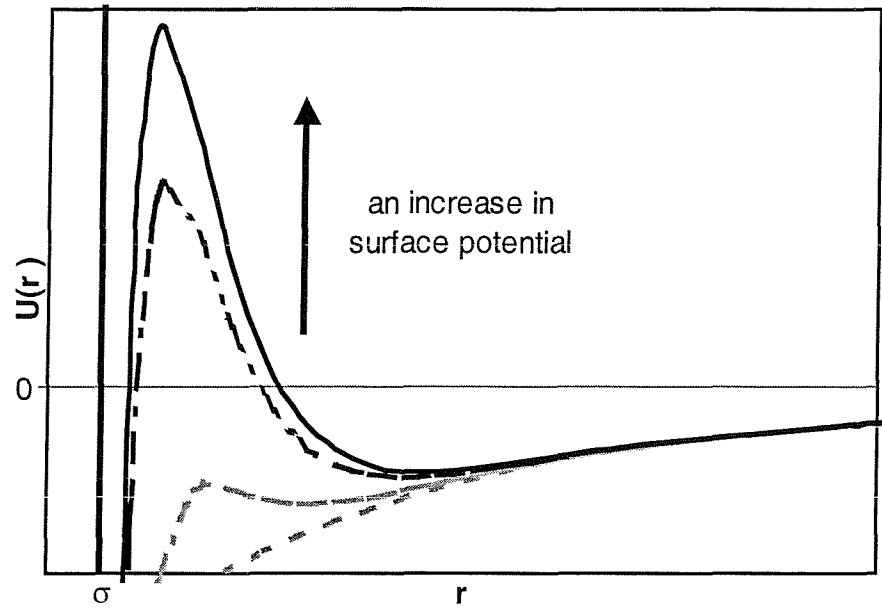
$$U_{el}(r_{ij}) = \pi \epsilon_r \epsilon_0 \psi_0^2 \sigma \ln(1 + e^{-\kappa|r_{ij}-\sigma|}). \quad (2.5)$$

ϵ_r is the relative permittivity of the medium, ϵ_0 is the permittivity of the free space. This expression is valid for $\kappa\sigma$ much larger than unity. κ is the Debye screening length and is defined as

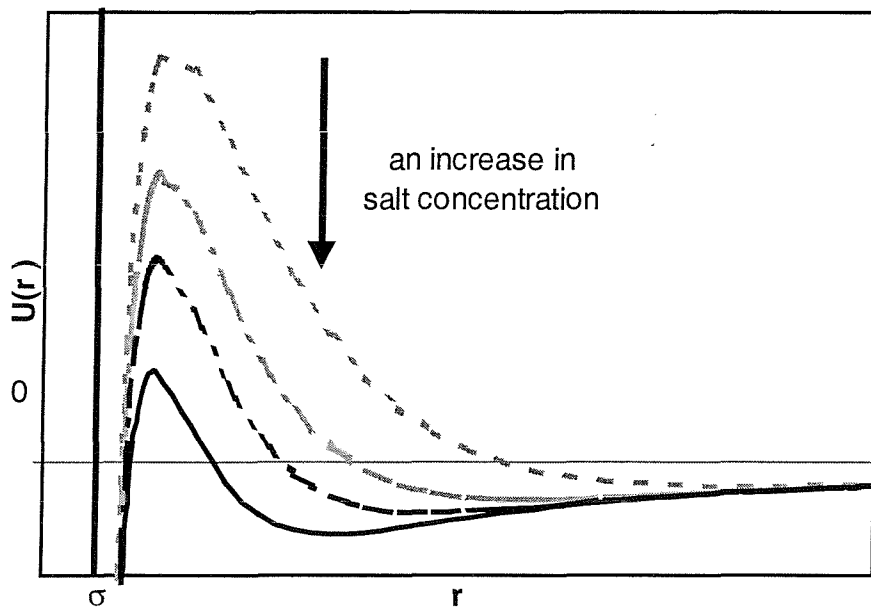
$$\kappa = \sqrt{\frac{2e^2 C N_A}{\epsilon_r \epsilon_0 k_B T}}, \quad (2.6)$$

where N_A is the Avogadro's number and C is the ionic strength.

The interplay between the repulsive interaction due to the overlap of the double layers and the attractive van der Waals interaction produces the characteristic shape for the total interaction potential. The van der Waals interaction is always dominant at close separations. If there is no barrier that prevent particles coming close to their neighbours, the coagulation will inevitably occur to form irreversible bonds. If the surface of the



(a)



(b)

Figure 2.5. The effect of increasing (a) the surface potential and (b) the salts concentration towards the net interaction potential of colloids in ionic concentration.

particle is charged, the electrostatic repulsive interaction can dominate at a distance beyond the primary maximum. This results in the formation of the so-called primary maximum barrier, which can inhibit the coagulation process. The dilution of the salt concentration in the solvent or increasing the surface charges will increase the height of the primary maximum. When this barrier is sufficiently high, the coagulation may effectively cease. The ionic concentration which will give a low enough barrier for the primary maximum so that coagulation becomes dominant, is known as the critical coagulation concentration (ccc)[80].

At larger separations, the electrostatic potential starts to decay more rapidly than the van der Waals potential which results in the attractive interaction become dominant again. Depending on the strength of the repulsive interaction, we may observe another minimum, known as the secondary minimum, at a distance larger than the primary maximum. When the depth of the secondary minimum is significant compared to the thermal energy, it can also induce an aggregation process, known as flocculation. In the flocculation process, the aggregation is largely reversible as the depth of the secondary minimum rarely exceeds a few $k_B T$. From Fig 2.5, we can also observe that the secondary minimum becomes deeper when the surface charge is decreased or when the salt concentration is increased.

2.3. Structure and dynamics

Depending on the extent of the quench below the phase coexistence line or on the size of the attractive interaction, a concentrated suspension can form interesting structures while it tries to reach its equilibrium. The colloidal gel is a special type of aggregation process when a space-filling network or a percolating structure is formed. They can be stable for a considerable time. In the gelation process, the colloidal particles form aggregates which grow rapidly in size until they fill the available space. Further restructuring is then only possible by connecting these aggregates and it results in a structure spanning the whole system, known as a gel. Gels are important in manufacturing many consumer products because the formation of these structures will promote stabilisation of the components in the products as it prevents a phase separation over the life of the products.

When the depth of the attractive interaction is many $k_B T$, the particles interact to form a strong bond through coagulation and the suspensions will form irreversible gels. When the interaction is deep and short ranged, the dynamics of the colloids are mainly governed by Brownian motions. The colloids can then be approximated as the sticky spheres which only interact through random irreversible collisions. The gel which is formed in the solution has an open structure and can be described as a fractal object[71,181-185]. The fractality is measured by using a scaling parameter called the fractal dimension, d_f , describing the number N_d of particles with diameter σ in the gel within a distance of r from a reference point,

$$N_d(r) \approx \left(\frac{r}{\sigma} \right)^{d_f} . \quad (2.7)$$

In a compact crystalline aggregate, the fractal dimension is 3 as the number of particles increase linearly with the volume. In a more open structure, this value is less than 3 and the more open the structure the smaller the fractal dimension. The fractal dimension for aggregates in the dilute suspension have been measured in the experiment and it was found to be between about 1.8 in a fast coagulation to 2.1 in a very slow aggregation. Computer simulation studies[81-83] have been carried out and confirmed these two limiting behaviours in the growth of irreversible aggregates. The lower value of fractal dimension relates to the diffusion-limited aggregation in which every collision leads to the bond formation and hence the aggregation rate is only limited by the time taken for the particles to collide due to the Brownian diffusion. The upper value of the fractal dimension refers to the reaction-limited aggregation where the probability of the bond formation limits the aggregation rate.

In a suspension where particles interact with a shallower potential, typically of the order of few $k_B T$, as in flocculation, a reversible gel is formed. The bonds are usually formed at the secondary minimum and the gel is usually referred as the transient or weak gel. The structure of this gel is very easily disrupted and we can often find a crystalline region in the local structure because of the possibility of the rearrangement within the cluster

Gels in many consumer products fall into this category and the strength of the structure often determine the quality and the shelf-life of the products. For this reason, there have been numerous studies to investigate many aspects of the structure and the strength of transient gels. A review of current techniques for investigating the structures and the dynamical behaviour of colloid-polymers mixtures has been given by Poon and Haw[71].

Victor and Hansen[80] used a perturbative method to study the charge stabilisation of a monodisperse colloidal suspension. They show the possibility of a colloidal suspension undergoing a reversible liquid-gas phase separation by controlling the salt concentration, which has been observed in several experiments. The work was then extended by Kaldasch *et al.*[84] who took into account the existence of the colloid crystal. Several experiments have also been carried out on monodisperse colloidal suspension. Carpineti *et al.*[85] studied the aggregation of a very dilute solution of spherical polystyrene particles in water. The particles interact through DLVO interaction which is controlled through varying the salt concentration. The aggregation was studied using small angle light scattering to measure the long-range correlation of the structure in the suspension[71,180]. In their experiment, they observed the presence of bright rings in the scattering. The peak position and the intensity of the scattering were observed to decrease and increase with time. Bibette[86] studied droplets of silicone-oil-in-water emulsion stabilised by SDS surfactants with the range of volume fraction higher than those studied by Carpineti and Giglio. He observed similar phenomena with the presence of the ring in the scattering was seen. He observed that the ring position reached some fixed value and did not change with time, indicating the formation of a rigid network which grows and fills the whole volume of the solution.

We will use several methods to probe the structures of the gels. The local structure is analysed by plotting the radial distribution function. The radial distribution function gives the ratio between the probability that any two particles in the system are found at a distance of r compared with a random distribution at the same number density[1,2]. This is,

$$g(r) = \frac{\Delta N(r)}{\frac{4\pi}{3} \rho [(r + \delta r)^3 - r^3]} \quad (2.8)$$

where $\Delta N(r)$ is the number of particles whose centres are between the distance r and $r + \delta r$ from a reference particle and ρ is the number density

From the $g(r)$, we can also calculate $N_d(r)$ to study the fractal nature of the gel structure since,

$$N_d(r) = 4\pi\rho \int_0^r s^2 g(s) ds. \quad (2.9)$$

The fractal dimensionality, D , is then determined from the slope of the linear region of a plot of $\log N_d(r)$ against $\log(r)$.

Another method to study the local order of the structure is by computing the coordination number. This is measured by counting the nearest neighbours of a particular particle.

Using the coordination number, we shall use the following definition to determine whether any particular colloid is within a crystalline region. We will assume that a crystal consists of one or more particles with a coordination number of 12 surrounded by neighbouring particles which may also have the maximum coordination number. The particles with the maximum coordination number make up the crystal domain and the neighbouring particles which do not have the maximum coordination number, will form the boundary.

We analyse the long-range order of the structure by calculating the structure factor, $S(k)$.

From the Fourier transform of $g(r)$,

$$S(k) = 1 + 4\pi\rho \int_0^\infty [g(r) - 1] r^2 \frac{\sin(kr)}{kr} dr \quad (2.10)$$

It will be interesting to study the mobility of the particles as the system evolves to form structural network. The particle mobility is measured by calculating the mean square displacement, which is defined as

$$W(t) = \frac{1}{6N} \sum_i^N \left[\left| \mathbf{r}_i(t) - \mathbf{r}_i(0) \right|^2 \right], \quad (2.11)$$

where $W(t)$ is the mean square displacement at time t and $\mathbf{r}_i(t)$ is the positional vector of particle i at time t .

2.4. Rheological behaviour

Due to the large difference in size between colloidal particles and the surrounding solvent particles, a suspension system has a rich non-equilibrium behaviour in contrast to a fluid system. Most molecular fluids exhibit Newtonian behaviour. A Newtonian fluid is characterised by the linear relation between the shear rate and the stress, where the slope is the shear viscosity. Colloidal suspensions, on the other hand, show more varied behaviours under shear. The behaviour can vary from Newtonian in dilute suspensions to a non-Newtonian behaviour in the concentrated suspensions[78,162,186-189]. The non-Newtonian behaviour is characterised by the shear rate dependence of viscosity and the apparent elastic behaviour when the shear flow stops, revealing the solid-like behaviour of the suspension. This phenomenon has been observed even in hard sphere suspension, which exhibit the shear thinning when sheared at moderate rates[87,88,177]. This is largely due to a much slower structural relaxation time, τ_R , the time taken for a particle to diffuse a distance equal to its diameter, which depends on the particle size. A typical value for a colloidal particle is in the order of 1 second. This is significantly longer than the corresponding value for a molecular fluid, which is in the order of 10^{-12} second. Therefore, when a shear flow is imposed on a molecular fluid, the intrinsic structural relaxation time, τ_R^{-1} , for the fluid is typically much smaller than the shear rate. Hence the perturbation from the equilibrium structure due to the shear is not significant. The fluid is then considered Newtonian as its viscosity is largely independent of the shear rate. In the case of colloidal suspensions, a shear rate that is larger than the intrinsic structural relaxation time is easily attained in experiments. The consequence is that the structure perturbed by the shear flow is very different compared to the equilibrium structure. In the case of the hard sphere suspensions, the suspension will form some spatial correlation in the direction of the shear flow and this results in the variation of the viscosity with the shear flow.

As we explore the phase diagram by quenching from the fluid into the two-phase regime, it is interesting to study the changes in the rheological properties of the system. In general, all systems will have some characteristic response in relaxing after being subjected to an external stress[41,78]. An ideal solid will have an elastic recovery in which the system returns to the original shape while an ideal liquid will stay in its position as it cannot resist stress and has to deform or flow to release the stress. Most materials exhibit both characteristics where they have a partial elastic recovery and some deformations within their structure. Colloidal systems are known to exhibit these properties depending on their interactions and the concentration. In general, the colloidal systems will exhibit more solid-like characteristic with increasing concentration and with the increasing strength of the interparticle interactions.

There are several ways to apply the stress to measure the stress response of a weakly aggregating suspension. Several experiments have measured the stress response using an oscillatory shear which usually in a sinusoidal pattern. Goodwin *et al.*[89] measured the storage moduli at high frequency. A steady shear experiment was also used to characterise the shear behaviour of the suspension. Rueb and Zukoski[90,91] investigated the mechanical properties of the gel. They measured the linear stress response of the gel as it recovered after the cessation of a shear flow at various volume fractions and temperature.

They observed the compactification of the gel as the result of the shear in which the fractal dimension increases from 1.4 to 2.5 after the shear was applied. The modulus was found to have a power law function of volume fraction. They also observed the increase of the elastic modulus at the end of the experiment with decreasing temperature.

In this work, we will study the formation of the transient gel due to the presence of salts. We will vary the salt concentration to alter the effective interaction between the colloidal particles. We will look at various aspects of the system such as the local structure and the particle's diffusion. In the case where the transient gels are formed, we will also study the mechanical strength of the resulting network and its correlation with the interaction potential. This is carried out by applying a small step-strain to induce the stress across the network and calculate the resulting stress response.

Chapter 3

Phase diagram construction

In this chapter we outline the use of the perturbation method to predict the behaviour of a system of colloidal particles immersed in an electrolyte solution. The main objective of this study is to provide us with reasonable estimates of the input parameters for our simulations to study the particle gel formation induced by the presence of salts.

The statistical mechanics framework of the perturbation theory used to predict the phase separation of molecular system was first developed by Zwanzig [92,35]. It was later extended by several other workers [93-99] and also utilized for predicting phase behaviour of colloidal system under various conditions [47][48].

3.1. Theory

The starting treatment in the perturbation theory, following the work of Zwanzig, is to split the sum of the pair potentials, U_{tot} , into two parts. The first part is the reference potential, U_{ref} , which has well-known thermodynamic and structural properties and the second part is the perturbation potential, U_{per} ,

$$U_{\text{tot}} = U_{\text{ref}} + U_{\text{per}}. \quad (3.1)$$

The configurational integral of a system with this potential is

$$Z_N = \int \dots \int e^{-U_{\text{tot}}/k_B T} d\mathbf{r}_1 \dots d\mathbf{r}_N = \int \dots \int e^{-(U_{\text{ref}} + U_{\text{per}})/k_B T} d\mathbf{r}_1 \dots d\mathbf{r}_N. \quad (3.2)$$

This is the integral of the Boltzmann factor over the configurational space. \mathbf{r}_i is the vector position of particle i , N is the number of particles in the system and $d\mathbf{r}_i$ is the integral over the configurational space of the i th particle. The configurational integral is decomposed by multiplying and dividing by the configurational integral of the reference system, Z_{ref} ,

$$\begin{aligned}
 Z_N &= Z_{\text{ref}} \frac{1}{Z_{\text{ref}}} \int \dots \int e^{-(U_{\text{ref}} + U_{\text{per}})/k_B T} d\mathbf{r}_1 \dots d\mathbf{r}_N \\
 &= Z_{\text{ref}} \left\langle e^{-U_{\text{per}}/k_B T} \right\rangle_{\text{ref}}
 \end{aligned} \tag{3.3}$$

where

$$Z_{\text{ref}} = \int \dots \int e^{-U_{\text{ref}}/k_B T} d\mathbf{r}_1 \dots d\mathbf{r}_N.$$

The second term in Eqn (3.3) is interpreted as the canonical average of the Boltzmann factor of the perturbed system over the reference system. Finally we use Eqn (3.3) to separate the contribution of the reference and the perturbed potential in the Helmholtz free energy of the system by writing,

$$\begin{aligned}
 \frac{A}{k_B T} &= -\ln \left(\frac{Z_N}{N! \Lambda^{3N}} \right) \\
 &= -\ln \left(\frac{Z_{\text{ref}}}{N! \Lambda^{3N}} \right) - \ln \left\langle e^{-U_{\text{per}}/k_B T} \right\rangle \\
 &= \frac{A_{\text{ref}}}{k_B T} + \frac{A_{\text{per}}}{k_B T}.
 \end{aligned} \tag{3.4}$$

A_{ref} is the free energy contribution from the reference system, A_{per} is the contribution from the perturbed potential and Λ is the thermal de Broglie wavelength. Barker and Henderson expanded the second term to evaluate the free energy contribution from the perturbed potential. In their method, the range of intermolecular distance is divided into intervals. The width of the intervals is assumed small enough so that the pairwise perturbation potential, u_{per} , can be regarded as constant between r_i and r_{i+1} . If N_i is the number of particles that reside between r_i and r_{i+1} , Barker and Henderson [93] derived the following expansion for the free energy up to second order,

$$\begin{aligned}
 \frac{A}{k_B T} &= \frac{A_{\text{ref}}}{k_B T} + \frac{1}{k_B T} \sum_i \langle N_i \rangle_{\text{ref}} u_{\text{per},i} - \\
 &\quad \frac{1}{(k_B T)^2} \sum_i \sum_j \left(\langle N_i N_j \rangle_{\text{ref}} - \langle N_i \rangle_{\text{ref}} \langle N_j \rangle_{\text{ref}} \right) u_{\text{per},i} u_{\text{per},j}.
 \end{aligned} \tag{3.5}$$

$\langle \dots \rangle_{\text{ref}}$ is an average over the configurations of the reference system. It is most convenient to compute the Helmholtz free energy as a function of the pairwise potential and the radial distribution function of the reference system. By definition, the average number of particles at interval i is,

$$\langle N_i \rangle = \frac{N\rho}{2} \int_{r_i}^{r_{i+1}} g_{\text{ref}}(r) 4\pi r^2 dr \quad (3.6)$$

where g_{ref} is the radial distribution function of the reference system and ρ is the number of the fluid density. The term in the second order approximation is evaluated by assuming that the number of particles in each intervals are largely uncorrelated such that,

$$\langle N_i N_j \rangle - \langle N_i \rangle \langle N_j \rangle = 0 \text{ for } i \neq j. \quad (3.7)$$

The second order term can be evaluated using the macroscopic compressibility approximation,

$$\langle N_i^2 \rangle - \langle N_i \rangle^2 = \langle N_i \rangle k_B T \left(\frac{\partial \rho}{\partial p} \right)_0. \quad (3.8)$$

Eqn (3.5) becomes

$$\begin{aligned} \frac{A}{Nk_B T} &= \frac{A_{\text{ref}}}{Nk_B T} + \frac{2\pi\rho}{k_B T} \int_0^\infty u_{\text{per}}(r) g_{\text{ref}}(r) r^2 dr. \\ &- \frac{\pi\rho}{k_B T} \left(\frac{\partial \rho}{\partial p} \right)_{\text{ref}} \int_0^\infty [u_{\text{per}}(r)]^2 g_{\text{ref}}(r) r^2 dr \end{aligned} \quad (3.9)$$

3.2. The Effective diameter

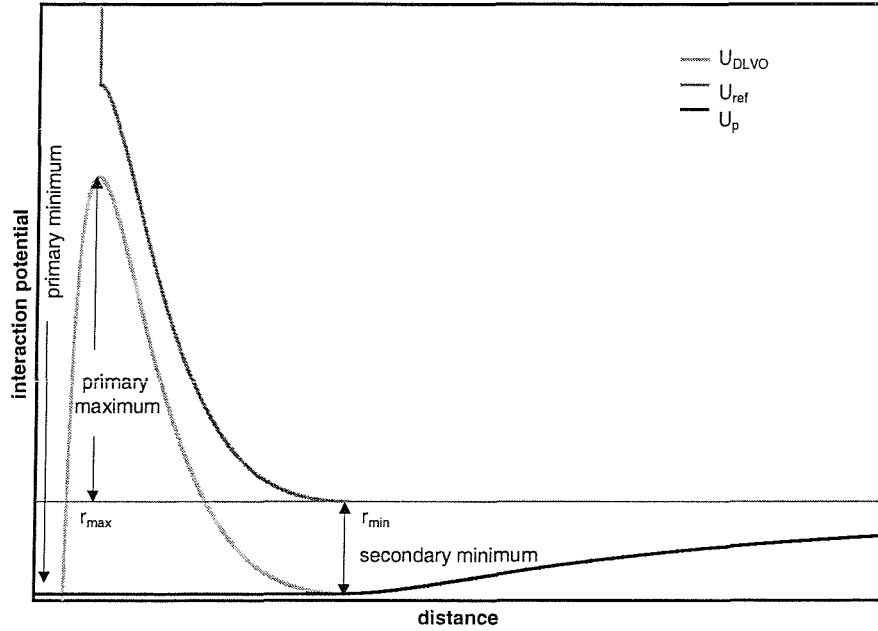


Figure 3.1. The schematic profile of the DLVO, reference and the attractive perturbation potentials as a function interparticle distance. The corresponding locations for the primary maximum and the secondary minimum are included.

We follow the method of Weeks, Chandler and Andersen[96] to separate the total pair potential into a purely repulsive part, u_{ref} , and purely attractive potential. The repulsive or reference part has the form

$$\begin{aligned}
 u_{ref}(r) &= \infty && \text{for } r < r_{max} \\
 u_{ref}(r) &= u_{DLVO}(r) - u_{DLVO}(r_{min}) && \text{for } r_{max} \leq r \leq r_{min} \\
 u_{ref}(r) &= 0 && \text{for } r > r_{min}.
 \end{aligned} \tag{3.10}$$

The attractive part is

$$\begin{aligned}
 U_{per}(r) &= U_{DLVO}(r_{min}) && \text{for } r \leq r_{min} \text{ and} \\
 U_{per}(r) &= U_{DLVO}(r) && \text{for } r > r_{min}.
 \end{aligned} \tag{3.11}$$

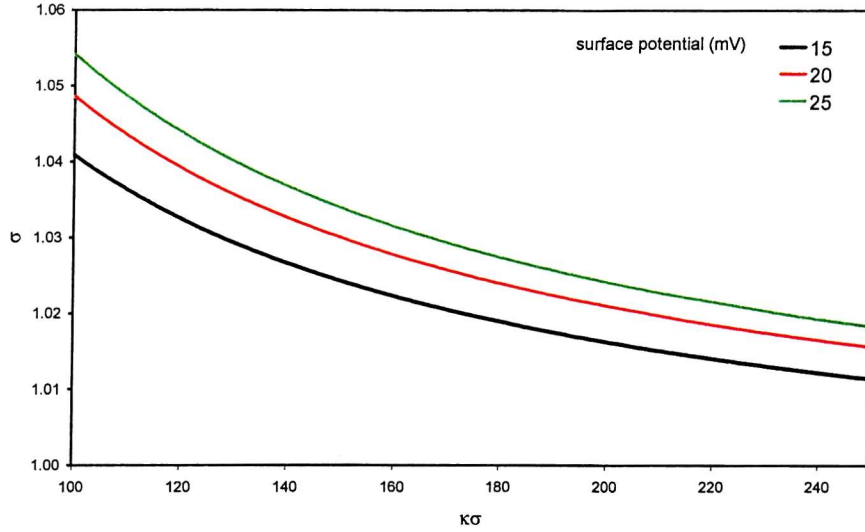


Figure 3.2. The effective hard sphere diameter as a function of the inverse Debye length at different surface potentials calculated using the Barker-Henderson equation.

u_{DLVO} is the pairwise additive DLVO potential and r_{min} is the location of the secondary minimum. In this treatment of pairwise potential, we neglect the attractive region close to the particle surface, the primary minimum, and assume a hard sphere potential for any distance of less than the primary maximum. This is a reasonable approximation in the case where the height of primary maximum is large enough ($u_{max} \geq 15k_B T$) to prevent any neighbouring particle coming closer than the primary maximum.

Although the properties of the chosen reference potential are not known, we can obtain an estimate by relating the fluid with the chosen reference potential to a hard sphere fluid. The equation suggested by Barker and Henderson[93] is utilised to calculate the effective hard sphere diameter of the thermodynamically equivalent fluid

$$\sigma_{eff} = r_{max} + \int_{r_{max}}^{r_{min}} \left[1 - e^{-u_{ref}(r)/k_B T} \right] dr . \quad (3.12)$$

So that

$$A_{\text{ref}}(\rho_{\text{ref}}) = A_{\text{HS}}(\phi_{\text{eff}})$$

where $\phi_{\text{eff}} = \pi\rho_{\text{ref}}\sigma_{\text{eff}}^3 / 6$ is the volume fraction of the equivalent fluid and

$$g_{\text{ref}}(r, \rho_{\text{ref}}) = g_{\text{HS}}(r, \phi_{\text{eff}}).$$

In Fig 3.2, we show the plot of the effective hard sphere diameter as a function of Debye length at different surface potentials. Increasing the steepness of the potential and the range of the repulsive tail as the inverse Debye length increases results in a reduction in the effective hard sphere diameter.

3.2.1. The hard sphere reference system

In this section, we show how to calculate the properties of the hard sphere system which mimics the reference potential. The choice of the hard sphere potential is very suitable, as there is a wealth of information available regarding its properties and also that these properties depend on one parameter only, the volume fraction. Depending on the volume fraction, there are two possible states in which hard sphere particles can exist, the fluid phase and the solid phase. For simplicity, we assumed that the solid phase consists of a face centred cubic crystal. The fluid phase occurs when the volume fraction is smaller than 0.497. At larger volume fraction, the solid phase appears and persists up to the maximum limit of the packing density at $\phi \approx 0.740$.

The total Helmholtz free energy for the hard sphere reference system is the sum of the ideal, A_{ideal} , and the excess free energy, A_{ex} ,

$$A_{\text{HS}} = A_{\text{ideal}} + A_{\text{ex}} \tag{3.13}$$

The ideal Helmholtz energy for both fluid and solid phase is taken as,

$$\frac{A_{\text{ideal}}}{Nk_B T} = \ln(\rho) + 3\ln(\Lambda) - 1. \quad (3.14)$$

The excess free energy of the fluid phase is calculated using the Carnahan-Starling equation[36]. The compressibility factor is

$$Z_{HS}^{\text{liq}} = \frac{p}{\rho k_B T} = \frac{1 + \phi + \phi^2 - \phi^3}{(1 - \phi)^3}. \quad (3.15)$$

The associated excess free energy for the liquid phase is,

$$\frac{A_{\text{ex}}^{\text{liq}}}{Nk_B T} = \int_0^\phi [Z_{HS}^{\text{liq}} - 1] \frac{\partial \phi}{\phi} = \frac{\phi(4 - 3\phi)}{(1 - \phi)^2} \quad (3.16)$$

The equation of state for the solid phase is taken from the expression given by Hall[103] who fitted the results from Monte Carlo simulations for an fcc hard sphere solid by Alder *et al.*[104],

$$Z_{\text{Hall}} = (12 - 3\gamma)/\gamma - 2.557696 + 0.1253077\gamma + 0.1762393\gamma^2 - 1.053308\gamma^3 + 2.8186121\gamma^4 - 2.921934\gamma^5 + 1.118413\gamma^6, \quad (3.17)$$

where $\gamma = 4(1 - \phi / \phi_c)$ and $\phi_c = \pi \sqrt{2} / 6 \approx 0.7404$, the maximum possible volume fraction for an fcc crystal. The expression for the free energy of solid is given by,

$$A_{\text{HS}} = -s_0 + \ln(6\phi_c / \pi\sigma^3) - 3 \ln(2\alpha/3) + \int_0^\gamma d\gamma [Z_{\text{Hall}} - Z_{\text{LJD}}] / (\gamma - 4) \quad (3.18)$$

where σ is the hard sphere diameter, the entropy constant, s_0 , is -0.24 , $\alpha = (\phi_c/\phi) - 1$ and $Z_{\text{LJD}} = 3 + 3/\alpha$ is the high-density limit of the Lennard-Jones-Devonshire cell theory[101].

The Percus-Yevick approximation is used to compute the radial distribution function of the fluid phase[105,106],

$$g_{\text{HS}}(r) = \sum_{i=0}^{\infty} H(R-i) g_i(R) \quad (3.19)$$

where $H(R)$ is the Heaviside step function and $R = r/\sigma$ and i is an integer. $g_i(R)$ is computed from

$$g_0(R) = 0 \quad (3.20a)$$

$$Rg_i(R) = \frac{(-12\phi)^{i-1}}{(i-1)!} \sum_{j=0}^2 \lim_{t \rightarrow t_j} \frac{d^{i-1}}{dt^{i-1}} (t-t_j)^i t \left[\frac{L(t)}{S(t)} \right]^j e^{(t(R-i))} \quad \text{with} \quad (3.20b)$$

$$S(t) = (1-\phi)^2 t^3 + 6\phi(1-\phi)t^2 + 18\phi^2 t - 12\phi(1+2\phi) \quad \text{and} \quad (3.20c)$$

$$L(t) = \left(1 + \frac{\phi}{2}\right)t + 1 + 2\phi \quad (3.20d)$$

where t_j ($j = 0, 1, 2$) are the roots of the equation $S(t)$.

The calculation of the radial distribution function, $g(r)$, for hard sphere solid follows the method outlined by Choi *et al.* [107],

$$\tilde{g}_{\text{HS}}(r, \phi) = \sum_{i=1}^{\infty} \tilde{g}^i(r, \phi), \quad (3.21a)$$

The function calculates the radial distribution function as a sum of all contributions from all neighbour shells and \tilde{g}^i represents the contributions from i -th neighbour shell. The contribution from the nearest neighbour shell ($i = 1$) is

$$\tilde{g}^1(r, \phi) = \frac{A\sigma}{r} \exp\left\{-[W_1(\phi)(r-r_1)/\sigma]^2 - [W_2(\phi)(r-r_1)/\sigma]^4\right\} \quad (3.21b)$$

where

$$\begin{aligned} W_1(\phi) &= 1.5338/\phi^* - 0.37687\exp[-989.6(\phi - 0.52)^2] \\ &\quad - 2.5146 - 1.3574\phi^* - 8.5038\phi^{*2} \end{aligned} \quad (3.21c)$$

$$W_2(\phi) = 0.80313/\phi^* - 1.208\exp(5.6128\phi^*) + 67.808\phi^{*2} - 67.918\phi^{*3}, \quad (3.21d)$$

$$r_1(\phi) = \frac{1 - 8.0521\phi^* + 18.003\phi^{*2}}{1 - 8.2973\phi^* + 20.546\phi^{*2} - 13.828\phi^{*3} + 103.95\phi^{*4} - 582.74\phi^{*5} + 1245.7\phi^{*6}} \quad (3.21e)$$

A is computed to satisfy the virial theorem,

$$\tilde{g}_{HS}(1, \phi) = (Z_{HS} - 1) / 4\phi. \quad (3.21f)$$

and

$$\phi^* = \phi_c - \phi \quad (3.21g)$$

The contributions from all other shells, which are assumed to have the same Gaussian width, W_g , are

$$\tilde{g}^i(r, \phi) = \frac{W_g(\phi)}{24\phi\sqrt{\pi}} \frac{n_i \sigma^2}{r r_i} \exp\left\{-[W(\phi)(r - r_i) / \sigma]^2\right\} \text{ for } i < 1. \quad (3.21h)$$

The width, W_g , is

$$W(\phi) = 1.9881/\phi^* - 3.5276 + 6.9762\phi^* - 26.205\phi^{*2}. \quad (3.21i)$$

r_i and n_i (for $i > 1$) are the distance and the number of particles in the i -th nearest neighbour lattice sites respectively. For an fcc crystal, there are 12 neighbours in the first shell, 6 neighbours in the second shell and 24 in the third shells. r_i , the distance of the i th neighbour shells from a reference potential in an fcc crystal is

$$r_i = d_0 i^{1/2} \quad (3.22a)$$

where d_0 is the distance of the nearest neighbouring shell, which for an fcc crystal is

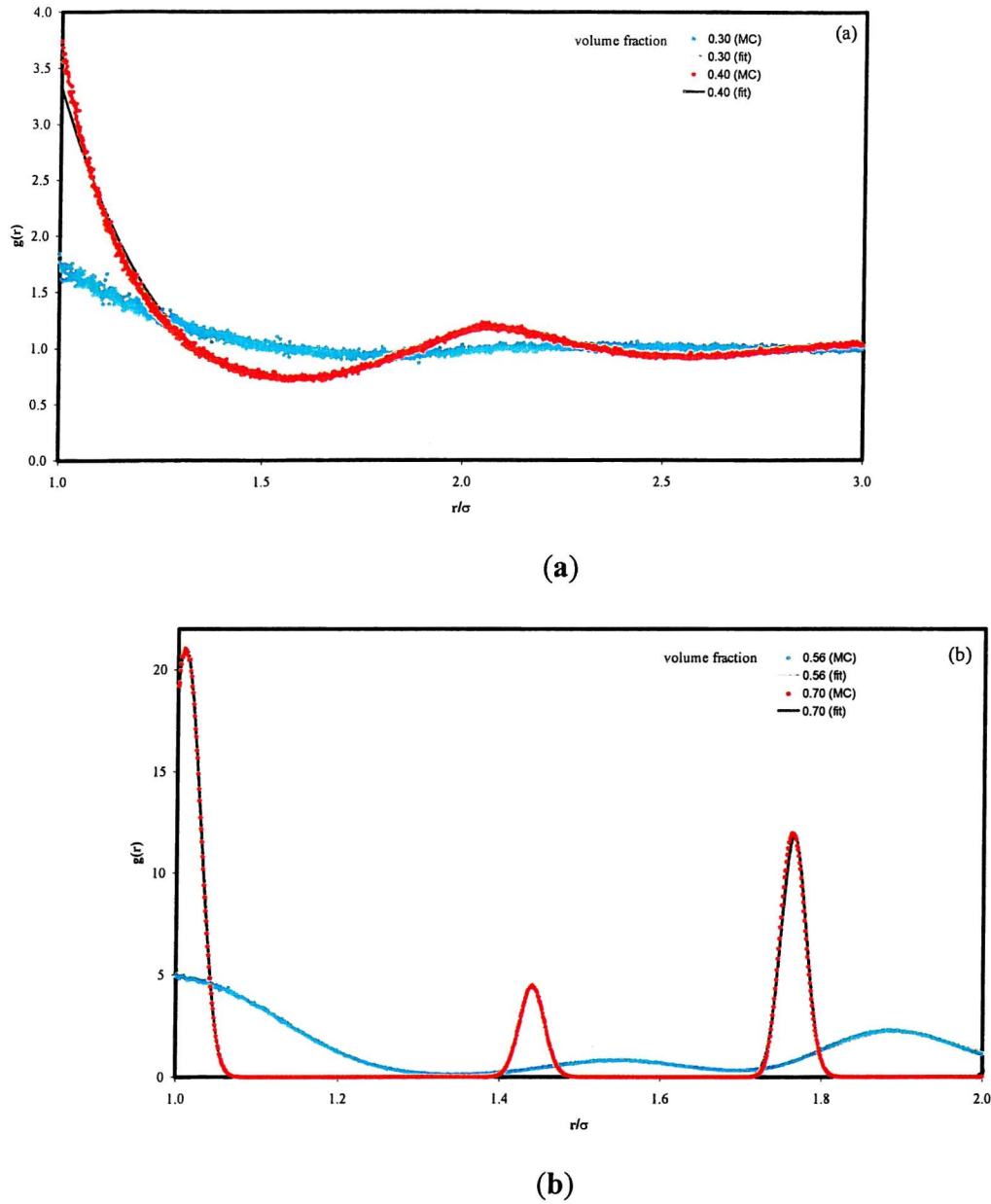


Figure 3.3. Comparison between the $g(r)$ obtained analytically and from the Monte Carlo simulations for (a) fluid and (b) solid phases (fcc) at several values of volume fraction.

$$d_0 = 2^{1/6} (\pi \sigma^3 / 6 \phi)^{1/3}. \quad (3.22b)$$

Fig 3.3 shows the comparison between the $g(r)$ obtained from the analytical calculation and from the Monte Carlo simulations for fluid and solid at two values of the volume fraction.

3.3. Calculation procedure

A numerical routine is implemented to compute the thermodynamics properties and generate the phase diagram as a function of Debye length. Two phases are in equilibrium when the pressure, P , the temperature, T , and the chemical potential, μ , or equivalently for a one component system, the Gibbs free energy, G , in both phases are equal. The thermodynamics relationships for the pressure and the Gibbs free energy in term of the Helmholtz free energy are,

$$\frac{G}{k_B T} = \frac{\partial}{\partial \rho} \left(\frac{\rho A}{k_B T} \right)_{P,T} \quad \text{and} \quad (3.23)$$

$$\frac{P}{k_B T} = \frac{\rho G}{k_B T} - \frac{\rho A}{k_B T}. \quad (3.24)$$

The free energy for both solid and fluid phases is obtained from Eqn (3.9). The volume fraction of the reference system is computed by first calculating the effective Barker-Henderson diameter using Eqn (3.3). The radial distribution functions for both solid and liquids are obtained from Eqn (3.19) Eqn (3.22a). The macroscopic compressibility for the hard sphere system, which appears in the second order term of the free energy calculation, is estimated using Eqn (3.25), which is valid for both solid and liquid phases with the appropriate Z ,

$$\left(\frac{\partial \rho}{\partial P} \right)_{HS} k_B T = \frac{1}{Z_{HS} + \phi \frac{\partial Z_{HS}}{\partial \phi}}. \quad (3.25)$$

We determine the coexistence phases at a value of the inverse Debye length by using the common tangent construction method. This is illustrated in Fig (3.4) which shows the connection between each point in the phase diagram and the plot of free energy as a function of volume fraction. Two phases are said to coexist when their slopes are equal so that we can draw a straight line which connects these phases and just touches the free energy curve. From Eqn (3.23) and (3.24), it can be seen that the slope relates to the Gibbs

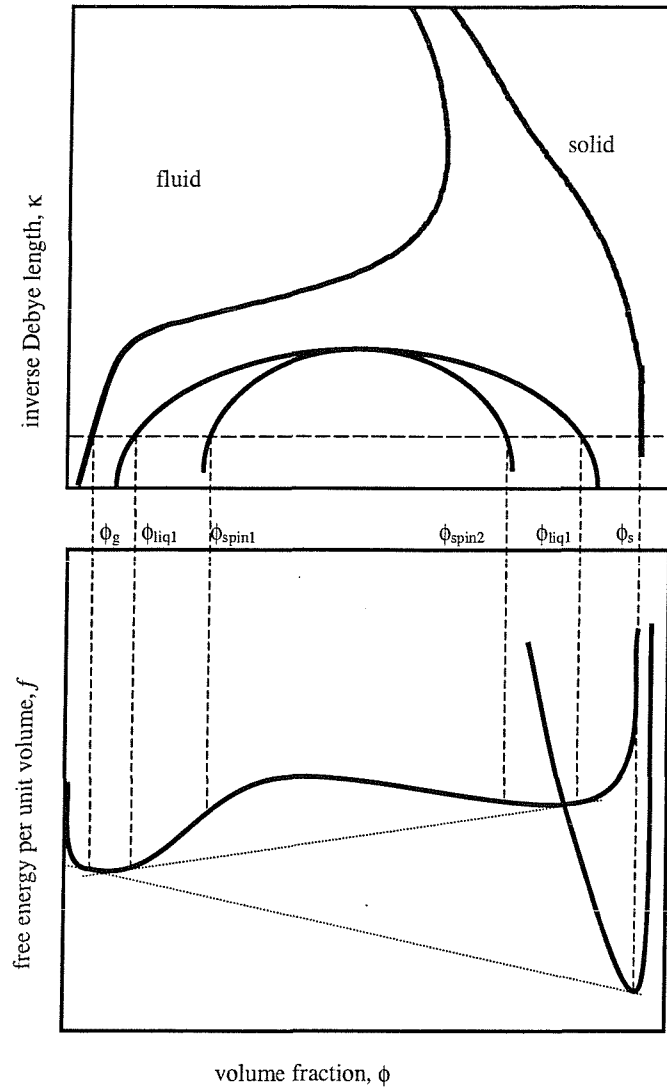


Figure 3.4. The schematic phase diagram and the plot of free energy per unit volume for one value of inverse Debye length, κ , to illustrate how the phase diagram is constructed.

free energy and the pressure relates to the point where the straight line intersect with the y-axis at $\phi = 0$. Hence the requirements for a coexistence where the Gibbs free energy, the pressure and the temperature are equal is fulfilled. Further points are obtained by repeating this procedure for different values of the Debye length.

In addition to the fluid-solid coexistence line, we also plot the spinodal line which marks the boundary between the unstable and metastable phase[179]. This line is constructed by looking for the condition at which the second derivative of the free energy is equal to zero.

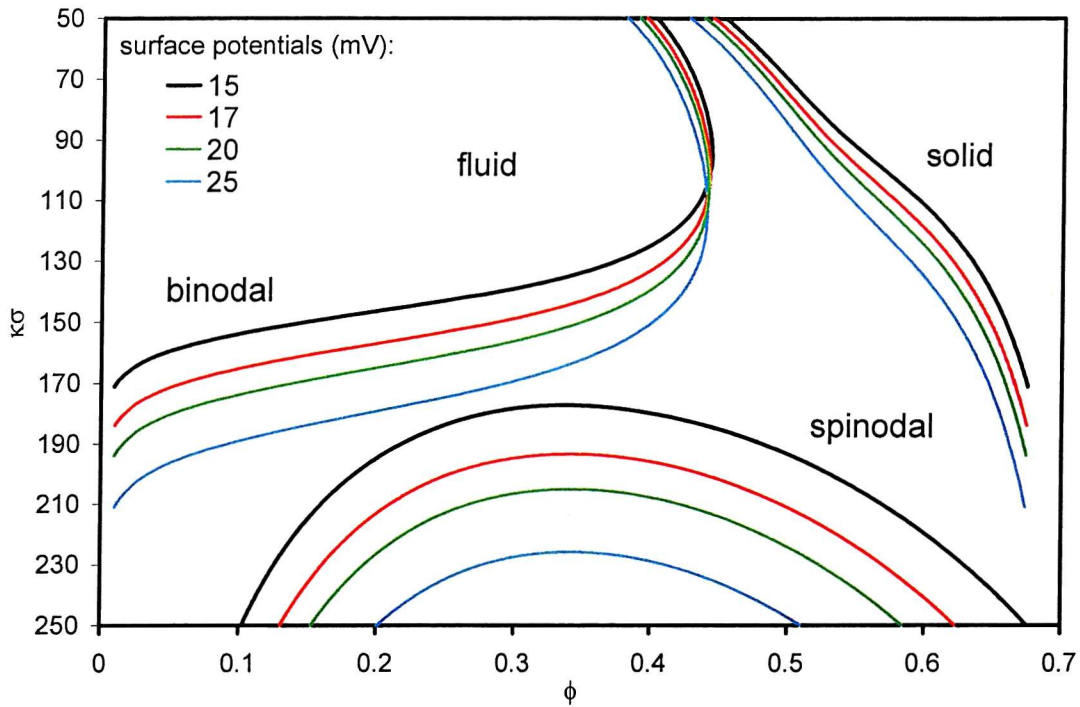


Figure 3.5. The phase diagram for the DLVO potential at different surface potentials, showing the solid-fluid binodal and the spinodal lines.

This is also illustrated in Fig 3.4. The hidden fluid-fluid coexistence line that lies below the fluid-solid line can also be constructed by applying similar method as used to construct the fluid-solid coexistence line, although we found that the line lies extremely close to the spinodal line.

In this study, the system is assumed to consist of colloidal particles whose mass density is comparable to the density of the solvent, which is taken as water ($\epsilon_R = 80.37$), so that the gravitational force can be considered insignificant. The diameter of the particles is $\sigma_0 = 1 \mu\text{m}$ and its Hamaker constant is 20 eV. We vary the surface potential between 17 and 25 mV. Fig 3.5 shows how the coexistence lines vary with different surface potentials. For all values of surface potential, the critical points lie below the solid-fluid coexistence line and hence no liquid regime is predicted. The coexistence line is found to shift downward to a higher κ value as the surface potential is increased.

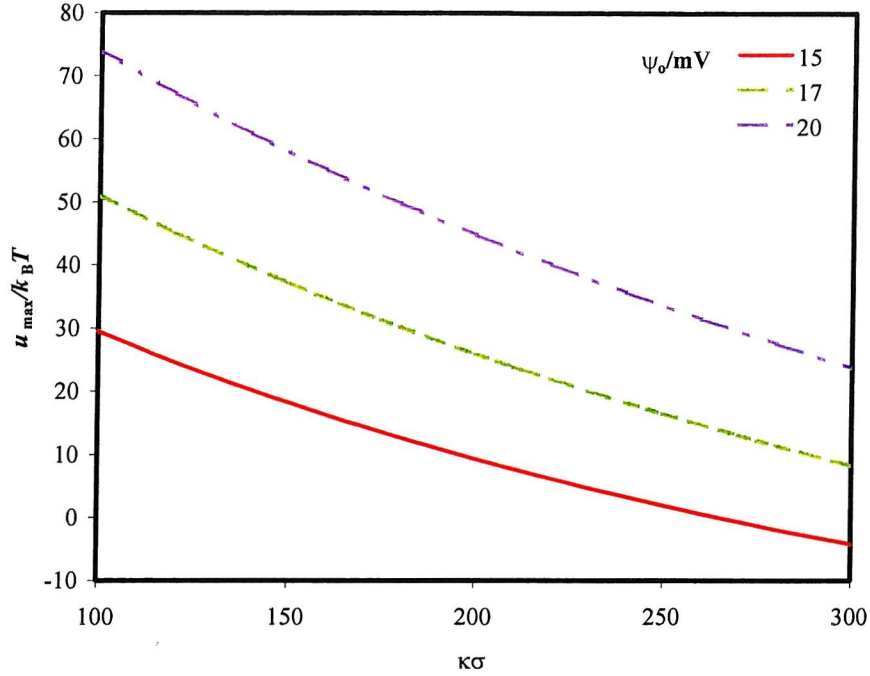


Figure 3.6. The height of the primary maximum as a function of the inverse Debye length for three different values of surface potential.

We should bear in mind that there is an upper limit for the inverse Debye length where the resulting structure of colloidal system is primarily determined by the secondary minimum. The effect of primary maximum becomes important when its height is low enough so that the coagulation occurs at a time scale comparable to the time scale of simulation. In Fig 3.6, we show the relation between the height of the primary maximum, the inverse Debye length and the surface potential.

The time scale for the coagulation, t_c , equivalent to diffusion over the primary maximum barrier can be estimated using the following equation[11,15],

$$t_c \sim \left(\frac{3\pi \mu \sigma_0^2}{4 k_B T \kappa \phi} \right) \exp\left(\frac{u(r_{\text{prim}})}{k_B T} \right), \quad (3.26)$$

Based on the Eqn (3.26), if we specify the time scale of the coagulation must be longer than 3 days, a system at moderate volume fraction with surface potential equals to 17 mV, the maximum inverse Debye length is roughly $\kappa = 260\sigma^{-1}$. For a system with a lower

Part I. Brownian Dynamics Simulation Of Colloidal Particles In Ionic Solution

surface potential, the maximum limit can be lower. The corresponding limit for system with surface potential of 15 mV is $\kappa = 170\sigma^{-1}$.

Based on this study, we decide to run a set of Brownian dynamics simulations with inverse Debye length varied between 100 and 250 where the surface potential is chosen at 17 mV. We will also vary the volume fraction between 5 % and 40 %. The range of inverse Debye length should ensure that the simulated system would explore the broad region from the dispersed or fluid phase down to unstable region below the spinodal line.

The upper limit is mainly set by the critical coagulation concentration, that is the minimum salt concentration before the coagulation sets in. This is because the van der Waals interaction becomes more dominant at short range as the salt concentration is reduced. Consequently, this will lower the height of the primary maximum that prevents the coagulation from occurring.

Chapter 4

The model and the simulations

The simulation code is written in FORTRAN and the system is simulated in a three dimensional box of volume V . The model consists of N spherical particles and the volume fraction, ϕ , of the system is,

$$\phi = \frac{\pi N \sigma^3}{6 V}$$

where σ is the diameter of the colloidal particles. The periodic boundary conditions are applied in all directions to simulate a macroscopic system. In our simulation, we set the diameter of the particles, σ , the viscosity, η , and the energy, $k_B T$, are set to unity.

$$\begin{aligned} k_B T &= 1 \\ \eta &= 1 \\ \sigma &= 1 \end{aligned}$$

Time is in units of the Brownian relaxation time, τ_R . This is defined as the time for a particle to diffuse a distance on the order of one diameter in the absence of other forces and is given as,

$$\tau_R = \frac{\eta \sigma^3}{k_B T} .$$

For a particle of one micron in diameter suspended in water ($\eta = 0.001 \text{ Ns/m}^2$) at room temperature, the relaxation time is in the order of 0.24 s.

The trajectories of the interacting particles were calculated using the position Langevin equation in finite time steps as shown in chapter one,

$$\mathbf{r}_i(t + \Delta t) = \mathbf{r}_i(t) + \frac{\Delta t}{m\xi} \mathbf{F}_i^C(t) + \Delta \mathbf{r}_i^B \quad (1.20)$$

$\Delta \mathbf{r}_i^B$ is the displacement resulting from the Brownian force and is also taken to have a mean average of zero. It has the mean square value of $6k_B T \Delta t / 3\pi\eta\sigma$, where Δt is the timestep used in the simulation. We set the time step for the simulation at $4.71 \times 10^{-6} \tau_R$. This corresponds to the mean square displacement of $10^{-6} \sigma^2$.

The conservative force is calculated from the DLVO interaction. The force exerted by particle j on particle i at a distance of r_{ij} is given by,

$$\mathbf{F}_i(r_{ij}) = - \frac{\partial U_{DLVO}(\mathbf{r}_{ij})}{\partial \mathbf{r}_i}.$$

The equation for the DLVO potential is given in chapter two which we state here again,

$$U_{DLVO}(r_{ij}) = U_{el}(r_{ij}) + U_{vdw}(r_{ij})$$

with

$$U_{vdw}(r_{ij}) = - \frac{A_H}{12} \left[\frac{\sigma^2}{r_{ij}^2 - \sigma^2} + \frac{\sigma^2}{r_{ij}^2} + 2 \ln \left(\frac{r_{ij}^2 - \sigma^2}{\sigma^2} \right) \right] \text{ and}$$

$$U_{el}(r_{ij}) = \pi \epsilon_r \epsilon_0 \psi_0^2 \sigma \ln \left(1 + e^{-\kappa[r_{ij} - \sigma]} \right).$$

In this study, we use the following parameters suitable for colloidal particles ($\sigma = 1 \mu\text{m}$, $A_H = 0.1 \text{ eV}$, $\psi_0 = 17.7 \text{ mV}$) immersed in water ($\eta = 8.854 \times 10^{-4} \text{ Pa.s}$) at room temperature in the presence of a monovalent salt. The equation for the electrostatic repulsion is valid for large value of the inverse Debye length, κ . We therefore choose to

Parameter	Reduced Value	Reduced Units	Typical Real Units
Energy	1.0	$k_B T$	4.143×10^{-21} J
Particle diameter	1.0	σ	10^{-6} m
Viscosity	1.0	η	8.854×10^{-4} Pa.s
Electronic charge	1.0	e	1.602×10^{-19} C
Brownian relaxation time	1.0	$\tau_R k_B T / \eta \sigma^3$	0.24 s
Hamaker constant	3.86829	$A_H / k_B T$	1.602×10^{-20} J
Inverse Debye screening length	100-250	$\kappa \sigma$	$1-2.5 \times 10^8$ /m
Ionic strength	$0.5-3.5 \times 10^6$	$C \sigma^3$	$1-6$ mol/m ³
Permittivity of free space	1.429	$\epsilon_0 k_B T \sigma / e^2$	8.854×10^{-12} C ² /Jm
Relative dielectric constant of water	80		80
Surface potential	0.684	$\psi_0 e / k_B T$	0.017 V

Table 4.1. The values for the parameters used in the simulation.

vary κ between 150 and 250. The surface potential is chosen to values that will give sufficiently high maximum barrier as we are mainly interested in the study weak aggregation. The values for the parameters are summarised in table 4.1.

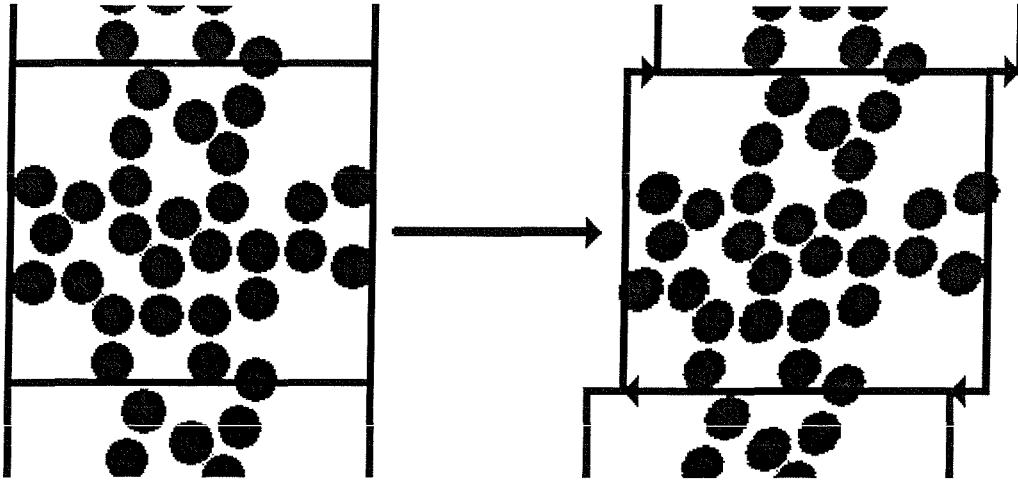


Figure 4.1. The illustration showing the step-strain is imposed by moving the image of the simulation box at the top and bottom in the opposite direction at the first step of the simulation runs.

To measure the effect of stress on the gel structure, one can use a compressive or shear stress and apply an oscillating shear or just a short pulse[164]. In this study we will employ the step-strain method by applying a sudden shear displacement and measure the stress relaxation as the gel network is trying to release the stress. Fig 4.4 illustrates how the step-strain is imposed in the simulation model using the Edwards sliding boundary conditions.

In a very small deformation, a colloidal suspension will have a stress response which increases linearly with the strain amplitude. Under this condition, the changes of the stress, σ_{xy} , as a function of time can be written as[78,162]

$$\sigma_{xy}(t') = \int_{-\infty}^{t'} G(t' - t) \dot{\gamma}(t) dt . \quad (4.6)$$

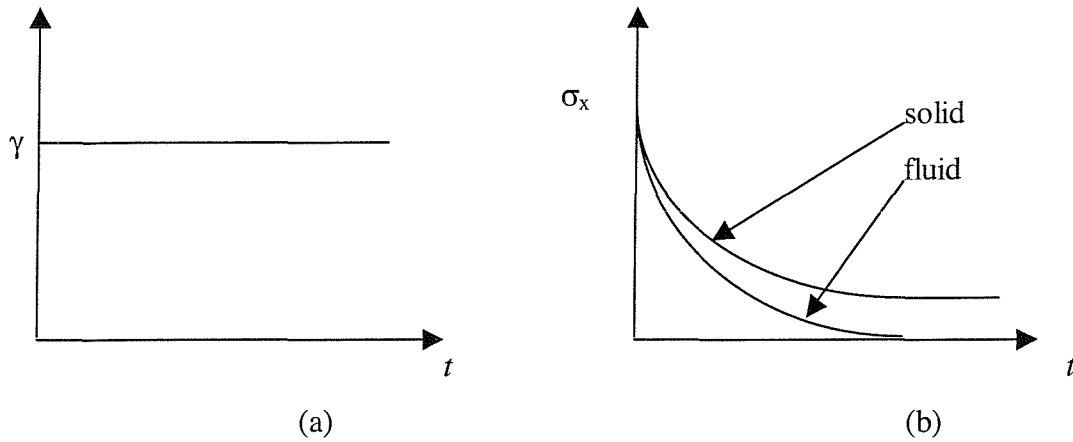


Figure 4.2. (a) The step-strain is applied at $t = 0$ and (b) the stress responses of the solid and fluid to the step-strain.

$G(t)$ is called the relaxation modulus of the suspension and $\dot{\gamma}$ is the shear rate. In this study, we measure the mechanical strength by imposing a sudden strain of γ at the first step between $t' = -\Delta t$ and $t' = 0$. The shear rate is then equal to $\gamma/\Delta t$ and the shear stress becomes,

$$\sigma_{xy}(t') = \int_{t_0 - \Delta t}^{t_0} G(t' - t) \left(\frac{\gamma}{\Delta t} \right) dt. \quad (4.7)$$

We modify the equation by calculating the average value of the relaxation modulus between $t_0 - \Delta t$ and t_0 ,

$$\begin{aligned} \int_{t_0 - \Delta t}^{t_0} G(t) dt &= \Delta t G(t_0 - \Delta t + c\Delta t) \\ &= \Delta t G(t_0 - (1 - c)\Delta t) \end{aligned} \quad (4.8)$$

where $0 \leq c \leq 1$. Eqn. [4.8] can then be written as,

$$\begin{aligned} \sigma_{xy}(t') &= \frac{\gamma}{\Delta t} \Delta t G(t' - (t_0 - (1 - c)\Delta t)) \\ &\approx \gamma G(t') \end{aligned} \quad (4.9)$$

for $t_0 = 0$ and $t' \gg \Delta t$.

In the simulation, the relaxation modulus is the unknown quantity and we compute the stress tensor by through the virial equation,

$$\sigma_{\alpha\beta} = \rho k_B T - \frac{1}{V} \sum_{i=1}^{N-1} \sum_{j=i+1}^N \frac{r_{\alpha ij} r_{\beta ij}}{r_{ij}} \frac{dU_{ij}}{dr_{ij}} \quad (4.10)$$

where V is the volume of the simulation box and U_{ij} is the interaction potential between i and j and $r_{\alpha ij}$ is the α -component of the interparticle vector.

In the limit of t approaching zero, the relaxation modulus will give the high frequency limit of the storage modulus, G_∞ . The storage modulus at infinite frequency can also be calculated using the equation proposed by Zwanzig and Mountain[108],

$$G_\infty = \rho k_B T + \frac{2\pi\rho^2}{15} \int_0^\infty dr g(r) \frac{d}{dr} \left(r^4 \frac{dU_{ij}}{dr} \right). \quad (4.11)$$

In the long time limit, the modulus will decay and reach some equilibrium value. In a fluid system, the stress is expected to decay immediately to zero, i.e. relax completely, after a short period of time. A complete relaxation may not occur within the length of the simulation in a system which exhibits a solid-like response. Fig 4.2 shows the step-strain history and the comparison of the stress response for the solid and fluid.

Chapter 5

Particle gels formation with the inverse Debye length

In this study, we choose a fixed volume fraction, $\phi = 0.3$ and a fixed quenched temperature at room temperature, while the inverse Debye length, κ , is varied. The range of κ chosen for the studies is obtained using the theoretical phase diagram as a guide. Based on the phase diagram, we decided to vary κ between $\kappa = 150\sigma^{-1}$ and $250\sigma^{-1}$. This ensures that the simulations will cover the fluid-phase region down to the unstable phase region above the critical coagulation concentration.

For systems well below the spinodal line, the formation of the percolating gel, the network that fills the whole simulation box, is observed. We will examine the structural evolution, the long-range and the short-range orders. The long-range order is analysed through the structure factor and also by calculating the fractal dimensionality to measure the compactness of the structures. The evolution of the local order is studied by looking at the coordination number and the radial distribution function.

We will attempt to relate the structure of the networks to their mechanical strength by carrying out the step-strain simulation to measure the viscoelastic response. The stiffness of the structure can be measured by calculating the high frequency shear modulus and the elasticity is measured through the equilibrium modulus.

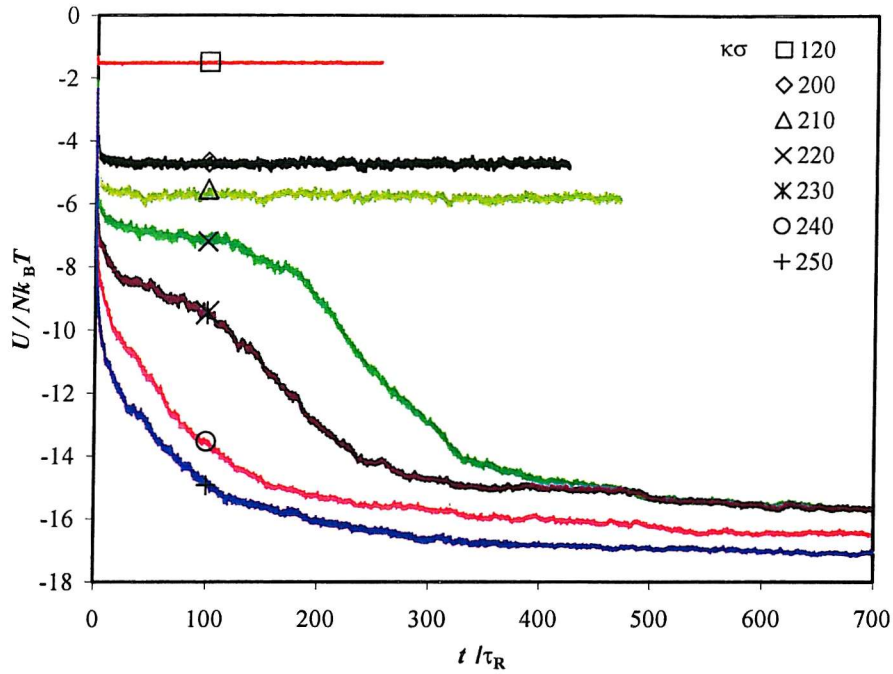


Figure 5.1. The average configurational energy as a function of time at different κ

We first plot the configurational energy per particle as a function of time in Fig. 5.1. The energy is calculated as the sum of the pairwise two-body conservative potentials, which in our study is the DLVO potential. Fig. 5.1 reveals that for systems with κ less than $220\sigma^{-1}$, the equilibrium states are reached almost immediately on the simulation timescale with no aggregates detected. The systems are essentially still in the fluid phase after the quenches. This is confirmed in Fig. 5.2, which show the configurations in the late stages, taken at time $471.24\tau_R$. In Fig. 5.2(a), the configuration for $\kappa = 200\sigma^{-1}$ is above the unstable region. The configuration demonstrates that the suspension stays dispersed throughout the simulation.

At $\kappa = 220\sigma^{-1}$, the plot of the interaction potential as a function of time displays an inflection point at intermediate times. Beyond this point, the interaction potential decreases rapidly with time until it levels out at larger times. This suggests a dramatic departure towards the formation of a more compact structure in the system for $\kappa > 220\sigma^{-1}$. The interaction potential then shows a slow decrease until the end of the simulation and because equilibrium has not been reached. This marks the boundary of the phase separation and comparison with the predicted spinodal line shows in Fig. 3.5 that the

boundary is slightly lower than the prediction from the equilibrium phase diagram.

We shall also show that this transition relates to the onset of crystallization in the gel structure. Indeed, as we increase κ to $220\sigma^{-1}$, we start to see the formation of a gel in which the suspension forms a percolating network that fills the entire simulation box. This can be seen in Fig. 5.2(b). This transition is also observed by Soga *et al.*[30] who studied colloidal systems with the depletion potential at 30% volume fraction. Comparison with their results reveals that this transition occurs at comparable depth of the minimum in the interaction potential at around $-3.7k_B T$. The inflection point is observed at earlier times with a further increase of κ . At $\kappa = 240\sigma^{-1}$, the transition occurs so early that the inflection point is no longer detected.

In Fig. 5.2, we may also observe the changes in the resulting gel structures as κ is varied. The gel formed at lower κ is seen to have larger voids surrounding it, which suggests a denser gel is formed in this system.

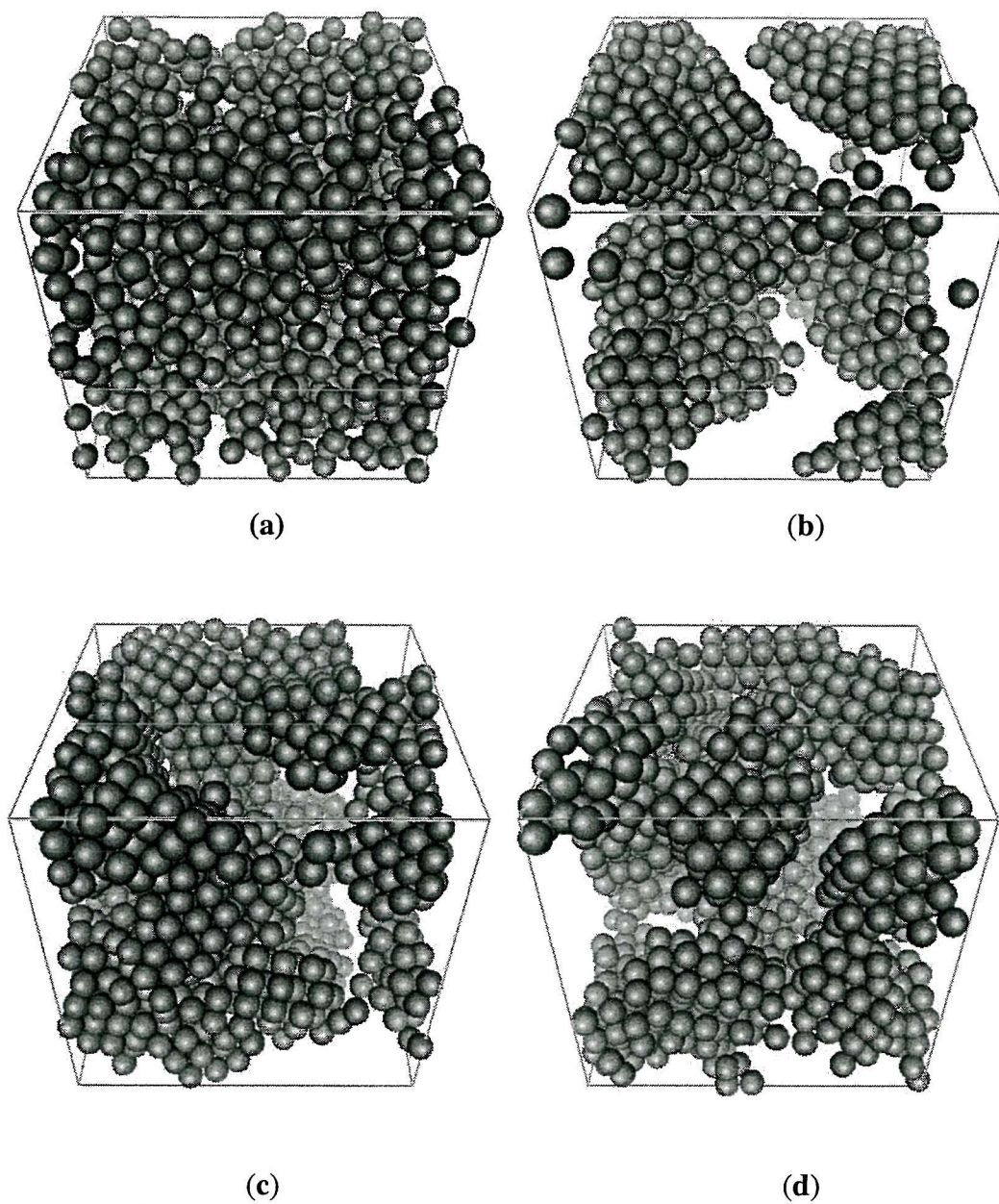


Figure 5.2. The pictures of the resulting structures taken at times $471.24\tau_R$ and $\phi = 0.3$ for $\kappa =$
(a) $200\sigma^{-1}$, (b) $220\sigma^{-1}$, (c) $230\sigma^{-1}$ and (d) $250\sigma^{-1}$.

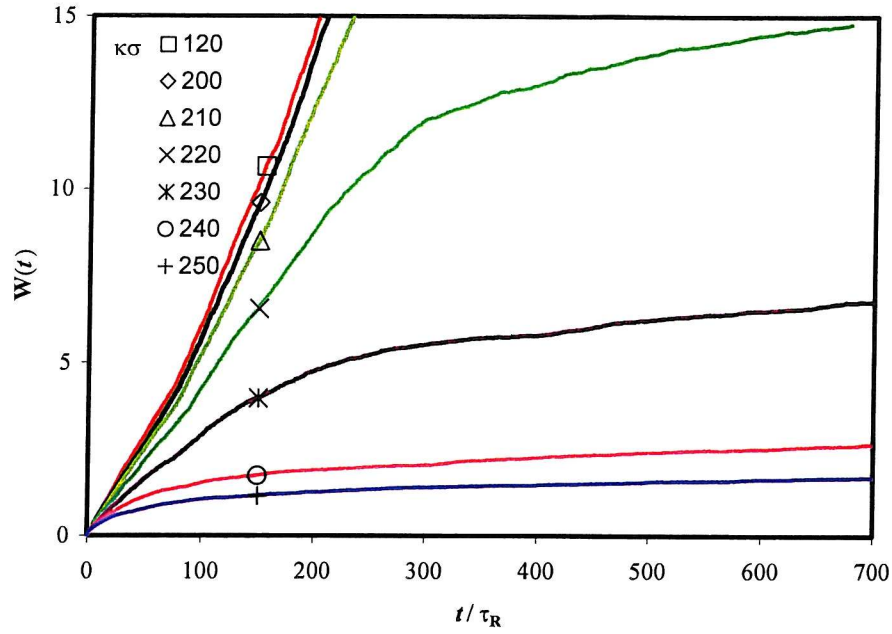
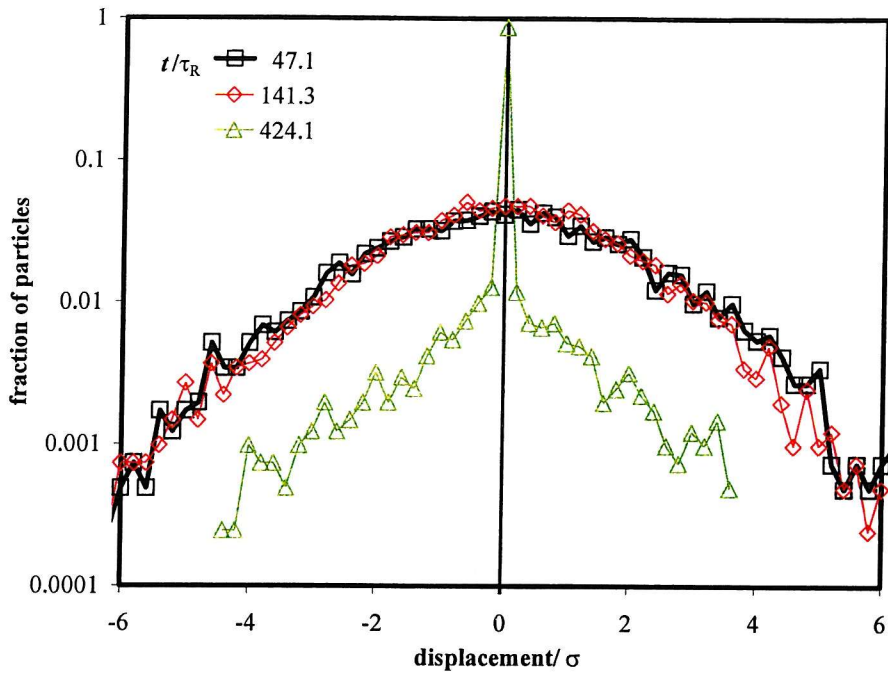


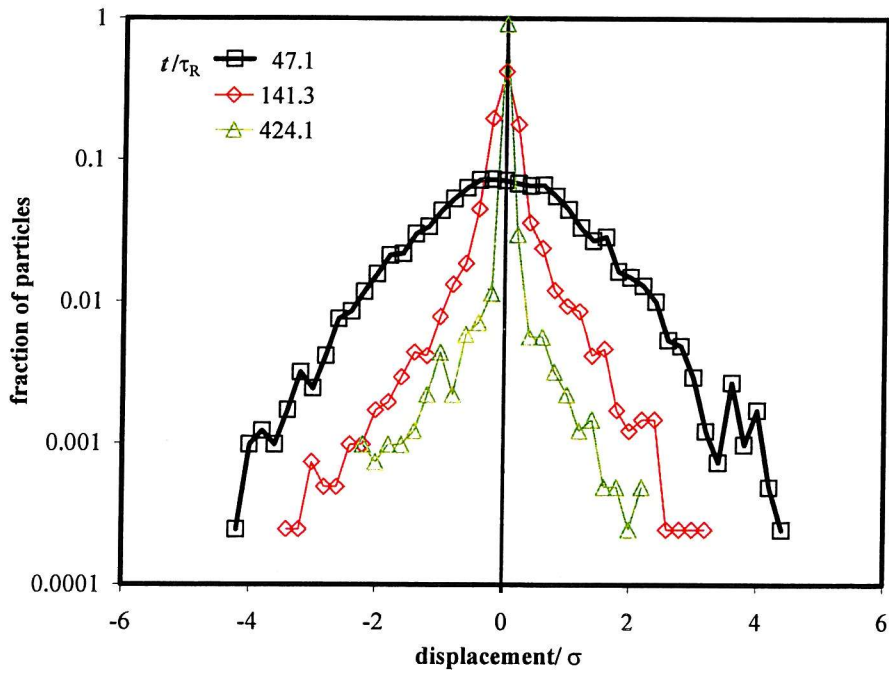
Figure 5.3. The mean square displacement as a function of time at different inverse Debye length.

The effect of the clustering on the mobility of the particles can be seen in the plots of the mean square displacement in Fig. 5.3. The graph also exhibits similar trends to the observed in the energy profile. We found and there are little differences between these plots for systems of κ less than $220\sigma^{-1}$. For suspensions with κ higher than $220\sigma^{-1}$, we observe the transition in the corresponding mean square displacement plot. In early stage of the simulation, the plot shows that the system behaves essentially as a liquid where the plot increases linearly with time. The slope depends on κ .

In the intermediate stage, roughly at $t \approx 300\tau_R$, the particles in the systems start to diffuse more slowly, which is shown in the decrease of the slope of the line. This corresponds to the beginning of the cluster formation of particles within the system which causes the reduction in the mobility. As the clusters start to connect with their neighbours to form a percolating structure, the slope of the line decreases continuously until the end of the simulation. Further decrease in the diffusivity of the particles are also observed as we simulate systems with larger κ .



(a)



(b)

Figure 5.4. The distribution profiles of the displacement at different stages for $\kappa =$ (a) $220\sigma^{-1}$ and (b) $250\sigma^{-1}$.

In Fig. 5.3, we also notice that even in the system with the largest κ , the mean square displacement still shows a continuous increase at the end of the simulation, albeit a very slow one. This is rather surprising considering that most of the particles have become part of the gel network. In order to understand this, we analyse the distribution profiles of the distance displacements at different times. We choose $47.12\tau_R$, which is long compared to the relaxation time but much shorter than the length of the simulation and which are $741.5\tau_R$ and $424.1\tau_R$. We improve the statistics by considering the displacement in all axial directions, Δr_x , Δr_y and Δr_z . The distribution profiles of the distance displacement in the axial directions during that time are shown in Fig. 5.4. The results show that when the systems is dispersed as in the early stages of the simulation, the distribution profile is nearly Gaussian. Once a structure is formed within the system, the movements of the particles are restricted and this are reflected in the increasing fraction of particles, which barely move. However, there is a small fraction of particles which still move quite significantly, and these particles can be expected to be found outside the core structures in the open regions. This is more pronounced for $\kappa = 250\sigma^{-1}$.

In Fig. 5.5, we illustrate the structural evolution of the system undergoing phase separation. The configurations are from a system with $\kappa = 220\sigma^{-1}$ and taken around the time of the onset of the nucleation. The configurations show that even when the system still show fluid behaviour at early stage Fig. 5.5(b), the suspension already reveals the dense and dilute regions which later develops to form the gel network.

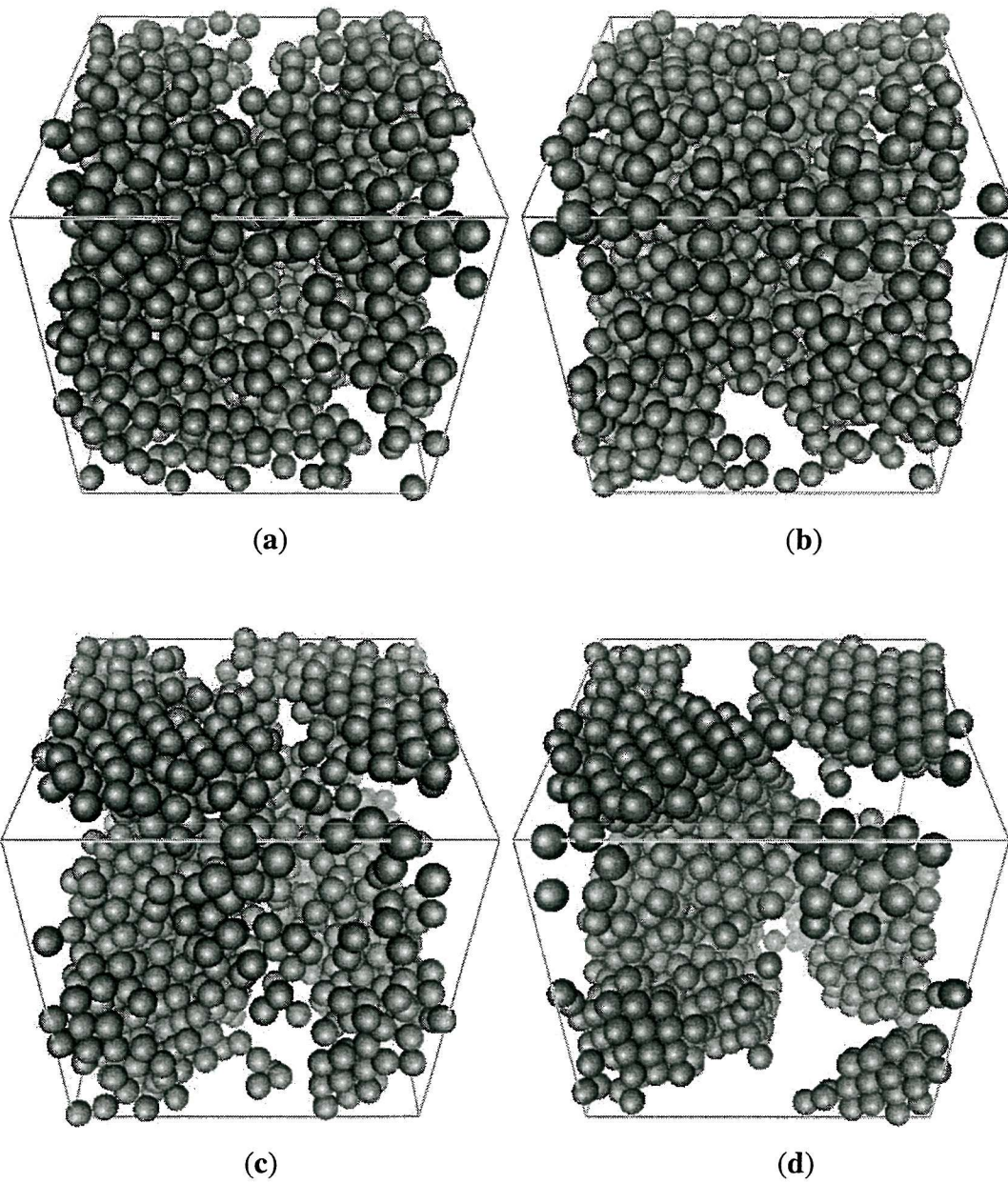


Figure 5.5. The snapshots of the structural evolution in the system containing 1372 particles at $\kappa = 220\sigma^{-1}$ and $\phi = 0.3$. The snapshots are taken at times (a) $94.25\tau_R$, (b) $164.93\tau_R$, and (c) $282.74\tau_R$ and (d) $400.55\tau_R$. The snapshots illustrate how the gel network develops.

5.1. Local structure and short range order

We study the evolution of the local structure by monitoring the profile of the distribution of the coordination numbers. This is defined as the number of the nearest neighbours in a particular particle. Our model has an interaction which dominates over the Brownian motion only at a very short range. Hence this can be thought of as the number of particles that directly interact with a given particle. The cut-off for a nearest neighbour distance is defined as the distance at which the potential is $-k_B T$. We anticipate that this is a reasonable definition as the random Brownian force is expected to dominate over any bond formed with energy of less than $k_B T$. Although this cut-off distance varies slightly with κ , the difference is only about 0.01% between the largest and the smallest κ values.

In Fig. 5.6 and 5.7, we present the distribution profiles of the coordination number as a function of time for different values of κ . The profiles in Fig. 5.6 are for systems above the spinodal line and both graphs show that the equilibrium values are quickly attained within a few τ_R . On closer inspection, there are several interesting differences that can be identified. At $\kappa = 120\sigma^{-1}$, the majority of the particles have just one or no neighbour within the cut-off distance. In this system, we also found particles with larger coordination numbers. It is unlikely that these neighbours form long-lived bonds that lead to nucleation as the distribution profile of the coordination number stays unchanged throughout the run. The visual inspection for this suspension also shows that the systems can be considered as liquids and we do not see any long-range order in the suspension.

As we study suspensions with larger κ values, there are significant changes in the distribution profiles. We observe the shift in the peak of the distribution profiles with κ , from 1 for $\kappa = 120\sigma^{-1}$ to 3 for $\kappa = 200\sigma^{-1}$ and 4 for $\kappa = 210\sigma^{-1}$. The spectrum of the distribution profiles also broadens towards higher coordination number at the expense of the lower coordination number, although we still do not detect any visible order within the suspensions. All these systems can still be regarded as stable liquids.

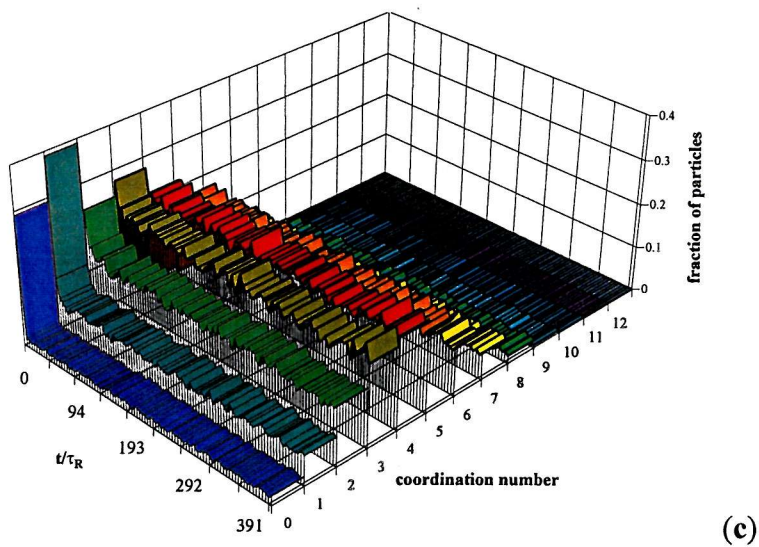
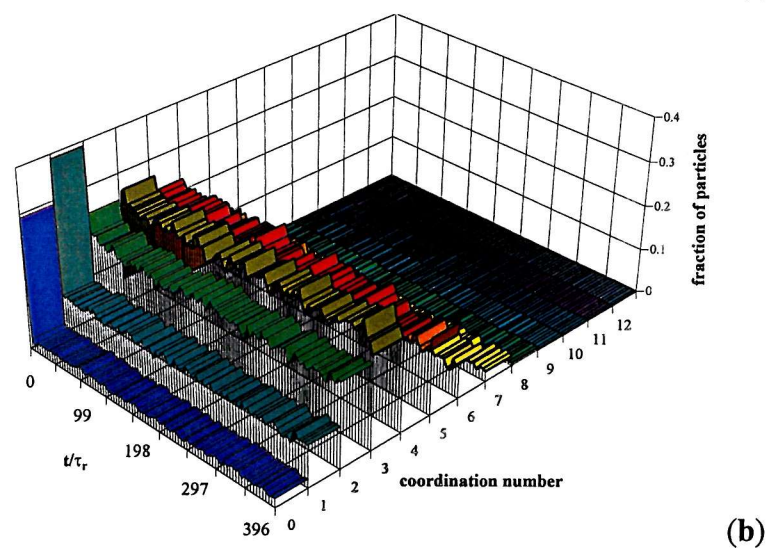
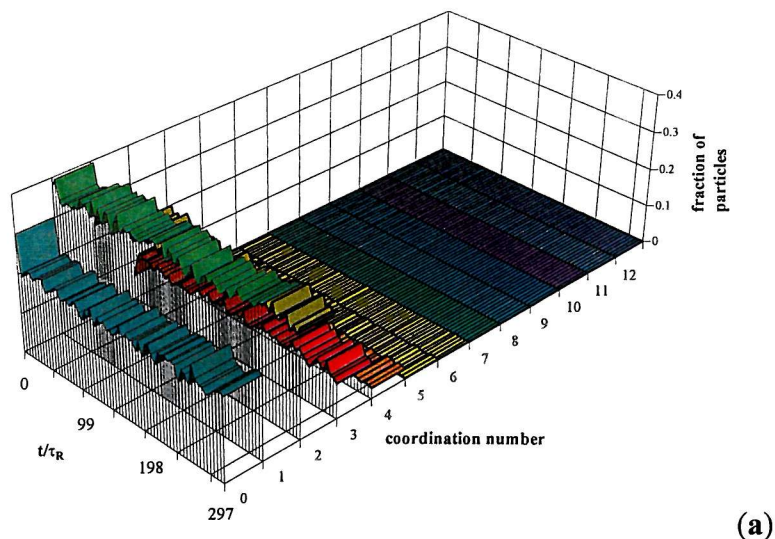


Figure 5.6. The distribution profiles of the coordination numbers shown as a function of time for $\kappa\sigma$ equals to (a) $120\sigma^{-1}$, (b) $200\sigma^{-1}$ and (c) $210\sigma^{-1}$.

In Fig. 5.7, we show the corresponding profiles for systems below the spinodal line. The distribution profiles are very different when compared to those for liquid systems. At early stages, the distribution profiles are peaked at 4. For $\kappa = 220\sigma^{-1}$, which is just below the spinodal line, this peak persists up to intermediate time before the peak shift to higher coordination number. This is the indication of the phase separation through the nucleation process followed by the cluster growth. The phase separation, once it is induced, progresses rapidly and the peak of the distribution shifts even further until it reaches the full coordination number as the particles form larger aggregates. At this stage, the suspension produces a compact structure, which is shown by the large fraction of particles with the full coordination number.

As κ is increased, the onset of the phase separation appears sooner. This is shown by the rise of the fraction of full coordination number which occur at earlier times while the fraction of particles with small coordination number decreases rapidly. The nucleation onset, which occurs at earlier stages with increasing κ , is also followed by slower rearrangements. This is shown by slower rise of the number of particles with full coordination number with larger κ . Presumably this is due to increasing difficulty of the particles in the cluster to rearrange as the secondary minimum is getting deeper. This is consistent with theory that predicts a shift towards glassy behaviour where the structural evolution is arrested and the systems is more or less completely disordered at all levels.

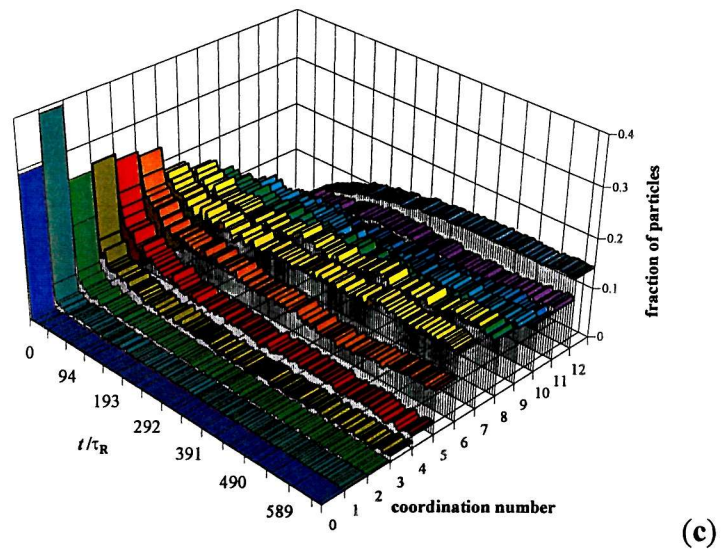
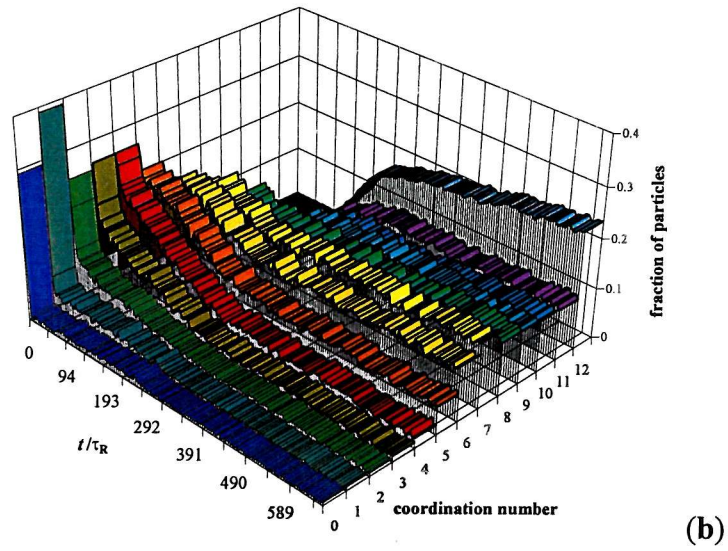
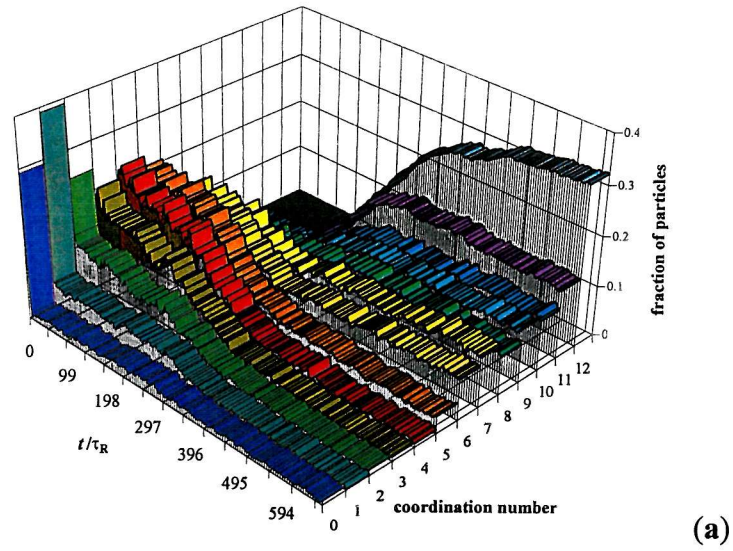
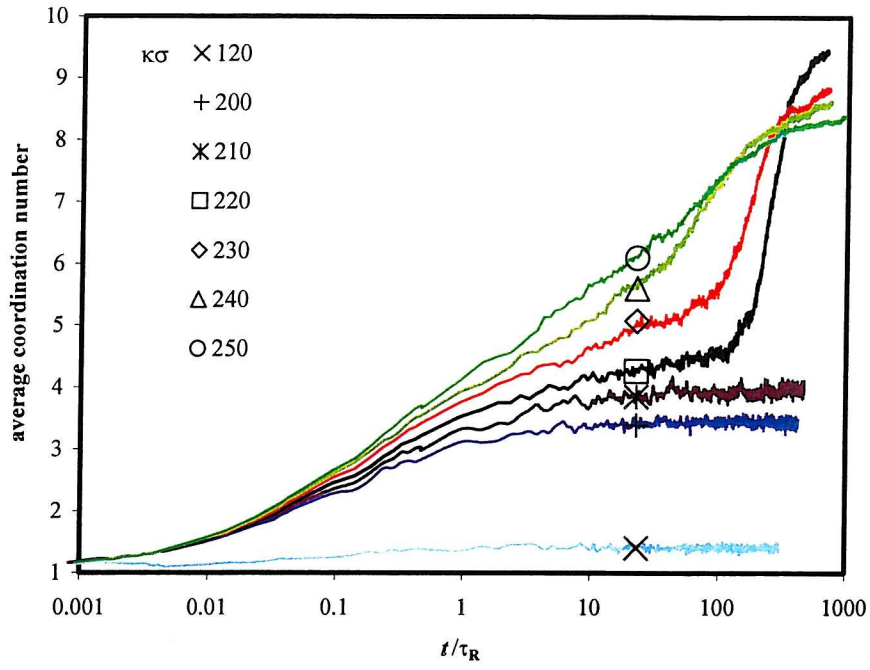
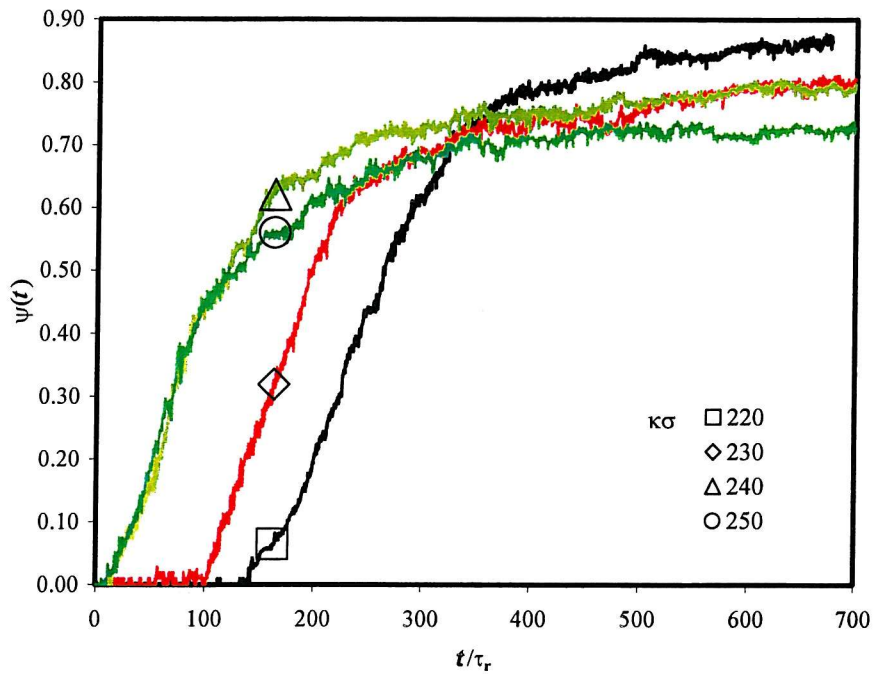


Figure 5.7. The distribution profiles of the coordination numbers shown as a function of time for κ equals to (a) $220\sigma^{-1}$, (b) $230\sigma^{-1}$ and (c) $250\sigma^{-1}$.



(a)



(b)

Figure 5.8. (a) The average coordination numbers as a function of time at different κ values and (b) the fraction of particles which are parts of the crystal domain.

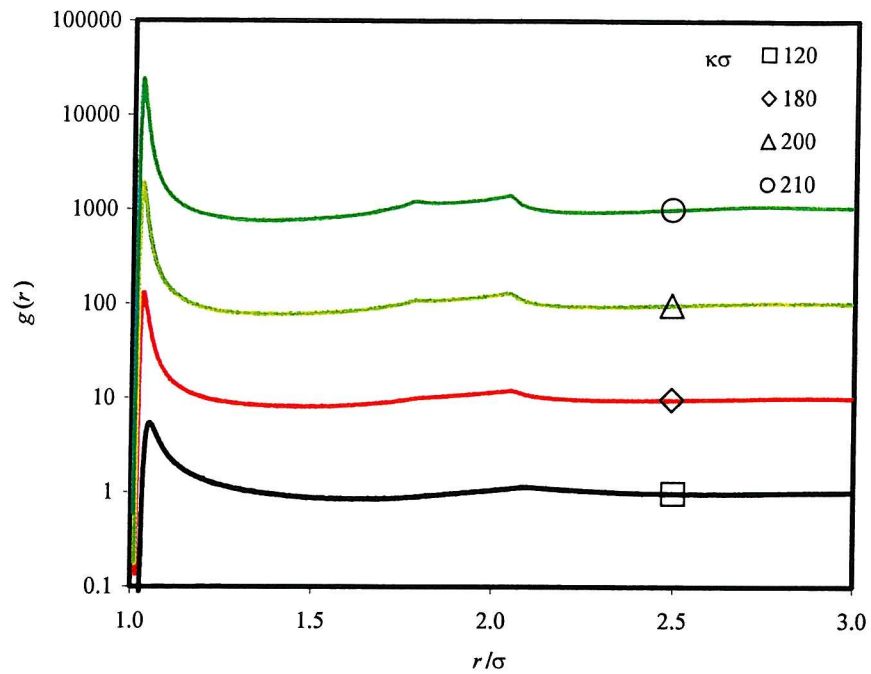
In Fig. 5.8(a), we show the plots of the average coordination number as the systems evolve. We can see clearly here for systems in liquid phase, the average coordination number is shown to increase at early stages before it reaches equilibrium within $10 \tau_R$. Meanwhile for systems quenched below the spinodal line, the coordination number increases monotonically at all time, although its rate varies at all stages. Initially, the increases in rate are the same for all systems as they only depend on the short-time diffusion coefficient. At intermediate times, the rates start to diverge, with higher rates observed for systems with larger κ . At the largest κ , the average coordination number is seen to increase logarithmically with time.

For systems quenched just below the spinodal line, we observe the inflection points similar to those observed in the energy plots. Beyond this point, the average coordination number rises steeply with time and the rate of change of the coordination number fall again later. The inflection point appears at earlier time with larger κ values. The transition becomes less visible at larger κ and it has disappeared in the system for $\kappa = 250\sigma^{-1}$. We observe a logarithmic increase in the average coordination number at this value of κ .

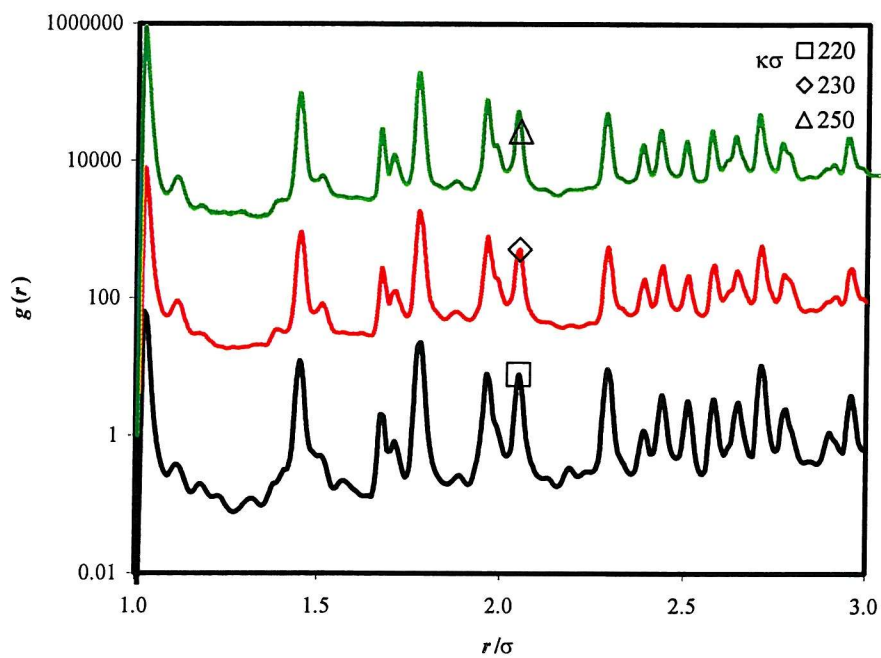
We study the onset of the nucleation by looking at the appearance of the crystal domain. The nucleation process starts with the formation of the crystal domain that leads to further growth. A particle is considered to be part of the core of the crystal domain when it has the full coordination number of 12. The domain will include the core and the neighbouring particles which may not have the full coordination number. In Fig. 5.8(b), we show the fraction of particles that belong to the crystal domain as a function of time. The inflection point corresponds to the onset of nucleation. For $\kappa = 220\sigma^{-1}$, the inflection point occurs at around $140\tau_R$ and it happens at $100\tau_R$ for systems with $\kappa = 230\sigma^{-1}$. The fraction of particles in the crystallite then rises with time until most of the particles belong to the crystal domain. Further increase is then only possible by means of rearrangement of the particles within the boundary to attain the full coordination number. We can see the effect of the shallower secondary minimum which results in easier rearrangement of crystallite and for $\kappa = 220\sigma^{-1}$. In this case about 90 % of the particles are members of the crystal domains.

In the intermediate range, the local structure is studied through the radial distribution function, $g(r)$ at different κ values. For suspensions quenched into liquid regimes, the resulting $g(r)$ is relatively unchanged as the suspensions reach equilibrium in short times. In Fig. (5.9(a)) we show the equilibrium $g(r)$ for systems with κ less than or equal to $220\sigma^{-1}$. All the plots display distinct peaks at distances of $\sigma, 2\sigma, 3\sigma \dots$, denoting orders at short and intermediate ranges. The noticeable effect of increasing κ is the sharpening and the increasing height of the first peak as nearest neighbours becoming more firmly attracted to neighbours with deepening secondary minimum in the potential. The other changes in the $g(r)$ with increasing κ are the increase of the peaks at 2σ and the appearance of a small peak at a distance of $\sqrt{3}\sigma$, which is associated with the second nearest neighbours.

As we cross the phase separation boundary, there are significant changes in the shape of the radial distribution functions. In Fig 5.9(b), we show the corresponding $g(r)$ for systems below the spinodal line. The resulting plots of $g(r)$ is very different from that of a fluid. We note that the peaks at $\sqrt{3}\sigma$ and also $\sqrt{2}\sigma$ at are significant which indicate the presence of the second nearest neighbours in the crystallite. The $g(r)$ is taken at $t = 471\tau_R$ and at this point, all the systems are still evolving unlike the fluid systems which would have reached their equilibrium. Hence the $g(r)$ here represents an average radial distribution function for a segment of the simulation runs.



(a)



(b)

Figure 5.9. The radial distribution function for system at equilibrium for systems (a) above and (b) below the spinodal line. The plots in 9(a) and 9(b) are shifted by 1 and 2 decades respectively for clarity.

In Fig. 5.10, we show the evolution of the radial distribution function for $\kappa = 220\sigma^{-1}$, $230\sigma^{-1}$ and $250\sigma^{-1}$ at different times during the run. In our simulation we calculate the average of the radial distribution function every $0.5\tau_R$ and the time refers to the time at the end of a segment when the average is calculated.

The graphs show that all of the crystallization starts with the rapid increase of the peak at $\sqrt{3}\sigma$ and as the simulation progress, this is followed by appearances of other peaks in different locations. The formation of these peaks relates to the phase separation where the crystal appears. In systems at $\kappa = 220\sigma^{-1}$, the peak at $\sqrt{3}\sigma$ is unchanged up to intermediate times before a rapid rise occurs. This rise is accompanied by the appearance of the peak at $\sqrt{2}\sigma$. This is consistent with the picture of the nucleation in a metastable region. For a suspension quenched into this region, the system will initially relax to a state corresponding to a local free energy minimum. In the absence of any disturbances, the system will remain there indefinitely, as there are local maxima that prevents the system from relaxing further to the state with the true free energy minimum. The Brownian motion however provides the fluctuations that induce the creation of clusters. This cluster has a maximum free energy at some critical diameter. If the fluctuations form a cluster whose diameter is less than the critical diameter, the system can decrease its energy by decreasing the size of the cluster. On the other hand, if the cluster size is larger than the critical diameter, the cluster will grow into larger aggregates or possibly form a network of aggregates.

In the system with $\kappa = 220\sigma^{-1}$, the $g(r)$ suggests that the clusters which are formed are easily disrupted by the Brownian motion. The cluster which is large enough to induce the nucleation does not appear spontaneously and it may take sometime before a cluster larger than a critical size formed. In our simulation, this nucleation process occurs at $t \approx 200\tau_R$.

Once this cluster is formed, further nucleation occurs spontaneously and leads to a more ordered system indicated by the appearance of other peaks in $g(r)$. This also explains why although some order at intermediate range has been observed at κ lower than $220\sigma^{-1}$. There is no further growth of the clusters is seen during the simulations as the clusters are

broken down by the Brownian force before they reach a critical size.

The maximum barrier that prevents the nucleation decreases with κ and hence the onset of the nucleation occurs at earlier time with increasing κ . At $\kappa = 250\sigma^{-1}$, the system may already be in the unstable region where the maximum free energy barrier has vanished and the nucleation process happens immediately after the quench. This is shown by the appearance of the peaks at a very early stage in the simulation.

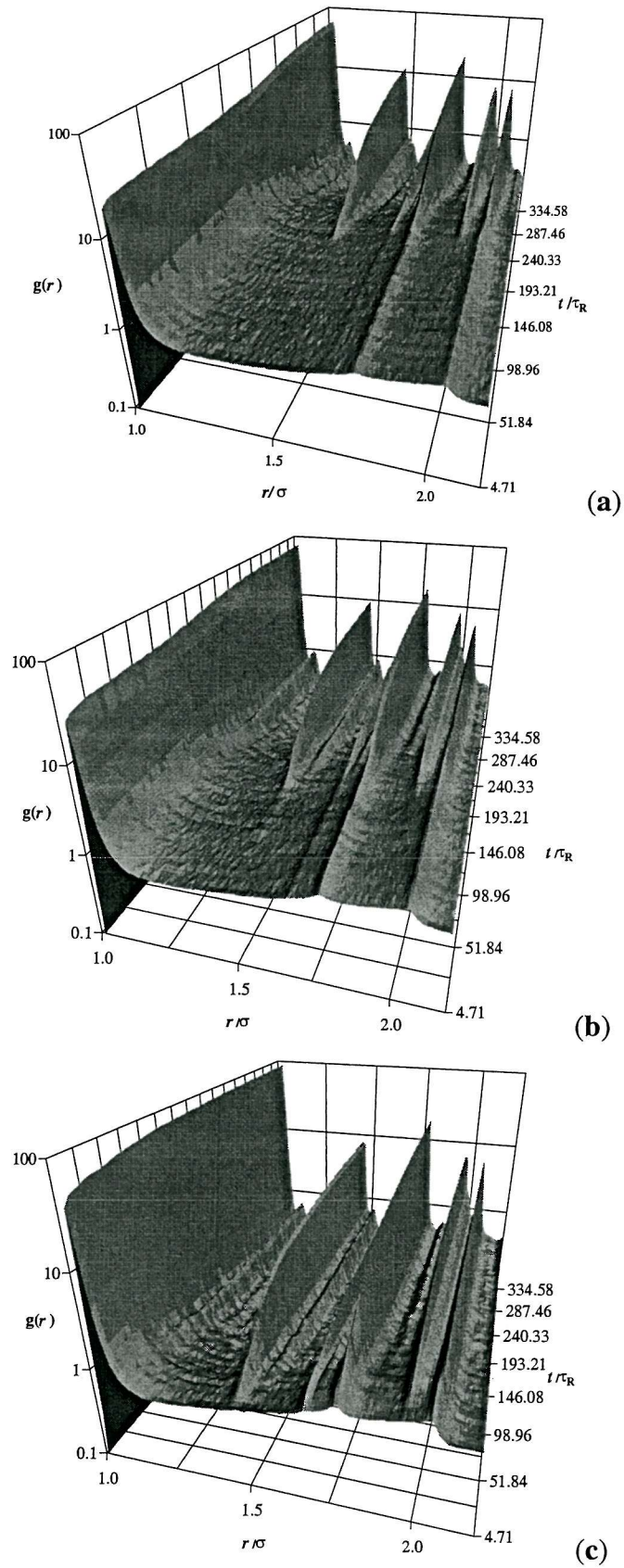


Figure 5.10. The radial distribution function for $\kappa =$ (a) $220\sigma^{-1}$, (b) $230\sigma^{-1}$ and (c) $250\sigma^{-1}$ as a function of time. Each point is averaged over $1 \tau_R$.

5.2. Long-range order

We analyse the long-range order of the system and compare this order at different values of κ . We plot the structure factors, $S(k)$, which describe the average distribution of the particle separations in the colloidal systems. In a fluid hard sphere suspension, the strongest correlation in $S(k)$ will be at $k \approx 2\pi/\sigma$, which corresponds with the average distance of the nearest neighbours. In our model of colloidal suspensions, the resulting structure factor plot for $\kappa = 120$, Fig. 5.11(a), shows such a plot corresponding to that for the hard sphere fluid.

For $\kappa = 200\sigma^{-1}$ and $210\sigma^{-1}$, although the resulting radial distribution function suggests that the system is in the liquid state, a significant fluctuation is observed in the $S(k)$ at small k . This can be seen in Fig. 5.11(b) and 11(c). This suggests the continuous formation of weak structures which disintegrate after a short time due to the Brownian motion. This behaviour gives a time-dependent correlation at small k in the absence of peak growth in $g(r)$.

For the systems quenched well below the spinodal line where the percolating structure starts to form, different behaviour is again observed as shown in Fig. 5.11(d) – 11(f). In these systems, the peaks at small k are observed to increase continuously as the simulation progress. This is similar to the behaviour observed in the simulations of diffusion-limited aggregation at small volume fraction. This peak is interpreted as the increase of the structural correlation in the long-range order with the characteristic length of about $2\pi/k_{\max}$, where k_{\max} is the peak of the structure factor at small k [93].

At $\kappa = 220\sigma^{-1}$, the structure factor plot suggests that the system is globally unstable and it develops through spinodal decomposition which is shown by the continuous growth of the peak at small k . On the other hand the evolution of the radial distribution function and the coordination number suggests that the resulting structure develops through the nucleation and growth mechanism which starts with appearance of a cluster of radius larger than some critical value.

Part I. Brownian Dynamics Simulation Of Colloidal Particles In Ionic Solution

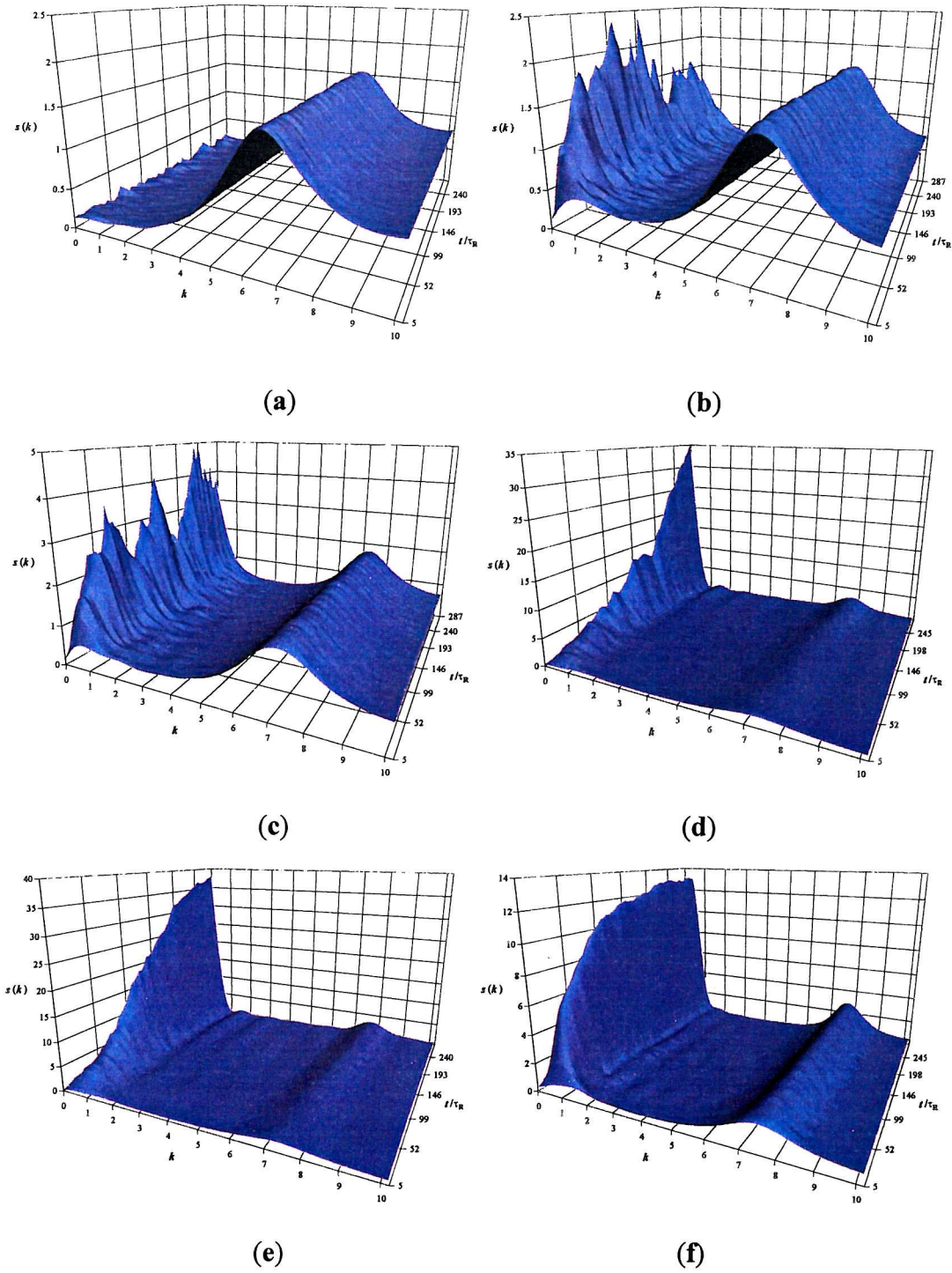
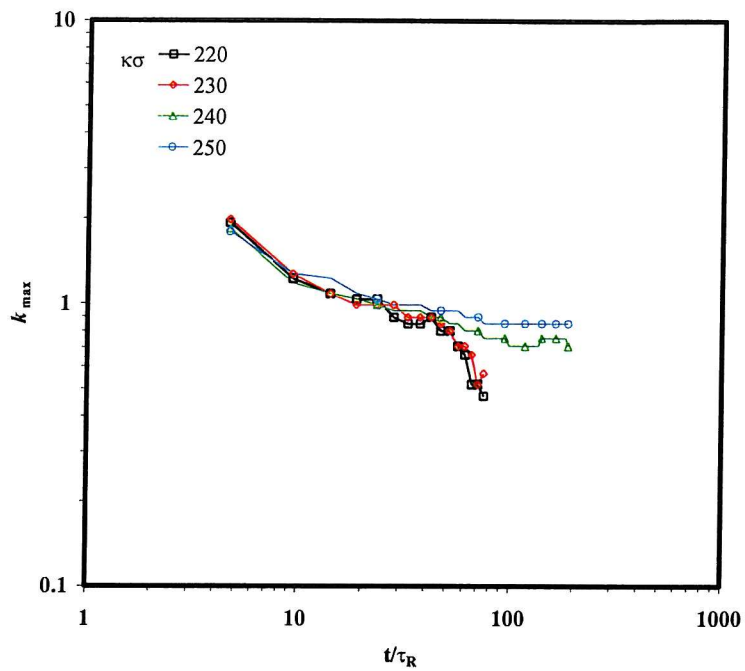


Figure 5.11. The structure factors calculated from the structure factor as a function of time for $\kappa =$ (a) $120\sigma^{-1}$, (b) $200\sigma^{-1}$, (c) $210\sigma^{-1}$, (d) $220\sigma^{-1}$, (e) $230\sigma^{-1}$ and (f) $250\sigma^{-1}$.

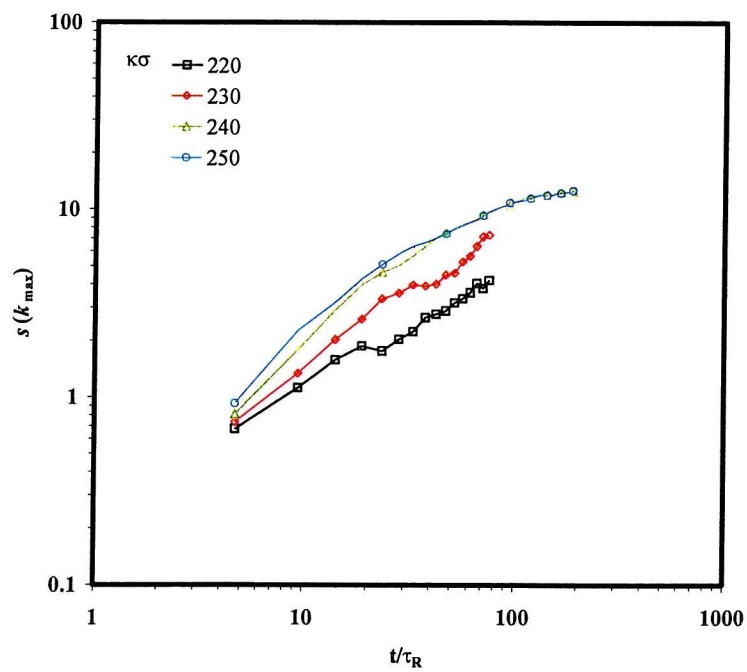
This is again similar with observations by Soga *et al.*[29] for a system with the depletion potential quenched to just below the phase coexistence line. They propose that the onset of the nucleation is induced by the hidden fluid-fluid binodal line, below the fluid-solid binodal line. This hidden coexistence line induces the formation of slightly dense regions which in turn promote the formation of large enough clusters to start the nucleation process.

The size of the clusters within the systems relates to k_{\max} , which is the position of the first peak in the structure factors. The smaller k_{\max} , the larger the size of the clusters that are formed. In Fig. 5.12(a), we show the changes of k_{\max} as the runs progress. The shift of k_{\max} toward smaller values indicates the growth of the clusters as the colloidal particles aggregate. We observe from the shift that all systems exhibit similar rates for the cluster growth at early times. At intermediate times, the growth rates decrease for systems with higher κ , while the rates are relatively unchanged for lower κ .

The shift in the k_{\max} is largely insensitive to κ at early stages, suggesting that the growth of these systems is regulated by the same mechanism. At early stages, k_{\max} shifts towards lower k as a function of $t^{-0.5}$. For systems with $\kappa = 220\sigma^{-1}$ and $230\sigma^{-1}$ at some intermediate time, k_{\max} decreases more steeply as t^{-1} and k_{\max} reaches a wavelength which is the size of the simulation box at quite an early stage. For these systems, the structure factors can only be evaluated at early stages. For larger κ values, the shift in the k_{\max} slows down as the structures evolve and changes little beyond $t \approx 100\tau_R$. This means that the systems may form arrested structures which evolve very slowly and which are disordered over large length scale.



(a)



(b)

Figure 5.12. The changes in (a) the position and (b) the height of the structure factor peaks as a function of time.

The growth of mass corresponds to the growth of the height of the first peak, $S(k_{\max})$. Our results, as shown in Fig. 5.12(b) suggest that the behaviours are rather different depending on how close the systems are to the spinodal line. In the systems well below the spinodal line, the growth rate changes continuously over time. Since these systems should be in the unstable region, we expect the phase separation to take place soon after the quench which results in a high growth rate at early times. The rate then starts to decrease as the mass increases and the diffusion is slower. For systems with lower κ , the peaks height are shown to increase roughly as a power-law function of time, which we found to be $t^{0.6}$. This is because the attractive interaction is weaker in these systems and the high mobility of the particles means that there is rapid progress towards a crystalline structure.

We measure the compactness of the resulting structures by plotting the average number of particles within a radius r , $n(r)$, which can be obtained from the radial distribution function. From the plots, we can also measure the fractal dimension of the structure to analyse the structural evolution. For all systems in our simulations, we are able fit a power law function to the plots from the distance of 2σ up to the distance of half the simulation box.

In Fig. 5.13(b), we show that for systems in the fluid phase, the fractal dimensionality does not deviate from 3. Surprisingly, the more open structure is found in the system of $\kappa = 220\sigma^{-1}$, which is about 2.6 at late stages. This is larger than the typical values observed for the reaction-limited cluster aggregation[81]. This is because the resulting structure for this system is a higher density crystalline network surrounded by low density regions.

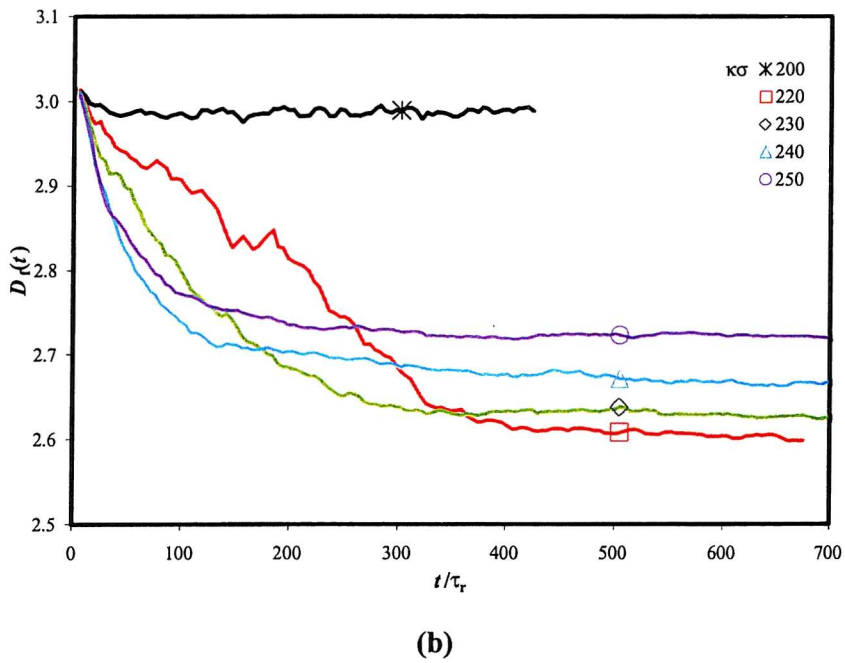
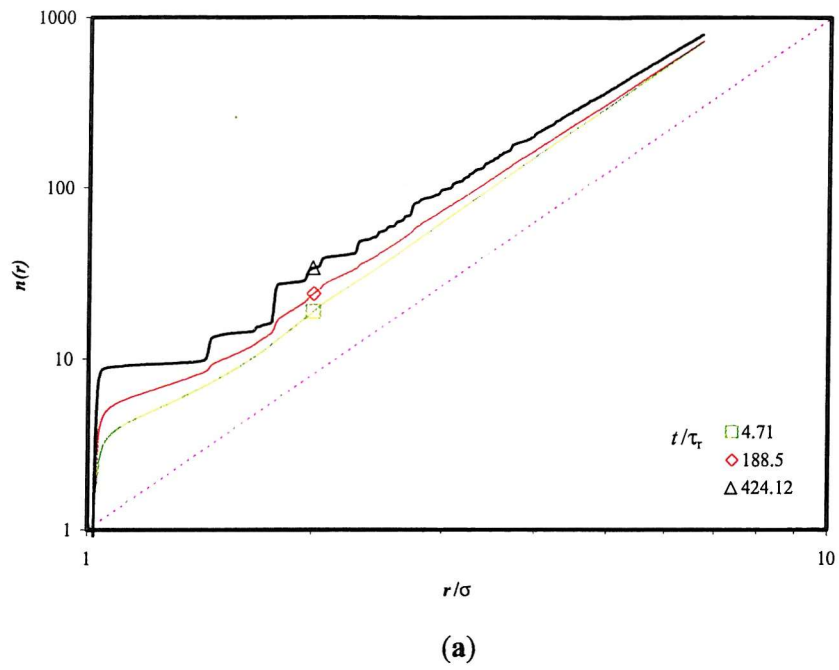


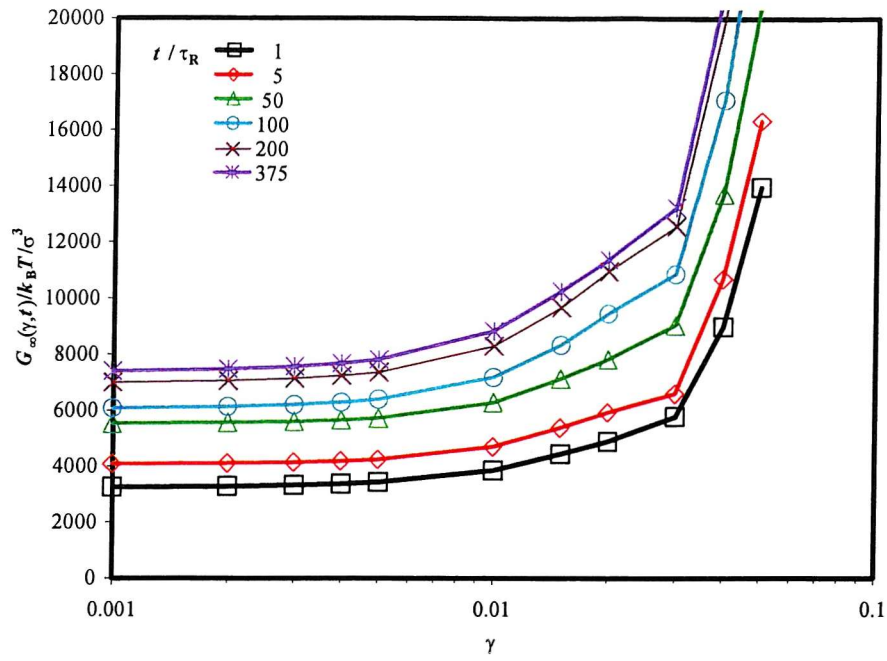
Figure 5.13. The plots of (a) $n(r)$ of the gel system at $\kappa = 220\sigma^{-1}$ at different gel ages. The dashed line is the guideline with the slope of 3. (b) The resulting fractal dimension calculated from the plots of $n(r)$ at various κ as a function of time.

5.3. Mechanical stability

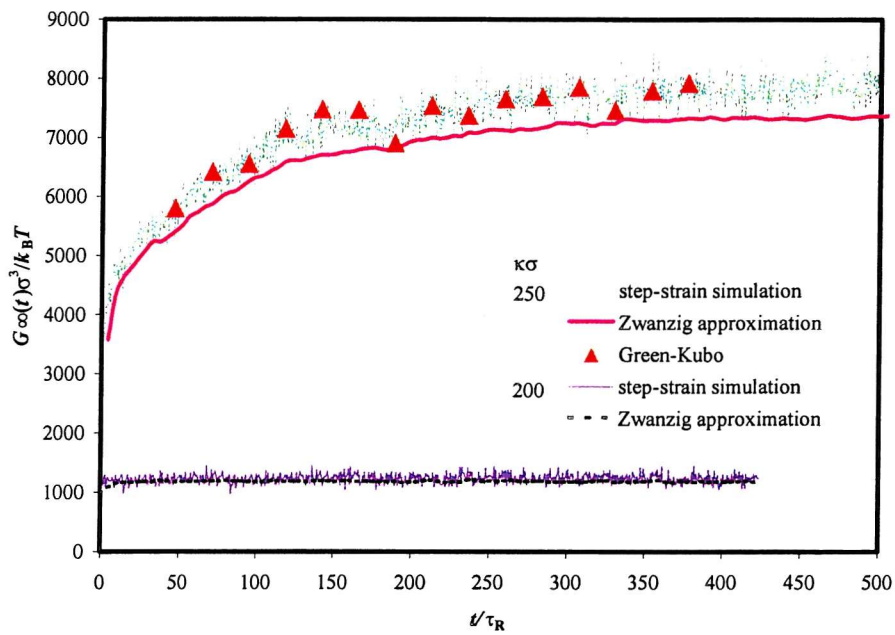
In order to probe the correct linear regime for a simulation study of the mechanical strength, we need to explore the relationship between the shear modulus and the strain magnitude to ensure that the gels are within the linear viscoelastic regimes when the strain is applied. In this regime, the resulting shear stress increases linearly with the size of the step-strain. Therefore the shear modulus, the ratio between the shear stress and the step-strain, should be independent of the size of the step-strain.

We first analyse the high frequency shear modulus, G_∞ , which is obtained by calculating the modulus just after the strain is applied (The method is described in chapter 4). The strain magnitude is a measure of the stiffness of the structure. The dependency of G_∞ on the strain magnitude is studied by varying the strain magnitude at different gel ages. G_∞ is strongly influenced by the softness of the particles and in the limit of the hard sphere potential, G_∞ becomes infinite.

We study the increase of G_∞ as a function of the strain magnitude for system of $\kappa = 250\sigma^{-1}$ and $\phi = 0.3$ and the results are plotted in Fig. 5.14(a) for different gel ages. The figure shows that for small step-strain of less than 0.5%, the modulus is independent of the size of the strain. If the strain magnitude increase beyond 0.5%, G_∞ starts to increase. If a strain magnitude of 1 % or larger is applied, G_∞ rises sharply. This is because at large strain magnitude, the cores of the particles start to overlap as the gel network is deformed by the strain. This causes the steep rises of the repulsive forces which results in the steep rise in the shear modulus. We note that the structure becomes stiffer as the gel ages. This is because the percolating structure emerges and evolves as the simulation progresses. As the structure develops, the resulting network grows stronger and provides higher resistance when an external strain is applied.



(a)



(b)

Figure 5.14. (a) The storage modulus at infinite frequency as a function of the step strain, taken at different times during the run for $\kappa = 250\sigma^{-1}$ and $\phi = 0.3$ and (b) The comparison of the G_∞ obtained using 3 different methods for systems with 2 different κ values.

As a further check, the results from the non-equilibrium simulation are compared with the results obtained by the Green-Kubo method[96] and the formulation from Zwanzig[97] for two different systems. The system at $\kappa = 200\sigma^{-1}$ is fluid and system at $\kappa = 250\sigma^{-1}$ is gel phase.

The Green-Kubo method allows us to extract the shear modulus from the stress relaxation of an unsheared system by calculating the shear-stress autocorrelation function,

$$C_s(t) = \frac{V}{k_B T} \langle \sigma_{xy}(t) \sigma_{xy}(0) \rangle. \quad (5.1)$$

The shear modulus at infinite frequency using the Green-Kubo method is

$$G_\infty = C_s(t = 0). \quad (5.2)$$

The Zwanzig formula to calculate the shear modulus at infinite frequency

$$G_\infty = \rho k_B T + \frac{2\pi\rho^2}{15} \int_0^\infty dr g(r) \frac{d}{dr} \left(r^4 \frac{dU_{ij}}{dr} \right). \quad (5.3)$$

In Fig. 5.14(b), we show that G_∞ calculated by different routes agrees well with each other. A small deviation observed at larger κ due to an approximation in the Zwanzig equation that assumes the system is homogeneous which is not strictly valid in the phase separating regime.

The studies are repeated for systems with other κ values and the results are presented in Fig. 5.15. The results show the same behaviour as shown in the evolution of the configurational energy with time. This is anticipated as G_∞ is strongly influenced by the interaction of the nearest neighbours.

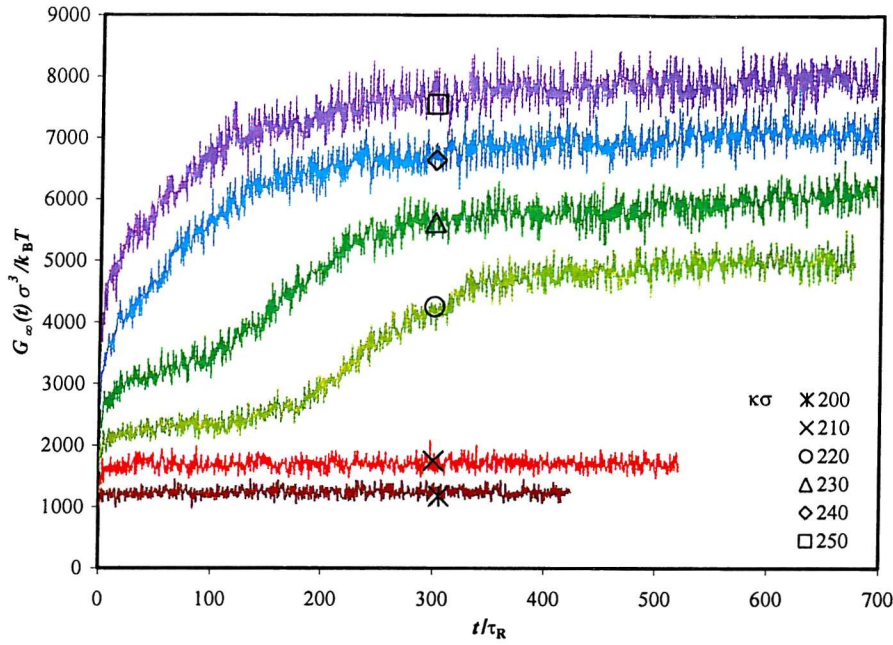


Figure 5.15. The storage modulus at infinite frequency as a function of time for various κ values at 30 % volume fraction.

In the fluid suspensions, we note that the storage modulus is very low and the values are relatively unchanged with time. Once the suspensions are well below the spinodal line, the stiffness is increasing steeply compared to the fluid case as the gel structures start to form.

The elastic properties of the suspensions are measured by plotting the shear modulus as the shear stress decays after the step-strain is applied. The method is described in chapter 2 and the shear stress calculated

$$\sigma_{\alpha\beta} = \rho k_B T - \frac{1}{V} \sum_{i=1}^{N-1} \sum_{j=i+1}^N \frac{r_{\alpha ij} r_{\beta ij}}{r_{ij}} \frac{dU_{ij}}{dr_{ij}} \quad (5.4)$$

In Fig. 5.16, we can see clearly the difference responses of the viscoelastic solids and liquids. When the suspension is in the fluid phase, the stress decays rapidly and relaxes completely well within the length of the simulation. The stress then only fluctuates around zero due to the thermal motion.

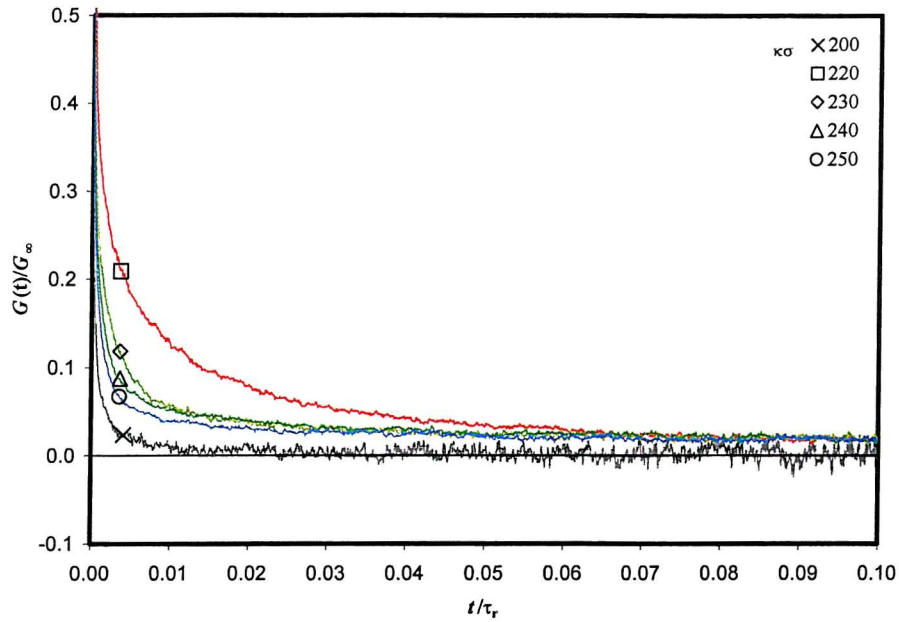


Figure 5.16. The decays of the normalized shear modulus after the gel is subjected to a 0.5 % step-strain as a function of time, taken at $t = 282.7\tau_R$ for two different κ values at $\phi = 0.3$.

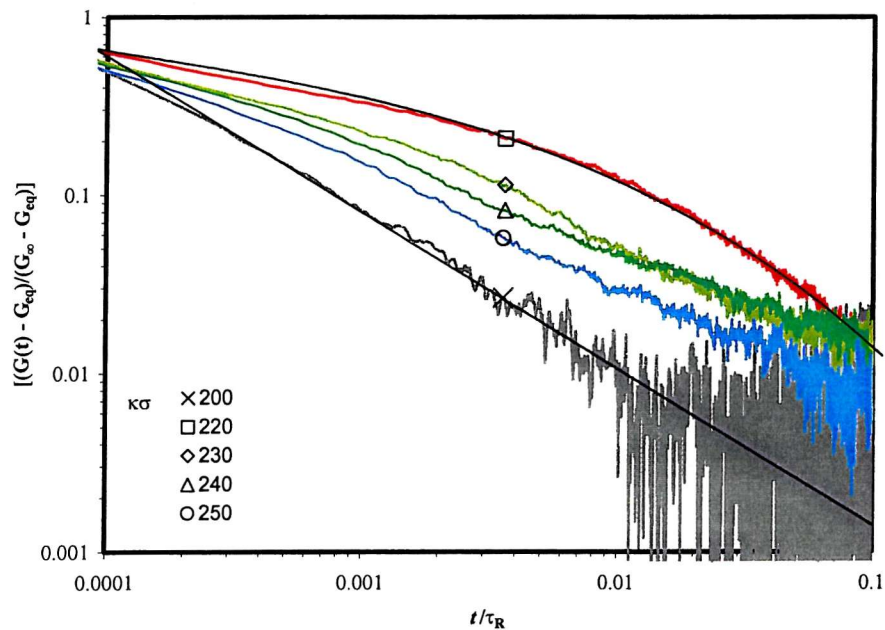


Figure 5.17. The stress decay after the step-strain is for system of various κ and 30 % volume fraction, taken at $t = 483\tau_R$. The plot for $\kappa = 200\sigma^{-1}$ is fitted to a power-law function and the plot for $\kappa = 220\sigma^{-1}$ is fitted to the stretch-exponential function.

When the gel is formed, the structure is able to sustain some stress within the system. The stress will then decay to some finite values that depend on the shape of the structure and the strength of the interactions.

If we plot the stress decay of each system, we notice two different behaviours at low and high κ as shown in Fig. 5.17. A faster decay of the relaxation portion to the shear modulus, $G(t) - G_{eq}$, is found for systems in the fluid phase where a gel formation is not observed. The shear modulus decay between $10^{-4}\tau_R$ and $10^{-1}\tau_R$ for this system can be modelled with a stretched exponential function[103],

$$G(t) = (G_{\infty} - G_{eq}) \exp(-(t/\tau')^{\alpha}) - G_{eq}. \quad (5.5)$$

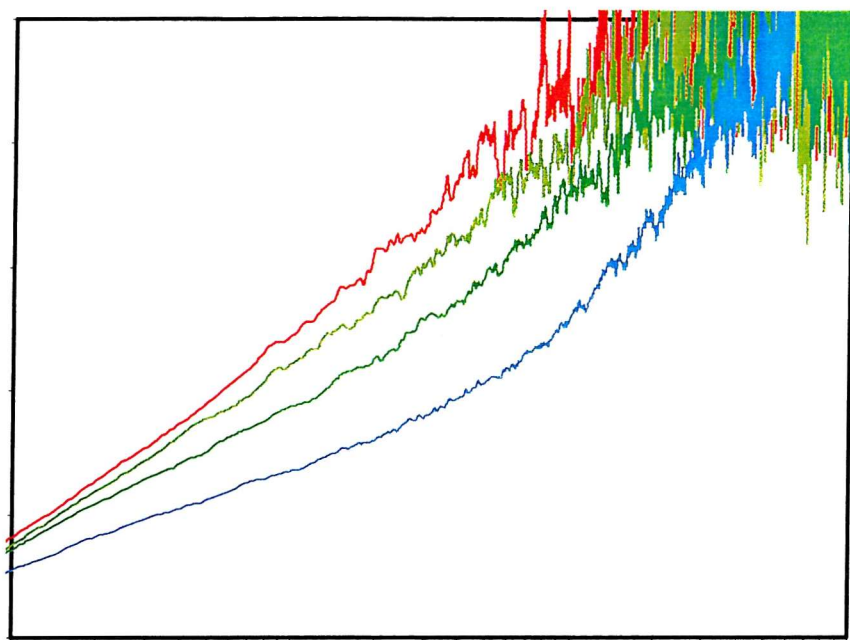
τ' and α are adjustable parameters. We also found that corresponding decay for system of $\kappa = 250\sigma^{-1}$ is also a stretched exponential function, although the decay rate is somewhat slower than that characterize of the fluid phase. Our simulation showed that the exponential constant, α , is about 0.875 ± 0.005 and 0.666 ± 0.008 for systems of $\kappa = 200\sigma^{-1}$ and $250\sigma^{-1}$ respectively.

While at systems just below the spinodal line, the stress decays as a power-law function of time,

$$G(t) = (G_{\infty} - G_{eq}) ((t/\tau')^{\beta}) - G_{eq}. \quad (5.6)$$

This can be observed in the plot of the stress decay for system of $\kappa = 220\sigma^{-1}$ where the value of the exponential constant is 0.302 ± 0.005 . This suggests a strong effect of the local order towards the relaxation behaviour of the structures.

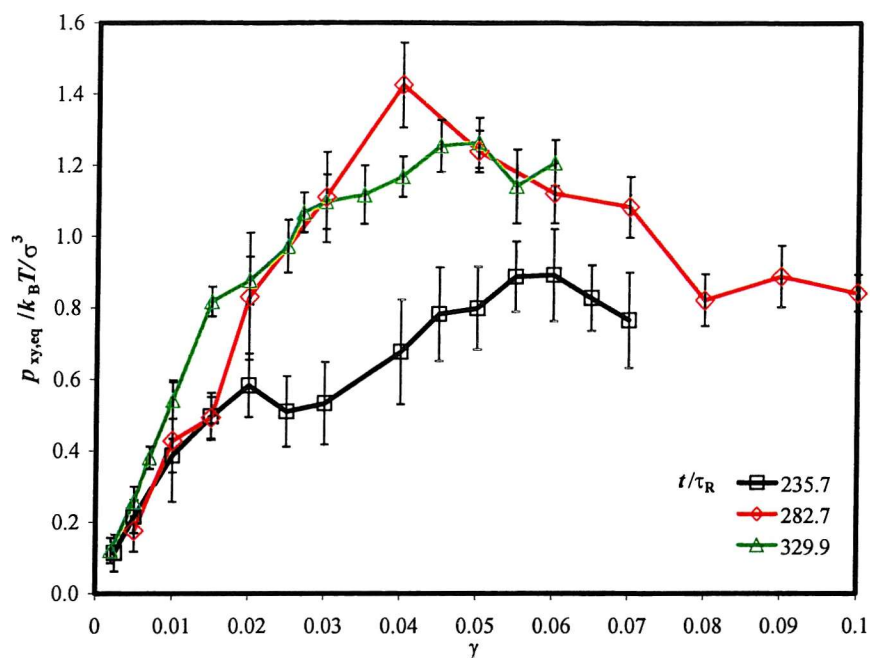
A transition in the relaxation behaviour can be observed in the simulation with $\kappa = 220\sigma^{-1}$. In this system, the shear modulus decay as a stretched exponential function at early stage, $t = 47.1\tau_R$, with the exponential constant, α , calculated to be 0.852 ± 0.005 . As the onset of



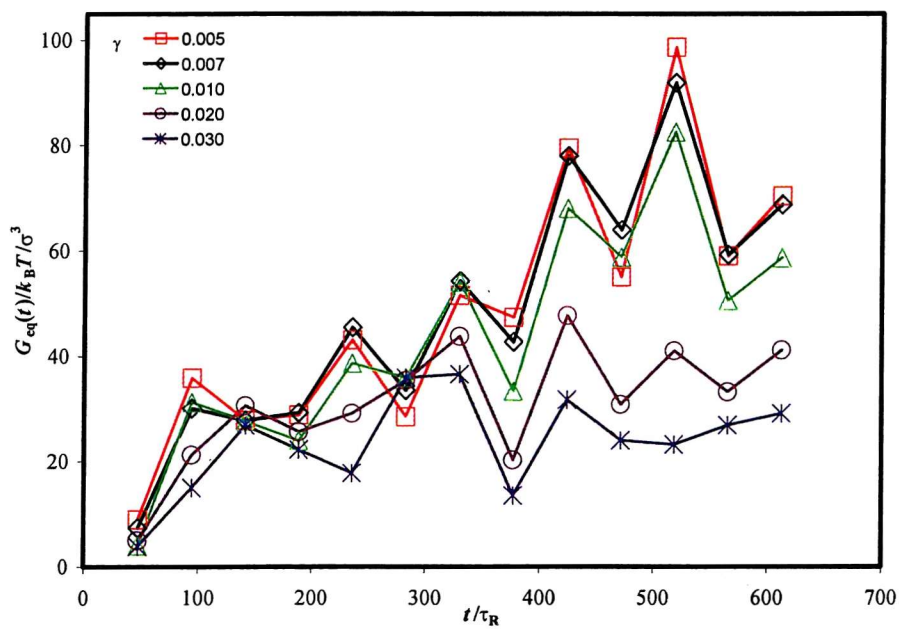
the nucleation is reached and the system progresses up to the age where the structure becomes locally highly ordered to form a crystalline gel, the decay of the shear modulus gradually changes. At late stage, $t = 377.0\tau_R$, the shear modulus decay follows a power law function with the exponential constant, β , of 0.302 ± 0.005 . This is shown in Fig 5.18(a). This behaviour is also observed by Lodge and Heyes[26] who carried out the simulation of colloidal gel interacting via a Lennard-Jones potential. In comparison, in structure with $\kappa = 250\sigma^{-1}$ as shown in Fig. 5.18(b), the dynamics is much slower and the relaxation behaviour has not shifted from a power law function even at the end of the simulation run.

The equilibrium stress is studied by plotting the resulting stress as a function of the strain magnitude. In Fig. 5.19(a), we present the equilibrium stress at several gel ages for gels with $\kappa = 250\sigma^{-1}$ and $\phi = 0.3$. Again we observe that the regime, where the stress increases linearly with the strain magnitude, only exists at relatively small strains. Beyond the linear regime, the stress increases at different rates, because the strain is now large enough to break some of the weaker bonds within the structures. The structures can still sustain the applied stress as at this point because the stronger bonds remain intact. If we increase the strain magnitude further, the stress still increases, although move slower as the structure is getting weaker due to the breaking of some of the bonds. At a certain point if the strain is increased further, we will reach a critical strain, which is characterized by the continuous decrease of the equilibrium stress with larger strain. The shear stress beyond this point decreases with strain magnitude as the gel breaks and it deforms to a new structure with less stress.

The linear response is more clearly observed by plotting the equilibrium modulus for several different strain magnitudes as a function of time. In Fig. 5.19(b), we show that at small strain, the plots are almost overlapping. This is because at small strain, the modulus is independent of the strain magnitude. At larger strain, the equilibrium modulus is smaller than the corresponding modulus for the gel of the same age calculated using smaller strains. We note that the plot for strains larger than 0.01 starts to deviate from the corresponding plots for small strains. This indicates a different regime where a modulus, independent of strain magnitude, is observed.



(a)



(b)

Figure 5.19. (a) The equilibrium modulus as a function of the step strain, taken at different times during the run for $\kappa\sigma = 250$ and $\phi = 0.3$ and (b) the temporal evolution of the equilibrium modulus for several different step-strain.

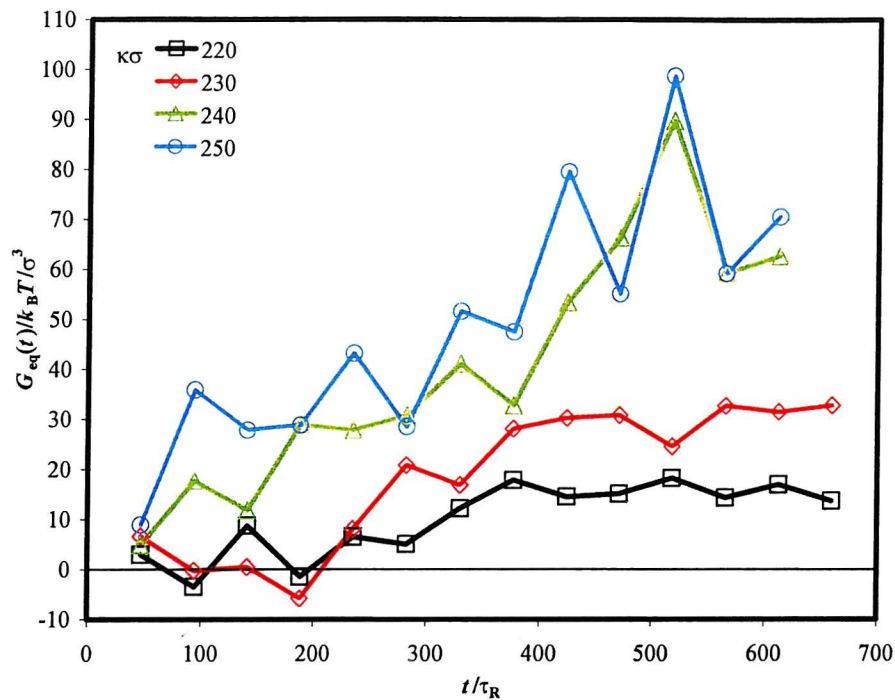


Figure 5.20. The equilibrium modulus for various κ at different gel ages.

The relationship between the storage modulus and the inverse Debye length is shown in Fig. 5.20. We found that the correlation between these parameters is a weak relationship. This may be indicative of weak solid behaviour in the gel. If we compare the equilibrium modulus and the modulus at high frequency, their ratio is about 0.01 at maximum.

Clear differences are observed between systems quenched close to the spinodal region and those quenched deeper into the unstable region. In Fig. 5.20, we can see that for systems of $\kappa = 220\sigma^{-1}$ and $230\sigma^{-1}$, the equilibrium modulus fluctuates around zero at early stages before the onset of the nucleation. The modulus starts to increase once the nucleation process occurs and rises rapidly until it reaches some equilibrium value that hardly changes with time.

In systems with larger κ , the equilibrium modulus rises straight after the quench without any delay, although it is rather hard to determine whether the modulus rises linearly because of the noise which is significant.

5.4. Summary

We have examined the behaviour of the colloidal particles immerse in electrolyte solutions of different concentration. The concentration of the ions in the solution determines the strength of the repulsive electrostatic interaction, which can be calculated using the DLVO equation. For weaker repulsions in the van der Waals attraction becomes more important and the effective interaction is more attractive. The simulations show a rich behaviour when the suspension is quenched. The effective range of the interaction determine whether the system will stay dispersed or undergo a phase separation. The simulation results agree well with the prediction of the phase diagram. If a colloidal system is in the liquid phase, the simulation results show that the suspension will stay dispersed and disordered after the quench.

If the colloidal interaction becomes more attractive, the phase diagram predicts that the suspension will be in the unstable and will phase separate. In our simulation, we observe the formation of a percolating structure known as a gel in all systems that are predicted to be in the unstable region. A transition can be observed in the system close to the solid-fluid binodal line during the runs. In this system, the suspension is fluid at early stage. At some intermediate time, a cluster will form in the suspension, which indicates growth to form larger clusters. These grow further to form a gel structure. We show that the transition occurs at earlier times for systems closer to the unstable region.

The simulations show that the growth rate of the cluster at early stages change with κ . In fluid phase, no clusters are found observed in the structure factor. If no long-range structures are formed, the value of $S(k)$ at small k is very small. If κ is lowered, the fluctuation of $S(k)$ increases. For systems well below the binodal line, the simulations show a peak at small k . The size of the peak increases constantly as the simulation progresses. This peak is related to the mass of the clusters. For systems at large κ , the peak increases more rapidly and slows down at later stage. In our simulations, the slows down is not observed for systems at smaller κ .

The simulation also showed that the location of the peak shifts towards the smaller value.

This is interpreted as the growth of the size of the clusters. From the simulation, we found that the rates of the growth similar for all system at early stages. At later stages the growth rates for systems with large κ decrease, while at smaller κ , this is not observed.

Once a gel is formed, the mobility of the colloidal particles decreases rapidly and at the largest value κ , 99 % of the particles barely move. For suspensions close to the binodal line, we found that the particles are still mobile enough to induce rearrangements within the percolating structures. The structures become more compact at a more rapid rate as the gel ages. This can be seen in the average number of nearest neighbours which are higher for systems close to the binodal line. We also analyse the fractal dimension for the gel structures. We found that a smaller dimension is observed for systems of smaller κ .

We study the mechanical strength of the gel by measuring the shear modulus at equilibrium and at high frequency. This is accomplished by carrying out the step-strain simulation at several gel ages. We found that all the gels are easily disrupted by applying a small strain into the structures. All the gels lose their linear elastic behaviour when subjected to a strain of more than 1 %.

The shear modulus at high frequency measures the stiffness of the gel structure, which we found is closely correlated with the average interaction potential. The equilibrium modulus measures the solid-like characteristic of the gel. This equilibrium modulus is also found to depend on the strength of the attraction.

Chapter 6

Particle gels formation with the volume fraction

Apart from varying the salt concentration to obtain a stronger particle gel, we may also vary the volume fraction or density of the colloidal particles. There may also be some commercial advantage in understanding the relationship between the mechanical strength of the particle gels and their volume fraction. For example in the manufacturing of toothpaste, the colloidal particles are used as the abrasive agents and are the major component. We may want to choose an optimum volume fraction which will give an adequate abrasivities and prevent the suspension from phase separating and the products from degrading rapidly. An unnecessarily high volume fraction is also undesirable as the suspension will become more viscous and result in the increase of the manufacturing costs. The ability to select an optimum amount of the colloidal in a product may reduce the cost of the materials considerably, specially when the colloidal particles are made from expensive materials such as alumina or silica particles.

In this chapter, we study the effect of varying the volume fraction on the structural evolution of the colloidal suspension. The volume fractions of the colloids are varied between 5 % and 40 % of the volume of the suspensions. We will again study the changes in the kinetics of the gel formation in the systems from dilute up to moderately concentrated suspensions well within the unstable region. The Debye length is kept unchanged at $\kappa = 250\sigma^{-1}$. At this κ , the colloids coalesce to form reasonably strong bonds as they collide due to their diffusive motion. The phase separation is also expected to occur at all values of volume fraction that we are simulating as predicted by the phase diagram. All the simulation runs are carried out for at least $700\tau_R$. At this point, all the runs display the phase separation process forming the high- and low-density regions.

In Fig. 6.1, we present some examples of the snapshots of the suspensions at time of $500\tau_R$ after the quench, at several volume fractions.

We note differences in the resulting structures for systems with moderate density which are within the unstable region and the dilute suspensions. In the suspension of 5% volume fraction, the homogeneous system undergoes phase separation forming clusters surrounded by the low-density region. All the clusters are found to be unconnected with each other.

In the suspension of 10 % volume fraction, the systems is still outside the unstable region and we also do not observe a percolating structure spanning the whole simulation box. Comparison with the clusters in suspension of 5% volume fraction reveals some structural differences. In the denser suspension, we note that the clusters are larger and of stringy form. At 20% volume fraction where the system is now within the unstable region, the clusters start to form a percolating network, that is a network that spans the whole of the simulation box. The percolation is the good working definition of the gel states. This structure seems to be stable over a long period of time. Similar structures are observed in denser systems, which we will try to characterise.

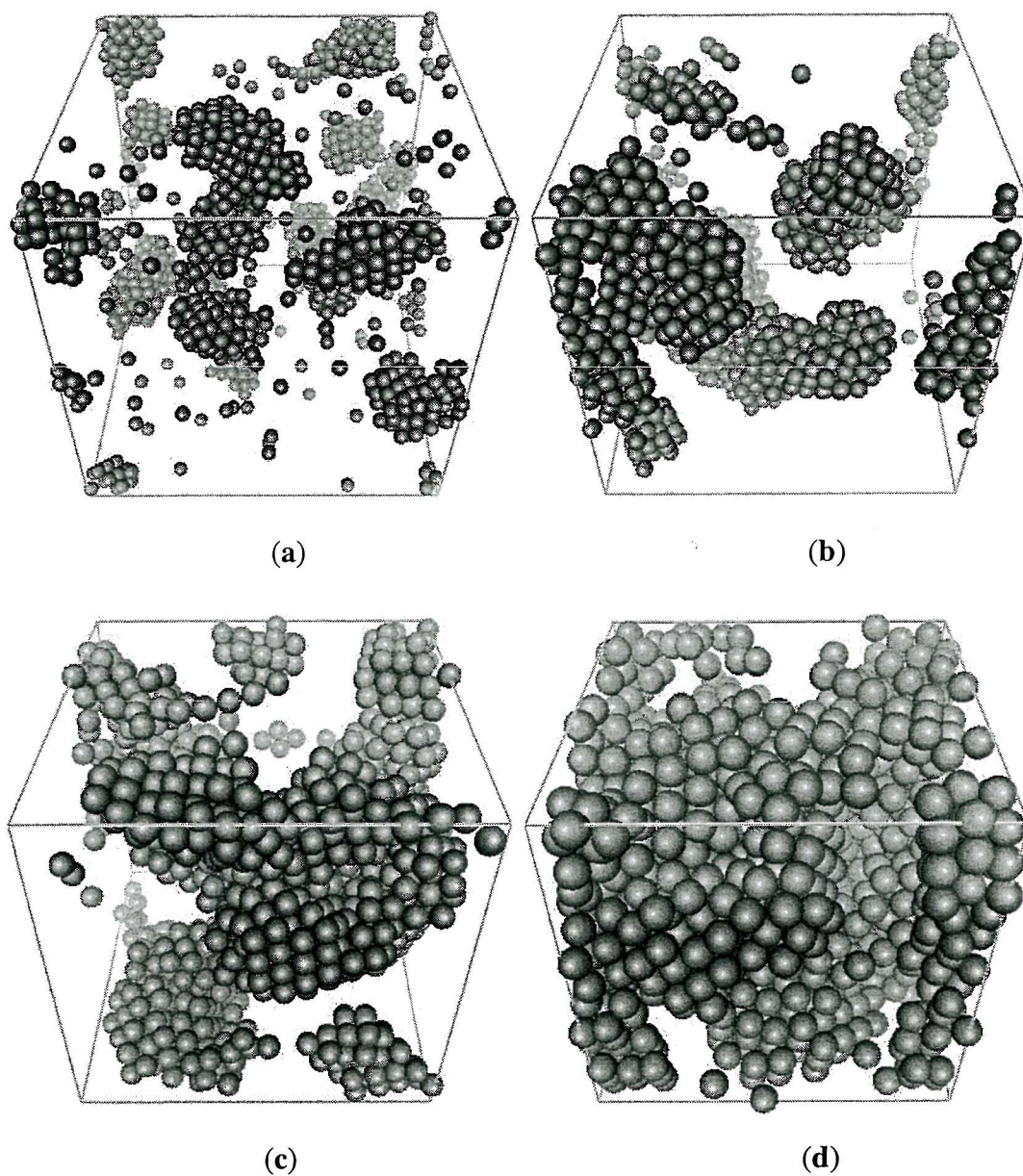


Figure 6.1. The pictures of the resulting structures taken at times $471.24\tau_R$ and $\kappa = 250\sigma^{-1}$ for $\phi =$ (a) 0.05, (b) 0.10, (c) 0.20 and (d) 0.40.

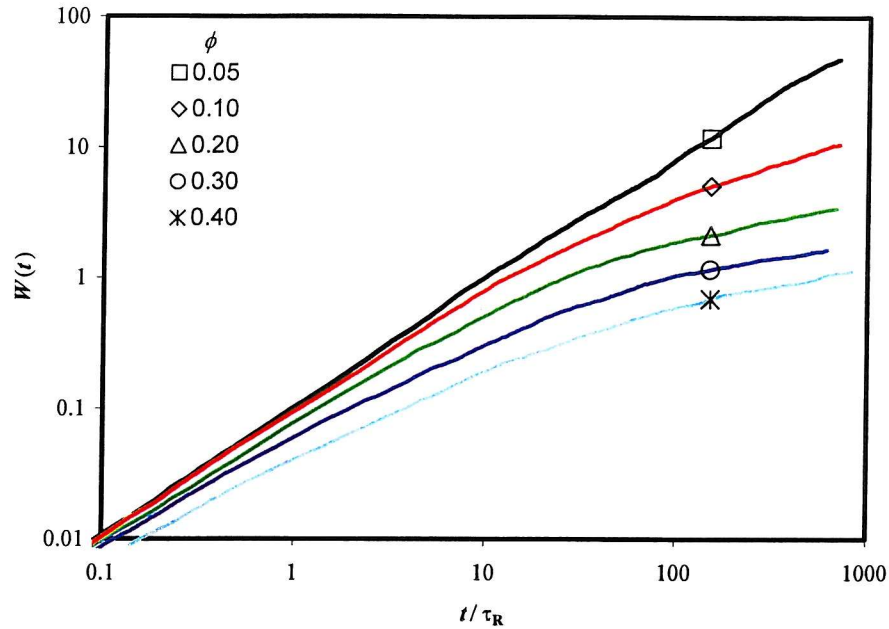
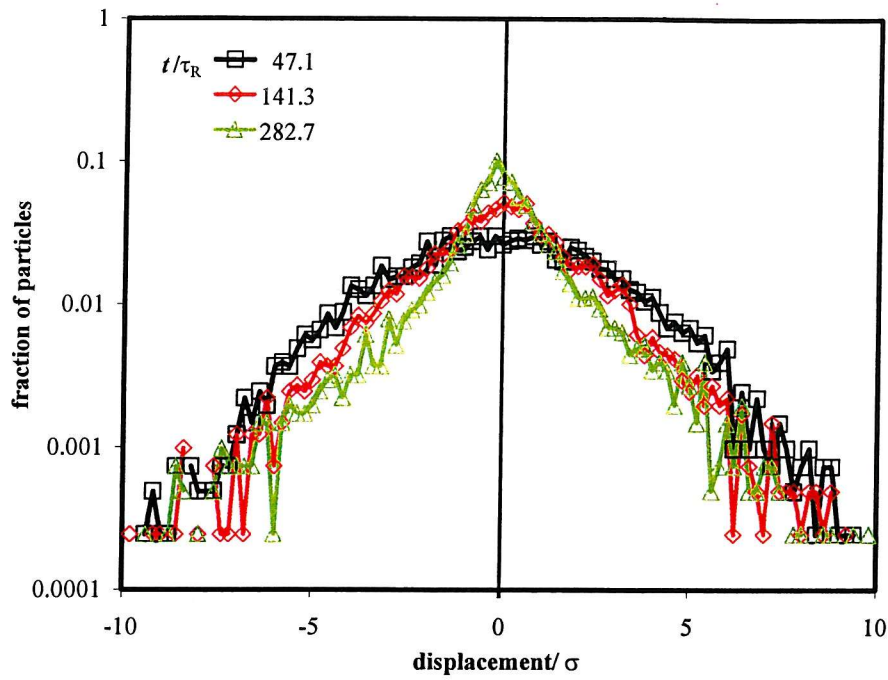


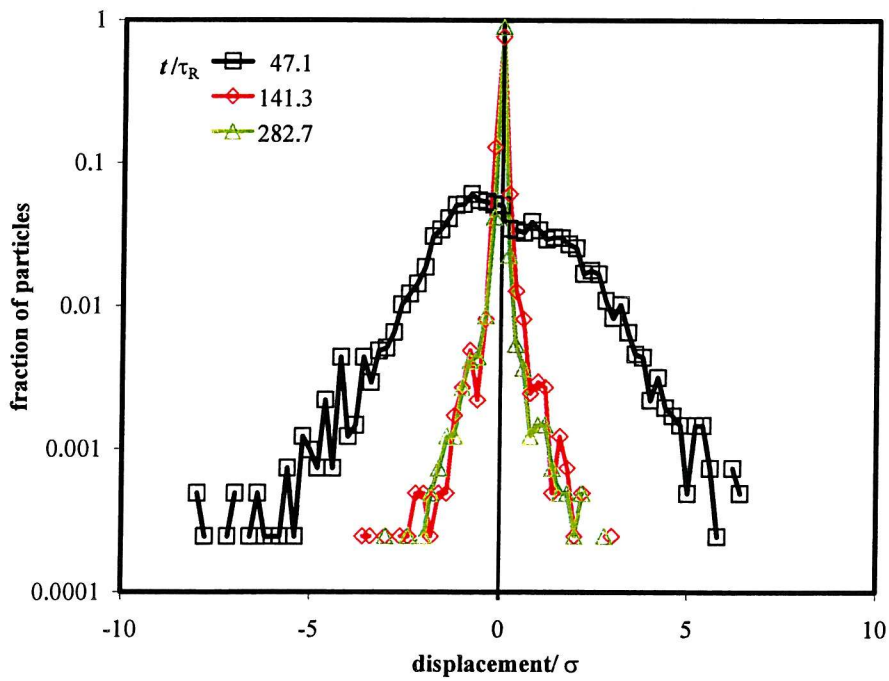
Figure 6.2. The mean square displacement, $W(t)$, as a function of time at different ϕ .

In Fig. 6.2, we show changes of the mean square displacement, $W(t)$, as the suspensions evolve. This shows the effect of clustering. The curves show a deviation from linearity at $t > 100 \tau_R$ as the structures develop. In the suspension of 5% volume fraction, there are still significant numbers of single particles in the system at late stage and the clusters formed are relatively small. The resulting plot of the mean square displacement then still shows a rapid increase with time. In the suspension of 10 % volume fraction, single particles are drastically reduced and the clusters formed are larger.

At larger volume fractions when the percolating network starts to form, the rate increase of $W(t)$ reduces significantly, as shown in Fig. 6.2 for the plot of 20% volume fraction and beyond. We do not observe any changes in the overall shape of the plots for systems with and without the formation of a percolating structure. This suggests that the mean square displacement, which measures the average diffusion, is largely determined by the fast moving particles. These particles are not part of the larger structures and their number become fewer as the suspension becomes more concentrated.



(a)



(b)

Figure 6.3. The distribution profiles of the displacement at different stages for $\phi =$ (a) 0.05 and (b) 0.40.

If we study the mobility of the particles within the systems, the effect of clustering can be observed at all volume fractions. This can be seen in Fig. 6.3, which displays the distribution profiles of the component of the displacement at two different volume fractions. We show that for system at 5% volume fraction, the distribution profile is still quite broad, although we note that there is some increase at zero displacement. This reflects the increasing number of particles becoming part of the aggregates. In the profile for more concentrated suspension which is presented in Fig. 6.3(b), the distribution profile becomes very sharp at longer times.

In Fig. 6.4, we present the graph of the configurational energy, U , for systems of for different volume fractions they evolve after the quench. Since the potential is short ranged, the evolution of the interaction potential should reflect the changes in the short-range orders. We note that U decays very rapidly at early stages. For suspensions with volume fraction of 10 % or larger, the configurational energy reaches $-15k_B T$ per particle within $200\tau_R$. Beyond this point, the interaction potential decreases very slowly and we observe that the equilibrium has not been reached at the end of the runs.

It is often useful to characterise the evolution of the interaction energy by fitting the plots to a power law function ($-U \propto t^\gamma$)[24], where γ is a constant. In Fig. 6.5(a), we present the graph of the interaction energy on a logarithmic plot. We observe that in the systems, there is no single value of γ that covers the whole runs. This may be due to changes in the kinetics as the colloids forming larger structures. At early stages, the colloids in the suspensions coalesce to form larger clusters. The mechanism that leads to further reduction in the interaction energy is dominated by the rearrangement of particles within these clusters. At later times, the structures within the clusters may become highly ordered and the drive towards the equilibrium is limited by the diffusion of these clusters.

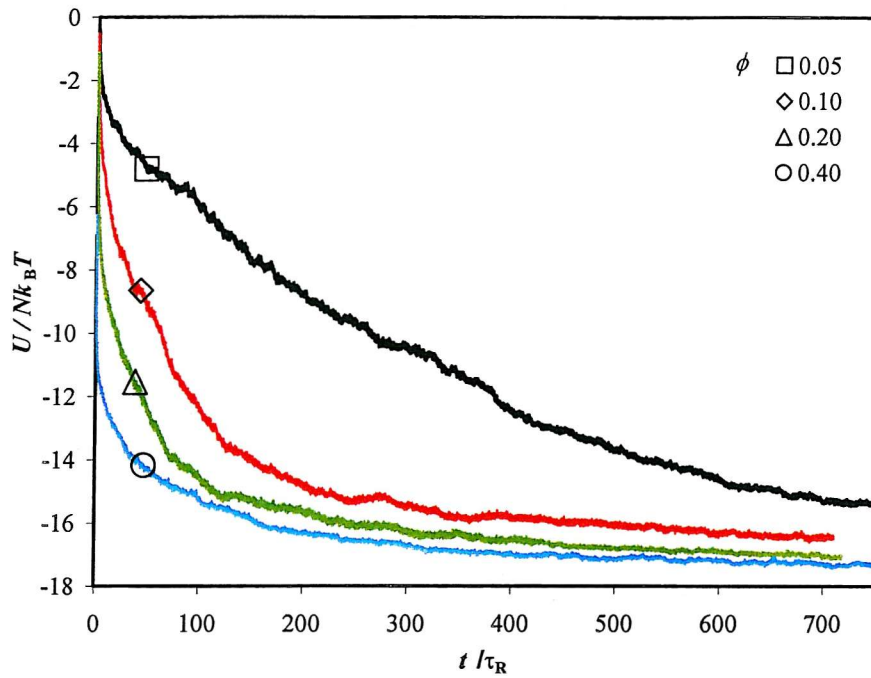
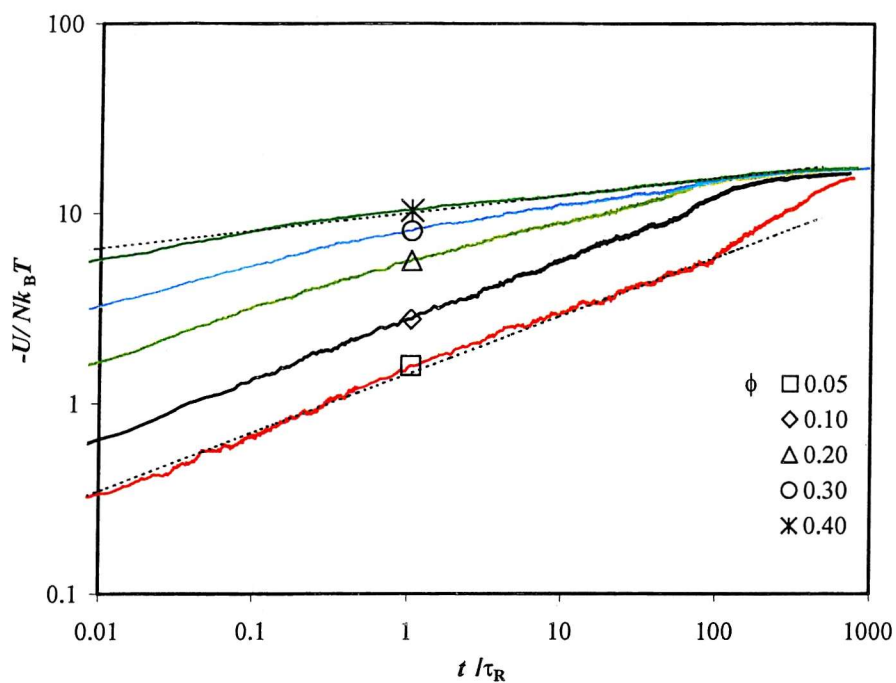


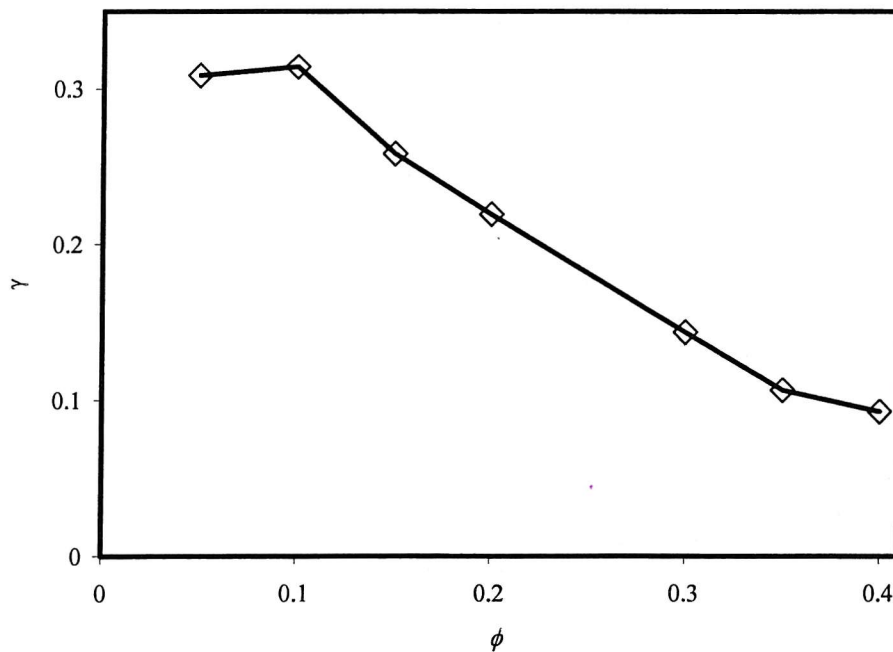
Figure 6.4. The average interaction potential as a function of time at different κ .

In Fig. 6.5(b), we plot the exponential constant obtained by fitting the plots of the interaction energy at early times as a function of volume fraction. The graph shows the different behaviour for systems of dilute and moderate suspensions.

We note that at dilute suspensions which are outside the unstable region, the exponential constant, γ , is largely constant at about 0.3. This index may characterize the short time diffusion of single particle, which is the same in all systems and which is the main drive towards the equilibrium. In denser suspensions, the systems may be more readily forming larger structures even at an early stage. The decays of the interaction potential may have already been dominated by the rearrangement within the structures. This then gives smaller exponential values with increasing volume fraction.



(a)



(b)

Figure 6.5. (a) The negative of the interaction energy as a function of time plotted in the double-log axis. The dashed lines are the fitted power law approximation and (b) the power-law exponent for early time as a function of volume fraction.

6.1. Local structure and short range order

In Fig. 6.6, we plot the changes in the coordination number with the structural evolution at various volume fractions. Initially, the peaks occur at the small coordination number, ranging from 0 in the system of $\phi = 0.05$ to 5 for a suspension of 40% volume fraction. As the simulations progress, the peaks appear to shift to larger coordination number and the distribution profiles also become broader. This reflects the rearrangement of the local structures and in the late stages, all the systems have more than one peak and one of the peaks is at the maximum coordination number. This suggests that the formation of a compact cluster has occurred.

There is also another peak observed which varies between 6 for dilute suspensions and 7 in more concentrated suspensions. This is due to the intermediate stages in the aggregation before the system evolves further to form a more compact cluster. Although this is hard to see from the snapshot pictures, it is possible that this number relates to the formation of a simple cubic crystal whose coordination number is 6. In the dilute suspension at 5% volume fraction, we still observe the peak at 0, although the fraction is much smaller than the initial value at early times.

We plot the growth of n_{12} , the fraction of particle with the maximum coordination number, in Fig. 6.7(a) to analyse the changes in the local order structures. In the suspension of 5 % volume fraction, there is a delay observed in the corresponding plot for n_{12} before a compact cluster appears. This is in contrast with the more concentrated systems in which the compact clusters appear almost immediately. This is because a large fraction of particles (about 45%) in the 5 % suspension are isolated. This may delay the formation of a compact aggregate, as the particles need to diffuse initially before they take part in the solidification process within the cluster.

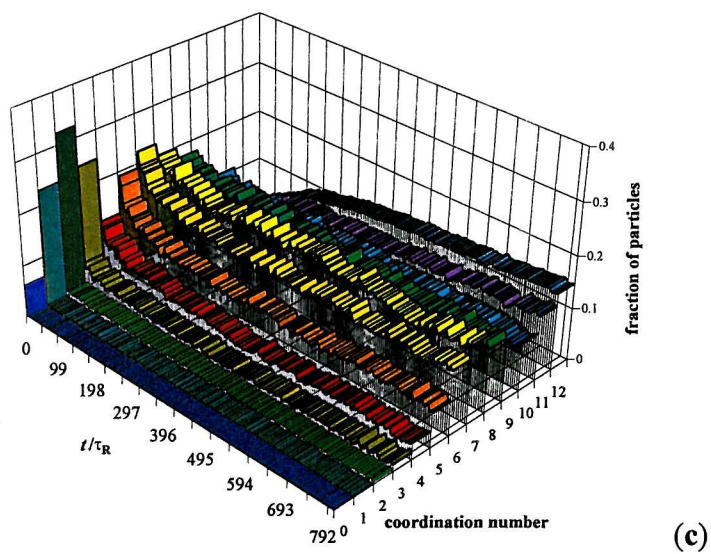
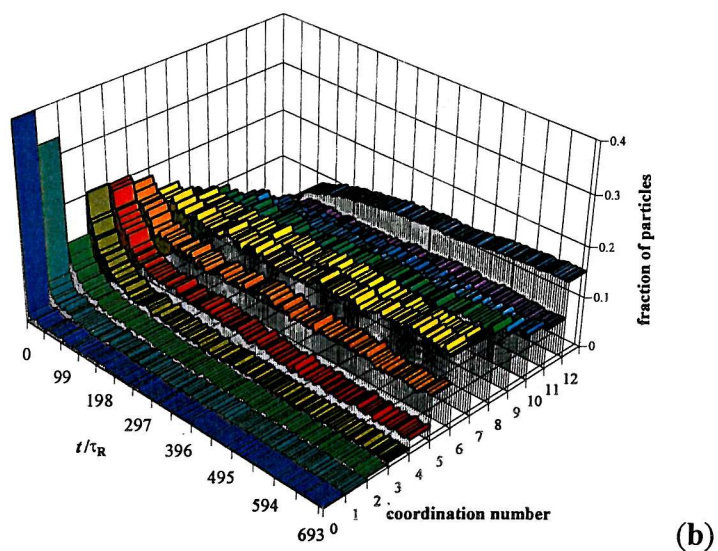
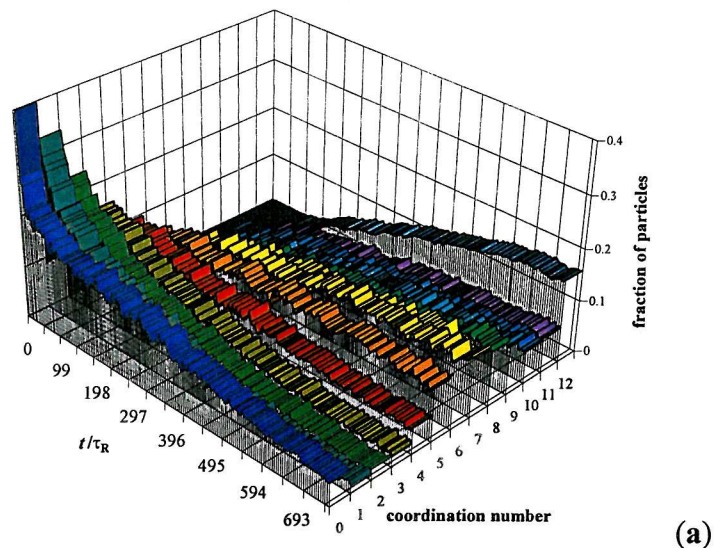
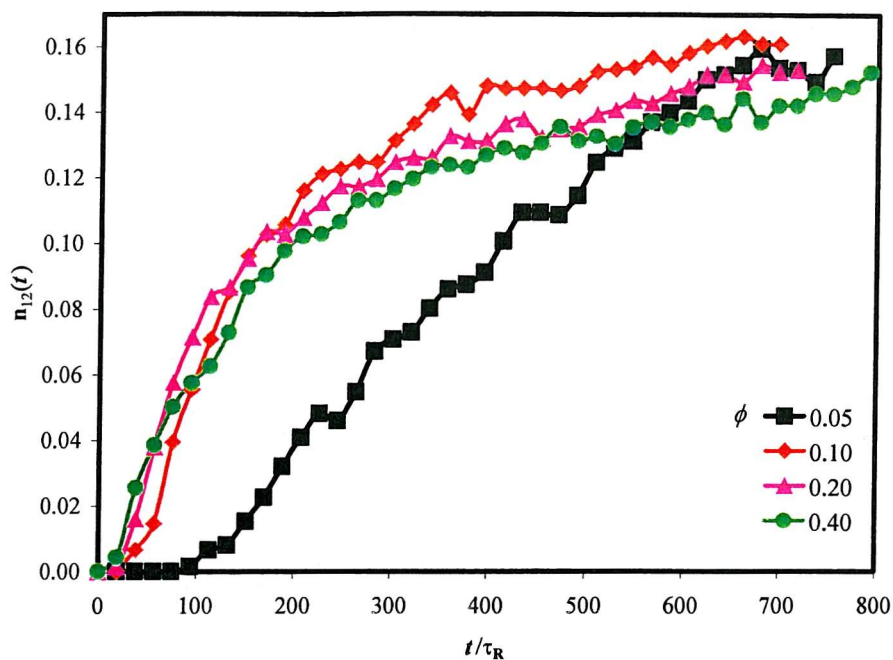


Figure 6.6. The distribution profiles of the coordination numbers shown as a function of time for ϕ equals to (a) 0.05, (b) 0.20 and (c) 0.40.

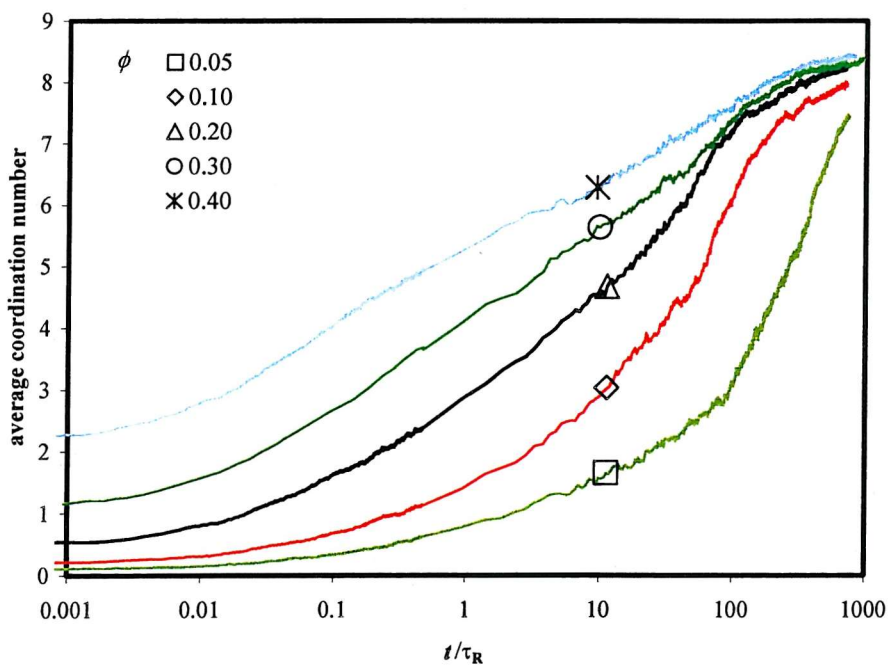
In the denser suspensions, the dense aggregates form immediately and the rates of the formation at early stage are shown to be independent of the bulk density of the suspension. In the intermediate stages and towards the end of the runs, the plots diverge. At this stage, the evolution of the dense aggregates is more advance in the more dilute suspensions. This is also shown in the 5 % suspension, where the rapid rearrangement within the clusters at intermediate time results in the significant fraction of the particles having the full coordination number. The results suggest that there is a competition within the clusters between the evolution towards the more compact clusters and the time for the particles from the bulk to diffuse onto the surface of the clusters. In the dilute suspensions, the diffusion time is expected to be smaller than the time needed for the rearrangement in the clusters and hence we observe the rapid growth of n_{12} . In a denser suspension, there may not be enough time for the particles within the cluster to form a denser aggregate before another particle diffuses onto the surface. This new particle will make the compactification in the clusters more difficult as it restricts the motion within the clusters.

In Fig. 6.7(b), we show the plots of the average coordination number as the systems evolve, which is plotted against the log of the time. This shows that the compactification processes are dependent on the density of the suspensions. In a dilute suspension, the growth rate is slow at early stages and it increases as the run progresses before slowing down again towards the end of the run. The shape of the plots alter as the suspension becomes denser. For the densest suspension that we simulate, the plot shows that the average coordination number increases logarithmically with time before the rate slows.

In Fig. 6.8, we show the changes in the radial distribution function for several volume fractions as a function of time. The delay of the onset of the appearance of the compact clusters can be observed in the corresponding plot for suspension of 5% volume fraction. On this plot, we can see the late appearance of the peak at $\sqrt{2}\sigma$. The higher degree of the correlation in the short-range order for dilute systems is shown in the size of the first peak of the radial distribution function.



(a)



(b)

Figure 6.7. (a) The fraction of particles with the maximum coordination number and (b) the average coordination numbers as a function of time for different volume fractions.

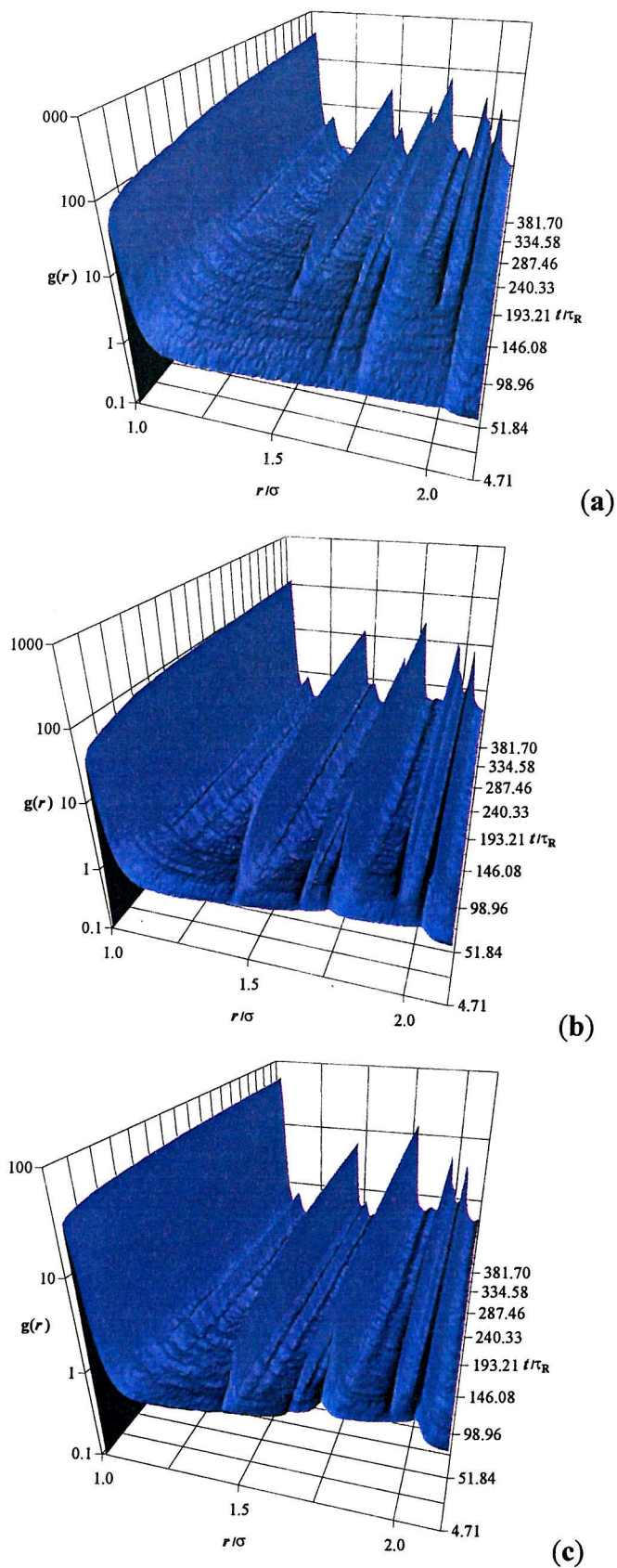


Figure 6.8. The radial distribution function for ϕ equals to (a) 0.05, (b) 0.20 and (c) 0.40. Each point is an average over $1 \tau_R$.



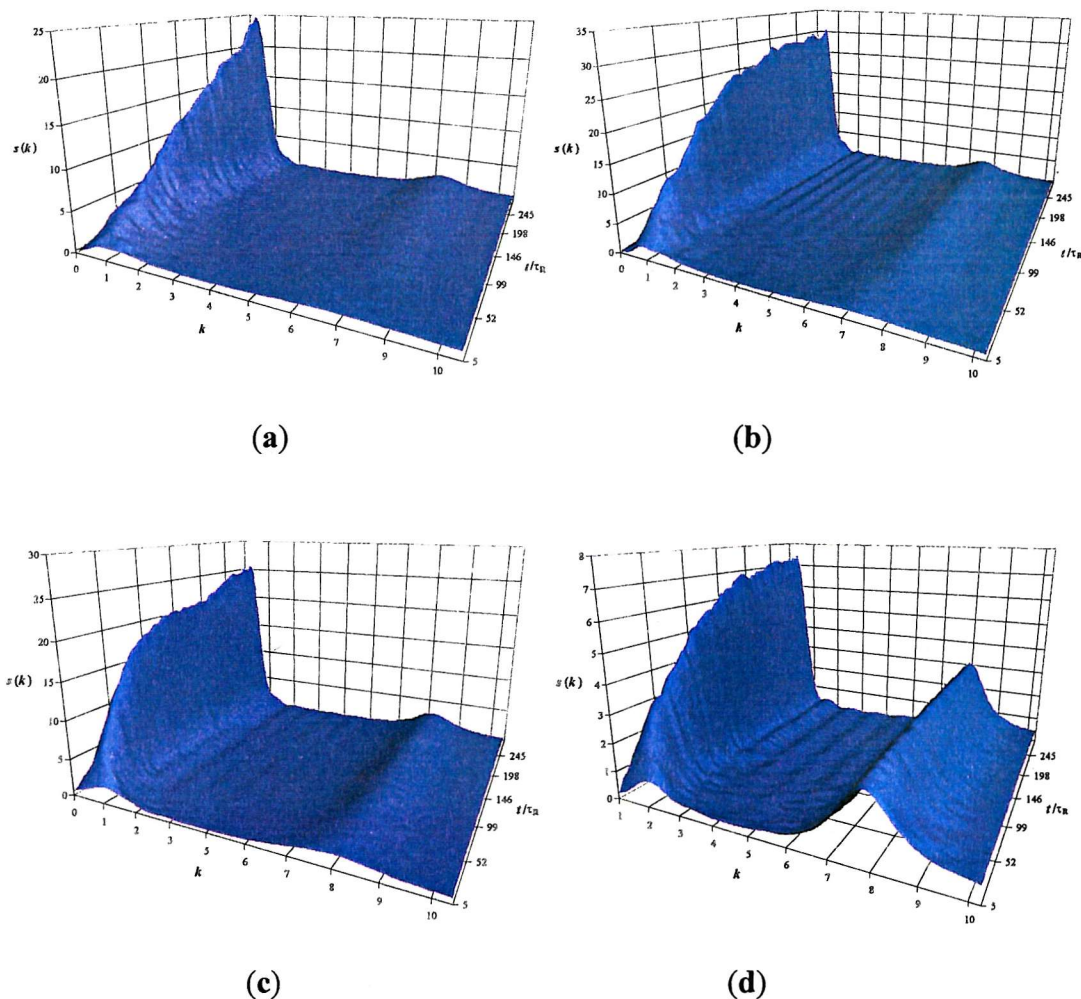
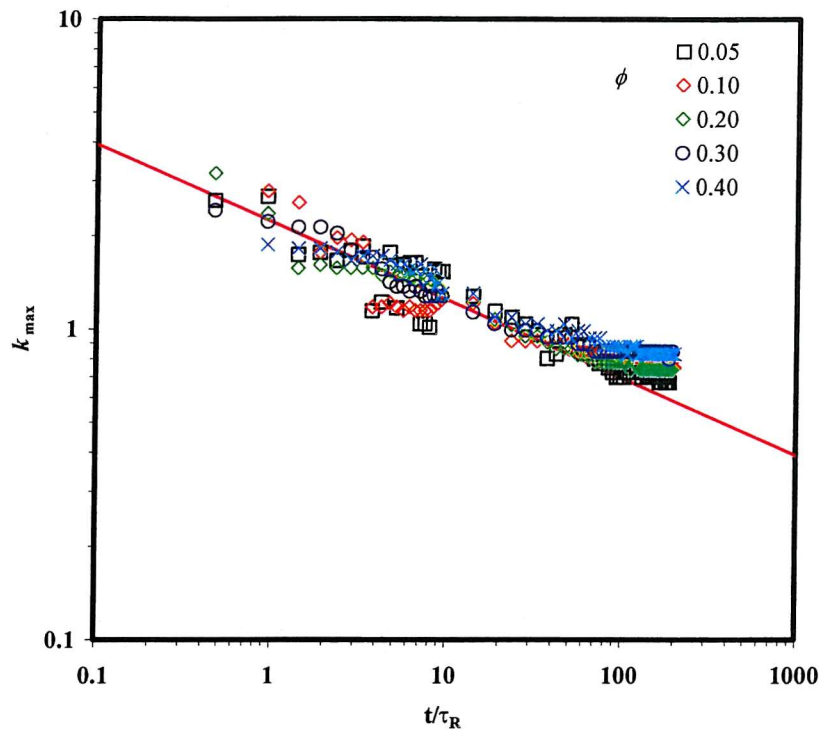


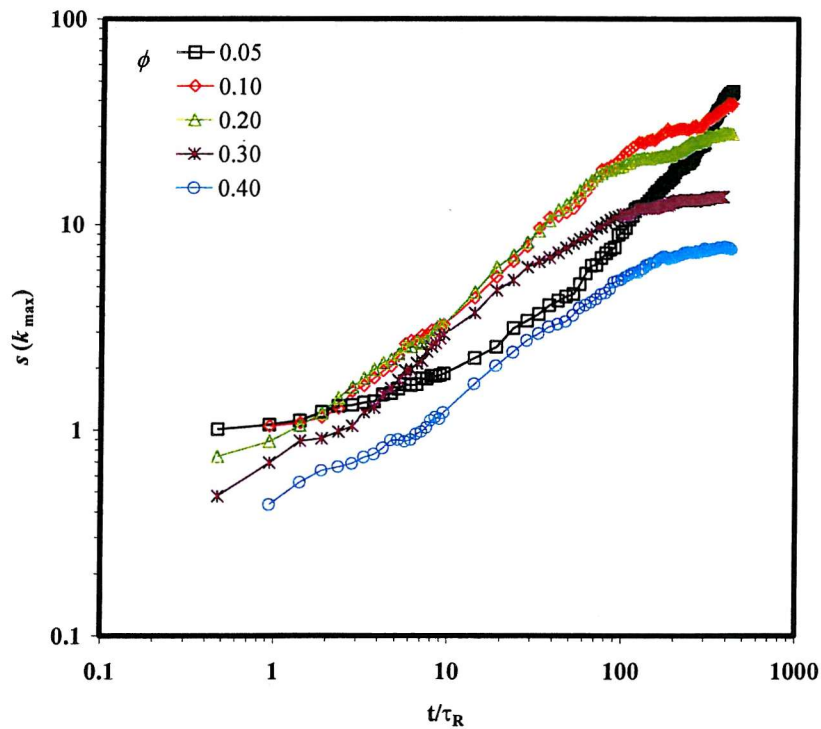
Figure 6.9. The structure factors calculated from the structure factor as a function of time for ϕ equals to (a) 0.05, (b) 0.10, (c) 0.20 and (d) 0.40

6.2. Long-range order

In Fig. 6.9, we display the structural evolution of the long-range order of systems with various volume fractions. As in the previous chapter, we are unable to follow the changes of the structure factor throughout the simulation run due to the problem with the cut-off in the radial distribution function. All the systems exhibit a high degree of correlation in the long-range order at early times which increases continuously over time.



(a)



(b)

Figure 6.10. The temporal changes in (a) the location of the peak at long wavelength, k_{\max} , and (b) the size of the corresponding peaks of the structure factors, $S(k_{\max})$, at different volume fraction.

We look at the structural changes in more detail by plotting the changes in the k_{\max} and $S(k_{\max})$ at different volume fraction. In Fig. 6.10(a), we compare the changes of k_{\max} across the systems. The graph shows that k_{\max} decreases following a power-law at intermediate times, up to $t \approx 100\tau_R$. Beyond some intermediate stage, the rate decay decreases.

Surprisingly, the plots for different volume fraction are almost identical which indicates that the density of the suspensions does not have any effect in the values and the changes in k_{\max} . The change in k_{\max} is often interpreted as the evolution of the clusters and the result seems to suggest that the growth of these clusters do not depend on the overall density of the suspension. At the later stages in the simulation, all the plots show a deviation from the straight line. This marks the stage where the growth of the clusters is limited by the presence of free particles or the size of the simulation box; i.e. the clusters form a percolating structure.

The $S(k_{\max})$ on the other hand increases at the rates that depend on the density of the suspension. This is shown in Fig. 6.10(b). The size of the peaks at large wavelength show that in general the structures become more compact with increasing volume fraction. We also note that the rate varies throughout the simulation, which may reflect different clustering mechanism during the phase separation processes. At this point just after the quench, the plots show that the $S(k_{\max})$ increases at lower rate than at the later stage. We observe that the rate is slowest in the most dilute solution, which is expected as the cluster growth largely depends on the rate of diffusion at early stage.

Beyond this stage, the $S(k_{\max})$ grows as a power law function of time, similar to the behaviour for the spinodal decomposition, although with smaller exponent, which suggest that the clusters are of a more open structure. In general, the power-law exponent decreases from 0.93 in a suspension of 5% volume fraction down to 0.64 for suspension of 40% volume fraction. We note that for suspension between 10 and 20% volume fraction, the corresponding plots of the $S(k_{\max})$ are almost overlapping. In more advance stages, the growths start to flatten out as the growth is restricted due to the fact that most particles now belong to clusters. Beyond this point, the peaks increase very slowly.

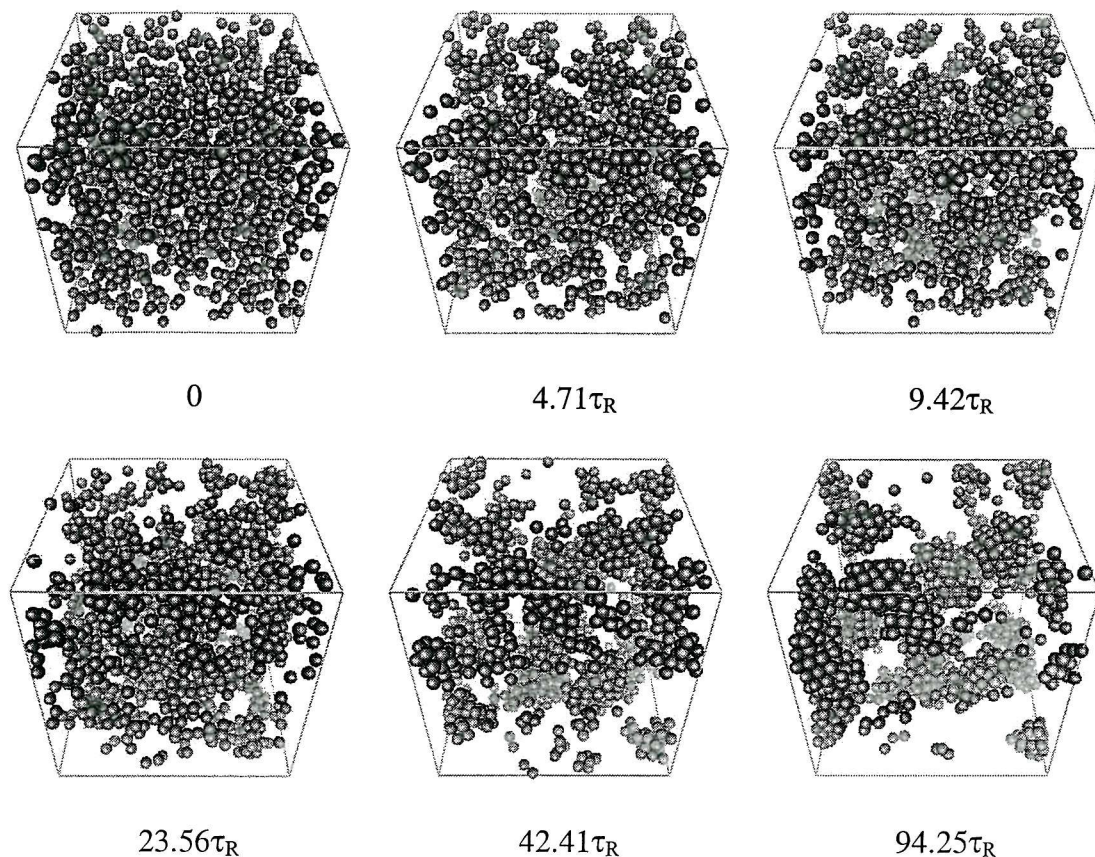


Figure 6.11. The phase separation process at early times after the quench for colloidal suspension of $\phi = 0.1$.

We study the structural evolution at the early stage by comparing the evolution at two different volume fraction. In Fig. 6.11, we display a series of snapshots for the structural evolution of a suspension at 10% volume fraction from early times up to $t = 94.25\tau_R$ after the quench. In this system, we do not observe the formation of a gel structure in the system.

Rather, the colloidal particles immediately aggregate to form clusters after the start of the quench. These clusters also coalesce to form larger aggregates as the simulation progresses. As the clusters grow bigger, their dynamics also slows down and the average distances between the clusters increase as the suspension phase separate to form the dense and dilute regions. If the structures of the clusters are not sufficiently open, they may not

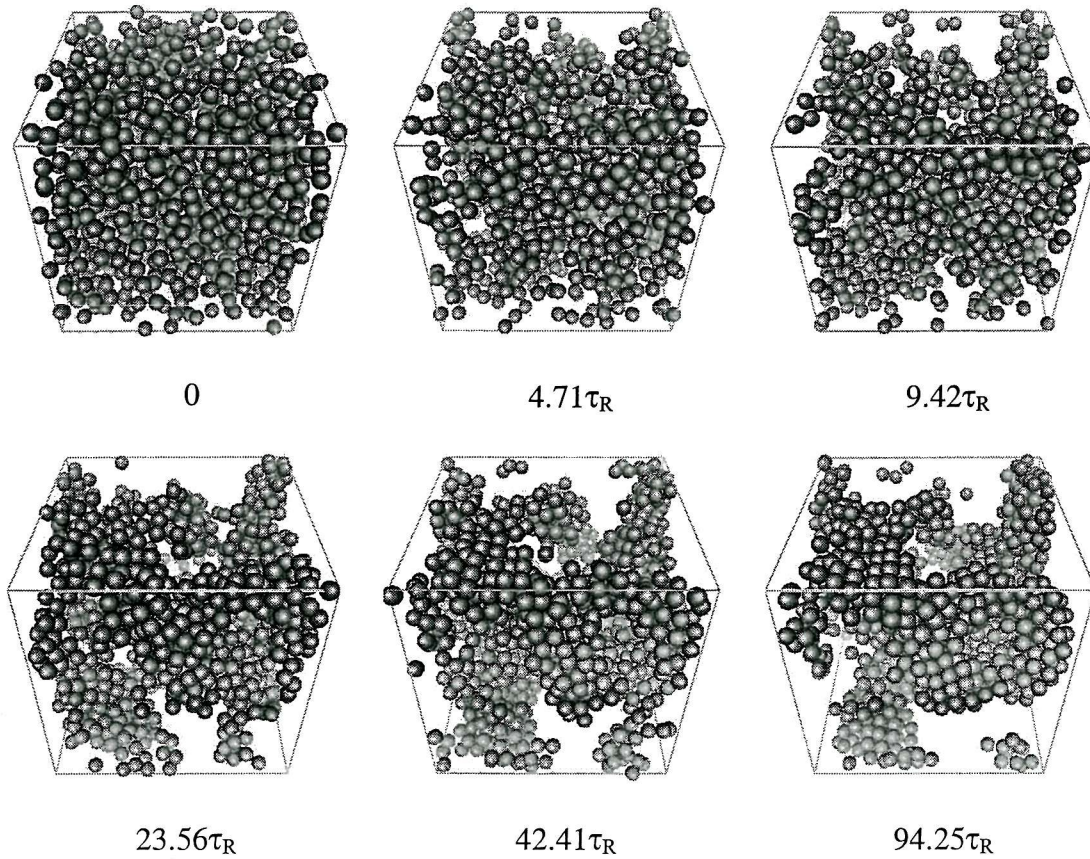
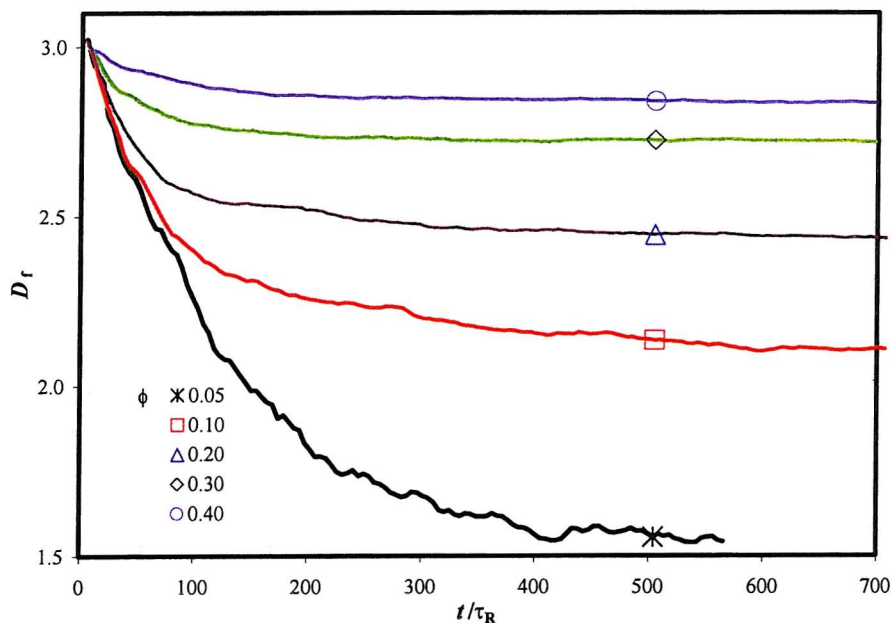


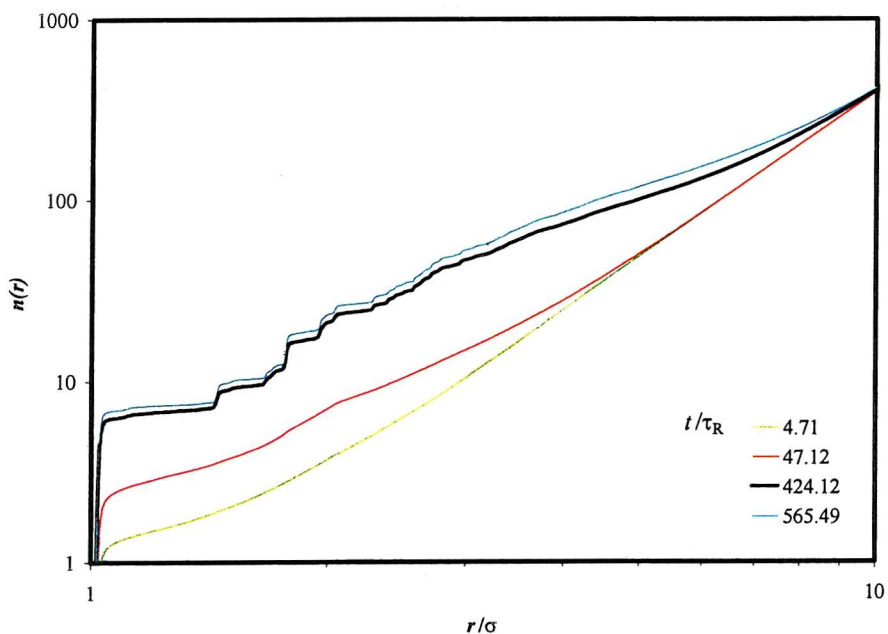
Figure 6.12. The phase separation process at early times after the quench for colloidal suspension of $\phi = 0.2$.

form the interconnecting structure which leads to the gel formation. This is what happens in this system when the clusters are not connected and the clusters instead undergo further rearrangement to form more compact structures.

A slightly different picture occurs in the system at 20 % volume fraction, which is shown in Fig. 6.12. In the early stage, the aggregates form soon after the quench and these go on forming larger aggregates. We would expect the size of aggregates should be the same as those from the 10 % volume fraction, as shown in Fig. 6.10(a).



(a)



(b)

Figure 6.13. The plots of (a) the fractal dimensionality calculated from the plots of $n(r)$ at several volume fractions as a function of time and (b) the changes of the $n(r)$ as a function of r at $\phi = 0.05$ at various times.

The difference is that in this more concentrated suspension, the clusters are large enough relative to the size of the box to allow them to form a percolating network or gel. Once these clusters connected to form the gel, the mobility decreases and this is shown in the slower growth rate.

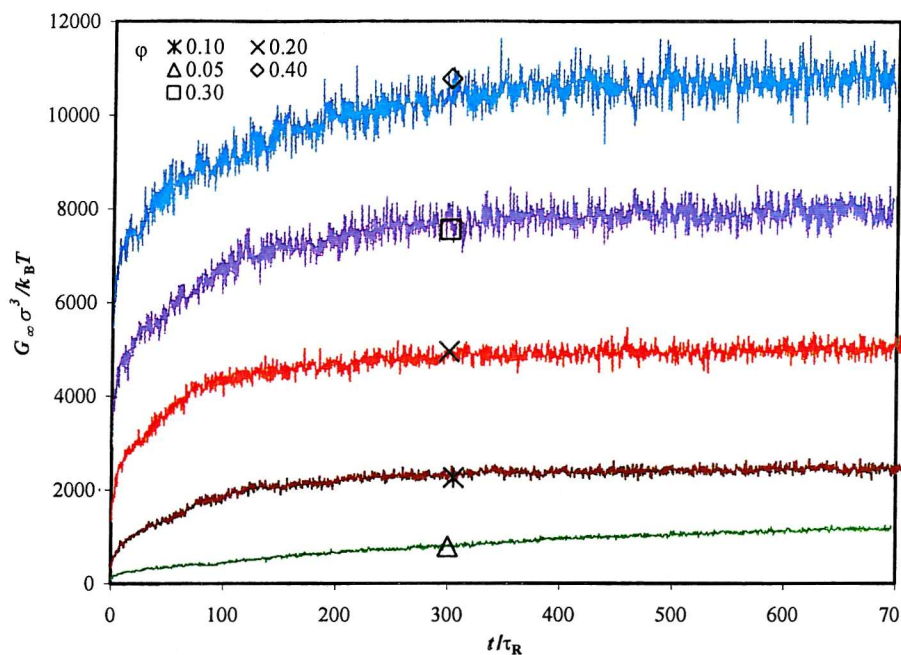
We study the long-range order by plotting the fractal dimension at these systems. In Fig. 6.13(a), we display the calculated fractal dimension at several volume fractions. The graph shows that the fractal dimension increases with increasing density. At 40% volume fraction, which is the largest density in our study, we obtained values close to 3 in the late stages.

In the systems where a gel does not form, the dimensionality describes the structure of the clusters within the network. If we look at the changes in the number of particles, $n(r)$, at large distance, we note that the growth of the $n(r)$ gradually changes to steeper increase. At a distance larger than the average radius of the clusters, the $n(r)$ is shown to increase as r^3 and the fractal behaviour has vanished. This is illustrated in Fig. 6.13(b), which shows the changes of $n(r)$ as a function of time in the suspension of 5% volume fraction at various time. We observe that for r larger than $7\sigma_R$, the rate of growth gradually changes until the slope of the line of $\ln(n(r))$ vs. $\ln(r)$ reaches the value of 3. In the denser suspension, we are unable to probe the boundary where the fractal behaviour vanishes as in most cases, $n(r)$ is limited by the size of the simulation box.

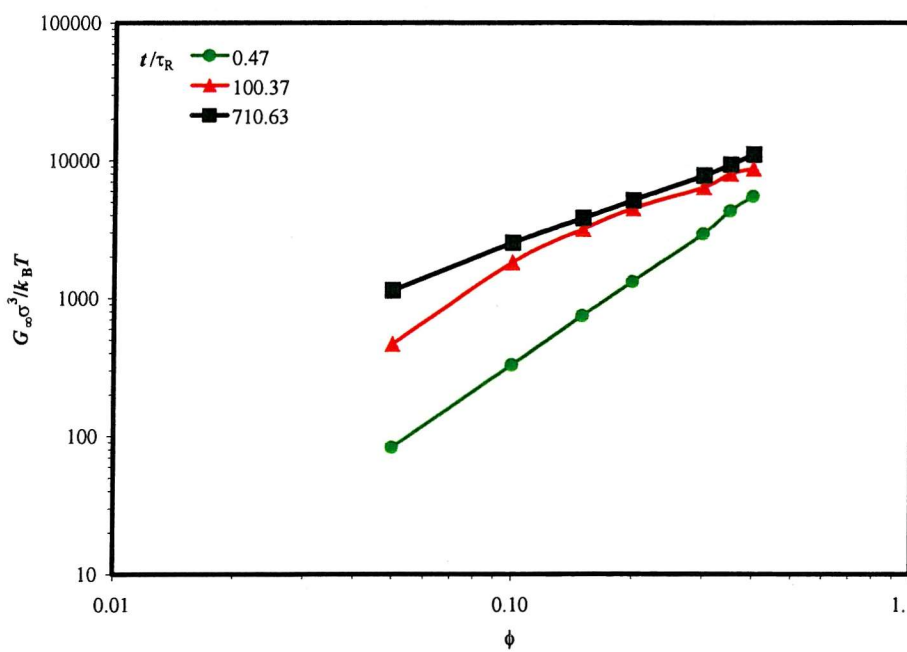
6.3. Mechanical stability

In Fig. 6.14(a), we present the change of the storage modulus with time at high frequency. We note that in all system, the change is similar, where G_∞ increases very rapidly at early stage and then levels out.

Towards the end of the runs, G_∞ is almost constant and we plot G_∞ as a function of the volume fraction at several stages in Fig. 6.14(b). The graph shows that G_∞ increases as a power law function of the volume fraction in moderate concentration. This behaviour can be observed at most times, although we note there is some deviation in the lower volume fraction at the intermediate stage. This result agrees qualitatively with the experiments of Narine and Marangoni[109-111]. They observed a power-law dependence of the mechanical properties of the fat crystal network. We also note that the power-exponent of the high frequency modulus varies depending on the age of the suspension after the quench.



(a)



(b)

Figure 6.14. (a) The storage modulus at high frequency as a function of time for various ϕ at $\kappa = 250\sigma^{-1}$ and (b) G_∞ plotted as a function of volume fraction at several gel ages.

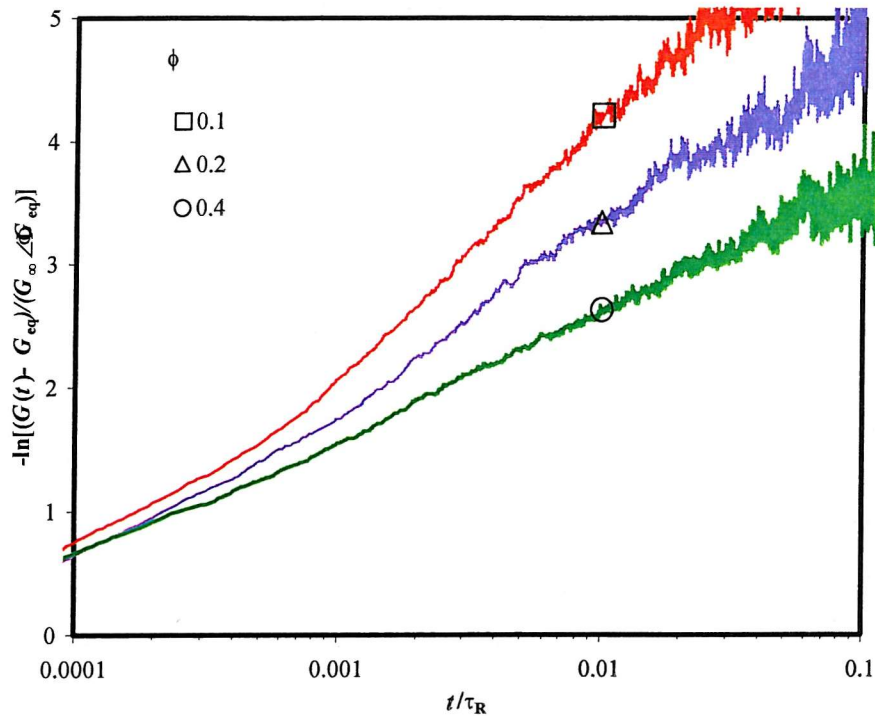


Figure 6.15. The stress decay after the step-strain for systems $\kappa = 250\sigma^{-1}$ taken at different volume fraction. The plots are taken at $t = 282.74\tau_R$.

In Fig. 6.15, we display the graph of the stress decay at different volume fraction, taken at $t = 282.74\tau_R$ after which these plots do not vary significantly. We observe that in all systems, the stress decay is a stretched-exponential function of time at all stages (see Eqn 5.1). This is because the suspensions do not form highly ordered clusters within the aggregates. As the volume fraction is increased, Fig 6.15 shows that the shear modulus decays at a slower rate and the exponential constant decreases from 0.892 for the system of 10% volume fraction to 0.412 for 40% volume fraction.

In the system at 10% volume fraction where we do not observe the gel formation, the corresponding plot shows the expected behaviour, in which the suspension relieves the stress at a rate faster than for the more concentrated suspensions.

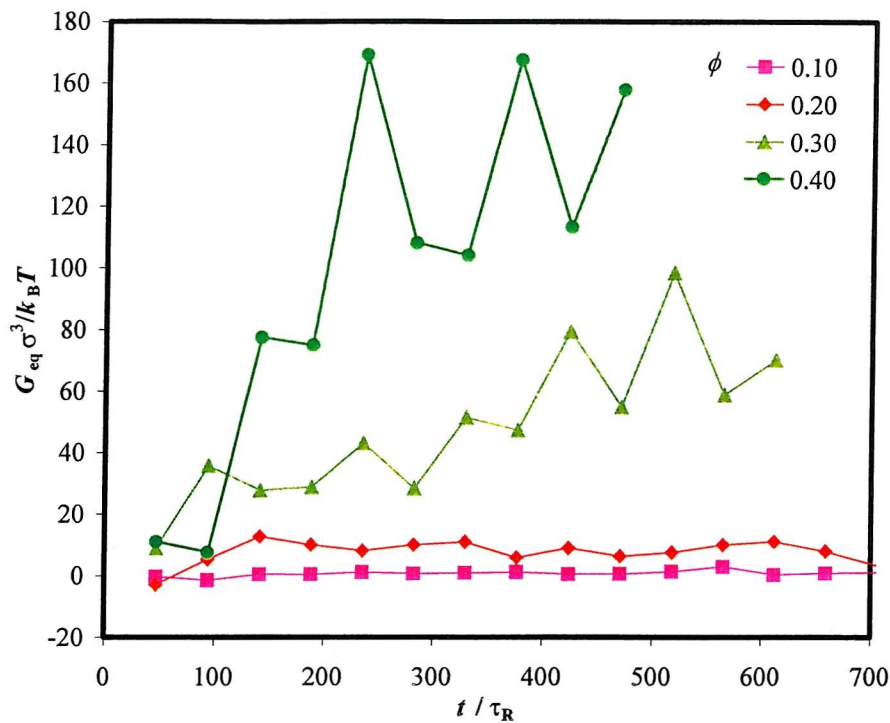


Figure 6.16. The equilibrium modulus for various κ at different gel ages.

In Fig. 6.16, we present the plot of the equilibrium modulus at different volume fraction. The graphs show that the solid-like behaviour of the suspension is strongly dependent on the volume fraction. At 10% volume fraction, we observe that the suspension can still be considered as a liquid as the average equilibrium modulus for this system close to 0. This means that the system manages to exert all of the applied stress all the time. At larger densities, a percolating network starts to form within the system. In the 20 % volume fraction, the equilibrium modulus becomes non- zero, although the resulting values are still quite small. This indicates that the gel is very weak and may be easily disrupted by applying a small stress.

As we observe the suspension with higher density, the resulting gel becomes stronger. This is shown in the corresponding plots for suspensions of 20 and 40% volume fraction. The plots show that the equilibrium modulus increases quite dramatically with density, although these values are still a small fraction of the high frequency shear modulus, which means that the systems still exert most of the applied stress.

6.5. Summary

In this chapter, we have studied the effect of the suspension density on the structures and their mechanical strengths. The gel networks are produced when the systems are within the unstable region which implies the importance of the spinodal decomposition in the gel formation. When a gel is formed, the dynamics of the colloidal particles decreases considerably and the distribution profiles of the motion show that most particles may hardly move at the late stages.

The simulation shows that when the gel does not form, the colloidal particles remain highly mobile. This can be seen in the displacement profiles, which show a broad distribution for system of small volume fraction. At low volume fraction, the average number of nearest neighbours is also smaller and we show that there is a large fraction of isolated particles which are highly mobile.

The structure factors reveal that at early stages, all systems form clusters of similar size which evolve by aggregating to form larger clusters. This is shown in the peak of the structure factor, which shifts to smaller k at the same rate for all systems. The gels are only formed when these clusters are close enough to form an interconnecting structure with their neighbours. In a dilute system, the structures of the cluster are more open as suggested by the shift in peaks of the structure factor to larger wavelength and by the fractal dimensionality. The resulting size may not be large enough for the clusters to form a percolating structure. We have shown that a gel is only formed from a suspension of more than 15% volume fraction. We showed that the fractal dimension is lower for a suspension at lower volume fraction.

We showed that the decrease in the interaction energy can be fitted to a power law with the same exponent for suspensions where the gel is not formed. Once the gel is formed, the exponent increases with increasing volume fraction.

The evolution of the mechanical strength has been studied by focusing on the changes in

the high frequency, G_∞ , the equilibrium shear modulus, G_{eq} and the decay rate of the modulus. The decay rate of the modulus is constant as the systems evolve. In all systems the decay follows a power-law function of time. This reveals that the structures are highly disordered at short range. G_∞ increases as a power law function of the volume fraction at most times, although the exponent is shown to decrease as the simulation progresses. The clear difference in the behaviour between the gel and the non-gel systems are observed in the results obtained for the equilibrium shear modulus. In a non-gel system, the stress decays to zero after some times, which shows that the systems cannot sustain a stress. Once the gel is formed, the systems will have a non-zero G_{eq} and this imply solid-like behaviour. This value rapidly increases with the increasing density in the suspensions.

PART II
DISSIPATIVE PARTICLE DYNAMICS
SIMULATION OF POLYMER
BRUSHES

Chapter 7

Polymer brushes

A single grafted polymer chain in dilute solution occupies a volume of a half-sphere whose radius depends on the size of polymer and the solvent quality. This radius is referred to as the Flory radius, R_F , and it scales as $R_F \propto N^{\nu}$, where N is the number of monomers per chain and ν is the scaling exponent. ν is equal to 0.6 for a good solvent and 0.5 for a poor solvent[4,112]. When a surface is grafted with the polymer chains where the distance between grafting points, D , is larger than the Flory radius of the chains, R_F , the interaction between polymer chains is negligible (Fig. 7.1(a)). Each chain then conforms to the same scaling law as a single grafted chain. The average distance between the grafting points is equal to $\sigma^{-1/2}$, where σ is the grafting density.

When the grafting density is increased and D becomes less than the Flory radius, the polymers start to overlap (Fig 7.1(b)). The chains respond by stretching away from the grafting surface to avoid overlapping with their neighbouring chains. Different scaling law applies in this condition and the grafting density begins to affect the configurations of the chains. The structure formed when the grafting density is high, is known as a polymer brush. A more complex situation is illustrated in Fig 7.1(c) in which two polymer brushes are compressed against each other; this will be the subject of our study.

There have been a significant number of experimental and theories on the properties of polymer brushes due to their wide range of applications in many areas, such as colloidal stabilisation and grafted lubricants. Early works on polymer brushes were carried out by Alexander[113] and de Gennes[4,112]. They pointed out that when the grafting density is high, the polymer chains are strongly stretched in the direction normal to the grafting surface. This deformation is a result of the balance between the entropic elastic energy

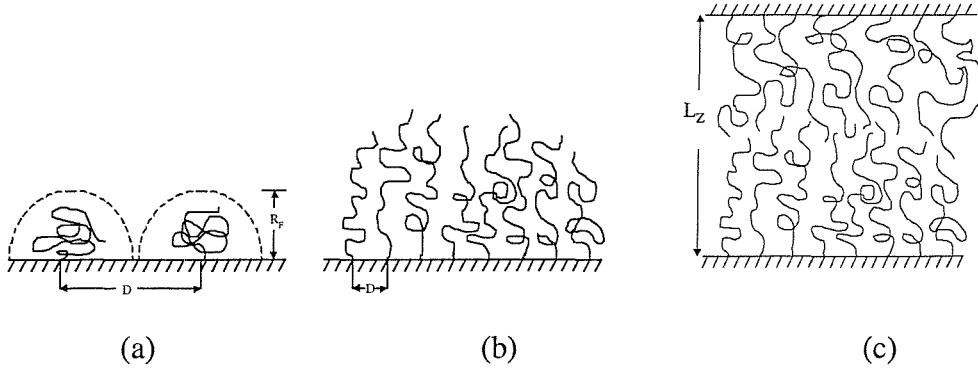


Figure 7.1 The schematic illustrations of polymer chains grafted onto flat surface at different spacing, D . (a) $D > R_F$, (b) $D \leq R_F$ and (c) two grafted polymer surfaces are compressed against each other. L_z is the separation distance between the grafted layers.

of the chain and the monomer-monomer interaction. The free energy can be written as a sum of these two terms using a Flory approximation. Alexander assumed a step-function profile for the polymer density to calculate the contribution of monomer-monomer interaction to the free energy calculation. The polymers density is independent of the position and equal to the average density in the brush, $\phi = N\sigma h$, where N is the length of chain, σ is the grafting density and h is the brush height. This leads to a simplified form of the binary interaction energy, $\epsilon_{\text{int}} \sim w\sigma N^2/h$, where w is the excluded volume parameter, which measure the strength of the repulsion between monomers. A simple expression for elastic contribution to free energy, ϵ_{el} , is obtained by assuming that the chains are uniformly stretched and their free ends are positioned on a single plane at the distance h from the grafting surface. This results in $\epsilon_{\text{el}} \sim h^2/Na^2$, where a is the mean statistical segment or Kuhn length, such that Na will give the full contour length of the polymer chain.

The free energy per chain, which is the sum of these two contributions, can then be written as:

$$\begin{aligned} \epsilon &= \epsilon_{\text{int}} + \epsilon_{\text{el}} \\ &\sim w\sigma N^2/h + h^2/Na^2. \end{aligned} \quad (7.1)$$

The equilibrium brush height, h^* , is then obtained by minimising the free energy with respect to height gives:

$$h^* \sim (w \sigma a^2)^{1/3} N. \quad (7.2)$$

The Flory approximation is expected to be valid for a high-density brush of weakly interacting chains. A rather different approach was employed by de Gennes who used the scaling arguments[112]. In this method, the polymer chains were treated as strings of “blobs”, which have diameters of the order of the distance between grafting points, act as hard spheres and fill the space densely. This approach gives the equilibrium brush height $h^* \sim N\sigma^{(1-\nu)/2\nu}$. Using $\nu = 3/5$ for a good solvent, the same correlation between equilibrium brush height, grafting density and chain length is obtained. The same assumption, in which a step-function density profile is suggested for the brush, is used for both approaches.

Milner *et al.* [114] elaborated further using self-consistent field method to obtain a more detail view of polymer brushes. In their approach, the physics are the same as the Alexander model where the stretching of the chains is balanced by interactions between the beads, but the balance is maintained locally along the chain rather than over the entire chain. They relaxed the assumption that all the free ends are located on the outer edge of the brushes and argued that when the chain is not strongly stretched, its configuration will fluctuate around its most favourable position. Their result showed that the density profile of the polymers is parabolic. The scaling of the brush height was found to be consistent with the Alexander model. In the high-density limit where the polymers are strongly stretched, the fluctuation diminishes and most of the free ends will then be concentrated close to the outer boundary, as assumed by Alexander and de Gennes.

Numerous experimental studies and computer simulations have been carried out to verify these results. The parabolic profile of monomer density is found to be consistent in general with the experimental results[115,116]] and also with results from computer simulations[117-121,153-154]. The theoretical treatment by Milner *et al.* only take into account the two-body interaction and neglect the three-body interaction. The theory is then valid only for brushes of low density. Grest has shown that at large grafting density, the brush height is a function of $\sigma^{1/2}$ instead of $\sigma^{1/3}$ [13]. This has not been proved experimentally as high grafting densities are not easily accessible.

Another problem, which was addressed by Shim and Cates[123], is the behaviour of the polymer chains when they are strongly stretched. Gaussian chains are found to be a good approximation for moderate chain distortions. In a rather dense brush, the chains will be strongly stretched and this will make the finite extensibility of the chains important. Shim and Cates addressed this problem by using a non-Gaussian stretching term to describe the elastic interactions.

All the analysis is focused on the polymer brush surrounded by solvent particles. There has been fewer theoretical and experimental studies conducted on dry brushes, where there are no solvent particles present. Most simulation studies are also carried out on polymer brushes immersed in solvent particles in which the solvent particles are explicitly or implicitly taken into account, depending on the simulation method employed. In the dry brush, the equilibrium height is determined by the incompressibility of the chains. When there are no free polymers and solvent particles surrounding the brush, the density of the brush is almost uniform and independent of the distance from the grafting surface[114,115]. Pakula and Zhulina[124] calculated various characteristics of the dry brush such as the equilibrium height, the distribution profiles of free ends and polymers, and compared their results with the simulations. In their calculation, they only took into account the elastic interaction as the chains are completely surrounded by identical neighbouring chains and hence the monomer-monomer interactions will be screened out.

The hydrodynamic penetration of a simple shear flow into a polymer brush was first studied by Milner[126]. He showed differences in the extent of flow penetration into the brush. For the brush with a step function profile, the pore size within the brush is independent of the distance from the grafting surface. In the case of a brush with a parabolic profile, the hydrodynamic penetration length varies with the distance from grafting surface and diverges at the outer boundary. It is expected that the flow will penetrate much further into the brush in this case than for a brush with a step function profile. Milner obtain the penetration depth quantitatively by assuming the flow did not distort the brush profile. The flow of the solvent inside the brush was also assumed to follow the Brinkman equation for flow in porous media:

$$\eta \nabla^2 \mathbf{v} - \frac{\eta}{\xi^2(\rho)} \mathbf{v} - \nabla \mathbf{P} = 0 \quad (7.3)$$

where η is the solvent viscosity and $\xi(\rho)$ is the pore size which depends on the local density. \mathbf{v} and \mathbf{P} are solvent velocity and pressure respectively. Doyle *et al.*[156,157] and Saphiannikova *et al.*[158] carried Brownian dynamics simulations to study the behaviour of polymer brushes under shear. They employed the Brinkman equation to calculate the average solvent velocity within the brush and observed the shear thinning behaviour which was in agreement with the experimental results by Klein *et al.*[140,159].

One particular situation involving polymer brush, which has attracted considerable interests, is when two brushes are brought into contact. An understanding of the resulting interactions is important for phenomena relevant to many industrial applications. When two parallel brushes are pushed towards each other, such that their distance is less than the sum of the individual equilibrium heights, they will repel each other. This results from the unfavourable long-range steric interaction mediated by the chains, which arises from mutually compressed and partially overlapped brush and acts to keep the surfaces apart. This is the basis of colloidal stabilisation[77,126].

The theoretical analysis of steric repulsion between two parallel brushes has been attained using both scaling and self-consistent field analytical approaches[126]. There have been several simulations of brushes immersed in a good solvent recently. Dickman and Hong[155] carried out a 2-D Monte Carlo simulation to determine the force between two surfaces grafted with polymers of moderate length ($N = 40$ and 60). They found the relation between the force and the separation width agreed qualitatively with the prediction from the self-consistent field. Peters and Tildesley[127] studied polymer brushes of short chains ($N = 20$) while Grest[128] investigated the brush of longer chains ($N = 100$). Both utilised molecular dynamics (MD) with the shifted and truncated Lennard Jones potential. For large shear rates, the results from both studies show that the chains became strongly stretched along the direction of the shear. There is a small decrease in brush height as the shear velocity is increased. Outside the brush, the profiles of solvent

velocity are linear as expected. Within the brush, the velocity decays and vanishes at some interpenetration length. Lai *et al.*[119,129,160] studied simulations of polymer brush with the solvent defined implicitly. The effect of the flow is modelled using the Brinkman equation. They used the modified Monte Carlo method to take into account the effective force acting upon the brush by the movement of solvent particles. Their results were in good agreement with the molecular dynamics simulations, which included solvent particles explicitly. Although these simulations results were found to differ considerably from some theoretical predictions of Barrat, Kumaran, Harden and Cates and Aubouy *et al.*[130-132]. All of these theories suggest that the height should increase under shear[128].

Neelov *et al.*[133-135,161] studied the conformational properties of two polymer brushes consisting of long flexible chains facing each other using a stochastic dynamics simulations. The brushes are compressed and sheared at a constant rate in the opposite directions. Their results showed that when the shear is applied on the system, the interpenetration between those two brushes reduces. They did not find any noticeable increase in the normal component of stress tensor as shear rate is increase.

In this theses, we present the study of two grafted polymer layers brought into close contact and moved under shear in the direction parallel to each other. We study the system with varying shear rates, pore separation and solvent quality. We also carry out a set of simulations of dry brushes with varying pore separation. We will employ the dissipative particle dynamics (DPD) method for the simulation. It has been reported that DPD is a simulation method suitable for polymer systems[55,65-69]. One advantage for DPD is that we are able to represent solvent particles explicitly and this enables us to study the interaction between solvent particle and polymers in more detail.

Chapter 8

The model and the simulations

The simulation is written in FORTRAN and the model consists of a set of polymer chains grafted onto two boundary walls and surrounded by solvent particles, as shown schematically in Fig. 8.1. The simulation is performed in a tetragonal cell with periodic boundary conditions applied in the x and y directions and two impenetrable walls confining the fluid particles in the z direction. The interaction radius, r_c , the particle mass, m , and energy parameter, ϵ , are taken as unity. All other variables are given in reduced units. The cell dimensions in reduced units are:

$$L_x = 7.425; \quad L_y = 7.425; \quad L_z = 17.035$$

Later on, the length L_z will be changed in the simulation to study the system under varying compression. We set the temperature and timestep at 2.0 and 0.02 respectively.

For a_{ij} in the conservative force equation, we choose the value of 60.0. This value is used for interaction between all the species in the athermal case. This means no energy is absorbed or released during the mixing and polymer beads ‘see’ solvent particles no differently from other beads. For the simulations with varying solvent quality, the value of a_{ij} between different species will be varied to include immiscibility in the system. The value of the spring constant k and the equilibrium spring length r_{eq} for the chains are - 225.0 and 0.85 respectively.

The boundary walls consist of 486 particles arranged in three square-lattice layers in xy plane with high enough density to provide sufficient repulsion to prohibit solvent particles and polymer beads from crossing the wall. The attached-end of polymer chains are chemically grafted onto the boundary layers nearest the fluid and correspond to a surface

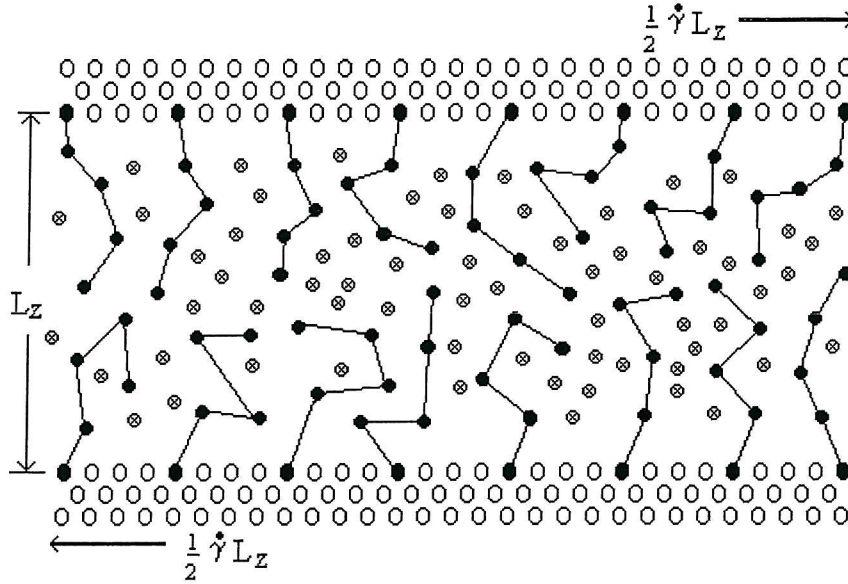


Figure 8.1. Schematic representation of the simulation box, showing the solvent and polymer particles confined between the walls. The arrows indicate the direction of the displacement of the wall particles to impose a shear field on the fluid.

coverage of 33%. The wall particles are connected to their initial lattice points by a Hookean spring force .

$$\mathbf{F}_i^w = k_{\text{wall}}(| \mathbf{r}_i - \mathbf{r}_{w,i} |) \quad (8.1)$$

where k_{wall} is the wall force constant and $\mathbf{r}_{w,i}$ is the lattice point for wall particle i . This allows the wall particles to interact with the surrounding ‘free’ solvent particles and move around their lattice points. k_{wall} is selected so that the chains will be stiff enough to prevent the wall particles moving significantly from their equilibrium positions. We choose the value for k_{wall} as -150.0 . An impenetrable barrier is also included within the wall, so that the solvent particles or polymer beads that cross the first layer of boundary wall will be reflected back into the channel and the sign of the velocity component normal to the grafting wall (v_z) is reversed.

The sliding periodic boundary technique, introduced by Ashurst and Hoover[127,137] is used here to simulate the steady uniform shear $\dot{\gamma}_a$. The shear is induced by moving the lattice points associated with the wall particles in the top and bottom wall in the opposite

direction. The magnitude of displacement is given by

$$\delta x = \pm \frac{1}{2} \dot{\gamma}_a L_Z \delta t \quad (8.2)$$

where δt is the time step used in the simulation. For determining γ and σ , we set $\sigma_R = 15.0$ where $\sigma_R = \sigma_{\text{ran}} (\delta t)^{-1/2}$, γ is then determined through the dissipation-fluctuation theorem. Initial runs showed that the temperature profiles across simulation cell depends upon the choice of dissipative parameter, γ . If the choice of γ is significantly lower than the strength of the conservative force, a_{ij} , the temperature profile will not be constant across the pore as it should be. This is caused by the difficulty in removing the energy produced from the gap between the layers. One way to overcome this problem is to adjust the dissipative parameter so that a constant temperature profile is obtained across the pore.

We analyse the temperature profile by constructing kinetic energy histograms for the particles. We divide the cell in z -direction into n bins, each with the width δz . Experience shows that dividing the simulation cell in z direction in 500 bins results into a smooth profile without loss of detail. We choose the value of $\delta z = 0.04$ which we also use when computing histograms for other profiles, such as the stress tensors and density. The histograms are updated every ten steps. The average bin temperature, T , is given by

$$k_B T(z_n) = \left\langle \frac{\sum_{i=1}^N H_n(z_i) m_i ([v_{x,i} - v_x(z_n)]^2 + v_{y,i}^2 + v_{z,i}^2)}{3 \sum_{i=1}^N H_n(z_i)} \right\rangle \quad (8.3)$$

where $\langle \rangle$ denotes time average. m_i is the mass of particle i located in bin n , $H_n(z_i)$ is the population of i in bin n at a given time and:

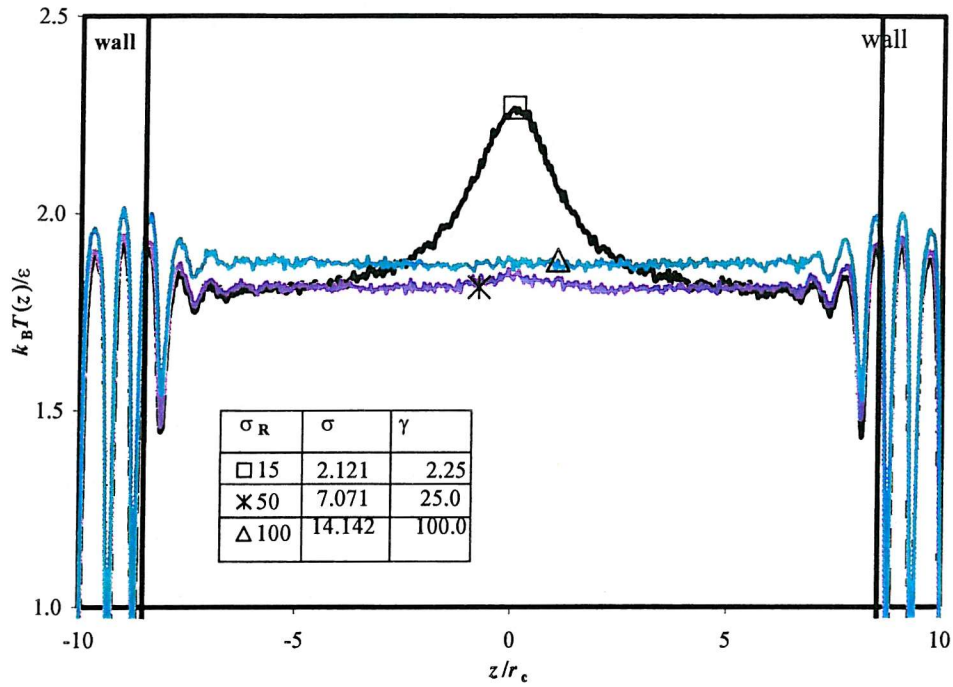


Figure 8.2. Temperature profile at different σ_R ($\Delta t = 0.02$, $\dot{\gamma} = 0.2$).

$$H_n(z_i) = 1 \text{ for } z_n - \delta z/2 < z_i < z_n + \delta z/2$$

$$H_n(z_i) = 0 \text{ otherwise.}$$

$v_x(z_n)$ is the instantaneous drift velocity in the x direction computed as

$$v_x(z_n) = \frac{\sum_{i=1}^N H_n(z_i) v_{x,i}}{\sum_{i=1}^N H_n(z_i)} \quad (8.4)$$

Fig. 8.2 shows how the temperature profile changes as we vary the random and dissipative force variables, σ and γ , by changing σ_R . At low σ , the system is unable to dissipate heat in the central region to maintain the temperature, hence we observe a large peak occurring in the middle of the pore. As σ_R is increased, the magnitude of the peak decreases and the temperature profile is approximately uniform when $\sigma_R = 50.0$. We decided to use a value of $\sigma_R = 50.0$ for all runs, as at this value, the profile is reasonably constant across the pore.

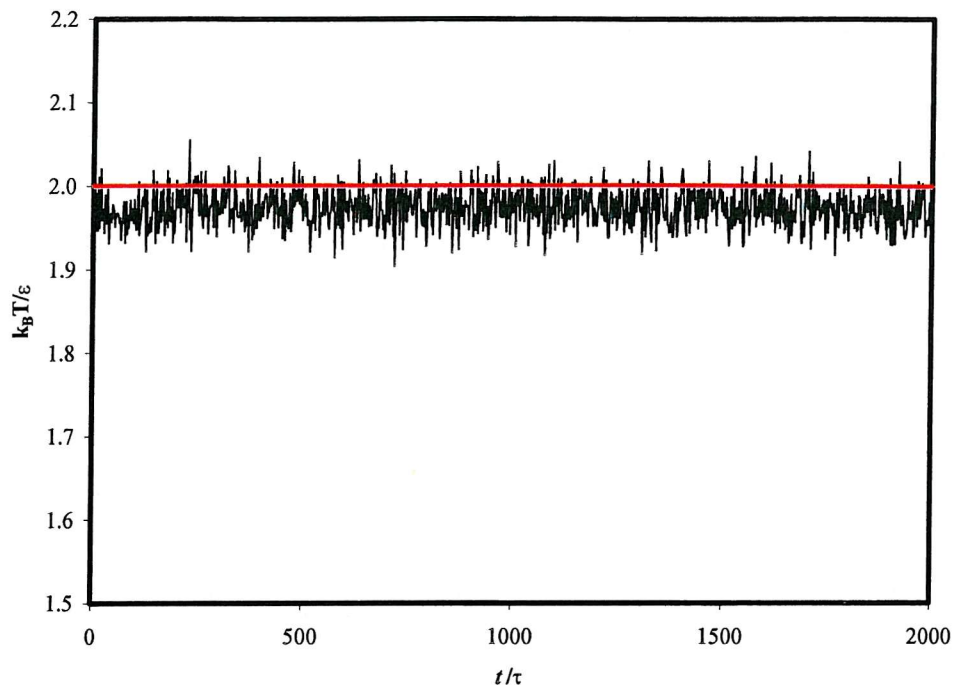


Figure 8.3. Graph of reduced temperature versus timestep ($\sigma_R = 50.0$, $\delta t = 0.02$).

The plot of $\langle T \rangle$ versus time is also presented here in Fig 2.3 to show that the temperature stays constant throughout the simulation run. Notice that on average the calculated temperature is slightly lower than the value we set. This is due to the effect of the finite time step that we choose in the simulation[137]. The fluctuation-dissipation theorem only holds in limit that the timestep equals 0 and in this limit we would expect the applied and measured temperature to be the same.

The simulations were performed at different reduced shear rates, ranging from 0 to 0.25. Each run at a given shear rate consisted of an equilibration stage of 50,000 steps, followed by a production stage of 50,000 timestep. As a summary, table 8.1 shows the reduced units for the fundamental quantities used in the DPD simulation.

Parameter	Reduced Value	Reduced Units	Typical Real Units
cut-off radius(r_c)	1.0	r_c / L	100 nm
$a_{\text{sol-sol}} = a_{\text{pol-pol}}$	60.0	$a_{ij} L / \epsilon$	
$a_{\text{sol-pol}}$	30.0 – 85.0	$a_{ij} L / \epsilon$	
time step (t)	0.02	$t (\epsilon / mL^2)^{1/2}$	25 ns
temperature ($k_B T$)	2.0	$k_B T / \epsilon$	300 K
random force variable (σ)	7.071	$\sigma (L^2 / m \epsilon^3)^{1/4}$	
dissipative force variable (γ)	12.5	$\gamma (\epsilon / m^3 L^2)^{1/2}$	
shear rate ($\dot{\gamma}$)	0.0 – 0.2	$\dot{\gamma} (m L^2 / \epsilon)^{1/2}$	5 m/s

Table 8.1. The values for the parameters used in the DPD simulation.

Chapter 9

Theta solvent determination

It has been known that the chain properties of the polymers in dilute solution exhibit the scaling relationship with the number of the beads in the chains, N_b . The scaling exponents for the polymers depend on the quality of the solvent. The chain properties of the polymers can be characterised by measuring the radius of gyration of the chains. The scaling law shows that the radius of gyration has the following behaviour,

$$R_g \sim N_b^\nu$$

where ν is the scaling exponent and the radius of gyration is

$$\langle R_g^2 \rangle = \frac{1}{N_b} \sum_{i=1}^{N_b} \langle (r_{i,x} - R_{CM,x})^2 + (r_{i,y} - R_{CM,y})^2 + (r_{i,z} - R_{CM,z})^2 \rangle. \quad (9.1)$$

The subscript CM refers to the centre of mass of the polymer chain, which is given as

$$\mathbf{R}_{CM} = \frac{1}{N_b} \sum_{i=1}^{N_b} \mathbf{r}_i. \quad (9.2)$$

In a good solvent, the solvent particles have a strong attractive interaction with the polymers. The resulting interaction between the polymer beads is repulsive as the beads prefer to interact with the solvent. This results in the swelling of the polymers. Flory estimates that in a good solvent, ν is 3/5. This is very close to the value of 0.59 determined through the experiments and computer simulations[4,56,138].

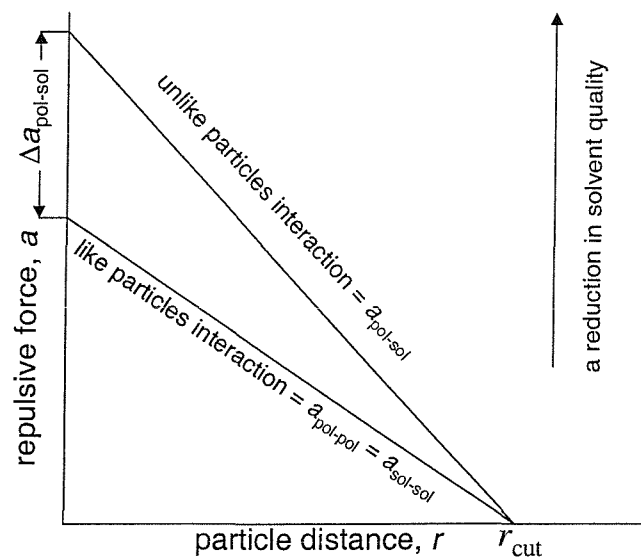


Figure 9.1. The figure illustrates different repulsive forces experienced by particles when they interact with like or unlike species.

In a poor solvent, the opposite happens and solvent particles interact less favourably with the polymers. The chains then collapse and the scaling exponent in this condition² reduces to $1/3$ [4].

In between these two types of solvents, there is a condition where the polymer-solvent interactions exactly compensate the polymer-polymer interactions. The solution in which this condition occurs is known as the theta solvent. The scaling exponent for a polymer in a theta solvent is $1/2$ [4].

Hoogerbrugge and Koelman[148] showed that it was possible to introduce immiscibility into DPD simulation by changing the interaction between two different species. Kong *et al.*[67] and Spenley[56] have carried out DPD simulations to model polymer in solvents with a range of quality. They found that the system followed simple dynamical scaling predictions. Spenley found that the dimension of the polymers in a good solvent scales with the number of the beads approximately to the power $\nu = 0.59$. This is in agreement with the predicted value from the theory and molecular dynamics simulations.

We will now use the same methods employed by Hoogerbrugge *et al.* and also Kong *et al.* for our simulation to study the behaviour of a polymer in dilute solvents of varying

quality. In this set of simulations, we specify the repulsive interaction between the same species to be equal and vary the interaction between different species, i.e. between the solvent and polymer particles. Fig 9.1 illustrates the different magnitude of repulsive forces acting on a particle when it interacts with like and unlike particles. The solvent quality is characterised using ξ , which is defined as,

$$\xi = (a_{\text{pol-sol}} - 0.5 (a_{\text{pol-pol}} + a_{\text{sol-sol}})) / a_{\text{pol-pol}}. \quad (9.3)$$

$a_{\text{pol-pol}}$ and $a_{\text{sol-sol}}$ are the parameters for polymer-polymer and solvent-solvent interactions respectively. Positive values of ξ result in a stronger repulsive forces between solvent particles and polymer beads. This will lead to immiscibility between these two species. Negative values indicate that particles experience less repulsion from particles of a different species. In our system, this will imply higher affinity between the polymer chains and the solvent particles.

In this section, we are trying to determine the location of the theta point in our model. This can be used as a guide for our study of simulating polymer brushes in solution of different qualities. This is carried out by plotting the scaling exponent for different solvent qualities. The scaling exponent can also be obtained from the static structure factor, $S(k)$. It has been shown that for $kR_g \geq 1$, the following behaviour is observed[4],

$$S(k) \sim k^{-1/\nu}. \quad (9.4)$$

The static structure factor, which is defined as

$$S(k) = \frac{1}{N_b} \sum_{ij} \langle e^{ik \cdot r_{ij}} \rangle = \frac{1}{N_b} \sum_{ij} \left\langle \frac{\sin(kr_{ij})}{kr_{ij}} \right\rangle \quad (9.5)$$

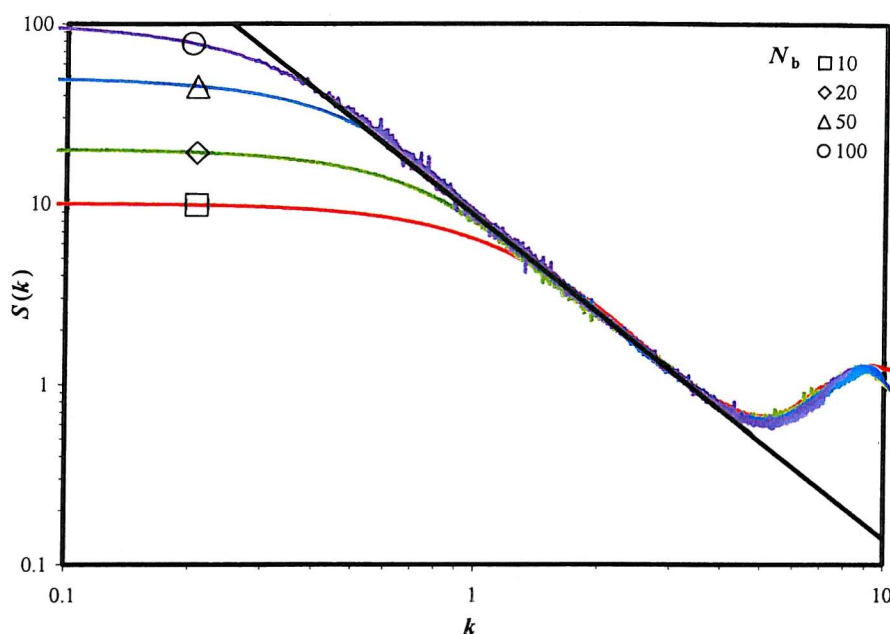


Figure 9.2. The structure factors for polymers of different chain lengths in an athermal solution. The straight line shows the range of k where the scaling function is valid.

We carry out a set of DPD simulations of polymers at different chain length and solvent qualities. The systems have the same density and we use the same values for the spring length. We use the same values for the like-particle interactions, $a_{\text{pol-pol}} = a_{\text{sol-sol}} = 60$ while the solvent-monomer parameter, $a_{\text{pol-sol}}$, is varied between 30.0 and 80.0.

We first run a set of simulation of a polymer chain with 50 beads immersed in a bath of solvent particles with the solvent quality is varied. The simulations are run for 150000 steps in which the first 50000 steps are used for the equilibration. We measure the scaling constant by plotting the structure factor.

9.1 Results

In Fig. 9.2, we show the graph of the structure factors for a polymer of different chain length immersed in an athermal solvent. We note that the scaling region expands to a lower k region with a longer chain. The lower boundary is found to be around $2.5/R_g$,

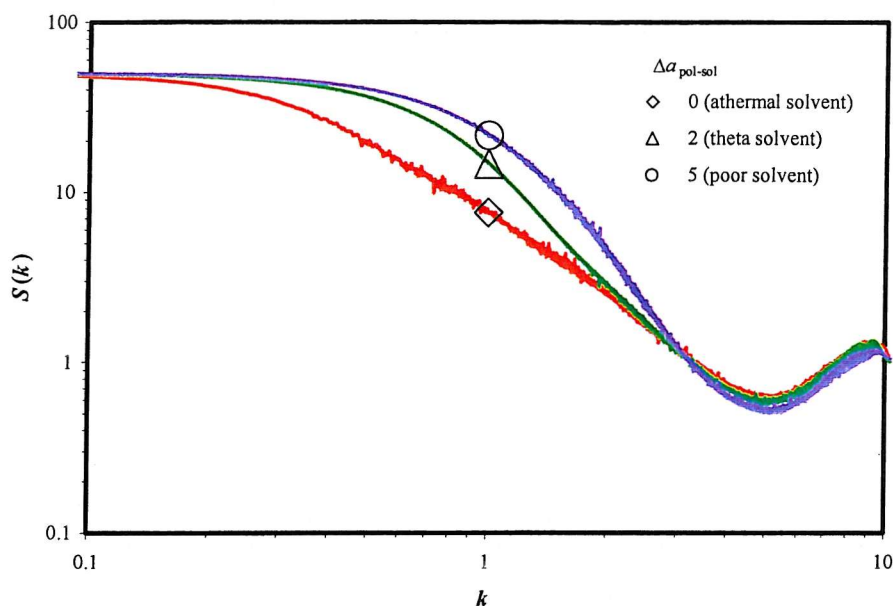


Figure 9.3. The structure factors of a polymer in a solution of different quality. The polymer chain consists of 50 beads.

which is similar to the value obtained by Pierleoni and Ryckaert[111] who carried out the molecular dynamics simulation of a dilute polymer in an athermal solution. From the plot of the structure factor for the polymers of 100 and 50 beads long, we obtained the value of $\nu \approx 0.58$ for both systems. Therefore we decided to carry out the simulations with polymer of 50 beads long for other runs to study the effect of the solvent quality on the static properties of the polymers.

In Fig. 9.3, we plot the structure factor for polymers immersed in solvents of different quality. The changes of the structure factors in the scaling region can be clearly observed. In the small and large k regions, all the plots are overlapping. In a system with a poorer solvent, the slope in the scaling region is steeper and the resulting scaling exponent is lower than the corresponding value for the system of polymer in good solvent. The scaling exponent of 0.5 is found for system with ξ at about 0.05. Based on this results, we determine that at this condition, the solvent is a theta solvent. The relationship between the solvent quality and the scaling exponent can be more clearly seen in Fig. 9.4 where we plot the scaling exponent as a function ξ .

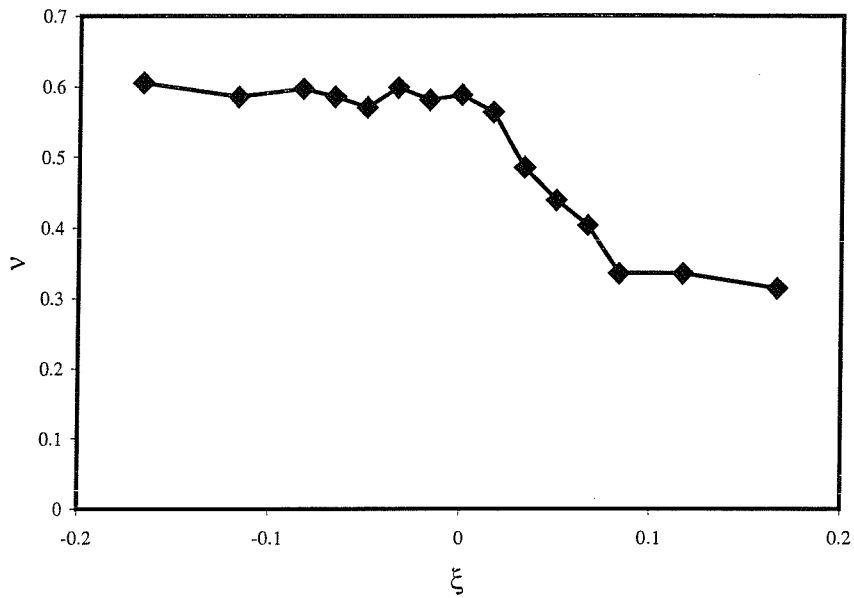


Figure 9.4. The scaling exponent calculated from the structure factor as a function of solvent quality.

For a polymer in a good solvent, where ξ is negative, the structure factor is identical to the corresponding plot of a polymer in an athermal solvent. This is because in a good solvent, the polymer is wet by the solvent and this results in the expansion of the chain. This expansion is restricted by the strength of the spring and for a reasonably stiff chain, the expansion should not vary greatly beyond that of the athermal solvent.

As ξ is increased to model a poorer solvent, the plots start to vary in the region where the scaling law is obeyed. The scaling exponent is also found to decrease with poorer solvent. We found that for $\xi = 0.033$, the scaling exponent is equal to 0.49 which indicate that the solvent is a theta solvent. If ξ is increased beyond the theta solvent, the scaling exponent decreases sharply until it reaches a limiting value at about 0.084. Beyond this point, the scaling exponent is about $1/3$, which indicate the solvent in this regime is classified as a poor solvent.

We runs another sets of simulation in which the number of the beads is varied for systems of polymers immersed in an athermal solvent, a theta solvent and a poor solvent

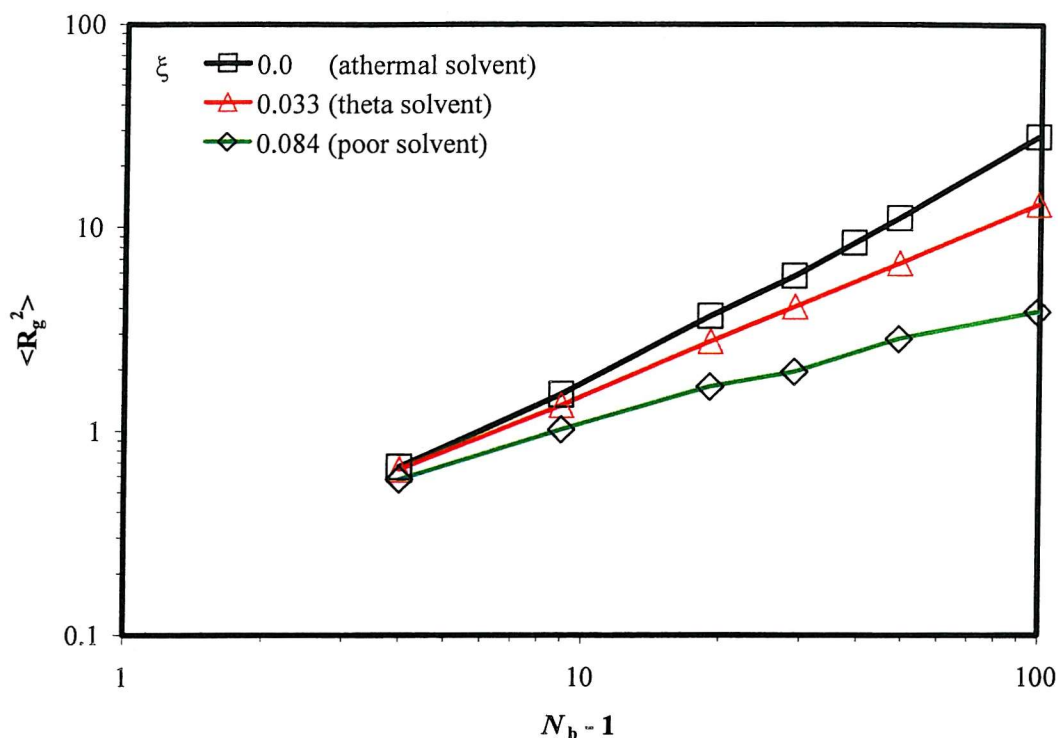


Figure 9.5. The mean square of the radius of the gyration for polymers immersed in dilute athermal, theta and poor solvents.

($\xi = 0.084$). The number of the beads in this run are varied between 5 and 100 while the total number of particles in the systems is kept unchanged at 10000.

We then plot the mean square of the radius of the gyration for the polymers. This is shown in Fig. 9.5. The scaling exponents for these systems are then extracted and we compare these results with those obtained from the structure factors. We found that the scaling exponent for systems of athermal, theta and poor solvent is 0.58, 0.47 and 0.33 respectively. These values agree well with the results obtained from the structure factors.

In conclusion, we show that the DPD simulations exhibit the scaling behaviour of the polymer at various solvent qualities. We obtained the scaling exponents that are close to the predicted values from the scaling law. A sharp transition is observed as the solvent quality is reduced from a good solvent to a poor solvent.

Chapter 10

Polymer brushes under varying shear rates

We present results of our study of the effect of shearing on the grafted brushes. In this set of simulations, we vary the shear rates at constant temperature and pore width, L_z . We have performed 5 runs at different reduced applied shear rates, ranging from 0.0 to 0.2 for periods of 100,000 timestep. If we assume that the pore width is 1500 nm with an average mass of polymers of 100,000 kg/kmol, we obtain the sliding velocities of about 5 m/s for the highest shear rate. This is a reasonable figure for lubrication.

10.1 Brushes structure

Fig. 10.1 shows the density profile for the polymers and solvent. The instantaneous number density in each bin is given by:

$$\rho(z_n) = \left\langle \frac{1}{L_x L_y \Delta z} \sum_{i=1}^N H_n(z_i) \right\rangle \quad (10.1)$$

where $\langle \rangle$ denotes time average. $H_n(z_i)$ is the population of i in bin n at a given time and

$$H_n(z_i) = 1 \text{ for } z_n - \Delta z/2 < z_i < z_n + \Delta z/2$$

$$H_n(z_i) = 0 \text{ otherwise.}$$

This calculation is also carried out to calculate the density profiles for the polymer monomers, solvent particles and the ends of the polymers.

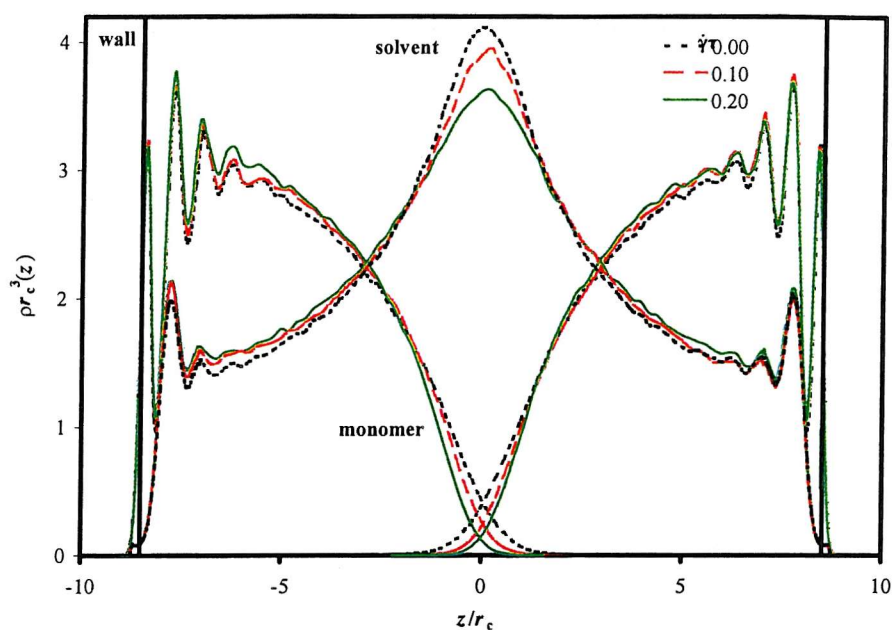


Figure 10.1. Density profiles for solvent particles and monomers at different shear rates.

From the density profiles of polymer brushes, we can see that there are three distinct regions[39]. In the region closest to the wall, the profile is oscillating rapidly out to a distance of 2.5 units from the wall. This behaviour reflects the interaction between monomer and wall particles. The second region is the scaling regime, in which we expect parabolic profiles, in agreement with self-consistent field theory, as we have set the brushes at moderate grafting density in a good solvent (see chapter 11 page 168).

Towards the middle of the pore, where the polymer density diminishes, there is a ‘tail region’ which is observable for brushes with finite length of polymer chains. This is caused by the free-ends fluctuates around their average configurations. Fig. 10.2 shows that the density profiles of the free-ends are non-zero everywhere in the brush regions and at higher shear rate, fewer polymers have their free ends in the boundary region between polymer and solvent.

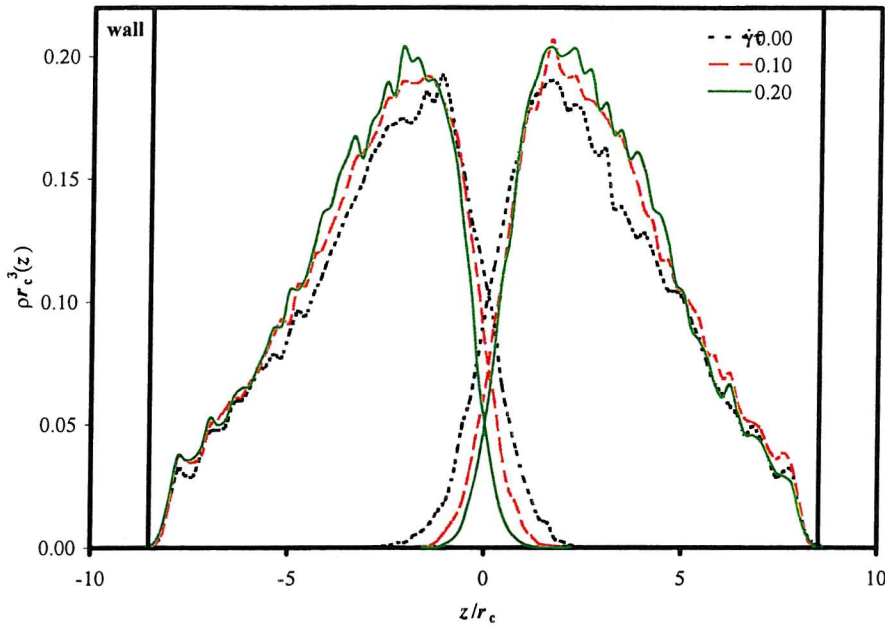


Figure 10.2. Density profiles for free-end of polymer chains at different shear rates.

As shear rate is varied, we see that the density profiles do not change very much. The density profiles maintain their parabolic shapes at all shear rates, which is expected when the grafting density is moderate. Only in the tail region do we see obvious differences where we notice a reduction in the width of the brush. This affects the amount of interpenetration. With the brushes slightly compressed, solvent particles are drawn towards the centre to balance the density across the pore. Hence there is a greater concentration of solvent particles in the centre region is observed.

We calculate the amount of interpenetration using the formula proposed by Murat and Grest[120,121]:

$$I = \frac{\int_{L_z/2}^{L_z} \rho_1(z) dz}{\int_0^{L_z} \rho_1(z) dz}, \quad (10.2)$$

where ρ_1 is the density profile of one of the brushes and z is the distance from grafting surface. Fig. 10.3 shows the schematic diagram of the density profiles of interpenetrating brushes. If we take the profile of brush 1, which is identical to the profile of brush 2, the amount of interpenetration is equal to the ratio between half of the interpenetrating area

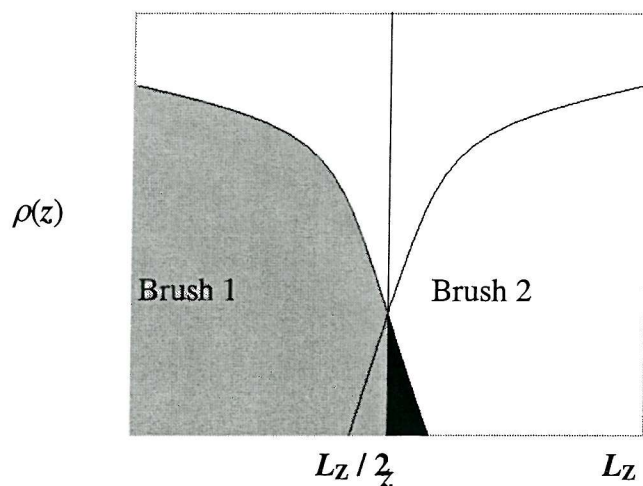


Figure 10.3 Schematic illustration of the density profile between interpenetrating brushes and the area shaded in black is the interpenetration region.

(area shaded in black) and the total area under the profile of brush 1 (area shaded in grey and black). We plot the resulting calculation of the amount of interpenetration as a function of shear rates in Fig. 10.4. The graph shows that the amount of interpenetration decreases as the shear rate increases. This result supports those reported in [133-135,139] on the simulations using molecular dynamics and Brownian dynamics in which the height of the brushes are observed to decrease slightly with increasing shear rate.

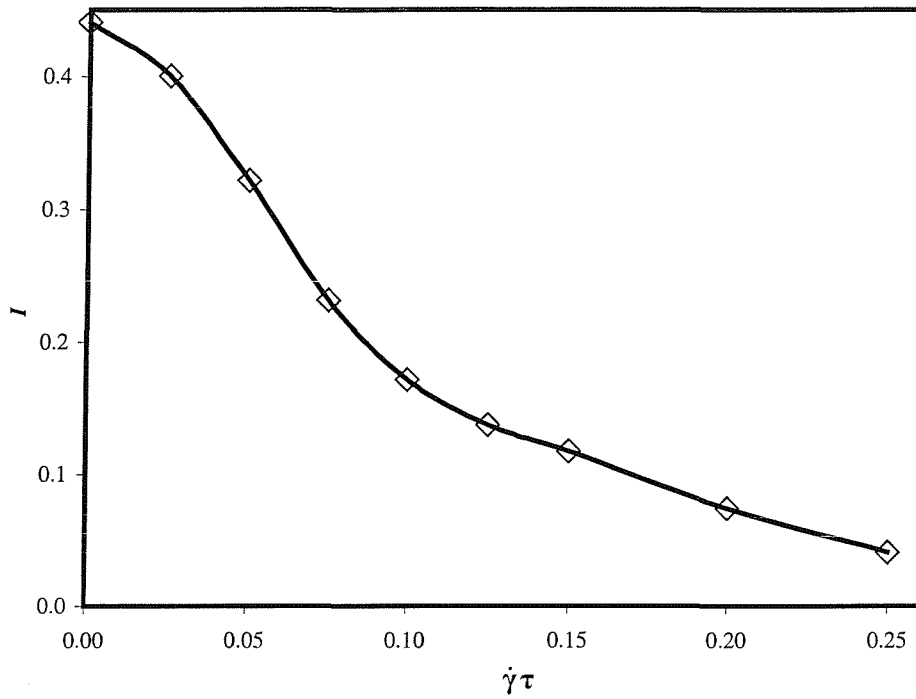


Figure 10.4 The amount of interpenetration, $I(L_Z)$ as a function of shear rates at constant L_Z .

We study the structure of the brushes by computing the mean end-to-end length of polymer chains and its components ($\langle h \rangle$, $\langle h \rangle_{\parallel}$ and $\langle h \rangle_{\perp}$),

$$\langle h_{\parallel} \rangle = \frac{1}{N} \sum_{i=1}^N \left\langle \left[(r_{x_{i,e}} - r_{x_{i,1}})^2 + (r_{y_{i,e}} - r_{y_{i,1}})^2 \right]^{1/2} \right\rangle, \quad (10.3)$$

$$\langle h_{\perp} \rangle = \frac{1}{N} \sum_{i=1}^N \left\langle \left[(r_{z_{i,e}} - r_{z_{i,1}})^2 \right]^{1/2} \right\rangle,$$

$$\langle h \rangle = \left(\langle h_{\parallel} \rangle^2 + \langle h_{\perp} \rangle^2 \right)^{1/2}.$$

' \parallel ' and ' \perp ' denote the parallel and perpendicular components, relative to the grafting surface. 1 and e in the subscripts denote the grafted-end and the free-end of polymer chains. We plot these results as a function of shear rate, in Fig. 10.5. $\langle h \rangle_{\parallel}$ increases under shear indicating polymer chains extend in this direction while $\langle h \rangle_{\perp}$ component decreases slightly.

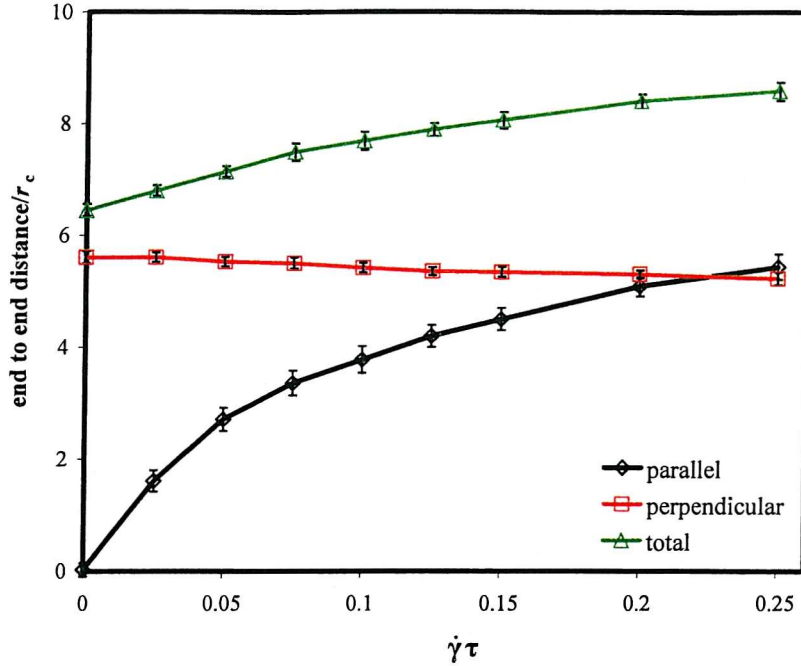
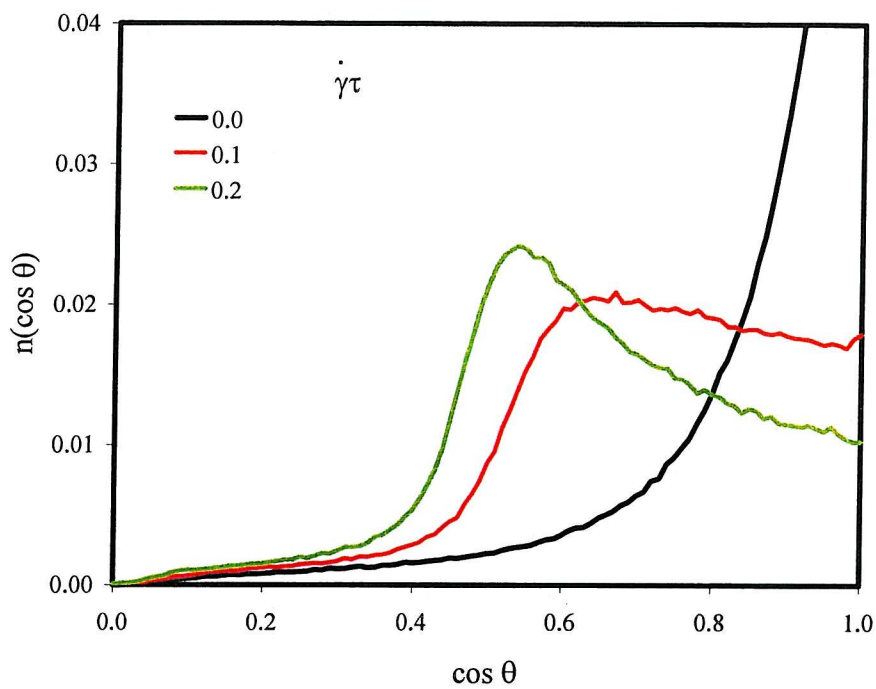


Figure 10.5. The mean end-to-end distance of polymer chains and its components

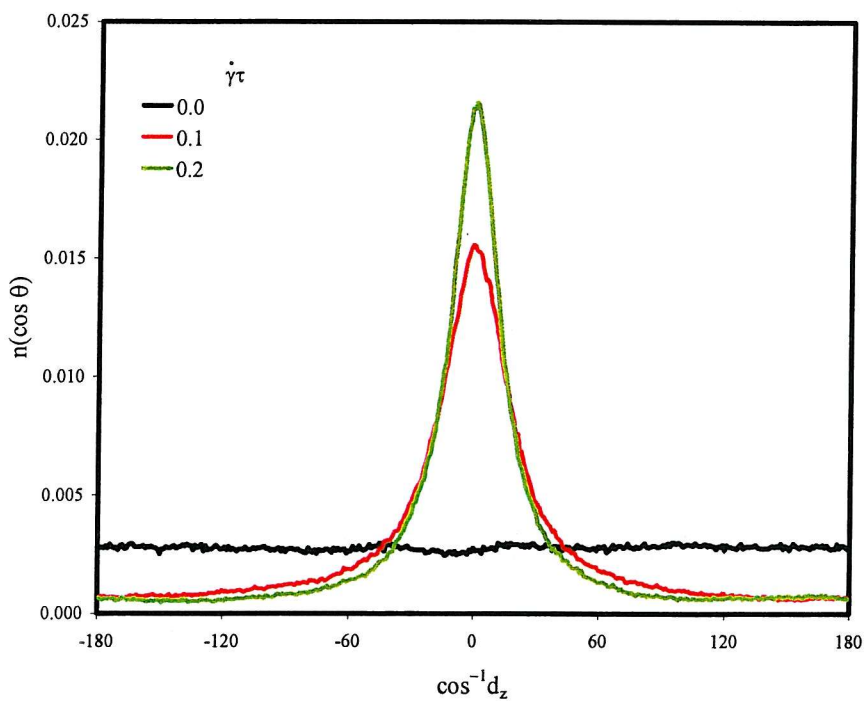
The orientation of a polymer chain, \mathbf{e}_i , can be characterised by diagonalising the moment of inertia tensor of the polymer and taking the eigenvector associated with the smallest eigenvalue to be the long axis of the chain. Defining the orientation of the molecule in this way, we calculate the angle, θ , between the molecule and the surface normal and use this to determine the distribution of orientations, $n(\cos \theta)$. The chain vector can be also used to calculate the azimuthal distribution $n(\phi)$. These are shown in Fig. 10.6(a). for different shear rates.

These distributions define the ordering of the chains with respect to the surface. We also consider the ordering of chains within the layer. The average orientation of the layer is the director, \mathbf{d} . It is the eigenvector corresponding to the largest eigenvalue of the \mathbf{Q} tensor defined as $\mathbf{Q} = \frac{1}{N} \left(\sum_i \mathbf{e}_i \mathbf{e}_i - \frac{1}{3} \mathbf{I} \right)$ where the sum is over all polymer chains. The extent of ordering within the layer can be characterized by the order parameter P_1

$$P_1 = \frac{1}{N} \langle \sum_i \mathbf{e}_i \cdot \mathbf{d} \rangle \quad (10.4)$$



(a)



(b)

Figure 10.6. (a) The azimuthal distribution $n(\theta)$ and (b) The distribution of tilt angles, $n(\cos \theta)$ for different shear rates.

Part II. Dissipative Particle Dynamics Simulation Of Polymer Brushes

The polymer chains are preferentially oriented along the direction normal to the grafted surface at zero shear rate. The maximum in $n(\cos \theta)$ occurs at $\cos \theta = 1$. When shear is applied, the layer tilts away from the normal in the direction of the shear. The maximum in $n(\cos \theta)$ is at $\cos \theta < 1$. The tilt is more pronounced at high shear rate.

In Fig 10.6(b), we show that the azimuthal distribution at equilibrium at different shear rates. In the absence of the field the chains are randomly oriented around the surface normal. With increasing shear rates the chains align in the direction of the flow. The width of the azimuthal distribution decreases with increasing shear rate.

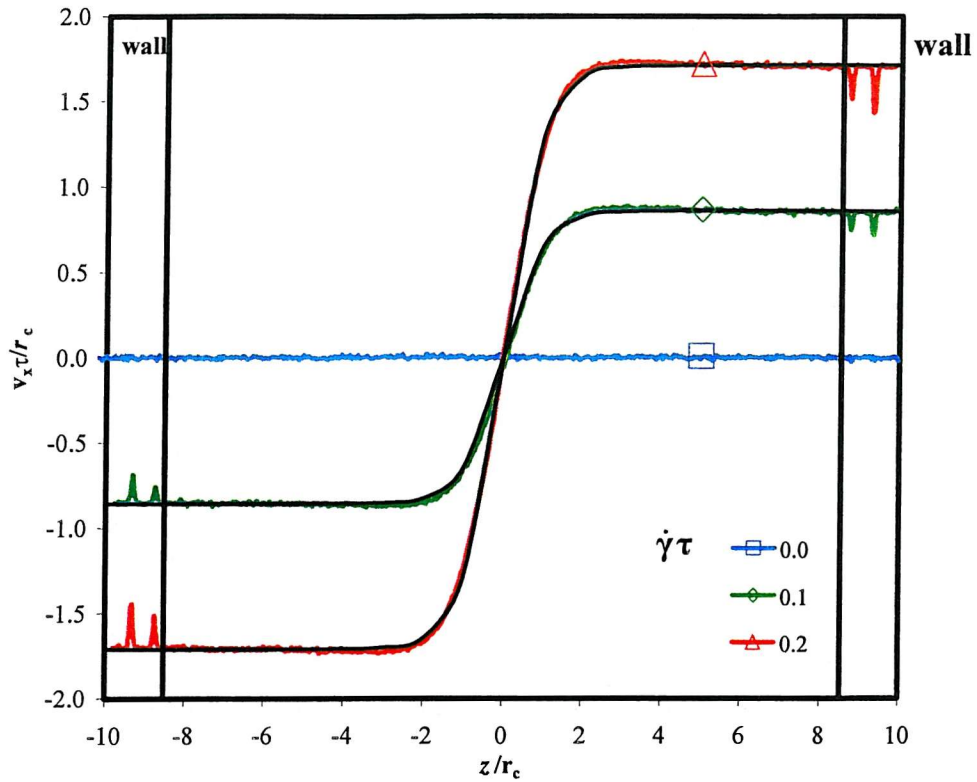


Figure 10.7. Velocity profile in the x-direction at different applied shear rates. The fitted hyperbolic tangential functions are plotted as black lines.

10.2 Rheological behaviour

Fig. 10.7 shows the typical sigmoid shape of the velocity profiles at all shear rates. The net velocity in the x direction does not change significantly across most part of the pore but there is a steep change around the middle of the pore. The profiles become steeper as the shear rate is increased. The analysis shows that the profiles can be reasonably described by a tanh function of z and pore width, L_z . The equation for v_x is:

$$v_x(z) = \frac{\dot{\gamma} L_z}{2} \left(\frac{\tanh(z)}{\tanh(L_z/2)} \right) \quad (10.5)$$

where $\dot{\gamma}$ is the applied shear rate and L_z is the pore width.

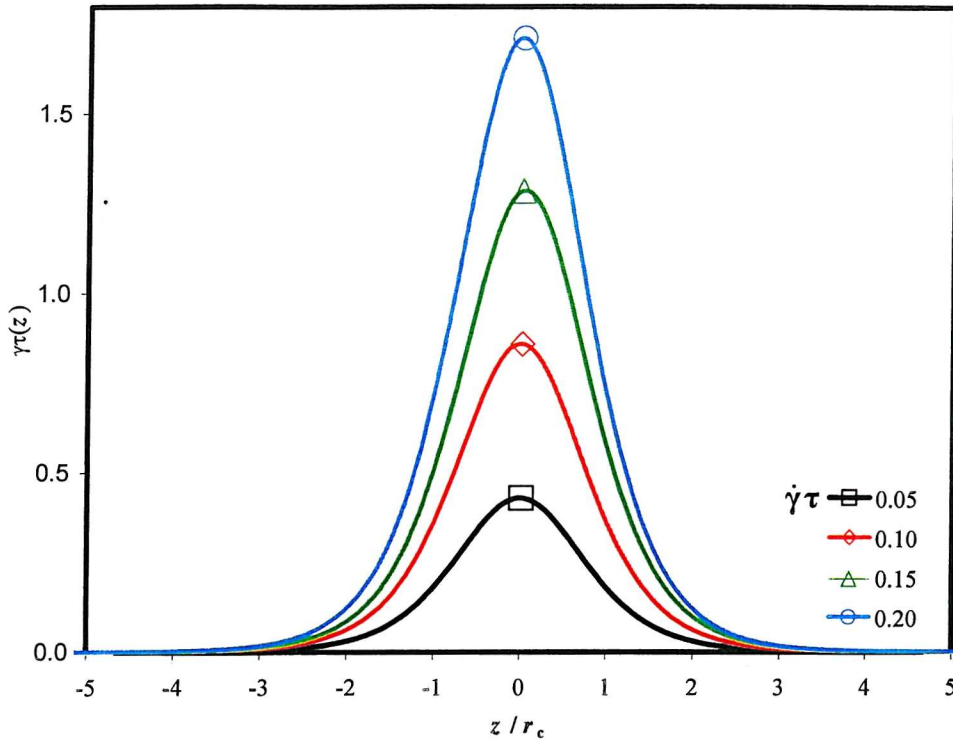


Figure 10.8. The shear rate profile at different applied shear rates.

The shear flow was induced by moving the lattice sites associated with the top and bottom wall atoms along the x -axis in the opposite directions. The magnitude of displacement, δx , is determined by the applied shear rate and given by

$$\delta x = \pm \frac{1}{2} \dot{\gamma} L_Z \delta t \quad (10.6)$$

where δt is the time step used in the simulation.

Eqn. (10.6) can also be rearranged to show the relationship between the applied shear rates and rate of displacement, $\delta x/\delta t$:

$$\dot{\gamma} \sim \frac{1}{L_Z} \frac{\delta x}{\delta t} \quad (10.7a)$$

As $\delta x/\delta t$ is basically the net velocity in the x direction, Eqn. (10.7a) can be used to give

the profile of shear rates across the pore, as shown in Fig 10.8:

$$\dot{\gamma}(z) = \frac{dv_x}{dz} \quad (10.7b)$$

Substituting Eqn. (10.7b) and differentiating gives

$$\dot{\gamma}(z) = \frac{1}{2 \dot{\gamma} \tanh(L_z/2)} \operatorname{sech}^2(z) \quad (10.8)$$

The profile of shear viscosity across the pore can then be determined, as shear viscosity is defined as

$$\eta(z) = \frac{-\langle P_{xz}(z) \rangle}{\dot{\gamma}(z)} \quad (10.9)$$

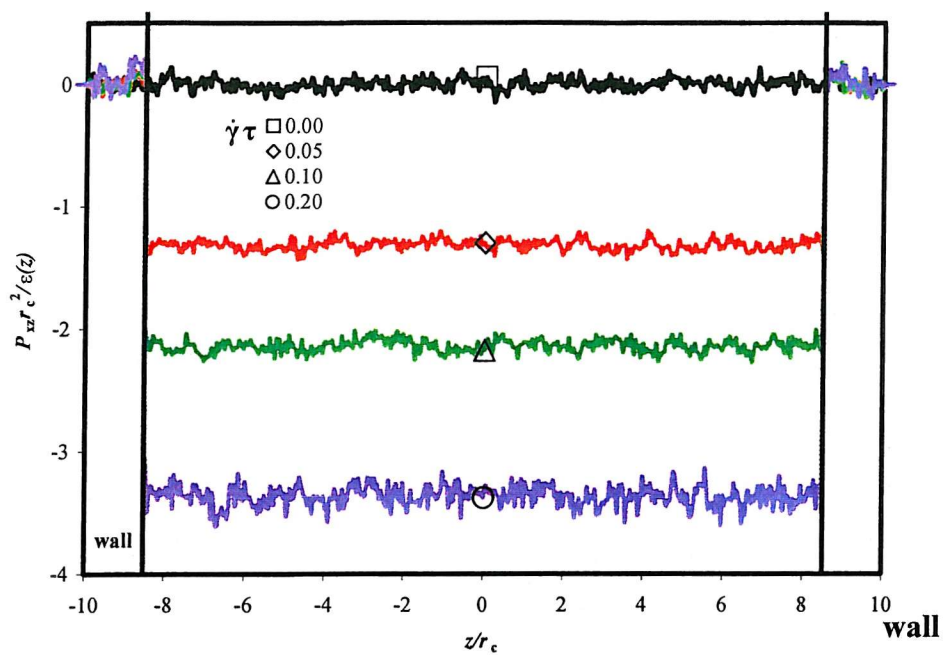
where P_{xz} is the off-diagonal component of stress tensor.

For stress tensor calculation, we employ the Irving-Kirkwood definition of stress tensor, written in its full form,

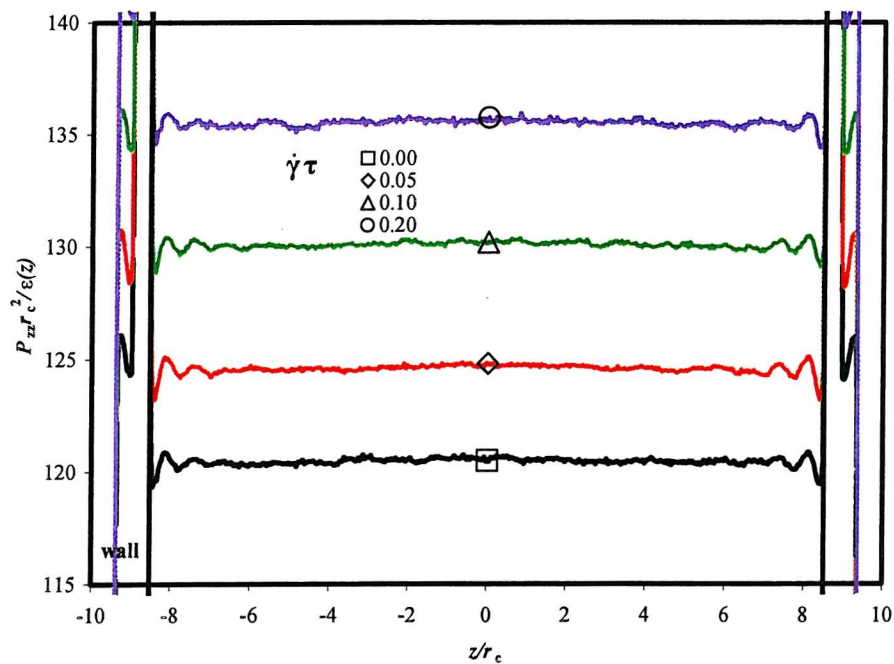
$$P(z) = \rho(z)k_B T \mathbf{I} + \frac{1}{L_x L_y} \left\langle \sum_{i < j} \mathbf{r}_{ij} \mathbf{F}_{ij} \times \frac{1}{|r_{z,ij}|} \theta \left[\frac{z - r_{z,i}}{r_{z,ij}} \right] \left[\frac{r_{z,j} - z}{r_{z,ij}} \right] \right\rangle \quad (10.10)$$

where \mathbf{I} is the unit tensor, $\langle \rangle$ denotes a configurational average and θ is a unit step function which is 1 for every positive value of its argument and 0 otherwise.

Fig. 10.9 (a) and 10.9(b) show the profiles of normal and off-diagonal stress tensor, P_{zz} and P_{xz} . The normal stress tensor is found to be constant across the pore, which is the requirement for mechanical stability. We observe that off-diagonal stress remains also constant across the pore and its value becomes more negative as the shear rate is increased. The value of P_{xz} should also be equal to P_{zx} or otherwise the system will rotate.



(a)

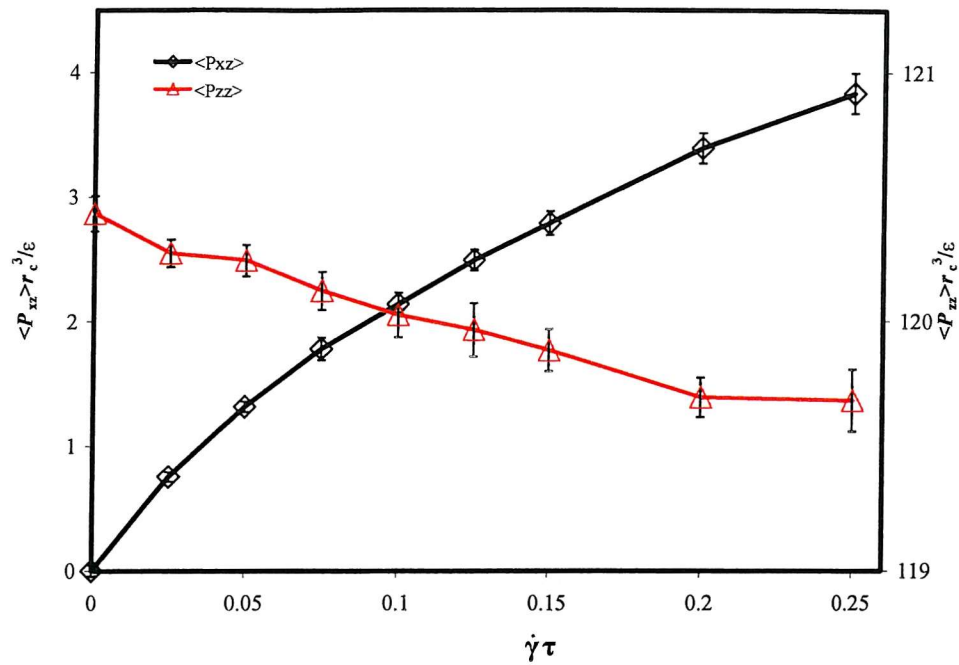


(b)

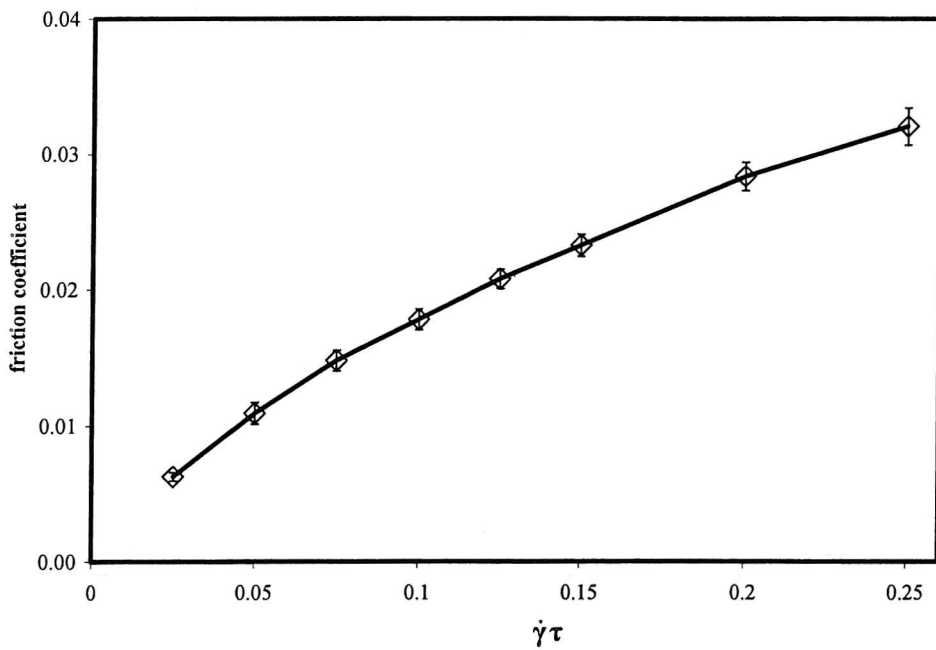
Figure 10.9 (a) The off-diagonal and (b) the normal component of the stress tensor profiles with varying shear rates.

We calculate the average of the off-diagonal, P_{xz} , and the normal stress tensor, P_{zz} , and plot these against shear rate. The resulting plots are shown in Fig 10.10(a). We also plot the ratio between these two stress tensor elements, $-P_{xz}/P_{zz}$, which is defined as the friction coefficient, in Fig 10.10(b). The graph shows that the normal stress tensor decreases slowly with shear rates but the magnitude of P_{xz} is increasing as the shear rate is increased. The shear-thinning property of the brushes system can be seen in the graph as P_{xz} does not increase linearly with shear.

Fig. 10.11(a) is a logarithmic plot of shear viscosity across the profile with varying shear rates. The brushes are behaving as an extension of the walls. The graph shows the region with the lowest viscosity is on the middle of the pore as this is the region where the solvent has the highest density. We plot the viscosity in the middle of the pore as a function of shear rate in Fig. 10.11(b). The plot shows that the viscosity reduces with shear rate [139-142]. This is consistent with the expected shear-thinning property of the polymer brush model. This is due to the increase in solvent density as the brushes repel more solvent particles from the brush region as the shear rate increases, resulting in less overlap between the brushes.



(a)



(b)

Figure 10.10. The plots of (a) the off-diagonal and the normal components of stress tensor and (b) the friction coefficient against shear rate.

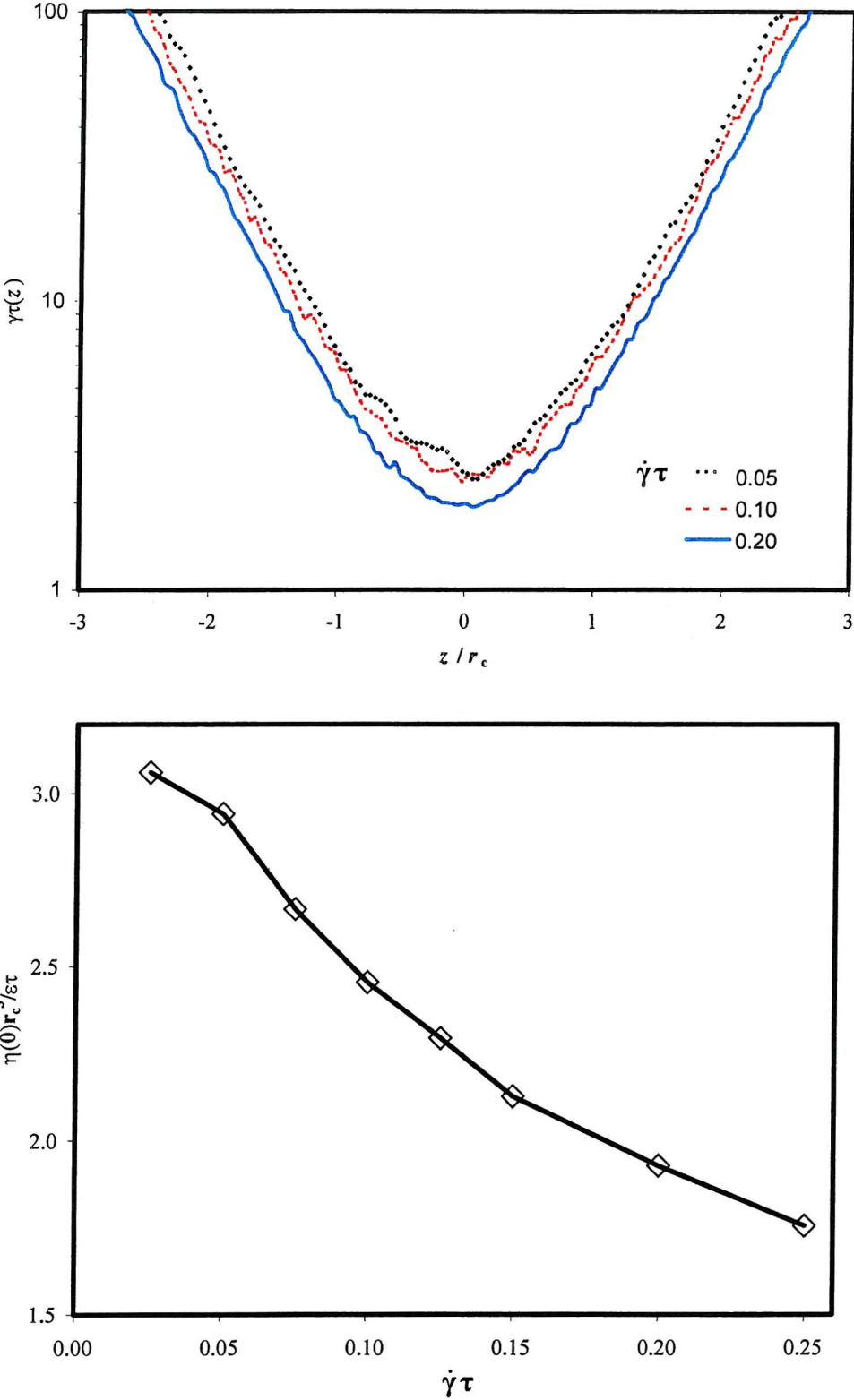


Figure 10.11. (a) The shear viscosity profile and (b) the viscosity measured at the middle of the pore at different applied shear rates.

We show how the profile of polymer brushes affects the net solvent velocity by computing the hydrodynamic screening length using the Brinkman equation[16], which describe flow in a porous medium:

$$\eta \nabla^2 \mathbf{v} - \frac{\eta}{\xi^2(\rho)} \mathbf{v} - \nabla P = 0 \quad (10.11)$$

where $\xi(\rho)$ is hydrodynamics screening length whose value is assumed to be a function of density and hence the position. The hydrodynamics screening length can be pictured as the pore size within the brush. η is the bulk solvent viscosity and P is the stress. The first term of the Brinkman equation is the viscous force due to dissipation within the solvent flow. This viscous force is balanced by the second term, the friction induced by the polymer segments and the stress gradient.

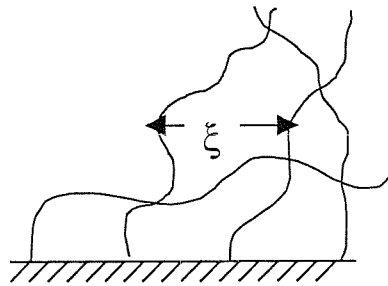


Figure 10.12. The Illustration of the hydrodynamics screening length within the brush.

We calculate the screening length as a function of z by modifying the Brinkman equation to take into account the shearing of the two brushes,

$$\eta \nabla^2 \mathbf{v} - \left(\frac{\eta}{\xi_1^2(\rho)} (\mathbf{v} - \mathbf{v}_{w,1}) + \frac{\eta}{\xi_2^2(\rho)} (\mathbf{v} - \mathbf{v}_{w,2}) \right) - \nabla P = 0 \quad (10.12)$$

where \mathbf{v}_w is the wall velocity and 1 and 2 denote the lower and upper brush. We use Eqn. (10.4) to describe the profile of solvent velocity in the x direction,

$$v_x(z) = \frac{\dot{\gamma} L_z}{2} \left(\frac{\tanh(z)}{\tanh(L_z/2)} \right).$$

At constant stress and substituting Eqn. (10.4) into (10.12), we obtain

$$-\dot{\gamma} L_z \operatorname{sech}^2(z) \tanh(z) - \frac{\frac{\dot{\gamma} L_z}{2} \left(\frac{\tanh(z)}{\tanh(L_z/2)} + 1 \right)}{\xi_1^2(z)} - \frac{\frac{\dot{\gamma} L_z}{2} \left(\frac{\tanh(z)}{\tanh(L_z/2)} - 1 \right)}{\xi_2^2(z)} = 0 \quad (10.13)$$

We define h as the height of the brush and denote *I*, *II* and *III* as the region below $(-L_z/2 \leq z \leq (L_z/2 - h))$, inside $((L_z/2 - h) \leq z \leq (h - L_z/2))$ and above $((h - L_z/2) \leq z \leq L_z/2)$ the interpenetration zone. In the region below the interpenetration zone, only the lower brush term is taken into account directly in the friction term. The hydrodynamics screening length profile in region *I* is then approximated as

$$\xi_I(z) = \left[-\frac{\cosh^2(z)}{2 \tanh(z)} \left(1 + \frac{\tanh(z)}{\tanh(L_z/2)} \right) \right]^{1/2}. \quad (10.14)$$

The same principle is applied to obtain profile of the screening length in the region above interpenetration zone (region *III*) as the brushes are identical,

$$\xi_{II}(z) = \left[\frac{\cosh^2(z)}{2 \tanh(z)} \left(1 - \frac{\tanh(z)}{\tanh(L_z/2)} \right) \right]^{1/2}. \quad (10.15)$$

In the interpenetration zone (region *II*), Eqn. (10.13) is solved with the boundary conditions $\xi_{I,I}(L_z/2 - h) = \xi_{I,II}(L_z/2 - h) = \xi_{2,II}(h - L_z/2) = \xi_{2,III}(h - L_z/2)$ and $\xi_{I,II}(h - L_z/2) = \xi_{2,II}(L_z/2 - h) = \infty$. We propose the solution for the screening length profile from the lower brush as

$$\xi_I(z) = \left[-\frac{\cosh^2(\frac{1}{2}(z+A))}{2 \tanh(\frac{1}{2}(z+A))} \left(1 + \frac{\tanh(\frac{1}{2}(z+A))}{\tanh(L_z/2)} \right) \right]^{1/2} \quad (10.16)$$

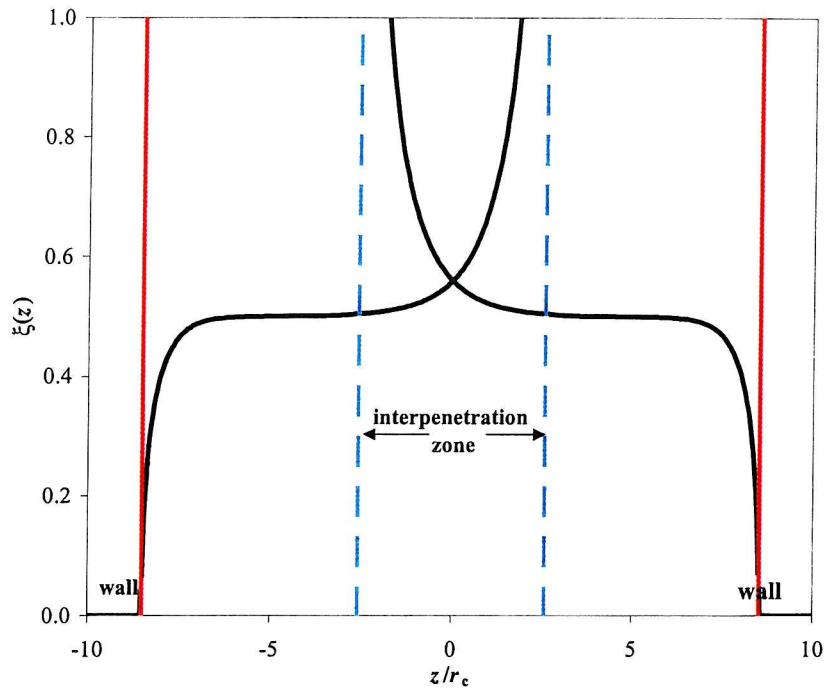


Figure 10.13. The screening length profiles along z-axis ($\gamma = 0.05$).

where $A = \frac{1}{2}L_z - h$. For the screening length profile from the upper brush, the solution will be

$$\xi_2(z) = \left[\frac{\cosh^2(\frac{1}{2}(z-A))}{2 \tanh(\frac{1}{2}(z-A))} \left(1 - \frac{\tanh(\frac{1}{2}(z-A))}{\tanh(\frac{1}{2}L_z)} \right) \right]^{\frac{1}{2}}. \quad (10.17)$$

The results for the screening length profiles from the brushes are plotted in Fig (10.13). The consequence of the solution for the screening length profile is that although shear rate, $\dot{\gamma}$, does not appear in the equation, its effect is shown in the slight reduction of the brush height as it is increased (see Fig. (10.1)).

We also plot a graph of the screening length from lower brush as a function of its local density, which is shown in Fig. 10.12. We choose the points from the region where the wall effect has diminished. The graph suggests that the screening length varies exponentially with the density. As a comparison, de Gennes[4] predicted the screening length of a polymer solution network in a good solvent to vary with the density as

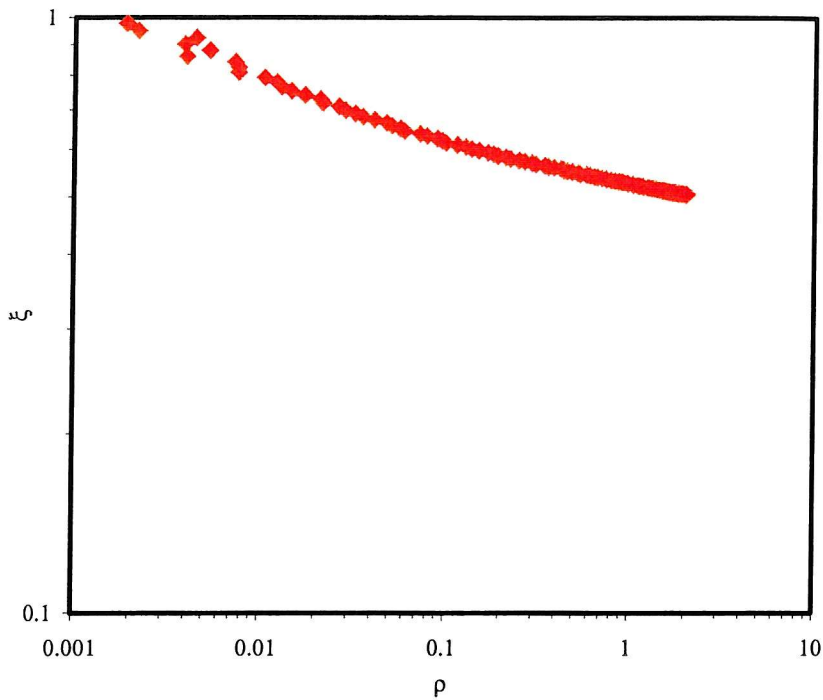


Figure 10.14. The screening length as a function of density. ($\gamma = 0.05$).

$$\xi(\rho) \cong c \rho^{-3/4}. \quad (10.18)$$

From Fig. 10.14, we found that the screening length is a function of $\rho^{-0.1}$. This means that the screening length in polymer brushes varies much less rapidly with density than in a polymer solution. It is not yet clear which factors give the less rapid decrease of the screening length with density. It could be the effect of grafting the polymers or simply a rather inappropriate approximation of the velocity profile.

10.3 Summary

In this chapter, we report the simulation under different shear rates. The density profile of the brushes shows the parabolic profiles which are in agreement with the self-consistent field theory. The brushes are close enough to have direct interpenetration between them. The interpenetration is greater for lower shear rates. This is because the polymers stretch in the presence of shear flow and the brushes are compressed. The velocity profiles can be fitted to a tanh function where the velocity does not change

significantly across most part of the pore but there is a steep change around the middle of the pore.

The viscosity is not constant at any point relative to the surfaces due to the effect of the polymer chains giving resistance to the solvent's movement. The viscosity is lowest in the middle of the pore where the solvent is at the highest concentration. The viscosity decreases as the shear rate is increased and this agreed with the shear thinning properties observed in other simulations and experiments. The screening length for the brushes is calculated using velocity profiles, which can be approximated as a tanh function. We found that screening length varies as a power-law function with density.

Chapter 11

Polymer brushes under varying compression

In this set of simulation, we vary the degree of compression on polymer brushes by altering the pore width, L_z . The brushes are still subjected to a shear of flow with shear rate, $\dot{\gamma} = 0.1$. As the compression increases, we expect an increase in both the normal and off diagonal element of the stress. These simulations were carried out for wet brushes, which include the solvent particles, and the dry brushes, without solvent.

11.1 Wet brushes

Graphs of the velocity profiles for wet brushes under different compressions are shown in Fig. 11.1. We observe that the tanh function profile is maintained at all pore widths. The profiles are scaled with the pore width.

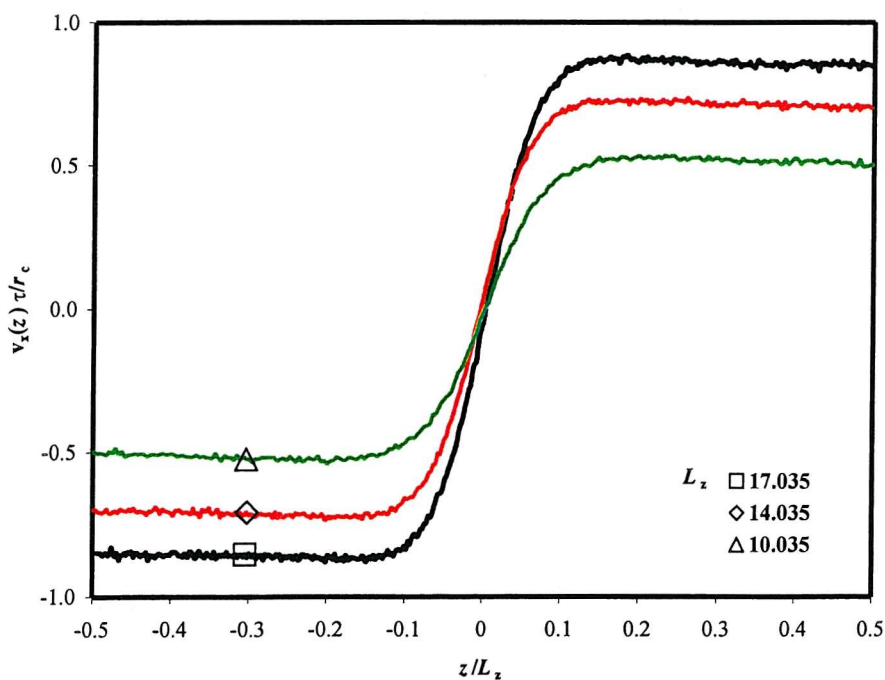


Figure 11.1. Velocity profiles along z -axis at different value of pore width. The co-ordinates are normalised by the pore width.

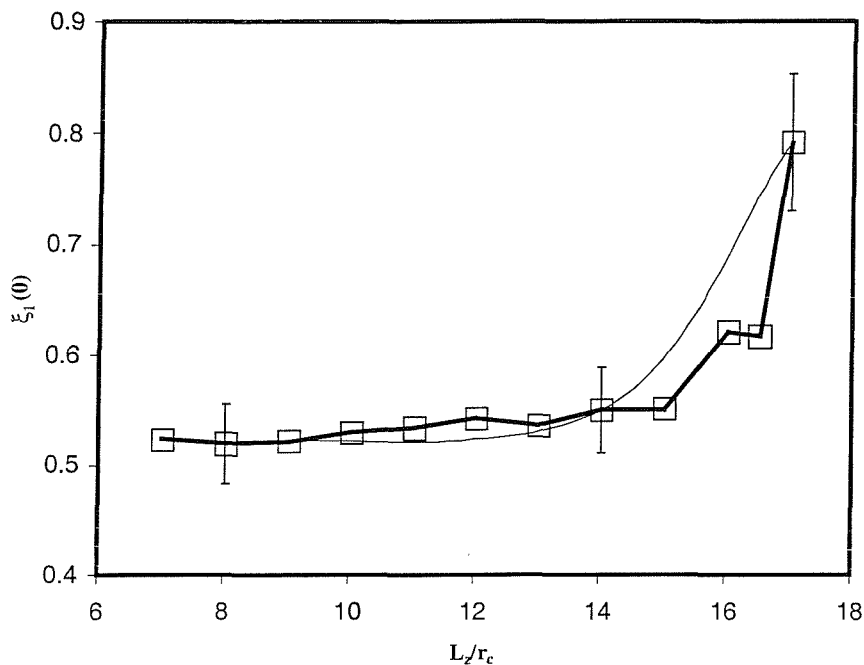


Figure 11.2. The plots of the screening length at the surface, $\xi_l(0)$, at different pore widths, L_z .

The screening length of the lower brush in the middle of the pore, $\xi_l(0)$, is calculated by using Eqn 3.16. We calculate the screening length at different compression using the velocity profiles obtained from the simulations. In Fig 11.2, we show the plot of the screening length versus pore width. The graph shows that the screening length increases with pore width. This increase becomes more rapid as the pore width reaches the value of twice the equilibrium height of the brush. This is expected as the pore width decreases, the density of the brushes in the system is increases and this results in decreasing screening length as the brushes are becoming more compact.

Fig 11.3 shows the density profiles of the lower brushes at different pore width plotted against $(z/L_z)^2$. For a parabolic profile, the plots would be linear with $(z/L_z)^2$. We also plot the profile of the system with one brush only as a comparison. The graph shows that the density profile for the one brush system is reasonably linear but shows some deviation from this behaviour. This is probably due to our choices of short chains and large grafting density so that the approximation derived by Milner *et al.*[126] is no longer valid. For the system of two brushes at the largest pore width studied ($L_z = 17.035$), the deviation is

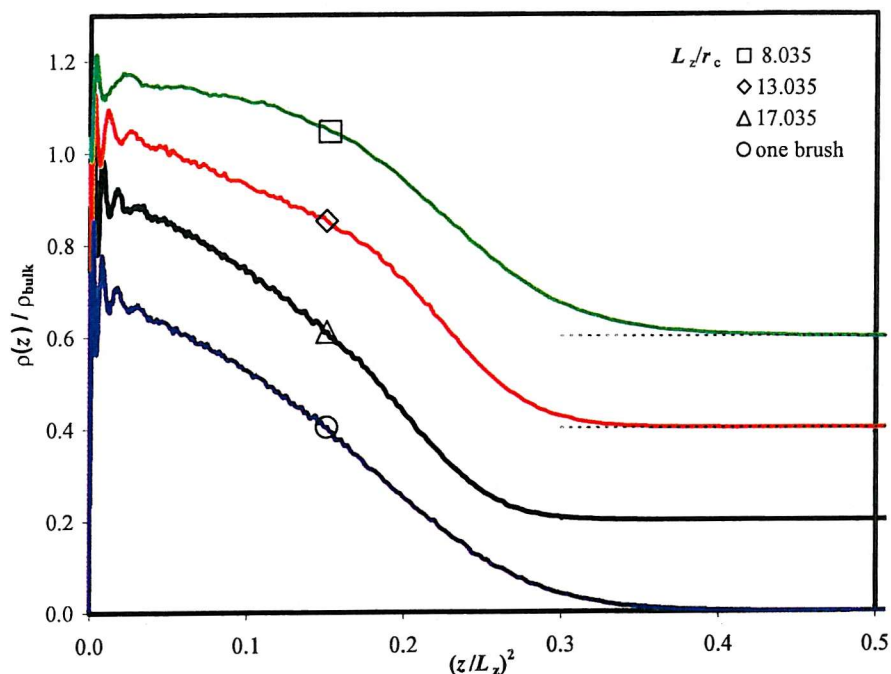
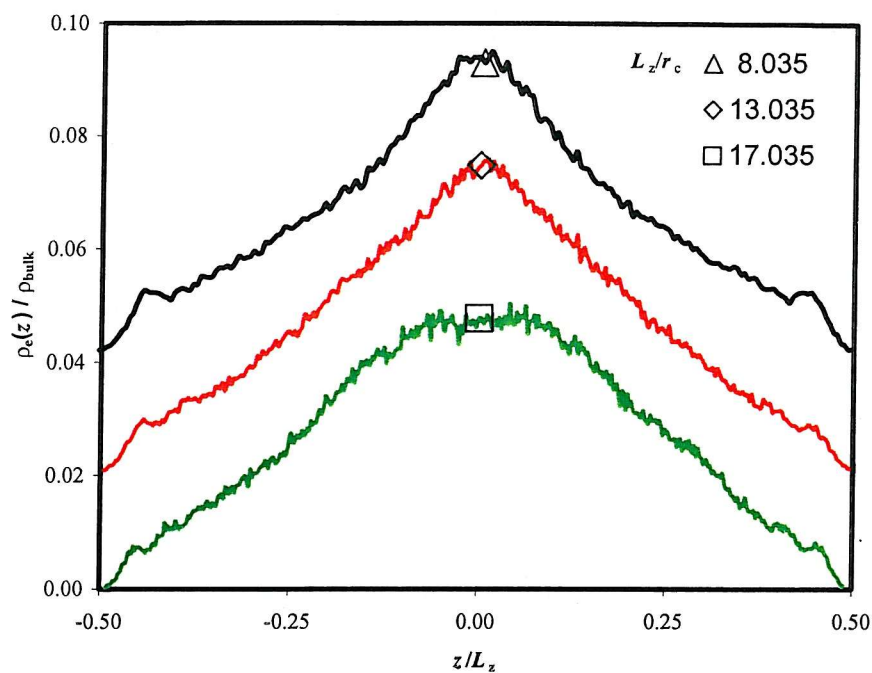


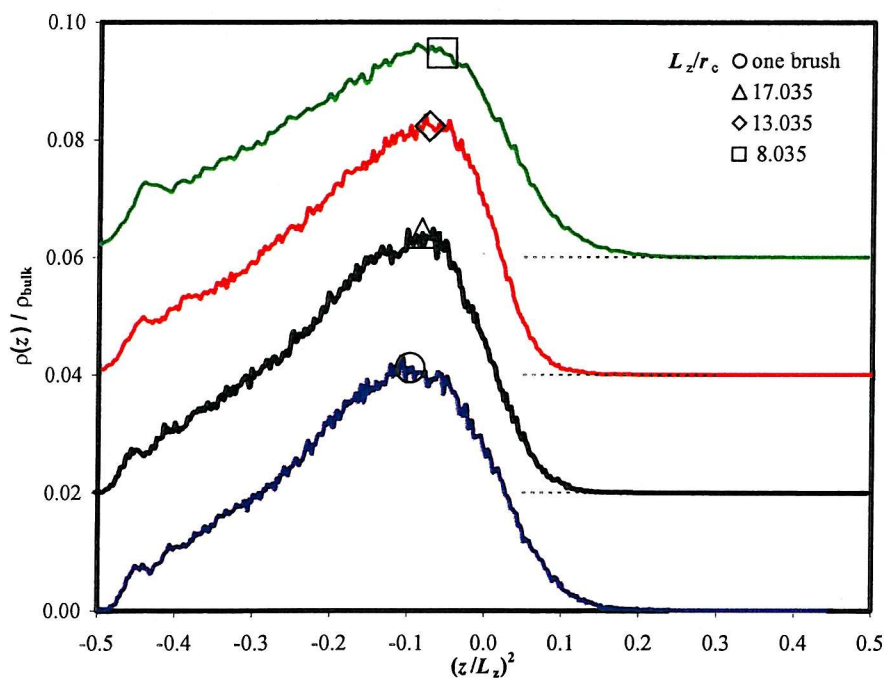
Figure 11.3. Density profiles of the lower brush at varying pore width as a function of $(z/L_Z)^2$. The profiles for L_Z equals to 17.035, 13.035 and 8.035 are shifted vertically by 0.2, 0.4 and 0.6 respectively for clearer view.

greater than the one-brush system as both brushes are close enough for the interpenetration to occur. This deviation increases as expected when the pore width is further reduced.

We plot the density profiles of the free-ends of the polymers across the pore in Fig. 11.4(a). It shows that the free-ends are concentrated in the middle of the pore. At the largest pore separation, $L_Z = 17.035$, the free-end profile is flat in the central region and as L_Z decreases, a peak appears which increases with increasing compression. The contribution of the lower brush to the free-end density profiles is plotted in Fig. 11.4(b). The plots show that for the profiles of one brush, the peaks are at a distance of 0.1 from the middle of the pore.



(a)



(b)

Figure 11.4. (a) The density profiles of the free-ends from both brushes and (b) from the lower brush only at varying pore width as a function of (z/L_z) . All the plots are shifted vertically by 0.02 from each other for a clearer view.

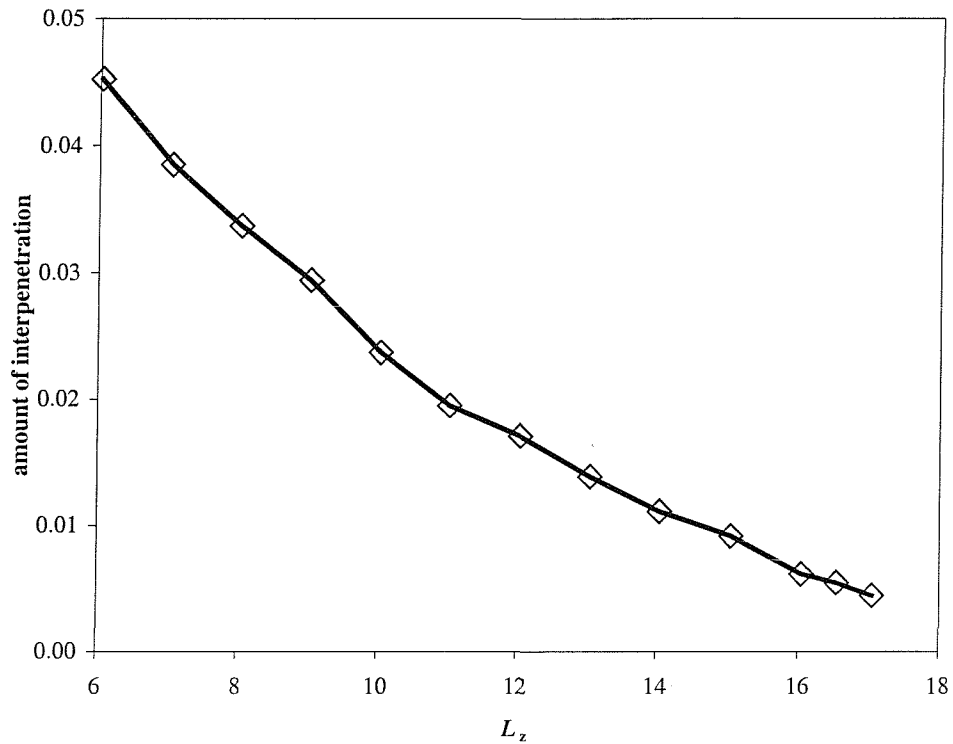
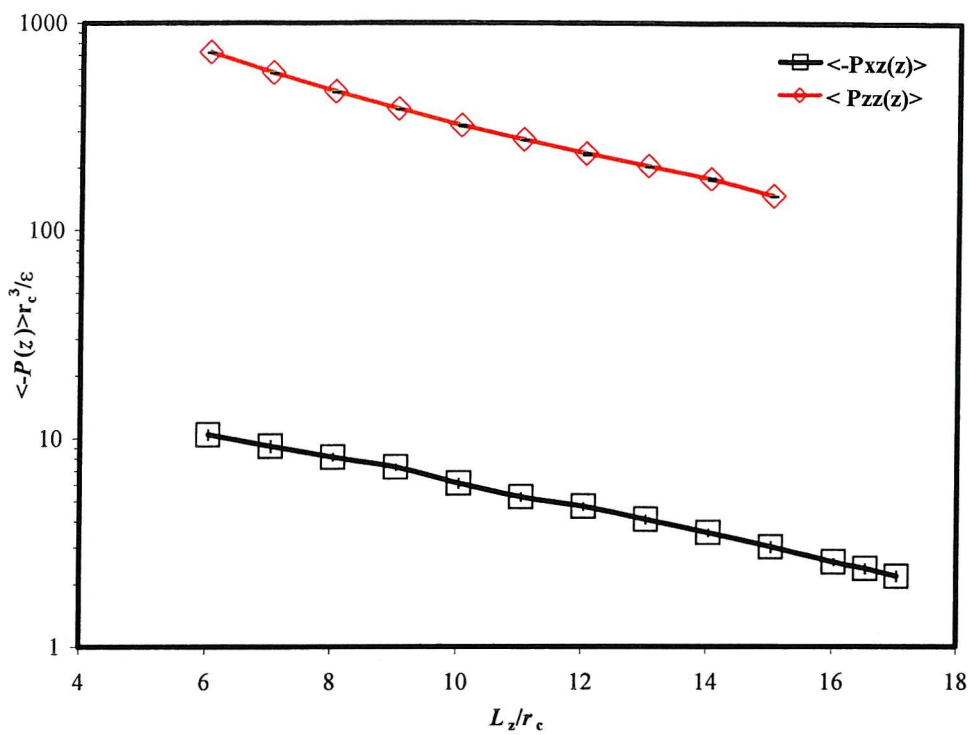


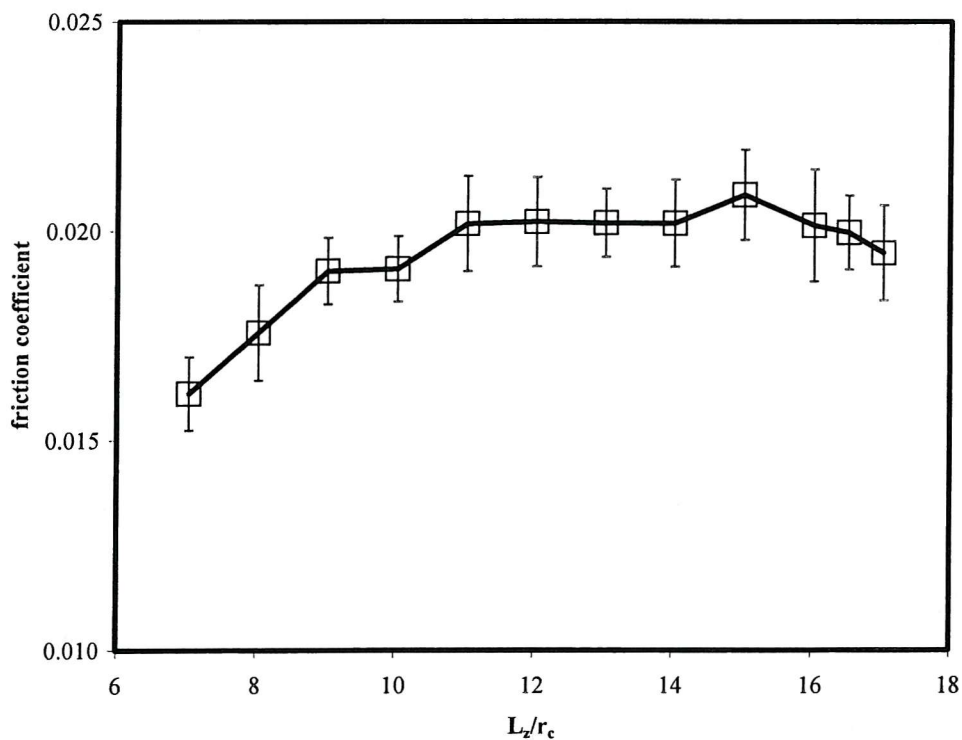
Figure 11.5. Amount of interpenetration at varying pore width for wet brushes system.

We observe that as the pore width is reduced, the interpenetration increases. Fig 11.5 shows that the amount of interpenetration is increasing monotonically as the pore reduces.

We analyse the friction coefficient and its components. We show that normal stress tensor component, P_{zz} , and off-diagonal stress tensor, P_{xz} , vary as a power-law function with pore width.



(a)



(b)

Figure 11.6 (a) The mean off-diagonal and the normal stress tensor and (b) friction coefficient as a function of pore width, L_z .

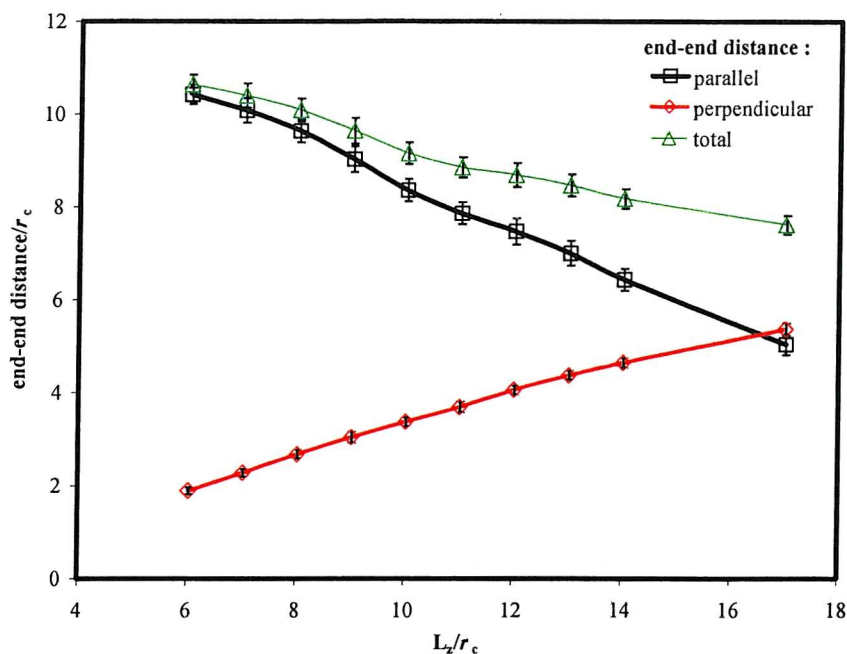


Figure 11.7. End-to-end distance with its components, parallel and perpendicular lengths, as a function of pore width for wet brushes.

The ratio between these two stress tensor components gives a friction coefficient, which agrees qualitatively with the results of experiment carried out by Klein *et al.* [141,142]. In the experiment, Klein measured those two stress tensor components for polystyrene in a good solvent (toluene) under varying sliding velocity. We plot the resulting friction coefficient, the ratio between off-diagonal and normal stress tensor in Fig. 11.6(a). The plot shows that friction coefficient does not change significantly for most of the range of pore width we are simulating. Only when the pore width is reduced to half of its original value do we see a small the reduction of the friction coefficient with pore width. This indicates insensitivity of friction coefficient to compression. This also suggests that in the wet brushes system, friction coefficient does not have a strong correlation with amount of interpenetration, which always increase with the reduction of the pore width.

Fig 11.7 shows how the end-end distance varies with pore width for wet brushes. It is clear that there is a linear reduction between the normal component of the end-to-end length with the pore separation. The repulsive interaction between these brushes causes their width to decrease. The stretching of the chains in the direction parallel to the grafting surface compensates this compression.

11.2 Dry brushes

We now present a set of simulations of the same system without the presence of the solvent particles. We follow the same procedure in which the pore separation is reduced between the simulations.

Fig 11.8 shows that density profiles for dry brushes are much steeper in comparison with the density profiles for wet brushes. Because of the absence of solvent particles, the polymer chains interact directly with each other. We obtain density profiles, which are close to the step function profiles assumed by Alexander[113]. Murrat and Grest[120] studied interaction between two brushes using molecular dynamics simulation. Their results showed that when the grafting density is high, a density profile close to a step function is attained.

Fig 11.9 shows the profiles of the free-ends. The graph shows how the profiles change as the system undergoes further compression. At large pore width, the free ends are concentrated at the outer region. As the width is reduced, the free ends are redistributed inside the brush and the peak in the profiles appears to be shifted away from the centre as the compression increases.

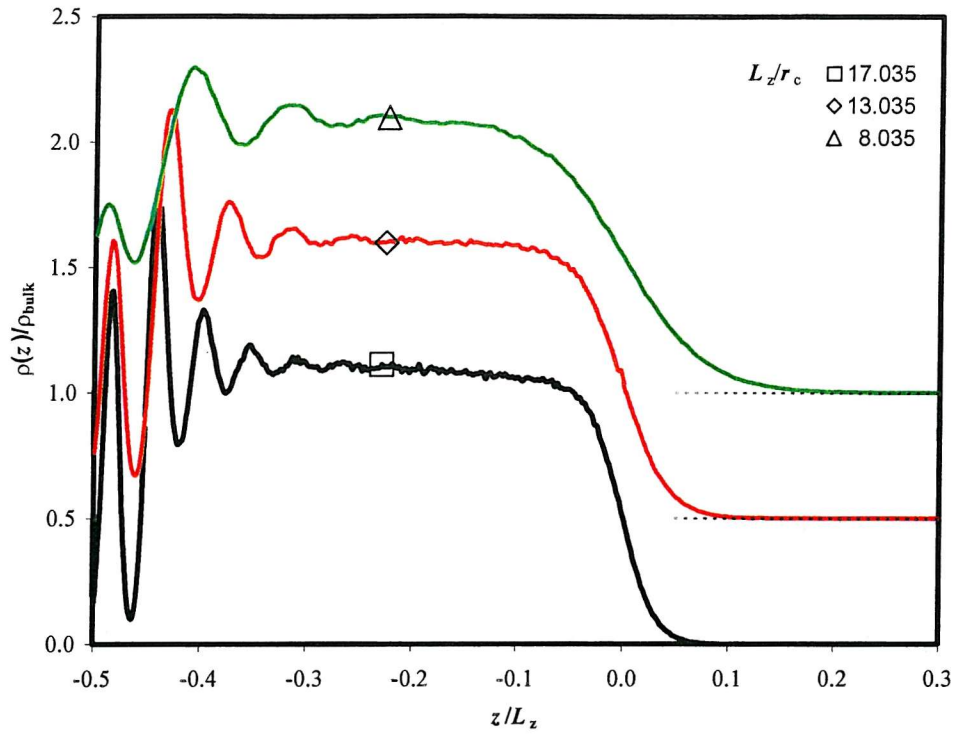


Figure 11.8. The density profiles of the lower brush at varying pore width. For $L_z = 13.035$ and 8.035 , the profiles are shifted by 0.5 and 1.0 respectively.

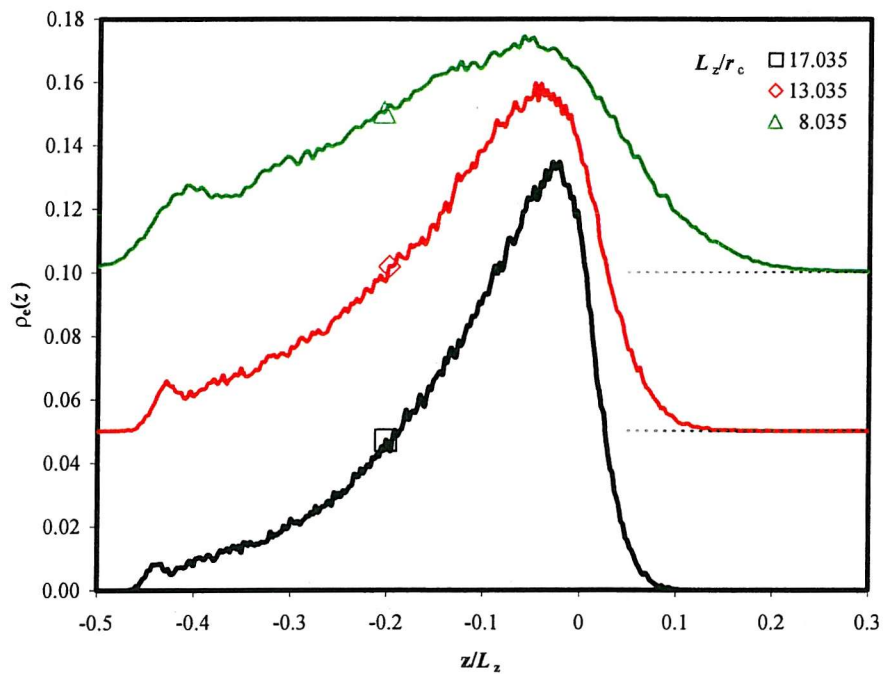


Figure 11.9. The contribution of each brush to the overall monomer density in the opposite region. For $L_z = 13.035$ and 8.035 , the profiles are shifted vertically by 0.05 and 0.1 respectively.

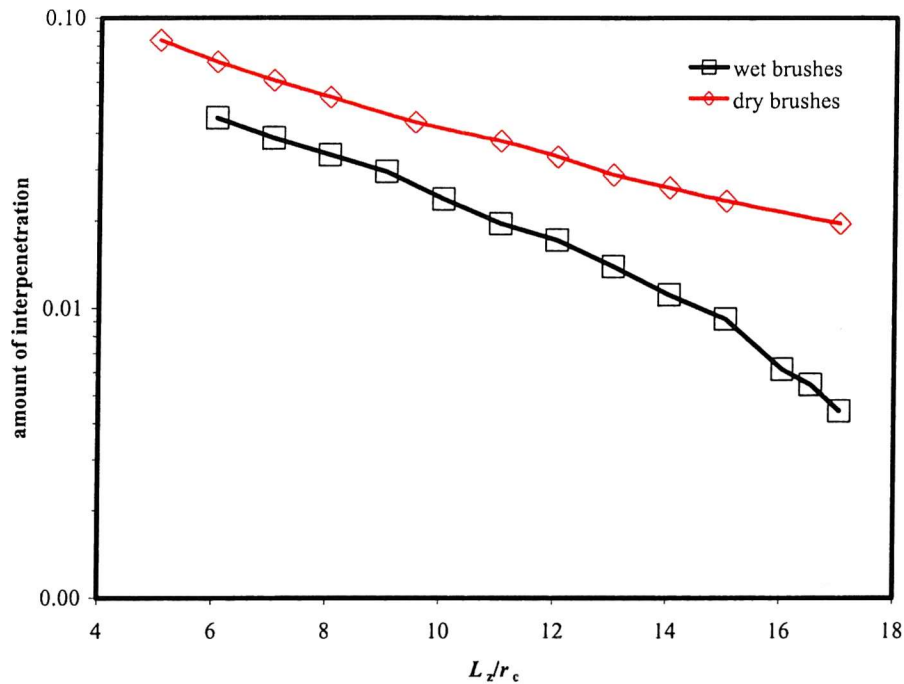
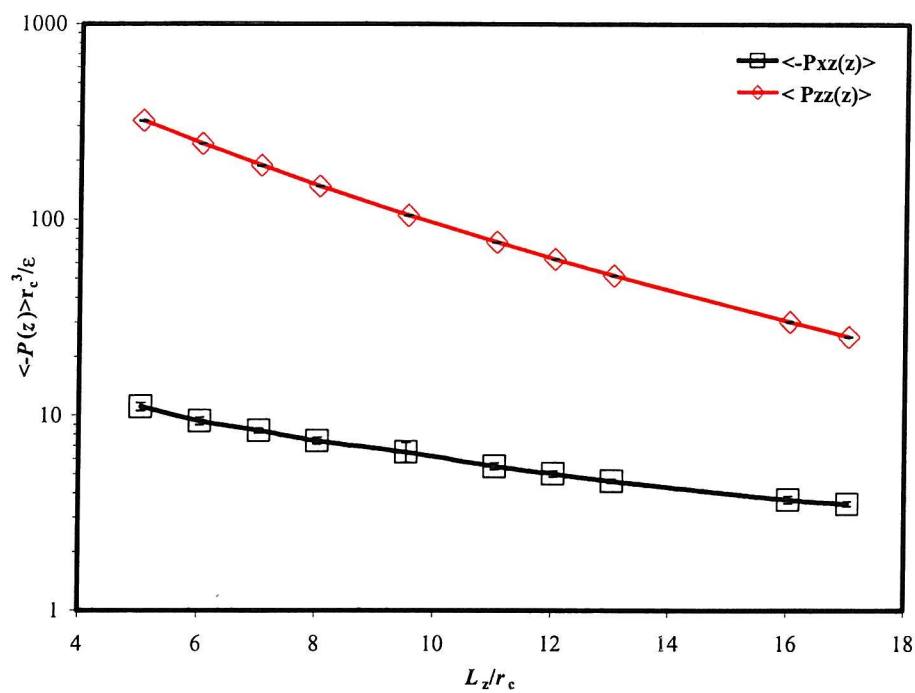


Figure 11.10. Amount of interpenetration, as calculated using Eqn. 11.1 for dry brushes and also wet brushes for comparison.

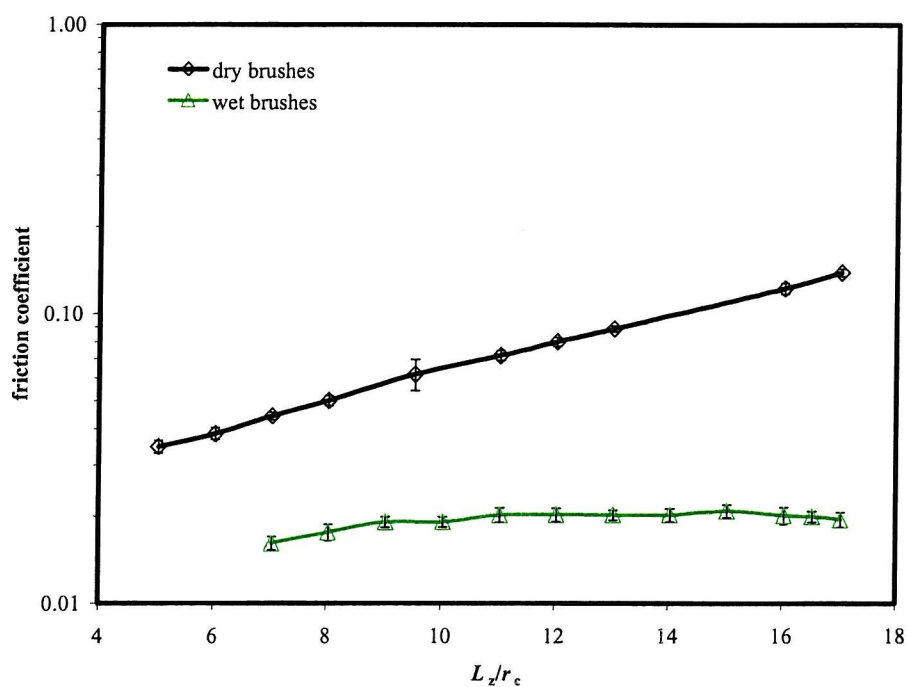
Fig 11.10 shows the amount of interpenetration for dry brushes, which increases as the pore width is reduced. We also show the plot with the wet brushes for comparison. The amount of interpenetration for dry brushes is shown to be larger than for wet brushes at all pore widths. This result is expected as the solvent particles in the wet brushes have tendency to occupy the central region and therefore reduce the brush height and interpenetration. For both systems, the amount of interpenetration is found to have a log-linear relationship with the width of the pore. A deviation from the behaviour is observed for the wet brushes at large pore width as they approach the value of twice the equilibrium height of the brushes.

The variation of the normal and off-diagonal stress tensor element with pore width is shown in Fig. 11.11(a). The graph also shows similar results for wet brushes system. A stark difference between the behaviour of wet and dry brushes is shown

Part II. Dissipative Particle Dynamics Simulation Of Polymer Brushes



(a)



(b)

Figure 11.11 (a) Off-diagonal and normal stress tensors as a function of pore width and (b) the comparison of friction coefficient for dry and wet brushes with varying pore width.

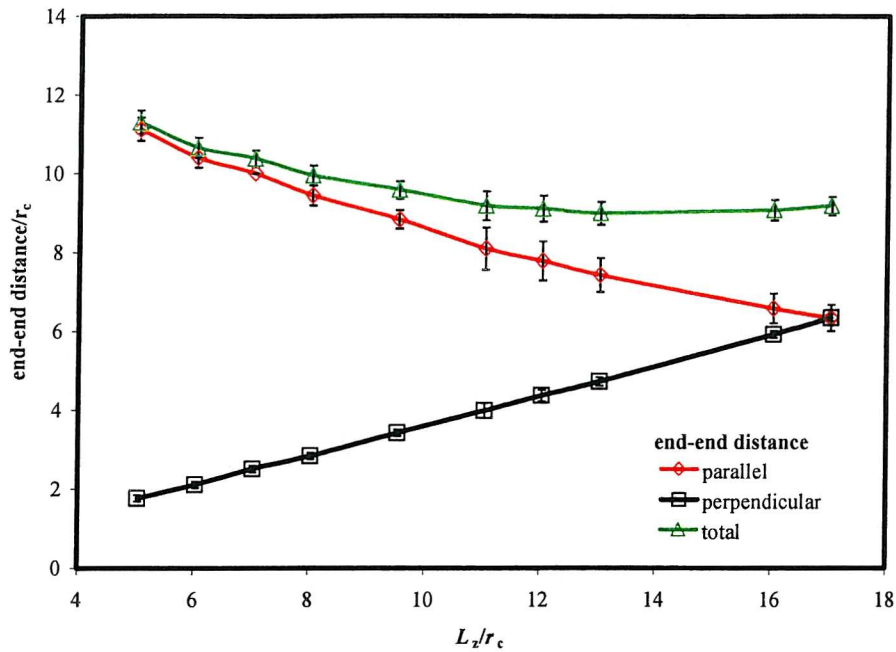


Figure 11.12. The end-to-end length with its components, parallel and perpendicular lengths, as a function of pore width for both dry brushes.

in Fig11(b). The plot shows the relationship between the friction coefficient and pore width for both wet and dry brushes. For dry brushes, friction coefficient decreases as pore width is reduced, although the values are still high when compared to those of wet brushes system. This shows that normal stress tensor increases more rapidly with compression than the off-diagonal stress tensor. This results in the apparent reduction in the friction coefficient as the system is compressed.

Fig 11.12 shows how the end-end distance varies with pore width for dry brushes. We observe a linear relationship between the normal component of the end-to-end length with pore separation.

These results show the behaviour of wet brushes as a lubricants. We calculate the friction coefficient between two brushes under shear in the presence of solvent particles and the result shows that the system are capable of maintaining the friction at a wide range of compressions. When the solvent particles are excluded from the system, the friction coefficient is significantly higher than the wet brushes system with the same pore width.

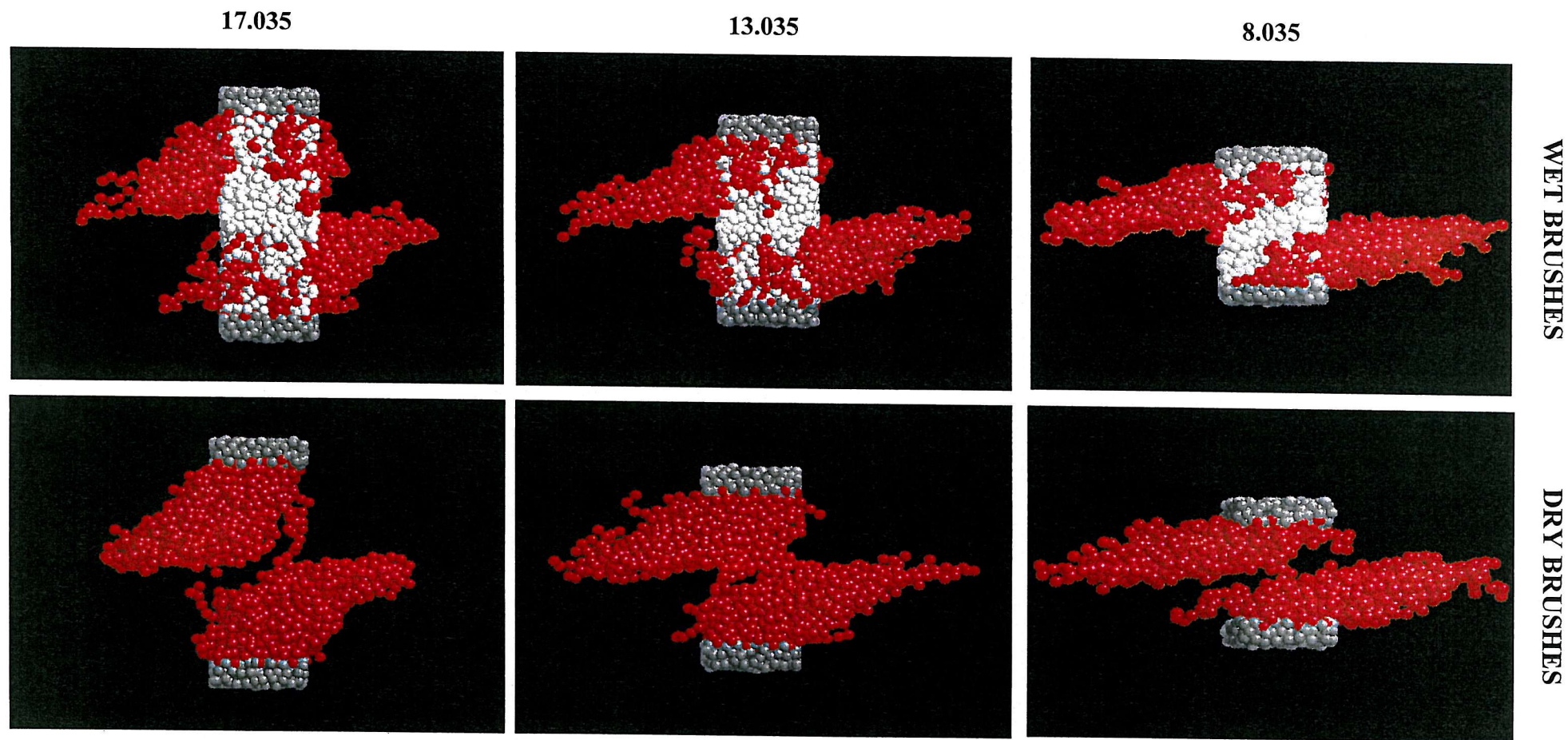
Although interestingly, the friction decreases as logarithmically as the system is compressed further, its value is still higher than that of the wet brushes. This is due to the solvent particles assisting the sliding of the brushes. The presence of the solvent particles, which are concentrated in the middle of the pore, also decreases the interpenetration between these brushes, which are thought to found a significant resistance towards the sliding movement between the brushes.

11.3 Summary

We varied the compression exerted to the system by reducing the pore width. We observe that velocity profile can still be approximated as a tanh function. We found that the off-diagonal and the normal pressure tensor are increasing with the pore width. The friction coefficient is found to be insensitive to compression, although the interpenetration between brushes is increasing monotonically.

For simulations of polymer brushes under varying compression with the solvent particles removed (dry brushes), the friction coefficient was found to actually decrease as pore width is reduced. The density profiles are also steeper in the outer region than the wet brushes at the same pore size. This is attributed to the stretching of the polymer chains in the dry brushes, which are restricted only by the flexibility of the spring and do not experience the compression exerted by the solvent particles.

Part II. Dissipative Particle Dynamics Simulation Of Polymer Brushes



● wall particles ○ solvent particles ● chain particles

Figure 11.13. Snapshots of the polymer brushes system at different pore widths.

Chapter 12

Changes of polymer brushes with solvent quality

So far, we have limited our model to simulate a system under athermal condition. This means that there are no preferences for polymer beads to interact with either solvent particles or other polymer beads. In this case, the DPD a parameter is equal for all interactions. We are also interested in studying the behaviour of brushes with solvents of varying quality. We will use the same methods employed to determine the theta solvent for a polymer in a dilute solution discussed in chapter 9. We use the same values for the like-particle interactions, $a_{\text{pol-pol}} = a_{\text{sol-sol}} = 60.0$. The solvent-monomer parameter, $a_{\text{pol-sol}}$, is varied between 30.0 and 80.0. We recall that the solvent quality is characterised using ξ , which is defined as,

$$\xi = (a_{\text{pol-sol}} - 0.5 (a_{\text{pol-pol}} + a_{\text{sol-sol}})) / a_{\text{pol-sol}}. \quad (9.3)$$

12.1 Brushes structure

Fig 12.1 shows how the density profile for the polymer beads changes as ξ is varied. When the quality of the solvent is good, the polymer beads have the tendency to adsorb solvent particles. If we improve further the quality of the solvent, the affinity of the chains towards the solvent also increases and it causes the chains to stretch. The polymer stretches until the resistance from the chains in the opposite brush is great enough to cancel the effect of the solvent. We can observe this behaviour in Fig. 12.1 where at a very negative value of ξ the density profiles do not change significantly as ξ .

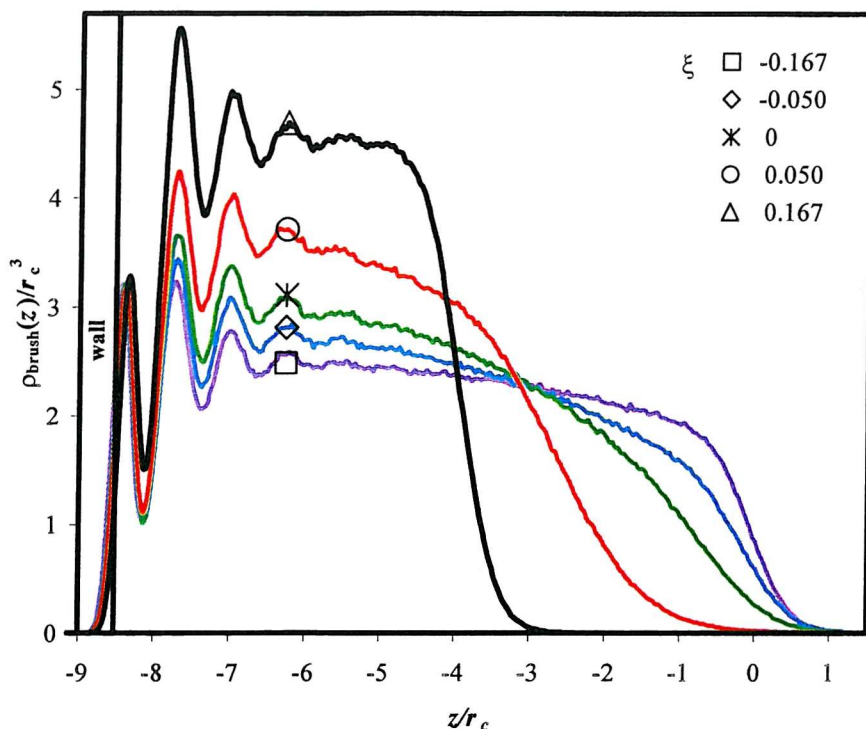


Figure 12.1. The density profiles for polymer brushes surrounded by solvent particles with varying solvent quality. Negative values denote good solvent, the more positive the number, the poorer the solvent.

If we increase ξ positively, the polymer chains and solvent particles now have a preference to be surrounded by their own species. The polymer chains will then concentrate further in the region close to grafting surface with decreasing solvent quality. It can be said that polymer chains undergo a phase separation to a polymer concentrated phase and polymer dilute (almost pure solvent) phase. The amount of interpenetration between these brushes then decreases rapidly and vanishes at $\xi \approx 0.083$ when the height of the brushes are now less than half of the pore width. This shows that the transformation of the brushes from the stretched to compressed state occurs at a narrow gap around the athermal condition, $\xi = 0.0$.

This is shown in Fig. 12.2 where the profiles of free-end density are plotted with varying solvent quality. When the value of ξ is negative, the free ends have the highest density in the region close to the middle of the pore. With the reduction in solvent quality, the free ends are redistributed within the brushes and the region with

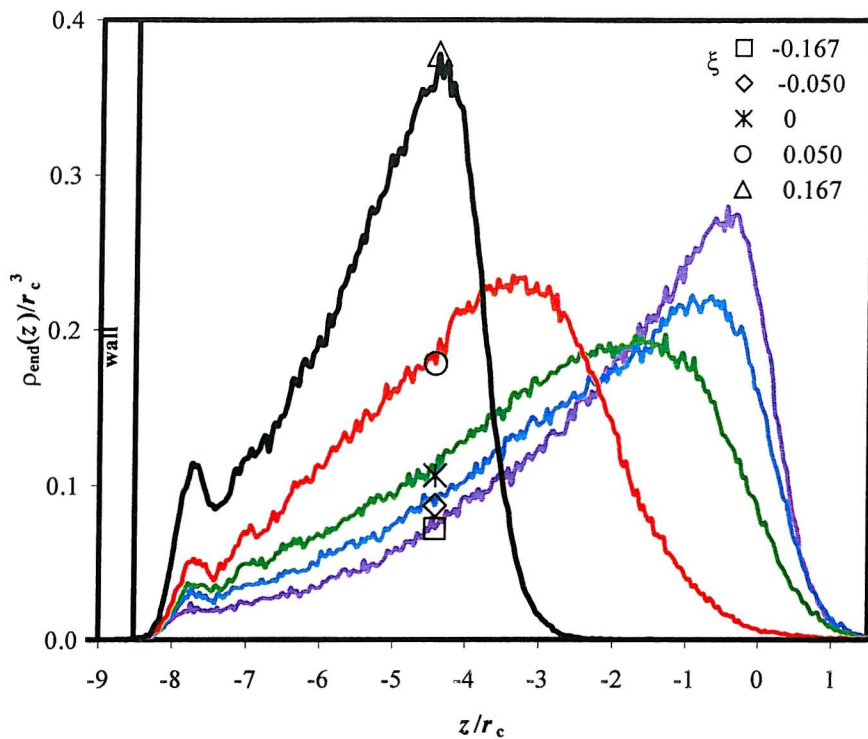


Figure 12.2. The density profiles of free ends polymer brushes with varying solvent quality.

highest free ends density is drawn away from the central region. The trend continues until ξ becomes positive and the most rapid change of free-ends profiles occurs when ξ is 0.0. The peak in the profile also decreases and reaches a minimum at the athermal condition. For poor solvents, the region with the highest free ends density is still drawn away from the central region, but this shift is now coupled with the collapse of the brushes. The collapse of the brushes continues until the excluded volume interaction prevents the height of the brushes from decreasing further. Beyond this point, further reduction in solvent quality does not shift the peak in the free-end density profile towards the grafting surface, but there are still some redistribution of the free-ends, which is observed in the increase in the peak height.

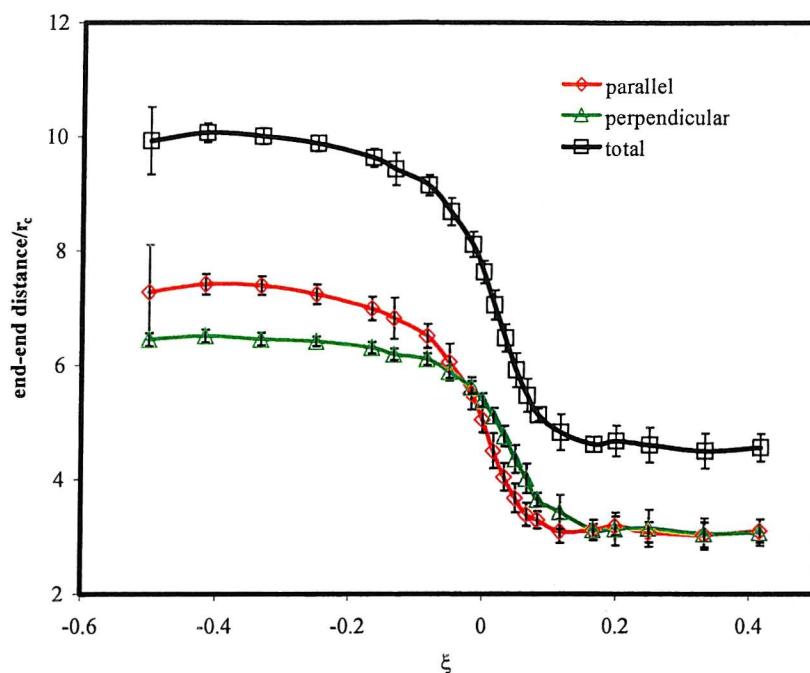


Figure 12.3 End-to-end distance as a function of solvent quality.

Fig 12.3 shows the graphs of the end-to-end distance with changes in solvent quality. The curve shows that when the solvent is very poor or very good, the end-to-end distance is insensitive to solvent quality. For systems with good solvent, the polymer chains stretch and the values for the end-to-end distance are relatively constant for very good solvent. In the poor solvent condition, the chains collapse and as the shear flow does not penetrate far into the brush, the chain configuration within the brush is not strongly affected by the shear. Hence the end-to-end distance are also constant for the range of poor solvent quality we simulate. In between these regimes we observe a narrow collapse transition, which we also found in the plots of interpenetration and friction coefficient.

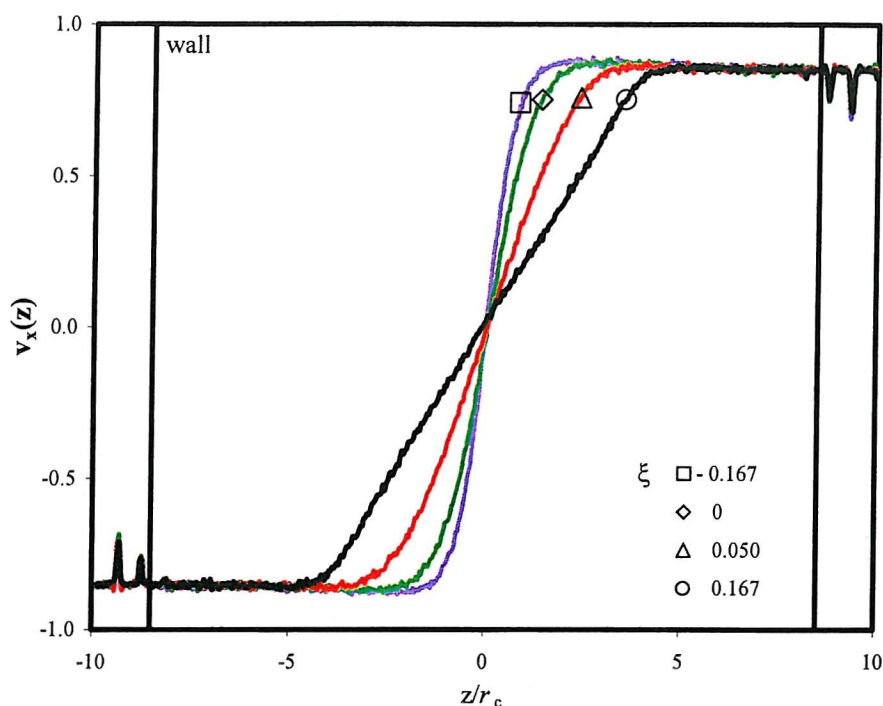
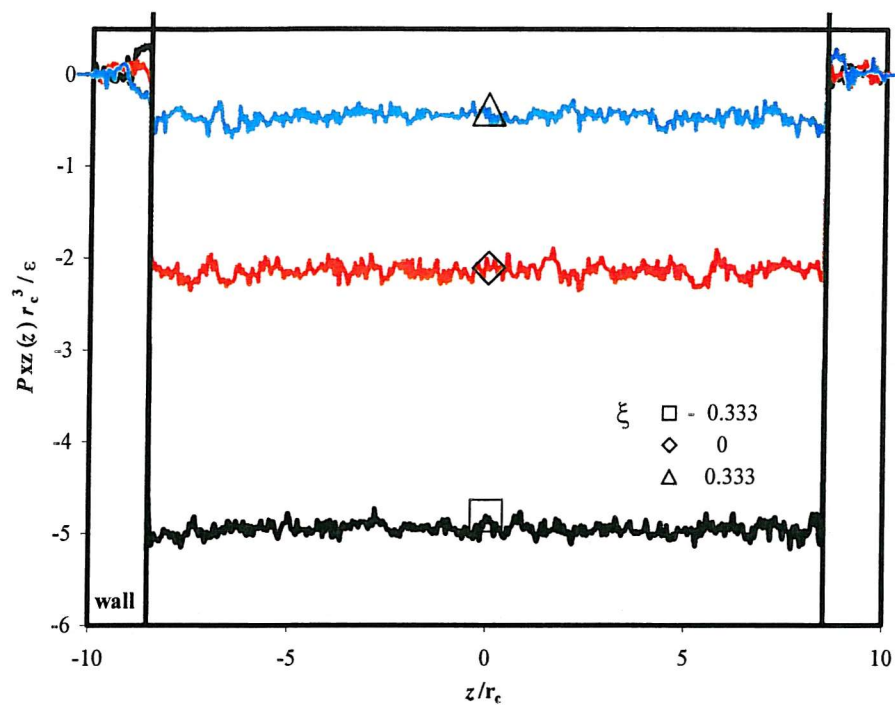


Figure 12.4. The velocity profiles for polymer brushes surrounded by solvent particles with varying quality.

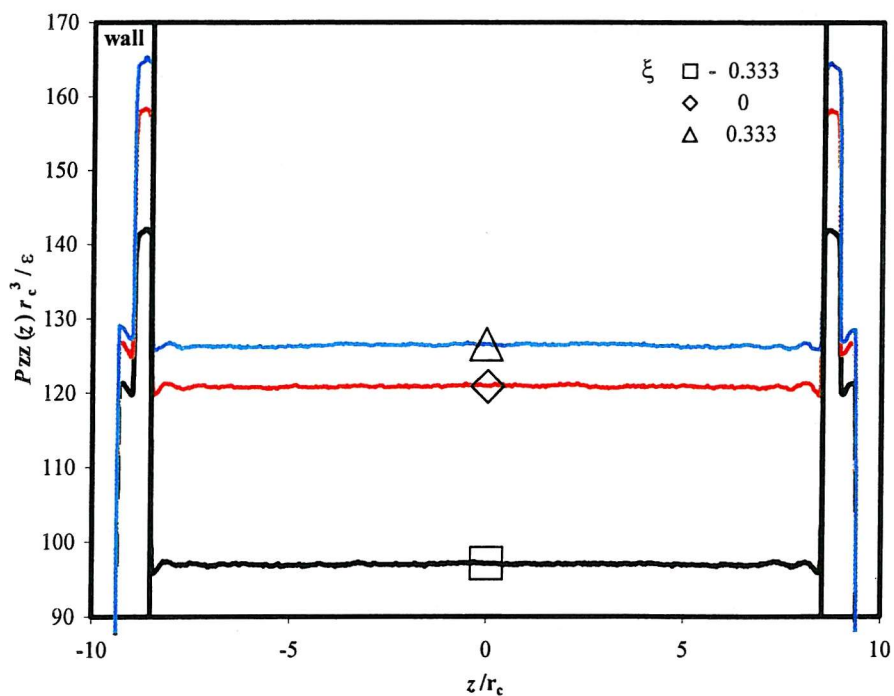
12.2 Rheological behaviour

Fig 12.4 shows the changes in velocity profiles with varying solvent quality. We can see that there are regions where the net velocity does not deviate from the wall velocity. This demonstrates the behaviour of polymer brushes are as extensions of the walls. The solvent particles, which diffuse into these regions, will be frozen and they will be dragged by the surfaces as they are sheared. When the solvent is good, these regions extend further towards the central region. The trend continues with the increase in solvent quality and hence the profile becomes steeper close to the middle of the pore.

If we make the solvent poorer, the velocity profile changes shape and becomes steeper. Poor solvent quality causes the solvent and polymer chains to phase separate and create two polymer-rich regions close to surface and a solvent-rich region separating them. The velocity inside the polymer-rich region is constant and equal to the wall velocity, denoting the solid-like behaviour of the brushes. The profile inside the solvent-region is linear. The bulk viscosity of the solvent determines the tangent of this straight line.



(a)



(b)

Figure 12.5. (a) The off-diagonal and (b) normal stress tensor profiles for polymer brushes system with varying solvent quality.

We consider the changes in the stress tensor components with solvent quality. First, we show that the normal and off-diagonal stress tensors are constant across the pore. Fig 12.5a and 12.5b shows the off-diagonal and normal stress tensor profiles at three different value of ξ , representing the system of brushes immersed in poor solvent, neutral solvent and good solvent. We then calculate the averages of these stress tensor components over the simulation time and also the pore width.

Fig 12.6 shows the normal and the off-diagonal stress tensor as a function of solvent quality. If we look at the changes in normal and off diagonal stress tensor as solvent quality is varied, there is a noticeable difference between these two profiles. The curve for off-diagonal stress tensor or shear stress is shown to be constant in poor solvent. It rises steeply at values close to athermal condition and then increase slowly with further improvement in solvent quality. The plot for normal stress tensor reveals that its value is slowly decreasing when the solvent is poor. The rate of reduction is then shown to increase in the good solvent regime. This can be explained by looking at the interaction between particles in the system. In poor solvent, the majority of interactions are between particles of the same species. The interaction between particles of different species only occurs in the interfacial region. This is the reason why normal stress tensor is rather insensitive towards solvent quality in the poor solvent regime. When the solvent in the system is good and the concentration of polymer chains is comparable to the solvent, the interactions between different species become important in determining the stress of the system.

Therefore the normal stress tensor is more sensitive to the solvent quality in the good solvent regime, than in the poor solvent regime. It should be noted that when the value of ξ is low, there is a region of low density occurs in the boundary between polymer-rich and solvent-rich region.

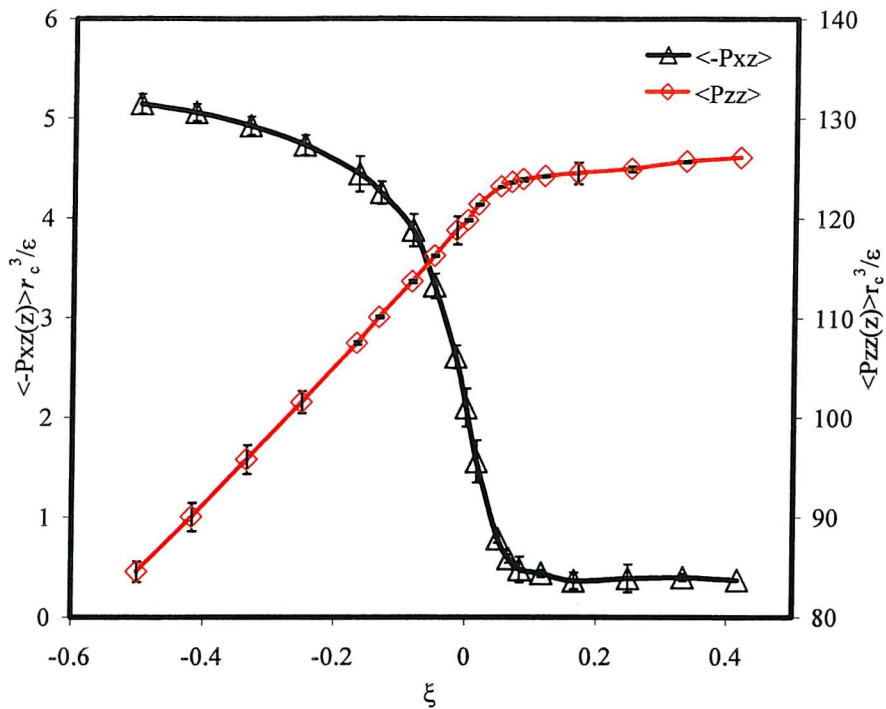


Figure 12.6 The averages of normal and off-diagonal stress tensor of polymer brushes as a function of solvent quality.

Fig 12.7 presents the change in friction coefficient as solvent quality is varied. The figure shows that when the brushes are mixed with poor solvent, the friction coefficient is very low and its value remains unchanged for most of the range studied. This is simply because when solvent quality is poor, there are three regions in the system; two polymer-rich region close to the walls and a solvent-rich region the middle of the pore. The absence of interpenetration between these brushes and the therefore existence of almost pure solvent region separating the brushes result in a very low friction coefficient. Close to the athermal solvent, the friction coefficient starts to rise steeply as the polymer chains stretch and creates some overlap with the chains from the opposite brush. The friction coefficient keeps increasing as the solvent quality is increased further below the athermal condition, although at a slower rate. These changes in the friction coefficient are more significant than those induced by changing the shear rate or compressing the system to a lower pore width.

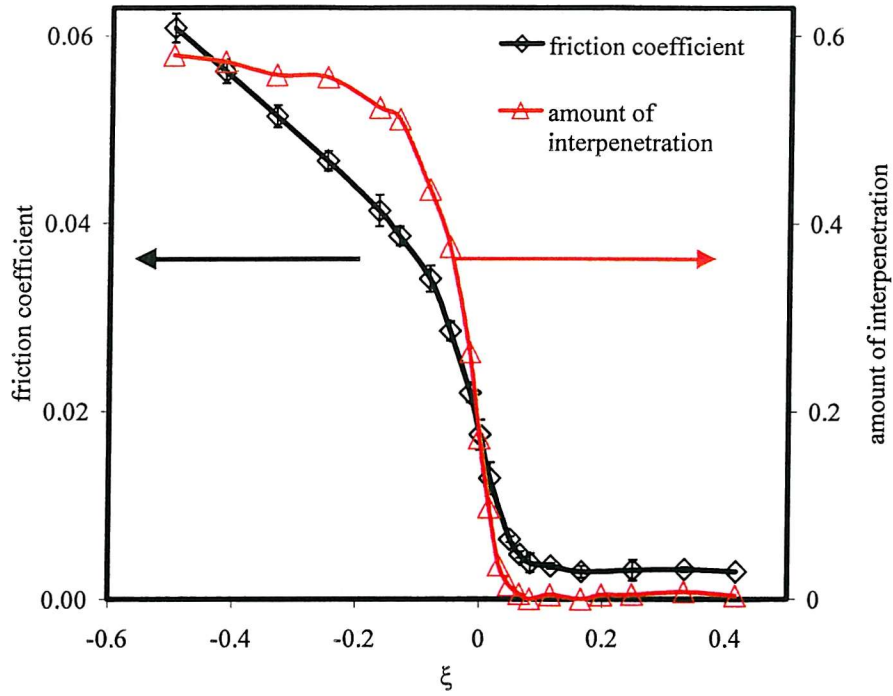


Figure 12.7. The friction coefficient and the amount of interpenetration as a function of solvent quality

For poor solvents, this phase separation behaviour can be quantitatively described by calculating the surface tension. It has been established by Kirkwood and Buff, and subsequently Irving and Kirkwood, that the surface tension is directly related to the difference between lateral and vertical components of the stress tensor. For a planar interface, the surface tension can be simply expressed as an integral of this difference over the region of interface:

$$\sigma_{\text{int}} = \int \left[p_{zz} - \frac{1}{2}(p_{xx} + p_{yy}) \right] dz \quad (12.1)$$

Where σ_{int} is the surface tension and p_{xx} , p_{yy} and p_{zz} are the xx , yy and zz components of the stress tensor.

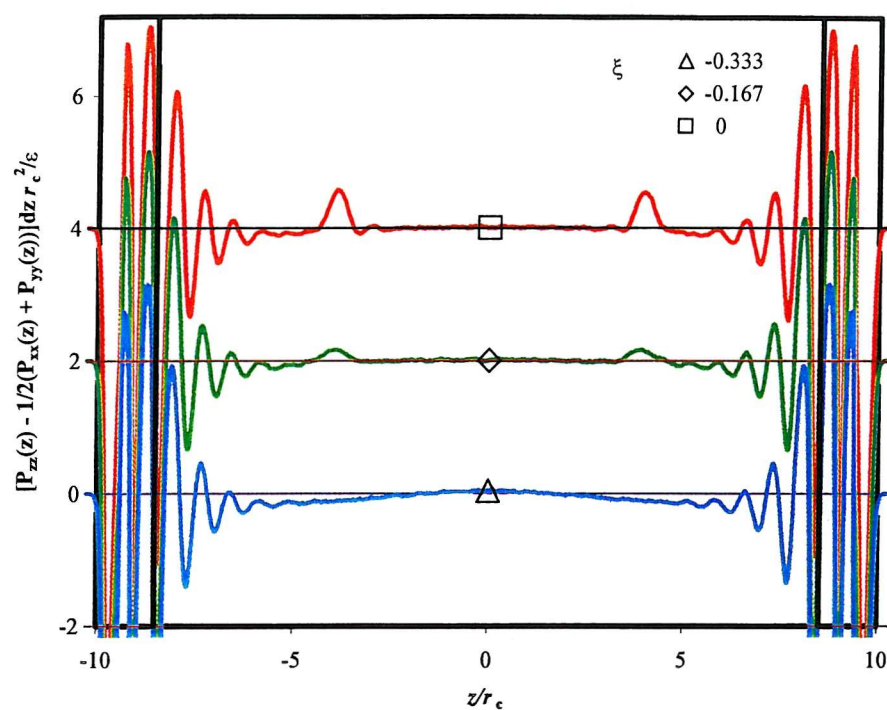


Figure 12.8 Profiles of integral of difference between lateral and vertical components of stress tensor at different solvent quality, measured in ξ . The profile for $\xi = -10$ and -20 are shifted by 2 and 4 respectively.

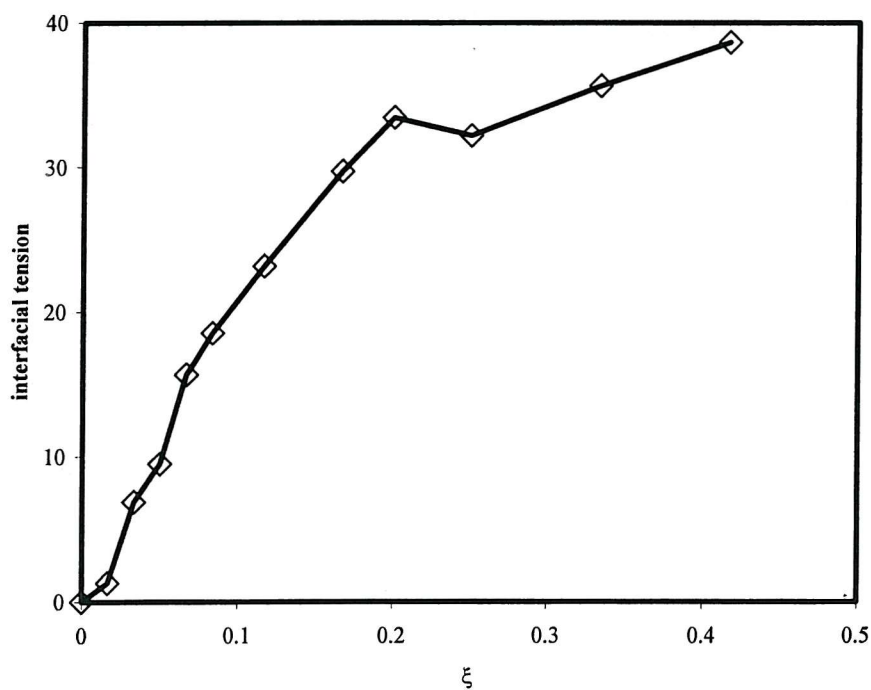


Figure 12.9. Surface tension as a function of solvent quality.

If we look at the profile of stress tensor difference in Fig 12.8, we observe that the resulting integral for this profile across the whole section is less than zero, even for poor solvents. We can also observe the surfaces separating polymers and solvents which are clearly identified. This is caused by the effect of polymer attached onto the grafting walls. To exclude the wall effects in the calculation, we will then subtract the integral for poor solvent results and scale it such that surface tension for athermal condition will be equal to 0. The resulting surface tension, which describes the tension at the polymer-solvent interface, is shown in Fig. 12.9. As expected, the graph shows that the surface tension increases monotonically with decreasing solvent quality.

12.3 Summary

We varied the solvent quality and observed a phase separation between the brushes and the solvent particles as the solvent quality is decreasing. A collapse transition of the brushes from a fairly stretched to compressed geometry is observed over a narrow range of solvent quality parameter in the simulations.

The velocity profile becomes steeper in a poorer solvent. In poor solvent, the velocity inside the polymer-rich region is constant and equal to the wall velocity, denoting the solid-like behaviour of the brushes. Because of the absence of interpenetration between the brushes, the friction coefficient for brushes in poor solvent is very low. Increasing the solvent quality results in the rise of the friction coefficient as the polymer chains stretch and create some overlap with the chains from the opposite brush. These changes in the friction coefficient are more significant than those induced by changing the shear rate or compressing the system to a lower pore width. The resulting surface tension decreases monotonically with increasing solvent quality.

Part II. Dissipative Particle Dynamics Simulation Of Polymer Brushes

Good solvent

($\xi = -0.33$)

Good solvent (athermal)

($\xi = 0.0$)

Poor solvent

($\xi = 0.33$)



● wall particles

○ solvent particles

● chain particles

Figure 12.11. Snapshots of the polymer brushes system at different solvent quality

Chapter 13

Conclusions

This thesis reports the application of mesoscale modelling technique to study of the behaviour of complex fluids. We demonstrated their usefulness in the areas where conventional molecular simulation is not applicable due to the size, complexity and long relaxation time of such systems. We gave a brief introduction of two techniques of mesoscopic modelling, the Brownian dynamics method and the dissipative particle dynamics method. Both techniques use the Langevin equation to describe the motion of the particles. The Brownian dynamics method represents the case where the solvent particles can be described implicitly. On the other hand, in the dissipative particle dynamics, we included the solvent explicitly along with other components in the simulation. Both parts of the theses are self-contained and here we summarise the general results and consider several possible extensions of the study for future research.

13.1 Part I: Brownian dynamics simulation of colloidal particles in ionic solution

In the first part of theses, we employ the Brownian dynamics method to study the aggregation of colloidal particles in an ionic solution. The model is simplified by describing the colloidal particles as spherical. We use the DLVO potential to describe the interaction between the colloidal particles in ionic solution.

In chapter three, we performed a preliminary study to construct the phase diagram of our system using perturbation theory. Based on this calculation, we specify the range of parameters to use in the simulations. The range of the simulation is chosen to ensure that we may explore the dispersed or fluid phase down to unstable region below the spinodal line.

Conclusions

In chapter five, we studied the effect of changing the ionic concentration on the behaviour of the colloidal solution. The simulation results show the behaviour predicted by the perturbation theory. The model shows that the behaviour of the system is very sensitive to the ionic concentration. The concentration of the ions in the solution determines the strength of the repulsive electrostatic interaction, which can be calculated using the DLVO equation. A weaker repulsion will result in the van der Waals attraction becomes more dominant and the effective interaction becoming more attractive. A change in the order of 10^{-4} mol/l may result in the colloids aggregating or stay dispersed within the simulation run as we have observed for systems at $\kappa = 210^{-1}$ and $220\sigma^{-1}$. This insight is important in determining the best condition for processing product that involves complex fluids.

If the colloidal interaction becomes more attractive, the phase diagram predicts that the suspension will be in the unstable region where it will phase separate. For a suspension quenched above the binodal line, no nucleation is observed. This is also reflected in the corresponding plot of the structure factor where only a small fluctuation is observed at small k .

A transition can be observed in the system quenched to just below the solid-fluid binodal line. In this case, the suspension is fluid at the early stage. At some intermediate time, a cluster whose size exceeds some critical value forms in the suspension. This is observed in the peak formation in the plot of structure factor. This peak initially increases as the simulation progresses and shifts toward smaller k and is related to the growth of the mass and size of the clusters within the system. The rate increase of k_{\max} corresponds to κ . In the later stages, the clusters become sufficiently large such that they can only progress further by interconnecting with their neighbours to form a gel structure. This is observed by the slow down of the rate increase of k_{\max} at some later stage when a gel structure is established. The rate of the shift for the peak is largely independent of κ at early stages. At later stage, the rates for systems of larger κ decrease, while at smaller κ , this is not observed. We observed that the transition point where the critical nucleus appears occurs at earlier time for the deeper quench and for a system quenched well below the binodal line, the nucleation is observed instantaneously.

Conclusions

Once a gel is formed, the mobility of the colloidal particles decreases rapidly and at the largest value κ , almost 99 % of the particles are stationary. For suspensions close to the binodal line, we found that the particles are still mobile enough to induce a rearrangement within the structures. The structures become more compact at a more rapid rate as the gel ages. This can be seen in the average number of nearest neighbours which are higher for system close to the binodal line. We also analyse the fractal dimensionality for the gel structures and found that a smaller dimension is observed for systems of smaller κ .

We study the mechanical strength of the gel by measuring the shear modulus at equilibrium and at high frequency. This is accomplished by carrying out a step-strain simulation at several gel ages. We found that all gels are easily disrupted by applying a small strain into the structures. All the gels lose their linear elastic behaviour when subjected to strain larger than 1 %. The shear modulus at high frequency measures the stiffness of the gel structure. The equilibrium modulus, which measures the solid-like characteristic of the gel, is also found to depend on the strength of the attraction. A different stress decay is also observed for the gels which depends on the depth of the quench. A shallow quench just below the binodal line results in a more compact structure and the corresponding stress decays as a power-law function of time. A deeper quench will induce a less ordered local structure. The stress decay for the gels in this system is then similar to that of a fluid, which decreases as a power-law function of time. Although in fluids, the stress will decay to zero while the gels decay to some constant, which is the equilibrium modulus.

In chapter six, we showed the effect of the suspension density towards the structures and their mechanical strengths. The gel networks are produced when the systems are within the unstable region which imply the importance of the spinodal decomposition in the gel formation. When a gel is formed, the movement of the colloidal particles decrease considerably and the distribution profiles of the displacement show that most particles may hardly move at later stages.

The simulation shows that when the gel does not form, the colloidal particles remain

Conclusions

highly mobile. This can be seen in the displacement profiles, which show a broad distribution for systems at small volume fractions. At low volume fraction, the average number nearest neighbour is also smaller and we show that there is large fraction of isolated particles which are highly mobile.

The structure factors reveal that at early stages, all systems form clusters of similar size which evolve further to aggregate and form larger clusters. This is shown in the peaks which shift to smaller k at the same rate for all systems. The gels are only formed when these clusters are close enough to form an interconnecting structure with their neighbours. In a dilute system, even when the structures of the cluster are more open as suggested by the peaks of the structure factor at large wavelength and by their fractal dimensionality, the resulting size may not be large enough for them to form a percolating structure. Hence we show that a gel is only formed in suspension of more than 15 % volume fraction. We show that the fractal dimensionality is lower for suspension of low volume fraction.

The decay rates of the modulus are found to be unchanged as the systems evolve. In all system the decays follow a power-law function of time. This reveals that the structures are highly disordered at short range. G_{∞} increases as a power law function of the volume fraction at most times, although the exponent is shown to decrease as the simulation progresses. Clear differences in the behaviour between the gel and the non-gel systems are observed in the resulting equilibrium shear modulus. In the non-gel systems, the stress decays to zero after some times which shows that the systems can not sustain the stress. Once the gel is formed, the systems will have a non-zero G_{eq} and this imply the solid-like behaviour exists in the systems. This value rapidly increases with the increasing density of the suspensions.

13.2 Part II: Dissipative particle dynamics simulation of polymer brushes

In the second part of the theses we present the study of the behaviour of polymer brush system using DPD. In the simulation, two grafted polymer layers are brought into close contact and moved under shear in the direction parallel to each other. We study the behaviour with varying shear rates, pore separation and solvent quality.

In chapter ten, we report the simulation under different shear rates. The density profile of the brushes shows the parabolic profiles which are in agreement with the self-consistent field theory. The brushes are close enough to experience interpenetration. The interpenetration is greater for lower shear rates. This is because the polymers stretch in the presence of shear flow and the brushes are compressed. The velocity profiles can be fitted to a tanh function where the velocity does not change significantly across most part of the pore but there is a steep change around the middle of the pore.

The viscosity is not constant at any point relative to the surfaces due to the effect of the polymer chains providing resistance to the solvent's movement. The viscosity is lowest in the middle of the pore where the solvent is at the highest concentration. The viscosity decreases as the shear rate is increased and this agrees with the shear thinning properties observed in other simulations and experiments. The screening length for the brushes is calculated using velocity profiles, which can be approximated as a tanh function. We found that screening length varies exponentially with density.

In chapter eleven, we varied the compression exerted on the system by reducing the pore width. We observe that velocity profile can still be approximated as a tanh function. We found that the off-diagonal and the normal pressure tensor are increasing exponentially with the pore width. The friction coefficient is found to be insensitive to compression, although the interpenetration between brushes is increasing monotonically. We calculate the friction coefficient in the wet brushes system under shear and show that the systems are capable maintaining the friction at a wide range of compressions. When the solvent

Conclusions

particles are excluded from the system, the friction coefficient is significantly higher than the wet brushes system with the same pore width. Although interestingly, the friction decreases as exponentially as the system is further compressed, its value is still higher than that of the wet brushes. This is due to the solvent particles which act to assist the sliding of the brushes. The presence of the solvent particles, which are concentrated in the middle of the pore, also decreases the interpenetration of the brushes, and provide a significant resistance towards the sliding movement between the brushes.

For simulations of polymer brushes under varying compression with solvent particles are removed (dry brushes), the friction coefficient was found to actually decrease as pore width is reduced. The density profiles are also steeper in the outer region than the wet brushes with the same pore size. This is attributed to the stretching of the polymer chains in the dry brushes, which are restricted only by the flexibility of the spring and they do not experience the compression exerted by the solvent particles.

In chapter twelve, we varied solvent quality and observed a phase separation between the brushes and the solvent particles as the solvent quality is decreasing. A collapse transition of the brushes from a fairly stretched to compressed state is observable over a narrow range of solvent quality parameters.

The velocity profile becomes steeper in a poorer solvent. In poor solvent, the velocity inside the polymer-rich region is constant and equal to the wall velocity, denoting the solid-like behaviour of the brushes. Because of the absence of interpenetration of the brushes, the friction coefficient for brushes in poor solvent is very low. Increasing solvent quality results in the rise of the friction coefficient as the polymer chains stretch and create some overlap with the chains from the opposite brush. These changes in the friction coefficient are more significant than those induced by changing the shear rate or compressing the system to a lower pore width. The resulting surface tension decreases monotonically with increasing solvent quality.

13.3 Future research

Several new directions have been identified following the results presented in this thesis. For the colloidal suspensions studies, it would be interesting to extend the study to include the effect of shear flow and to describe the hydrodynamics effects in more detail. It has been known for some time that the aggregation phenomena is sensitive to the actual shape and the roughness of the colloidal particles. In our studies the colloids are crudely represented as smooth spherical particles. Currently it will be too expensive to incorporate a more complicated description of particle's surface.

In terms of further attempts to understand the interaction between polymer brushes, it would be interesting to see whether a spherical surface will effect the flow of the solvent particles through the brush. This would be a more suitable model of polymers grafted onto colloidal particles. Other interesting modifications would be to make the model more realistic are by putting free polymers in the system or by specifying the polymers to be branched rather than linear.

In conclusion, we show that the mesoscale modelling technique can reveal many insights in the behaviour of complex fluid that is not possible to study using typical molecular modelling techniques. In the future we can expect further progress in the fields as it matures and the availability of a more powerful computer for future work which enable us to study these systems under a more complex conditions.

References

1. M.P. Allen, and D.J. Tildesley, *Computer Simulation of Liquids*, Clarendon Press, Oxford, (1993).
2. D. Frenkel and B. Smith, *Understanding molecular simulation*, Academic Press, San Diego (1996).
3. J. Israelachvili, *Intermolecular and Surface Force*, Academic Press, San Diego (1992).
4. P.G. de Gennes, *Scaling concepts in polymer physics*, Cornell University Press, Ithaca, NY (1979).
5. J.C. Shelley and M.Y. Shelley, *Computer simulation of surfactant solutions*, Curr. Opin. Colloid. Interface. Sci, **5**, 101 (2000).
6. S.Y. Chen, G.D. Doolen and W.H. Matthaeus, *Lattice Gas Automata For Simple And Complex Fluids*, J. Stat. Phys., **64**, 1133 (1991).
7. R. Benzi, S. Succi and M. Vergasolla, *The Lattice-Boltzmann equation: Theory and application*, Phys. Rep, **222**, 145 (1992).
8. D.L. Ermak, *A Computer Simulation of Charged Particles in Solution I. Technique and Equilibrium Properties*, J. Chem. Phys, **62**, 4189 (1975).
9. D.L. Ermak and J.A. McCammon, *Brownian Dynamics With Hydrodynamic Interactions*, J. Chem. Phys, **69**, 1352 (1978).
10. D.L. Ermak and Y. Yeh, *Equilibrium Electrostatic Effects On Behavior Of Polyions in Solution - Polyion-Mobile Ion Interaction*, Chem. Phys. Lett, **24**, 243 (1974).
11. M. Elimelech, J. Gregory, X. Jia and R. Williams, *Particle Deposition and Aggregation*, Butterworth-Heinemann Ltd, Oxford (1995).
12. S.F. Edwards and M. Muthukumar, *Brownian Dynamics Of Polymer-Solutions*, J. Chem. Phys, **82**, 5696 (1985).
13. M. Fixman, *Implicit Algorithm For Brownian Dynamics Of Polymers*, Macromolecules, **19**, 1195 (1986).
14. M. Fixman, *Brownian Dynamics Of Chain Polymers*, Faraday. Discuss, **83**, 199 (1987).
15. W.B. Russel, D.A. Saville and W.R. Scholwater, *Colloidal Dispersions*, Cambridge

References

- University Press, Cambridge (1999).
16. E. Braun, *A Model Of Brownian Dynamics For Colloidal Suspensions*, *Physica A*, **103**, 325 (1980).
 17. K. Gaylor, I. Snook and W. van megen, *Comparison Of Brownian Dynamics With Photon-Correlation Spectroscopy Of Strongly Interacting Colloidal Particles*, *J. Chem. Phys*, **75**, 1682 (1981).
 18. I. Snook and W. van Megen, *Dynamic Computer-Simulation Of Concentrated Dispersions*, *J. Chem. Soc. Faraday. Trans.*, **90**, 1133(1994).
 19. D.M. Heyes and P.J. Mitchell, *Self-Diffusion And Viscoelasticity Of Dense Hard-Sphere Colloids*, *J. Chem. Phys*, **88**, 1185 (1988).
 20. B.H. Bijsterbosch, M.T.A. Bos, E. Dickinson, et al., *Brownian Dynamics Simulation Of Particle Gel Formation: From Argon To Yoghurt*, *Faraday Discuss*, **98**, 97 (1994).
 21. M.T.A. Bos and J.H.J. van Opheusden, *Brownian Dynamics Simulation Of Gelation And Aging In Interacting Colloidal Systems*, *Phys. Rev. E.*, **53**, 5044(1996).
 22. J.F.M. Lodge and D.M. Heyes, *Brownian Dynamics Simulations Of Aggregation And Gel Formation In Lennard-Jones Fluids*, *Phys. Chem. Liq.*, **31**, 209 (1996).
 23. J.F.M. Lodge and D.M. Heyes, *Brownian Dynamics Simulations Of Domain Growth In Lennard-Jones Fluids*, *Mol. Simulat.*, **18**, 155 (1996).
 24. J.F.M. Lodge and D.M. Heyes, *Brownian Dynamics Simulations Of Lennard-Jones Gas/Liquid Phase Separation And Its Relevance To Gel Formation*, *J. Chem. Soc. Faraday. Trans.*, **93**, 437(1997).
 25. J.F.M. Lodge and D.M. Heyes, *Structural Evolution Of Phase-Separating Model Colloidal Liquids By Brownian Dynamics Computer Simulation*, *J. Chem. Phys*, **109**, 7567 (1998).
 26. J.F.M. Lodge and D.M. Heyes, *Rheology Of Transient Colloidal Gels By Brownian Dynamics Computer Simulation*, *J. Rheol.*, **43**, 219 (1999).
 27. J.F.M. Lodge and D.M. Heyes, *Transient Colloidal Gels By Brownian Dynamics Computer Simulation*, *Phys. Chem. Chem. Phys.*, **1**, 219 (1999).
 28. J.F.M. Lodge and D.M. Heyes, *Brownian Dynamics Computer Simulations Of Quenched Lennard-Jones-Like Fluids: I Morphology And Local Structural Evolution*, *Mol. Sim.*, **23**, 203 (1999).

References

29. K.G. Soga, J.R. Melrose and R.C. Ball, *Continuum Percolation And Depletion Flocculation*, J. Chem. Phys, **108**, 6026 (1998).
30. K.G. Soga, J.R. Melrose and R.C. Ball, *Metastable States And The Kinetics Of Colloid Phase Separation*, J. Chem. Phys, **110**, 2280 (1999).
31. A.M. Puertas, J.A. Maroto JA, A.F. Barbero and F.J. de las Nieves, *Particle Interactions In Colloidal Aggregation By Brownian Dynamics Simulation*, Phys. Rev. E., **59**, 1943(1999).
32. M. Hutter, *Local Structure Evolution In Particle Network Formation Studied By Brownian Dynamics Simulation*, J. Colloid. Interf. Sci., **231**, 337 (2000).
33. A. Einstein, *On the Theory of Brownian Movement*, Ann. d. Phys., **19**, 371(1906).
34. J.M. Deutch and I. Oppenheim, *The Concept Of Brownian-Motion In Modern Statistical-Mechanics*, Faraday Discuss., **83**, 1 (1987).
35. D.A. McQuarrie, *Statistical Mechanics*, Harper and Row, New York (1976).
36. R. Zwanzig, *Ensemble Method in the Theory of Irreversibility*, J. Chem. Phys, **33**, 1338 (1960).
37. H. Mori, *Transport, Collective Motion and Brownian Motion*, Prog. Theor. Phys., **33**, 423(1965).
38. G. Bossis, B. Quentrec and J.P. Boon, *Brownian Dynamics And The Fluctuation Dissipation Theorem*, Mol. Phys. **45**, 191(1982).
39. W.F. Vangunsteren and H.J.C. Berendsen, *On The Fluctuation Dissipation Theorem For Interacting Brownian Particles*, Mol. Phys. **47**, 721(1982).
40. T. Akesson and B. Johnson, *Brownian Dynamics Simulation Of Interacting Particles*, Mol. Phys. **54**, 369(1985).
41. M. Doi and S.F. Edwards. *The Theory Of Polymer Dynamics*, Clarendon, Oxford, (1986).
42. M. Fixman, *Simulation of Polymer Dynamics. I. General Theory*, J. Chem. Phys. **69**, 1527(1978).
43. J.F. Brady and G. Bossis, *Stokesian Dynamics*, Annu. Rev. Fluid Mech., **20**, 111 (1988).
44. L. Durlofsky, J. F. Brady and G. Bossis, *Dynamic Simulation Of Hydrodynamically Interacting Particles*, J.Fluid Mech. **180**, 21(1987).
45. M.R. Pear and J.A. McCammon, *Brownian Dynamics Of Alkanes With*

References

- Hydrodynamic Interactions*, Bull. Am. Phys.Soc., **26**, 368 (1981).
46. E. Dickinson, *Brownian Dynamics With Hydrodynamic Interactions - The Application To Protein Diffusional Problems*, Chem. Soc. Rev., **14**, 421 (1985).
 47. D.M. Heyes, *Brownian Dynamics Simulations Of Self And Collective Diffusion Of Near Hard Sphere Colloidal Liquids: Inclusion Of Many-Body Hydrodynamics*, Mol. Phys., **87**, 287(1996).
 48. P.J. Hoogerbrugge and J.M.V.A. Koelman, *Simulating Microscopic Hydrodynamic Phenomena With Dissipative Particle Dynamics*, Europhys. Lett. **19**, 155 (1992).
 49. P.J. Hoogerbrugge and J.M.V.A. Koelman, *Dynamic Simulations Of Hard-Sphere Suspensions Under Steady Shear*, Europhys. Lett. **21**, 363 (1993).
 50. P. Espanol and P.B. Warren, *Statistical-mechanics of dissipative particle dynamics*, Europhys. Lett., **30**, 191 (1995).
 51. P.V. Coveney and P. Espanol, *Dissipative Particle Dynamics For Interacting Multicomponent Systems*, J. Phys. A-Math. Gen., **30**, 779 (1997).
 52. E.S. Boek, P.V. Coveney, H.N.W. Lekkerkerker, *Computer Simulation Of Rheological Phenomena In Dense Colloidal Suspensions With Dissipative Particle Dynamics*, J. Phys-Condens. Mat., **8**, 9509 (1996).
 53. E.S. Boek, P.V. Coveney, H.N.W. Lekkerkerker, *Simulating The Rheology Of Dense Colloidal Suspensions Using Dissipative Particle Dynamics*, Phys. Rev. E, **55**, 3124 (1997).
 54. J. van der Werff J and C. de Kruif, *Hard-Sphere Colloidal Dispersions - The Scaling Of Rheological Properties With Particle-Size, Volume Fraction, And Shear Rate*, J. Rheol., **33**, 421 (1989).
 55. P. Espanol, *Dissipative Particle Dynamics for a harmonic chain: a first-principle derivation*, Phys. Rev. E, **52**, 5070 (1996).
 56. N.A. Spenley, *Scaling Laws For Polymers In Dissipative Particle Dynamics*, Europhys. Lett., **49**, 534 (2000).
 57. S. Jury S, P. Bladon, M. Cates et al., *Simulation Of Amphiphilic Mesophases Using Dissipative Particle Dynamics*, Phys.Chem. Chem. Phys., **1**, 2051(1999).
 58. R.D. Groot and T.J. Madden, *Dynamic Simulation Of Diblock Copolymer Microphase Separation*, J. Chem. Phys, **108**, 8713 (1998).
 59. R.D. Groot, T.J. Madden and D.J. Tildesley, *On The Role Of Hydrodynamic*

References

- Interactions In Block Copolymer Microphase Separation*, J. Chem. Phys, **110**, 9739 (1999).
60. J.B. Gibson, K. Chen and S. Chynoweth, *Simulation of particle adsorption onto a polymer-coated surface using the dissipative particle dynamics method*, J. Colloid. Interf. Sci., **206**, 464 (1998).
61. J.B. Gibson, K. Zhang, K. Chen *et al.*, *Simulation Of Colloid-Polymer Systems Using Dissipative Particle Dynamics*, Mol. Simulat., **23**, 1 (1999).
62. P. Malfreyt and D.J. Tildesley, *Dissipative Particle Dynamics Simulations Of Grafted Polymer Chains Between Two Walls*, Langmuir, **16**, 4732 (2000).
63. J.L. Jones, M. Lal, J.N. Ruddock *et al.* *Dynamics Of A Drop At A Liquid/Solid Interface In Simple Shear Fields: A Mesoscopic Simulation Study*, Faraday Discuss. **112**, 129 (1999).
64. A.T. Clark, M. Lal, J.N. Ruddock *et al.* *Mesoscopic Simulation Of Drops In Gravitational And Shear Fields*, Langmuir, **16**, 6342 (2000).
65. R.D. Groot and P.B. Warren, *Dissipative Particle Dynamics: bridging the gap between atomistic and mesoscopic simulation*, J. Chem. Phys, **107**, 4423 (1997).
66. A.G. Schlipper, P.J. Hoogerbrugge and C.W. Manke, *Computer simulation of dilute polymer solution with the Dissipative Particle Dynamics Method*, J. Rheol, **39**, 567 (1995).
67. Y. Kong, C.W. Manke, W.G. Madden and A.G. Schlipper, *Effect of solvent quality on the conformation and relaxation of polymers via Dissipative Particle Dynamics*, J. Chem. Phys, **107**, 592 (1997).
68. Y. Kong, C.W. Manke, W.G. Madden and A.G. Schlipper, *Modelling the rheology of polymer solutions by Dissipative Particle Dynamics*, Tribol. Lett, **3**, 133 (1997).
69. Y. Kong, C.W. Manke, W.G. Madden and A.G. Schlipper, *Simulation of a confined polymer in solution using the Dissipative Particle Dynamics method*, Int. J. Thermophys, **15**, 1093 (1994).
70. A.G. Schlipper, C.W. Manke and W.G. Madden, Y. Kong, *Computer simulation of non-Newtonian fluid rheology*, Int. J. Mod. Phys. C, **8**, 919 (1997).
71. W.C.K. Poon and M.D. Haw, *Mesoscopic structure formation in colloidal aggregation and gelation*, Adv. Colloid. Interfac., **62**, 1 (1995).
72. H.N.W. Lekkerkerker, *Strong, weak and metastable liquids*, Physica A, **244**, 227

References

- (1997).
73. G.A. Vliegthart, J.F.M. Lodge and H.N.W. Lekkerkerker, *Strong Weak And Metastable Liquids Structural And Dynamical Aspects Of The Liquid State*, Physica A, **263**, 378 (1999).
 74. P.N. Pusey, in J.P. Hansen, D. Levesque and J. Zinn-Justin(Eds), *Liquids, Freezing and the Glass Transition*, Vol **2**, Elsevier (1991).
 75. B.V. Derjaguin and L.D. Landau, *Theory of the Stability of Strongly Charged Lyophobic Sols and of the Adhesion of Strongly Charged Particles in Solutions of Electrolytes*, Acta Physicochim. URSS, **14**, 733 (1941).
 76. E.J.W. Verwey and J. Th.G. Overbeek, *Theory of the Stability of Lyophobic Colloid*, Elsevier, Amsterdam(1948).
 77. D.J. Shaw, *Introduction to colloid and surface chemistry*, Butterworth and Heinemann, Oxford (1997).
 78. R.J. Hunter, *Foundations of Colloid Science*, Vol **1**, Oxford University Press, Oxford(1987).
 79. R.J. Hunter, *Introduction to Modern of Colloid Science*, Oxford University Press, Oxford(1987).
 80. J.M. Victor and J.P. Hansen, *Spinodal Decomposition And The Liquid Vapor Equilibrium In Charged Colloidal Dispersions*, J. Chem. Soc. Farad. Trans., **2**, (1985).
 81. P. Meakin, *Formation Of Fractal Clusters And Networks By-Irreversible Diffusion-Limited Aggregation*, Phys. Rev. Lett. **51**, 1119 (1983).
 82. G.C. Ansell and E. Dickinson, *Short-Range Structure Of Simulated Colloidal Aggregates*, Phys. Rev. A, **35**, 2349 (1986).
 83. P. Meakin, *Aggregation Kinetics*, Adv. Colloid and Interface Sci., **28**, 249 (1988).
 84. J. Kaldasch, J. Laven J and H.N. Stein, *Equilibrium Phase Diagram Of Suspensions Of Electrically Stabilized Colloidal Particles*, Langmuir, **12**, 6197 (1996).
 85. M. Carpineti, F. Ferri, M. Giglio, *et al.*, *Salt-Induced Fast Aggregation Of Polystyrene Latex*, Phys. Rev. A, **42**, 7347 (1990).
 86. J. Bibette, D.C. Morse and T.A. Witten, *et al.*, *Stability-Criteria For Emulsions*, Phys.Rev.Lett., **69**, 2439(1992).
 87. J.F. Brady, *Model Hard-Sphere Dispersions: Statistical Mechanical Theory*,

References

- Simulations, And Experiments*, Curr. Opin. Colloid. Interface. Sci, **1** , 472 (1996).
88. D.R. Foss and J.F. Brady, *Brownian Dynamics Simulation Of Hard-Sphere Colloidal Dispersions*, J. Rheol, **44**, 629 (2000).
 89. J.W. Goodwin, R.W. Hughes, H.M. Kwaambwa and P.A. Reynolds, *The Phase Separation Behaviour And The Viscoelastic Properties Of Particles With Non-Adsorbing Polymers: Part I - Experimental Study*, Colloids Surfaces A, **161**, 339 (2000).
 90. C.J. Rueb and C.F. Zukoski, *Viscoelastic Properties Of Colloidal Gels*, J. Rheol, **41**, 197 (1997).
 91. C.J. Rueb and C.F. Zukoski, *Rheology of suspensions of weakly attractive particles: Approach to gelation*, J. Rheol, **42**, 1451 (1998).
 92. R.W. Zwanzig, *High-Temperature Equation Of State By A Perturbation Method . 1. Nonpolar Gases*, J. Chem. Phys., **22**, 1420 (1954).
 93. J.A. Barker and D. Henderson, *Perturbation Theory And Equation Of State For Fluids .2. A Successful Theory Of Liquids*, J. Chem. Phys., **47**, 4714 (1967).
 94. W.R. Smith, J.A. Barker and D. Henderson, *Approximate Evaluation Of Second-Order Term In Perturbation Theory Of Fluids*, J. Chem. Phys., **53**, 508 (1970).
 95. W.R. Smith, J.A. Barker and D. Henderson, *Perturbation Theory And Radial Distribution Function Of Square-Well Fluid*, J. Chem. Phys., **64**, 4244 (1976).
 96. D. Chandler and J.D. Weeks, *Equilibrium Structure Of Simple Liquids*, Phys. Rev. Lett., **25**, 149 (1970).
 97. D. Chandler, J.D. Weeks and H.C. Andersen, *Role Of Repulsive Forces In Determining Equilibrium Structure Of Simple Liquids*, J. Chem. Phys, **12**, 5237 (1971).
 98. H.C. Andersen, J.D. Weeks and D. Chandler, *Relationship Between Hard-Sphere Fluid And Fluids With Realistic Repulsive Forces*, Phys. Rev. A., **4**, 1597 (1971).
 99. J.D. Weeks, D. Chandler and H.C. Andersen, *Perturbation Theory Of Thermodynamic Properties Of Simple Liquids*, J. Chem. Phys, **55**, 5422 (1971).
 100. A.P. Gast, C.K. Hall and W.B. Russel, *Polymer-Induced Phase Separations In Non-Aqueous Colloidal Suspensions*, J. Colloid. Interf. Sci., **96**, 251 (1983).
 101. L.P. Voegtli and C.F. Zukoski, *A Perturbation Treatment Of The Order-Disorder Phase-Transition In Colloidal Suspensions*, J. Colloid. Interf. Sci., **141**, 79 (1991).

References

102. J. Kaldasch, J. Laven and H.N. Stein, *Equilibrium Phase Diagram Of Suspensions Of Electrically Stabilized Colloidal Particles*, *Langmuir*, **12**, 6197 (1996).
103. K.R. Hall, *Another Hard-Sphere Equation Of State*, *J. Chem. Phys.*, **57**, 2252 (1972).
104. B.J. Alder, W.G. Hoover and D.A. Young, *Studies In Molecular Dynamics .V. High-Density Equation Of State And Entropy For Hard Disks And Spheres*, *J. Chem. Phys.*, **49**, 3688 (1968).
105. M.S. Wertheim, *Exact Solution Of Percus-Yevick Integral Equation For Hard Spheres*, *Phys. Rev. Lett.*, **10**, 321 (1963).
106. W.R. Smith and D. Henderson, *Analytical Representation Of Percus-Yevick Hard-Sphere Radial Distribution Function*, *Mol. Phys.*, **19**, 411 (1970).
107. Y.M. Choi, T. Ree and F.H. Ree, *Hard-Sphere Radial-Distribution Functions For Face-Centered Cubic And Hexagonal Close-Packed Phases - Representation And Use In A Solid-State Perturbation-Theory*, *J. Chem. Phys.*, **95**, 7548 (1991).
108. R. Zwanzig and R.D. Mountain, *High-Frequency Elastic Moduli Of Simple Fluids*, *J. Chem. Phys.*, **43**, 4464 (1965).
109. S.S. Narine and A.G. Marangoni, *Microscopic And Rheological Studies Of Fat Crystal Networks*, *J. Cryst. Growth*, **199**, 1315 (1999)
110. S.S. Narine and A.G. Marangoni, *Relating Structure Of Fat Crystal Networks To Mechanical Properties: A Reviews*, *Food Res. Int.*, **32**, 227 (1999)
111. S.S. Narine and A.G. Marangoni, *Mechanical And Structural Model Of Fractal Networks Of Fat Crystals At Low Deformations*, *Phys. Rev. E.*, **60**, 6991 (2000).
112. P.G. de Gennes, *Conformations of polymers attached to an Interface*, *Macromolecules*, **13**, 1069 (1980).
113. S. Alexander, *Adsorption of chain molecules with a polar head a-scaling description*, *J. Phys (Paris)*, **38**, 983 (1977).
114. S.T. Milner, *Polymer brushes*, *Science*, **251**, 905 (1991).
115. G.S. Grest and M. Murat, *Monte Carlo, Molecular Dynamics simulation in polymer science*, K. Binder, Ed., Oxford University Press, 1994, Ch. 9
116. S.S. Patel and M. Tirrell, *Measurement of forces between surfaces in polymer fluids*, *Ann. Rev. Phys. Chem.*, **40**, 597 (1989).
117. P.Y. Lai and E.B. Zhulina, *Structure of a bidisperse polymer brush - monte-carlo simulation and self-consistent field results*, *Macromolecules*, **25**, 5201 (1992).

References

118. R. Dickman and P.E. Anderson, *Force between grafted polymer brushes*, J. Chem. Phys, **99**, 3112 (1993).
119. P.Y. Lai and K. Binder, *Grafted polymer layer under shear: a Monte Carlo simulation*, J. Chem. Phys, **98**, 2366, (1993).
120. M. Murat and G.S. Grest, *Interaction between grafted polymer brushes: a molecular dynamics study*, Phys. Rev. Lett., **63**, 1074 (1989).
121. Murat, M. And Grest, G.S., *Computer simulation of polymers*, R.J. Roe, Ed., Prentice Hall, Englewood Cliffs, 1991.
122. G.S. Grest, *Grafted polymer brushes: a constant surface pressure molecular dynamics simulation*, Macromolecules, **27**, 418 (1994).
123. D.F.K Shim and M.E. Cates, *Finite extensibility and density saturation effects in the polymer brush*, J. Phys (Paris), **50**, 3535 (1989).
124. T. Pakula and E.B. Zhulina, *Computer-simulation of polymers in thin-layers .2. Structure of polymer melt layers consisting of end-to-wall grafted chains*, J. Chem. Phys., **6**, 4691 (1991).
125. S.T. Milner, *Hydrodynamic penetration into parabolic brushes*, Macromolecules, **24**, 3704 (1991).
126. S.T. Milner, T.A. Witten and M.E. Cates, *Theory of the grafted polymer brush*, Macromolecules, **21**, 2610 (1988).
127. G.H. Peters and D.J. Tildesley, *Computer simulation of the rheology of grafted chains under shear*, Phys. Rev. E, **52**, 1882 (1995).
128. G.S. Grest, *Computer simulations of shear and friction between polymer brushes*, Current Opinion in Colloid and Interface Science, **2**, 271 (1997).
129. C.Y. Lai and P.Y. Lai, *Grafted polymers under strong shear: scaling and non-equilibrium Monte Carlo studies*, Macromol. Theory. Simul, **6**, 835 (1997).
130. J.L. Barrat, *A possible mechanism for swelling of polymer brushes under shear*, Macromolecules, **25**, 832(1992).
131. J.L. Harden. and M.E. Cates, *Deformation of grafted polymer layers in strong shear flows*, Phys. Rev. E, **53**, 3783 (1996).
132. M. Aubouy, J.L. Harden. and M.E. Cates, *Shear-induced deformation and desorption of grafted polymer layers*, J. Phys II France, **6**, 969 (1996).
133. I.M. Neelov, O.V. Borisov and K.Binder, *Shear deformation of two interpenetrating*

References

- polymer brushes: stochastic dynamics simulation*, J. Chem. Phys., **108**, 6973 (1998).
134. I.M. Neelov, O.V. Borisov and K.Binder, *Stochastic dynamics simulation of grafted polymer brushes under shear deformation*, Macromol. Theory. Simul., **7**, 141 (1998).
135. I.M. Neelov and K.Binder, *Brownian dynamics simulation of grafted polymer brushes under shear deformation*, Macromol. Theory. Simul., **4**, 119 (1995).
136. W.T. Ashurst and W.G. Hoover, *Shear viscosity via periodic nonequilibrium molecular-dynamics*, Phys.Lett A, **61**, 175 (1977).
137. C.A. Marsh and J.M. Yeomans, *Dissipative Particle Dynamics: the Equilibrium for Finite Time Steps*, Europhys. Lett, **37**, 511 (1997).
138. C. Pierleoni and J.P. Ryckaert, *Molecular-Dynamics Investigation Of Dynamic Scaling For Dilute Polymer-Solutions In Good Solvent Conditions*, J. Chem. Phys., **96**, 8539 (1992).
139. G.S. Grest, *Interfacial sliding of polymer brushes: a molecular dynamics simulation*, Phys. Rev. Lett., **76**, 4979 (1996).
140. J. Klein, E. Kumacheva, D. Mahalu, D. Perahia and L.J. Fetters, *Reduction of frictional forces between solid-surfaces bearing polymer brushes*, Nature, **370**, 634 (1994).
141. J. Klein, *Shear, friction and lubrication forces between polymer-bearing surfaces*, Ann. Rev. Mater. Sci., **26**, 581(1996).
142. J. Klein, *Shear of polymer brushes*, Colloids Surfaces A, **86**, 63 (1994).
143. K. Binder, P.Y. Lai and J. Wittmer, *Monte carlo simulations of chain dynamics in polymer brushes*, Faraday Discuss, **98**, 97 (1994).
144. J.M. Haile, *Molecular Dynamics simulation*, (Wiley Interscience, 1992).
145. A.R. Leach, *Molecular modelling – principles and applications*, (Addison Wesley Longman Ltd, 1996).
146. P.B. Warren, *Dissipative Particle Dynamics*, Current Opinion in Colloid and Interface Science, **3**, 620 (1998).
147. E. Ruckenstein and B. Li, *Interaction between grafted brushes*, J. Chem. Phys., **107**, **933** (1997).
148. G.S. Grest and M. Murat, *Structure of grafted polymer brushes in solvents of varying quality: a molecular dynamics study*, Macromolecules, **26**, 3106 (1993).
149. S. Asakura and F. Oosawa, *On interaction between two bodies immersed in a*

References

- solution of macromolecules*, J. Chem. Phys., 22, **1255** (1954).
150. S. Asakura and F. Oosawa, *Interaction between particles suspended in solutions of macromolecules*, J. Polym. Sci., 126, **183** (1958).
151. Y. Baxter-Drayton and J.F. Brady, *Brownian electrorheological fluids as a model for flocculated dispersions*, J. Rheol, **40**, 1027 (1996).
152. J.P. Hansen, *Colloidal suspension: an example of inhomogeneous, complex liquids*, J. Phys-Condens. Mat., **5**, B117 (1993).
153. T.L. Li and K.N. Park, *A Monte Carlo simulation of grafted poly(ethylene oxide) chains*, Comp. Theor. Polym. Sci., **11**, 133 (2001).
154. C.M. Chen and Y.A. Fwu, *Monte Carlo simulations of polymer brushes*, Phys. Rev. E, **63**, 1506 (2001).
155. R. Dickman and D.C. Hong, *New simulation method for grafted polymeric brushes*, J. Chem. Phys, **95**, 4560, (1991).
156. P.S. Doyle, E.S.G. Shaqfeh and A.P. Gast, *Rheology of Polymer Brushes: A Brownian Dynamics Study*, Macromolecules, **31**, 5474 (1998).
157. P.S. Doyle, E.S.G. Shaqfeh and A.P. Gast, *Rheology of "Wet" Polymer Brushes via Brownian Dynamics Simulation: Steady vs Oscillatory Shear*, Phys. Rev. Lett., **78**, 1182 (1997).
158. M. G. Saphiannikova, V. A. Pryamitsyn and T. Cosgrove, *Self-Consistent Brownian Dynamics Simulation of Polymer Brushes under Shear*, Macromolecules, **31**, 6662 (1998).
159. J. Klein, E. Kumacheva, D. Perahiaand and L.J. Fetters, *Shear forces between sliding surfaces coated with polymer brushes: The high friction regime*, Acta. Polym., **49**, 617 (1998).
160. P.Y. Lai and K. Binder, *Structure and dynamics of polymer brushes near the θ point: A Monte Carlo simulation*, J. Chem. Phys., **97**, 586 (1992).
161. I. Neelov, F. Sundholm and K. Binder, *Stochastic dynamics of polymer brushes under shear deformation*, J. Non-Cryst. Solids., **235**, 731 (1998).
162. T.S. Chow, *Mesoscopic physics of complex materials*, Springer-Verlag, New York (2000).
163. P.C. Hiemenz and R. Rajagopalan, *Principles of colloid and surface chemistry*, Marcel Dekker, New York (1997).

References

164. T.G. Mason, *Estimating the viscoelastic moduli of complex fluids using the generalized Stokes-Einstein equation*, Rheol. Acta., **39**, 371 (2000).
165. M.R. Pear and J.H. Weiner, *Brownian dynamics study of a polymer-chain of linked rigid bodies*, J. Chem. Phys., **71**, 212 (1979).
166. S.F. Edwards and M. Muthukumar, *Brownian dynamics of polymer-solutions* Macromolecules, **17**, 586 (1984).
167. H.C. Ottinger, *Brownian dynamics of rigid polymer chains*, Phys. Rev. E, **50**, 2696(1994).
168. L. Li and R.G. Larson, *Brownian dynamics simulations of dilute polystyrene solutions*, J. Rheol., **44**, 291 (2000).
169. S. Ravichandran, J. D. Madura and J. Talbot, *A Brownian dynamics study of the initial stages of hen egg-white lysozyme adsorption at a solid interface*, J. Phys. Chem. B, **105**, 3610 (2001).
170. S.H. Northrup and H.P. Erickson, *Kinetics of protein protein association explained by Brownian dynamics computer-simulation*, P. Natl. Acad. Sci. USA **89**, 3338 (1992).
171. E. Dickinson and S. Krishna, *Aggregation in a concentrated model protein system: a mesoscopic simulation of beta-casein self-assembly*, Food Hydrocolloid., **15**, 107 (2001).
172. C. M. Wijmans and E. Dickinson, *Brownian dynamics simulation of a bonded network of reversibly adsorbed particles : Towards a model of protein adsorbed layers*, Phys. Chem. Chem. Phys., **1**, 2141 (1999).
173. P. Strating, *Brownian dynamics simulation of a hard-sphere suspension*, Phys. Rev. E, **59**, 2175(1999).
174. H. Lowen, J.P.Hansen, J.N. Roux, *Brownian dynamics and kinetic glass-transition in colloidal suspensions*, Phys. Rev. E, **44**, 1169(1991).
175. W.J. Soppe and G.J.M. Janssen, *Brownian dynamics simulation of sediment formation of colloidal particles*, J. Chem. Phys., **99**, 6996 (1992).
176. Y.I. Chang and J.J. Whang, *Deposition of Brownian particles in the presence of energy barriers of DLVO theory: effect of the dimensionless groups*, Chem. Eng. Sci., **53**, 3923 (1998).
177. P.B. Visscheqa P.J. Mitchell, and D.M. Heyes, *Dynamic moduli of concentrated*

References

- dispersions by Brownian dynamics*, J. Rheol., **38**, 465 (1994).
178. M. Hutter, *Coagulation rates in concentrated colloidal suspensions studied by Brownian dynamics simulation*, Phys. Chem. Chem. Phys., **1**, 4429 (1999).
179. P.M. Chaikin and T.C. Lubensky, *Principles of Condensed Matter Physics*, Cambridge University Press, Cambridge (1995).
180. A.S. Kyriakidis, S.G. Yiantsios and A.J. Karabelas, *A study of colloidal particle brownian aggregation by light scattering techniques*, J. Colloid. Interf. Sci., **195**, 299 (1997).
181. P.W. Rouw and C.G. de Kruif, *Adhesive hard sphere collidal dispersion: fractal structures and fractal growth in silica dispersions*, Phys. Rev. A., **39**, 5399 (1989).
182. P. Meakin, *A historical introduction to computer models for fractal aggregates*, J. Sol-Gel Sci.Tech., **15**, 97 (1999).
183. B.K. Johnson, R.F. Sekerka and M.P. Foley, *Scaling of fractal aggregates*, Phys. Rev. E, **52**, 796, (1995).
184. M. Tirado-Miranda *et al.*, *Dynamic scaling and fractal structure of small colloidal clusters*, Colloids Surfaces A, **162**, 67 (2000).
185. A.E. Gonzalez and G. Ramirez-Santiago, *Scaling of the structure factor in fractal aggregation of colloids: computer simulations*, J. Colloid. Interf. Sci., **182**, 254 (1996).
186. D.M. Heyes and A.C. Branka, *Brownian dynamics simulations of self-diffusion and shear viscosity of near-hard-sphere colloids*, Phys. Rev. E, **50**, 2377, (1994).
187. W.H. Boersma, J. Laven and H.N. Stein, *Computer simulations of shear thickening of concentrated dispersions*, J. Rheol., **39**, 841 (1995).
188. S.L. Elliott and W.B. Russel, *High frequency shear modulus of polymerically stabilized colloids*, J. Rheol., **42**, 361 (1998).
189. M.C. Newstein *et al.*, *Microstructural changes in a colloidal liquid in the shear thinning and shear thickening regimes*, J. Chem. Phys., **111**, 4827 (1999).
190. R.R. Bilodeau and D.W. Bousfield, *Shear-thinning predictions from particle motion modeling*, J. Rheol., **42**, 743 (1998).
191. G. Bossis *et al.*, *Rheology and microstructure in colloidal suspensions*, Phys. Scripta , **49**, 89 (1993).
192. T.N. Phung, J.F. Brady and G. Bossis, *Stokesian dynamics simulation of Brownian*

References

- suspensions*, J. Fluid. Mech., **313**, 181 (1996).
193. R.D. Groot, *Mesosopic simulation of polymer-surfactant aggregation*, Langmuir, **16**, 7493 (2000).
194. R.C. Ball and J.R. Melrose, *A simulation technique for many spheres in quasi-static motion under frame-invariant pair drag and Brownian forces*, Physica A, **247**, 444 (1997).
195. C.M. Wijmans, B. Smit and R.D. Groot, *Phase behavior of monomeric mixtures and polymer solutions with soft interaction potentials*, J. Chem. Phys., **114**, 7644 (2001).
196. R.E. van Vliet *et al.*, *Pressure-induced phase separation of polymer-solvent systems with dissipative particle dynamics*, Macromol. Theor. Simul., **9**, 698 (2000).
197. R.L.C. Akkermans and W.J. Briels, *Coarse-grained dynamics of one chain in a polymer melt*, J. Chem. Phys., **113**, 6409 (2000).
198. K. Zhang and C.W. Manke, *Simulation of polymer solutions by dissipative particle dynamics*, Mol. Simulat., **25**, 157 (2000).
199. H. Graf and H. Lowen, *Phase diagram of tobacco mosaic virus solutions*, Phys. Rev. E, **59**, 1932, (1999).
200. W.C.K. Poon, *Crystallization of globular proteins*, Phys. Rev. E, **55**, 3762, (1997).
201. R. Piazza, *Interactions in protein solutions near crystallisation: a colloid physics approach*, J. Crys.Growth , **196**, 415 (1999).
202. C. Haas and J. Drenth, *Understanding protein crystallization on the basis of the phase diagram*, J. Crys.Growth , **196**, 388 (1999).